POLITECNICO DI TORINO
Repository ISTITUZIONALE

Hierarchical component-wise models for enhanced stress analysis and health monitoring of composites structures

Original
Hierarchical component-wise models for enhanced stress analysis and health monitoring of composites structures / GARCIA DE MIGUEL, Alberto. - (2019 Mar 11), pp. 1-236.

Availability:
This version is available at: 11583/2729658 since: 2019-03-29T08:54:39Z

Publisher:
Politecnico di Torino

Published
DOI:10.6092/polito/porto/2729658

Terms of use:
openAccess

This article is made available under terms and conditions as specified in the corresponding bibliographic description in the repository

Publisher copyright

(Article begins on next page)

04 August 2020

Doctoral Dissertation
Doctoral Program in Mechanical Engineering (XXXI cycle)

Hierarchical component-wise models for enhanced stress analysis and health monitoring of composites structures

Alberto García de Miguel

Supervisors
Prof. Erasmo Carrera
Dr. Alfonso Pagani

Politecnico di Torino February 2019

A las personas que me han llevado hasta aquí

Declaration

I hereby declare that, the contents and organisation of this dissertation constitute my own original work and does not compromise in any way the rights of third parties, including those relating to the security of personal data.

Alberto García de Miguel
February 2019

Acknowledgements

The content of this dissertation would be empty without the contribution and support of many colleagues. First, my most sincere acknowledgment is dedicated to Prof. Erasmo Carrera for his guidance and support. He embraced me as a student and made me the researcher I am today, with dedication, passion and affection. I am also deeply grateful to my supervisor Dr. Alfonso Pagani, who gave substance to my work and encouraged me with his example and devotion to research.

I would like to express my gratitude to Prof. Wenbin Yu, who shared with me his extensive knowledge in composite simulation and micromechanics during my stay at Purdue University.

This work was only possible thanks to the thoughtful support of my colleagues of the Mul2 Team at Politecnico di Torino: Marco, Enrico, Matteo, Mirella, Daniele, Manish, Andrea, Riccardo, Tommaso, among others, who were always available for any help. Especially, I highly value the contribution of Ibrahim Kaleel, Guohong Li and Alberto Fiordilino, with whom I had the pleasure to grow personally and professionally during these three years.

This research was carried out within the project FULLCOMP - FULLy integrated analysis, design, manufacturing, and health monitoring of COMPosite structures, funded by the European Commission under the program Marie Skłodowska-Curie Innovative Training Networks (MSCA-ITN-ETN) id. 642121. An especial mention goes to my FULLCOMP colleagues and friends: Margarita, Sander, Yanchuan, Gabriele, Sergio, Mayank, Lorenzo, Pietro and Giorgios.

My biggest recognition is dedicated to my family for their constant support and encouragement, and to Florencia, who has illuminated the way to this achievement.

Abstract

The simulation of composite structures demands the introduction of novel computationally-efficient models that must overcome the limitations of traditional metallic-oriented FEM codes. The multiscale nature of composite materials represents a great challenge from the modeling perspective and has reduced the confidence of engineers in the simulation tools, leading to the introduction of higher safety margins in the industry. As a consequence, the use of innovative solutions that exploit the advantages of composite materials in terms of specific properties and design variables is always penalized and, therefore, less attractive.

Addressing this issue, this thesis focuses on the development of a robust formulation for the mechanical analysis of composite structures at different scales. The Carrera unified formulation (CUF) is employed to generate a new beam theory based on a hierarchical non-local expansion of the mechanical variables over the cross-section: the hierarchical Legendre expansion (HLE). The finite element method (FEM) is employed to solve the governing equations of static and dynamic problems. Two classes of locking-free straight and curved beam elements are implemented by means of the mixed interpolation of tensorial components (MITC) method. The modeling of composites is based on a component-wise (CW) approach, for which the different constituents of the structure are kinematically independent.

The applications of the proposed model are divided in two parts: the first addresses the efficient computation of 3D stress fields, covering topics such as micromechanics, mixed elements based on the Reissner mixed variational theorem (RMVT) and free-edge analysis; the second part addresses the structural health monitoring (SHM) of metallic and composite structures, focusing on the use of higher-order structural theories for the time-domain analysis of Lamb waves. All the proposed theories and applications presented in this thesis are verified via analytical and numerical references.

Table of contents

List of figures xv

List of tables xxi

Nomenclature xxiii

1 Introduction **1**

1.1 Motivation 1

1.2 Objectives 3

1.3 Outline 4

1.3.1 Part I 4

1.3.2 Part II 5

1.3.3 Part III 6

I Hierarchical one-dimensional finite elements **7**

2 Hierarchical beam theories based on the unified formulation **9**

2.1 Preliminaries 10

2.2 Classical beam theories 11

2.3 Carrera unified formulation 14

2.3.1 Taylor expansion 14

2.3.2 Lagrange expansion 15

2.4 Hierarchical Legendre expansion 16

2.5 Cross-section mapping 19

2.5.1 First-order mapping 20

2.5.2 Second-order mapping 21

2.5.3 The blending function method 21

2.6 Examples 22

2.6.1 Square beam 23
2.6.2 Wing structure 24

3 Finite element method 29
3.1 Constitutive equations 29
3.2 Finite element formulation 33
3.2.1 Interpolation of the generalized displacements 34
3.2.2 Principle of virtual displacements 37
3.2.3 Fundamental nucleus 38
3.2.4 Assembly of the stiffness matrix 41
3.3 Example 41

4 Mixed interpolation of tensorial components for beam elements 49
4.1 Shear locking review 49
4.2 Geometrical and constitutive relations 51
4.3 MITC beam elements 52
4.3.1 Fundamental nucleus 55
4.4 Example 57

5 Locking-free curved beam elements 63
5.1 Curved finite elements and membrane locking 63
5.2 Curved beams: the general framework 65
5.3 Geometrical and constitutive relations 66
5.4 Locking-free beam elements 68
5.4.1 Fundamental nucleus 70
5.5 Examples 73
5.5.1 Circular arch 73
5.5.2 Laminated circular disk 76

II Analysis of composite structures via hierarchical beam models 79

6 HLE for composite simulation 81
6.1 Introduction 81
6.2 Composite modeling 83
6.2.1 Meso-scale 83
6.2.2 Micro-scale 87
6.3 Examples 89

6.3.1 Curved sandwich beam 89
6.3.2 Fiber-reinforced structures 91
6.3.3 Curved microstructure 95

7 Micromechanics: mechanics of structure genome 101
7.1 Micromechanics 101
7.1.1 The unit cell problem 102
7.2 Variational Asymptotic Method for UCs 104
7.3 Refined beam models for unit cells 105
7.3.1 Effective properties and local fields 109
7.4 Example 110

8 Refined beam elements based on mixed assumptions 115
8.1 Laminate considerations 115
8.2 Reissner's mixed variational theorem (RMVT) 116
8.3 Constitutive and geometrical relations 117
8.3.1 Geometrical relations 119
8.4 RMVT-based beam theories 119
8.5 Fundamental nucleus 120
8.6 Examples 123
8.6.1 Thick laminates 123
8.6.2 Composite sandwich 127

9 Free-edge analysis 133
9.1 The free-edge problem in the literature 133
9.2 High-fidelity beam models for free-edge analysis 136
9.3 Failure criteria 137
9.4 Examples 138
9.4.1 Pipes-Pagano problem 138
9.4.2 Failure evaluation of tensile specimen 142
9.5 Further developments 144

III Simulation of Lamb waves for structural health monitoring 147

10 Simulation of Lamb waves via higher-order beams 149
10.1 Introduction to Lamb waves 149
10.2 Beam theories for Lamb waves 152

10.2.1 Thin-walled theories 153
10.3 1D elements for wave propagation 154
10.3.1 Governing equations 155
10.3.2 Time integration scheme 155
10.4 Examples 157
10.4.1 Benchmark problem 158
10.4.2 Lamb waves in thin-walled beams 164

11 Structural theories for Lamb wave simulation in laminated structures 167
11.1 Lamb waves in composites 168
11.1.1 Numerical considerations 169
11.2 Higher-order plate elements for wave propagation 170
11.2.1 Thickness expansions 171
11.2.2 Finite element matrices 173
11.3 Examples 176
11.3.1 Laminates 177
11.3.2 Single-lap debond 182

References 191

Appendix A 2D Legendre polynomials 207

List of figures

1.1 Pyramidal diagram of multiscale design of composite materials. Image from [74]. 2
1.2 X-radiograph of a [25,-25,90]$_s$ tensile specimen from [54]. 3
1.3 Illustration of the operation of Lamb wave-based SHM systems. 4

2.1 Cartesian coordinate system used for a beam structure. 10
2.2 Possible displacements and shear deformations that can be predicted by the different classical theories. 13
2.3 Hierarchical set of F_τ 2D functions used to generate HLE. 17
2.4 Differences between various refined 1D CUF finite elements 19
2.5 Jacobian transformation of the quadrilateral domains of the cross-section, based on [189]. 20
2.6 Mapping of the cross-section domain by the BFM. 22
2.7 Geometry and loading case of the squared beam example. 23
2.8 Vertical displacement, u_z, along the bottom edge of the loaded section, $[:, L, -h/2]$. 25
2.9 Longitudinal, σ_{yy}, and shear, σ_{yz}, stresses through the thickness at the center of the beam structure, $[0, L/2, :]$. 26
2.10 Illustration of the monocoque wing structure. 26
2.11 HLE discretization of the wing profile and loading. 27
2.12 Deformations of the loaded section of the monocoque wing. 28
2.13 Monocoque wing under distributed line load. 28

3.1 Global and material reference systems. 30
3.2 Material rotation angles. 32
3.3 Lagrange and Legendre interpolation polynomials. 36

3.4 Construction of the stiffness matrix of CUF-based beam elements. The model shown includes 1 HLE domain of third-order and 8 four-noded beam elements. 42

3.5 Scordelis–Lo problem features. 43

3.6 HLE beam model for the Scordelis-Lo roof. 43

3.7 Deformation of the Scordelis-Lo roof. 44

3.8 Convergence of various Lagrange 1D meshes for increasing polynomial orders of the HLE. 46

3.9 Convergence analysis with respect to the number of DOF for a HL5 theory and all the discussed 1D meshes. 47

4.1 Strain tensor in the current coordinate framework. 51

4.2 MITC element interpolations of shear strains. 54

4.3 Cantilever beam under shear-bending loading. The beam is modeled using a single 1D element. 57

4.4 Distribution of shear stresses, σ_{yz}, over the beam's length for L4 expansion. The Timoshenko's analytical solution is $\sigma_{yz} = -1.0 \times 10^4$ Pa. 60

4.5 Convergence of the vertical displacement, u_z, at the tip for linear elements with different integration schemes. 60

4.6 Distribution of shear stresses, σ_{yz}, across the thickness of the beam for a single B4 MITC element at $y = L/3$. 61

5.1 Illustration of the membrane-bending coupling in curved structures. 64

5.2 Frenet-Serret coordinate system of a reference beam. 65

5.3 Characteristics of the arch under study. 73

5.4 Radial displacement, $\bar{u}_\xi$, against the number of two-noded curved elements. Slenderness ratios $L/h = 5$ and $L/h = 500$. 74

5.5 Radial displacement, $\bar{u}_\xi$, against the number of three-noded curved elements. Slenderness ratios $L/h = 5$ and $L/h = 500$. 75

5.6 Radial displacement, $\bar{u}_\xi$, against the number of four-noded curved elements. Slenderness ratios $L/h = 5$ and $L/h = 500$. 75

5.7 Features of the hollow laminated disk and proposed beam model. 76

5.8 Radial displacement, u_ξ, through the thickness of the laminated disk. References from [187]. 77

5.9 Radial, $\sigma_{\xi\xi}$, and circumferential, σ_{ss}, stress fields through the thickness of the laminated disk. References from [187]. 78

5.10 Stress fields over the eight-layer curved beam for the third order HL3 model. 78

6.1 Reference system of the current frame for meso-scale analysis. 84
6.2 Assembly procedure of the stiffness matrix through ESL and LW approaches 85
6.3 Reference system of the current frame for micro-scale analysis. 87
6.4 Different approaches available via HLE modeling. 88
6.5 HLE model of the curved sandwich. 89
6.6 Deformed of the sandwich beam. 90
6.7 Stress distributions across the thickness at point B and $y = L/2$. 91
6.8 Longitudinal and shear stress fields at midspan. 92
6.9 Geometry of the cross-ply beam. 92
6.10 Discretizations and stress fields computed using different approaches: LW (a), (d) and (g); CW (b), (e) and (h); and mixed LW-CW (c), (f) and (i). . . . 94
6.11 Stresses distributions through the thickness at [5b/8,L/2,:] computed by the HL6 model. The figure attached to the bottom of the graphs represent a vertical strip of the composite structure and the vertical black lines are added to indicate the domains of the fiber, matrix and layer in the model. Note: HEXA8 = solid, model 1 = LW, model 2 = CW, model 3 = mixed CW-LW. . 96
6.12 Geometry and section of the fiber-matrix microstructure. Distances in mm and forces in N. 96
6.13 Contour plots of the displacements (m). 98
6.14 Longitudinal stresses (Pa) over the naked fibers. 98
6.15 Radial stresses (Pa) over the naked fibers. 99
6.16 Shear stresses, $\sigma_{s\xi}$, (Pa) over the naked fibersl. 99

7.1 Coordinate reference systems of a periodic heterogeneous material and its UC. 103
7.2 Reference system for the beam modeling of the UC. 106
7.3 HLE beam model of the hexagonal pack UC. 110
7.4 Longitudinal stress σ_{11} generated by a unitary longitudinal strain ε_{11}. Reference values from [181]. 112
7.5 Shear stress σ_{13} generated by a unitary shear strain ε_{13}. Reference values from [181]. 112
7.6 Shear stress σ_{23} generated by a unitary shear strain ε_{23}. Reference values from [181]. 113
7.7 Shear stress σ_{12} generated by combined strains ε_{11} and ε_{13}. Reference values from [181]. 113

8.1 Typical displacement and transverse stress fields across the thickness of multilayered structures. 116

8.2 Representation of the proposed refined beam element (a) and the distribution of the unknowns over the cross-section (b) in a two-layer laminate. 120
8.3 Loading case of the laminates. 124
8.4 Longitudinal stress of the symmetric 3 layer laminate at *y=L/2*. References from [32]. 126
8.5 Transverse normal stress of the symmetric 3 layer laminate at *y=L/2*. References from [32]. 126
8.6 Transverse shear stress of the symmetric 3 layer laminate at *y=0*. References from [32]. 127
8.7 Longitudinal displacements of the anti-symmetric laminate at *y=0*. References from [25]. 128
8.8 Transverse normal stress of the anti-symmetric layer laminate at *y=L/2*. References from [25]. 128
8.9 Transverse shear stress of the anti-symmetric layer laminate at *y=0*. References from [25]. 129
8.10 Transverse shear stresses of the [0/90/0] and [0/90/0/90] laminates with imposed stress-free boundary conditions. References from [25]. 129
8.11 Loading case of the composite sandwich. 130
8.12 Longitudinal stress of the composite sandwich at $y = L/2$. References from [83]. 131
8.13 Transverse shear stress of the composite sandwich at $y = 0$. References from [83]. 132
8.14 Transverse normal stress of the composite sandwich at $y = 0$. References from [83]. 132

9.1 Free-edge stresses in generic composite beams. 134
9.2 Representation of the FEM modeling of composite laminates using CUF elements. 136
9.3 Geometry and mesh of the laminated beam under axial extension. 139
9.4 Transverse shear stresses along x at $y = L/2$ and $z = h/4$ computed via HLE mixed models. 140
9.5 Transverse shear stresses along z at $y = L/2$ and *x=b/2* computed via HLE mixed models. 140
9.6 Transverse shear stresses along x computed by the HLM4 model for different thicknesses computed via HLE mixed models. 141
9.7 Transverse shear stresses along z at $x = b/2$ computed via displacement-based LE models. 141

9.8 Dimensions and loading conditions of the tensile specimen 142
9.9 Out-of-plane stress components at the free-edge. 143
9.10 Failure index for matrix tension 145
9.11 Failure index for delamination 145
9.12 Failure index for fiber tension 145
9.13 Failure index for fiber tension using the modified criteria 146
9.14 Illustration of the capabilities of refined beam elements for free-edge analysis. 146

10.1 Symmetric and antisymmetric first Lamb wave modes. 150
10.2 Dispersion curves of a 5 mm thick aluminum plate. Data from GUIGUW software [20]. 151
10.3 Possible deformations of the beam's section for various theories. The dashed line corresponds to the Euler-Bernouilli model. 153
10.4 HLE modeling of beams 154
10.5 Geometrical features of the metallic strip used in the numerical assessment. Distances in mm. 158
10.6 Time signal of the normalized vertical displacement of the anti-symmetric Lamb wave at points A and B. 159
10.7 Convergence analyses for the $\mathrm{A_0}$ and $\mathrm{S_0}$ waves propagating along the aluminum strip. 160
10.8 Comparison between full integrated elements and MITC elements ($\mathrm{A_0}$). . . 161
10.9 Convergence of the p-order on the transverse direction for $\mathrm{A_0}$ and $\mathrm{S_0}$ modes. 162
10.10 $\mathrm{A_0}$ and $\mathrm{S_0}$ modes in a metallic strip for a single force excitation of 200 kHz. 163
10.11 $\mathrm{A_0}$ and $\mathrm{A_1}$ waves at three different stations ($y_A = 100$ mm in blue, $y_B = 200$ mm in red and $y_C = 300$ mm in grey) for a signal burst of 1.2 MHz. 164
10.12 $\mathrm{A_0}$ and $\mathrm{A_1}$ modes at $t = 6 \times 10^{-5}$ for a signal burst of 1.2 MHz. 165
10.13 Geometry and cross-section mesh of the C-section beam. 165
10.14 Screeshoot of the propagating waves at 5.6 $\times 10^{-}5$ s. 166
10.15 Cut of the C-beam. 166

11.1 Illustration of the fundamental modes of Lamb waves in an anisotropic plate, including out-of-plane symmetric ($\mathrm{S_0}$), out-of-plane antisymmetric ($\mathrm{A_0}$), shear horizontal symmetric (SH-$\mathrm{S_0}$) and shear horizontal antisymmetric (SH-$\mathrm{A_0}$). 168
11.2 Coordinate reference systems for plate elements. 170

11.3 Illustration of the different multi-layered approaches implemented in the present chapter. The curved lines represent possible displacement solutions over the thickness and the dots show the location of the pure displacement unknowns. For the sake of clarity, the stretching effects are not included. . 176

11.4 Top view of the composite plate studied. Units in m. 177

11.5 Contour plot of the vertical displacements (u_z) at $t = 7.5 \times 10^{-5}$ s showing the A$_0$ mode over the unidirectional composite plate. 178

11.6 Contour plots of the in-plane displacements along x (a) and along y (b) at $t = 5 \times 10^{-5}$ s showing the S$_0$ mode and the SH$_0$ mode, respectively. 179

11.7 Plots of the vertical displacements, u_z, at $t = 7.5 \times 10^{-5}$ s (a-c) and $t = 1.5 \times 10^{-4}$ s (d-f) showing the A$_0$ waves over the [0°$_2$/90°$_2$]$_S$ laminate. . . . 181

11.8 Plots of the vertical displacements, u_z, at $t = 1.125 \times 10^{-4}$ s showing the A$_0$ waves over the [45°/-45°/0°/90°]$_S$ laminate. 181

11.9 Characteristics and model kinematics of the composite single-lap joint. Units in mm. 183

11.10 Scaled plots showing the S$_0$ waves propagating over the pristine, (a) and (c), and the damaged, (b) and (d), lap joints. 184

11.11 Contour plot showing the A$_0$ waves over the lap joint at $t = 1.2 \times 10^{-4}$ s. . 185

11.12 In-plane displacements,u_y, over time obtained at point A. 185

List of tables

2.1 Pascal triangle. 14
2.2 Model features: degrees of freedom and expansion terms. 24
2.3 Solutions of displacements and stresses of the square beam example. 25
2.4 Displacement and stress results of the wing with point load. 27
2.5 Displacement and stress results of the wing with distributed loading. 28

3.1 Vertical displacement solutions obtained at point A using Lagrange beam elements for all HLE orders. 45
3.2 Vertical displacement solutions obtained at point A using one Legendre element of increasing order for all HLE orders. 46
3.3 Comparison of the normalized displacements, u_z/u_{ref}, against various results from the literature. 47

4.1 Displacements and shear stresses computed by the different beam elements. 58

5.1 Elastic properties of the materials. $E_2 = 1$ GPa. 73

6.1 Displacements and stress values of the curved sandwich at the evaluating points. 90
6.2 Material properties of the carbon/epoxy composite. 93
6.3 Displacements and stresses of the cross-ply beam for the different models. . 95
6.4 Material properties of the carbon/epoxy composite, taken from [98]. 97
6.5 Maximum deflection, u_{max}, of the curved microstructure. DOF between brackets. 97

7.1 Effective properties of the hexagonal pack (E_i and G_{ij} in GPa). References from [181]. 111
7.2 Computational time (s) of the homogenization and dehomogenization. Reference values from [181]. 111

8.1 Convergence analysis of the beam element discretization based on the maximum transverse displacement $\bar{u}_z = u_z \frac{100E_2h^3}{q_0L^4}$. Number of DOF between parentheses. 124

8.2 Maximum transverse displacement, $\bar{u}_z = u_z \frac{100E_2h^3}{q_0L^4}$, at $z = 0$ of the thick laminates considered. 125

8.3 Mechanical properties of the materials for the composite sandwich example. The values of Young's moduli and shear moduli are normalized with respect to G_{12} of the honeycomb (hc). 130

8.4 Normalized solutions of the maximum axial and transverse shear stresses. All the references are obtained from [83]. 131

9.1 Pipes and Pagano's problem: DOF of each HLE mixed model. 139

9.2 Mechanical properties of the IM7/8552 lamina. 142

9.3 Material strength values of the IM7/8552 lamina. 142

9.4 Model discretizations for the tensile specimen. 143

9.5 Comparison of the failure indices computed by the different models considered under the same loading value 144

9.6 Values of the tensile load corresponding to the onset of failure of each mode considered 144

10.1 Material properties of the Aluminum strip. 158

11.1 Computed group velocities of the fundamental Lamb waves propagating in the unidirectional laminate. 179

11.2 Computed group velocities of the A_0-wave propagating in the unidirectional laminate. 180

Nomenclature

Latin symbols

a, b	cross-section dimensions
$\mathbf{C}$	stiffness matrix of the material in the material frame
$\tilde{\mathbf{C}}$	stiffness matrix of the material in the global frame
c_g	group velocity of the wave
c_p	phase velocity of the wave
$\mathbf{D}$	geometrical differential operator
e	envelope of the displacement signal
E	Young's modulus
$E_{\tau s}$	cross-section integrals
f	frequency
F_τ	cross-section expansion functions of the displacements
G	shear modulus
g	determinant of the metric tensor
G_τ	cross-section expansion functions of the stresses
H	square root of the determinant of the metric tensor
i, j	nodal indexes
L	length of the beam
L_{ext}	work done by the external loads
L_{ine}	work done by the inertial loads
L_{int}	strain energy
$\boldsymbol{I}_3$	3×3 identity matrix
I_{ij}	FEM integrals
$\boldsymbol{J}_y$	Jacobian matrix of the beam element
$\boldsymbol{J}_\Omega$	Jacobian matrix of the cross-section expansion
$\boldsymbol{J}_S$	Jacobian matrix of the plate element
k	layer index
$\mathbf{K}$	global stiffness matrix
$\mathbf{K}^{ij\tau s}$	fundamental nucleus of the stiffness matrix
M	number of expansion terms

$\mathbf{M}$	global mass matrix
$\mathbf{M}^{ij\tau s}$	fundamental nucleus of the mass matrix
N_i, N_j	shape functions of the finite element
N_m, N_n	assumed interpolation functions of the strains
n_c	number of constituents
n_n	number of nodes per element
n_l	number of layers
p	polynomial order
p_b	polynomial order of the shape functions of the beam
$\mathbf{P}^{sj}$	fundamental nucleus of the loading vector
r	natural coordinate
R	radius
S	surface
$\mathbf{t}, \mathbf{b}, \mathbf{n}$	tangent, normal and binormal vectors of the curvilinear frame
$\boldsymbol{u}$	displacement vector
$\mathbf{U}$	vector of the displacement unknowns
$\boldsymbol{u}_\tau$, $\boldsymbol{u}_s$	generalized displacement vector
$\boldsymbol{u}_{\tau i}$, $\boldsymbol{u}_{sj}$	generalized nodal vector
V	volume
x, y, z	Cartesian global coordinates

Greek symbols

$\boldsymbol{\varepsilon}$	strain vector in the beam coordinate system
ϕ_i	Legendre modes
η	natural coordinate
κ	initial curvature of the beam
ν	Poisson ratio
$\boldsymbol{\sigma}$	stress vector in the beam coordinate system
ρ	density
τ	expansion index
T	initial torsion of the beam
ξ	natural coordinate
$\boldsymbol{\chi}$	fluctuations vector
ω	angular frequency
Ω	Cross-section surface

Acronyms and abbreviations

B*n*	1D Lagrangian element of *n* nodes
BFM	Blending Function Method
CUF	Carrera Unified Formulation
CW	Component Wise
DOF	Degrees Of Freedom
ESL	Equivalent Single Layer
EBBT	Euler Bernoulli Beam Theory
EBBT	First-order Shear Deformation Theory
GUW	Guided Ultrasonic Waves
HLE	Hierarchical Legendre Expansion
HL*p*	HLE model of order *p*
HLM*p*	HLE mixed model of order *p*
IC	Interlaminar Continuity
LE	Lagrange Expansion
L4, L9	four-noded and nine-noded LE
LW	Layer Wise
FEM	Finite Element Method
MITC	Mixed Interpolation of Tensorial Components
MITC*n*	1D MITC element of *n* nodes
MSG	Mechanics of Structure Genome
MSC	Micromechanics Simulation Challenge
PVD	Principle of Virtual Displacements
P*p*	1D Legendre element of order *p*
RMVT	Reissner's Mixed Variational Theorem
SBC	Stress Boundary Conditions
SLJ	Single Lap Joint
SHM	Structural Health Monitoring
SVT	Saint Venant Theory
TBT	Timoshenko Beam Theory
TE	Taylor Expansion
TOF	Time Of Flight
UC	Unit Cell
VAM	Variational Asymptotic Method
ZZ	Zig-Zag effect

Chapter 1

Introduction

1.1 Motivation

Composite materials are shaping today's aerospace. Not only that, applications in other fields such as automotive, energy, civil or biomedical are becoming more common every year. These materials are used in structural engineering due to their outstanding combination of mechanical properties and lightness, which make them appropriate for high performance applications. Both major aerospace companies, Airbus and Boeing, have been increasing the relative weight of composites in their commercial models since the 70's, leading to their latest releases, the A350 and the B787 respectively, which are made of more than 50 % of these materials.

Briefly, a composite is a material made of two or more constituents that have different mechanical or chemical properties, which combined exhibit properties that differ from those of the separate components. A well-known example are the fiber-reinforced polymers, which combine the high stiffness of the fibers (carbon, glass, aramid,...) with the ductile properties of the polymer matrix. In engineering applications, these materials are used to create lay-ups and textiles which can be manufactured for a broad variety of shapes in a more automated process. From the design standpoint, a major advantage resides in the increment of design variables, such as the material selection, the volume ratio between fibers and matrix, the ply orientation or the total number of plies, among others, which are not available in traditional metallic designs. As a consequence, the composite structure can be better optimized for the given load cases, thus reducing the total weight and cost.

Although the heterogeneity of composites is the driver of all these advantages, it comes with a price in terms of uncertainty and modeling assumptions. Multiscale approaches must be adopted to understand the mechanical response of composite structures under different working conditions. Therefore, the structural analysis is usually decoupled into different

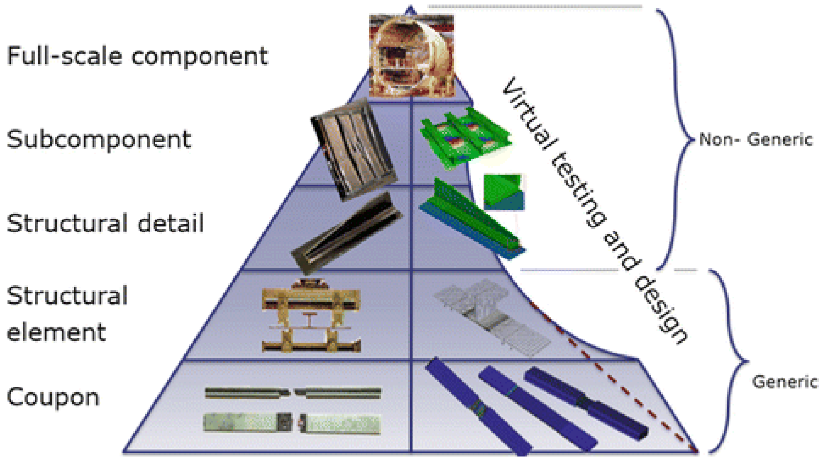

Fig. 1.1 Pyramidal diagram of multiscale design of composite materials. Image from [74].

models that address the physics involved in a certain scale. The effects of the arrangement of the constituents in the effective properties of the homogenized material are studied at the micro-scale. The lay-ups and woven fabrics that conform the test coupons are included in structural models at the meso-scale. Finally, the load bearing capabilities and dynamic response of the structural component is analyzed at the macro-scale with standard simulation tools, such as the finite element method (FEM) [224]. In this computational framework, the constitutive information acquired at each scale is typically transmitted following a bottom-up strategy [119], i.e. from the micro-structure to the component and final structure. However, most of the models used in this process were initially oriented to metallic structures, especially at the larger scales. Consequently, the confidence of the engineers in the simulation is reduced and a huge amount of resources is allocated to experimental tests throughout the design process. Figure 1.1 shows the pyramidal diagram of the virtual testing of composites. In this framework, the ideal scenario is to boost the development of reliable and efficient models for composites which will increase the confidence in the simulation.

One of the main limitations of the metal-oriented simulation tools is the inability to provide the correct state of stress of the structure. Unlike in isotropic thin-walled structures, the transverse and shear deformations play an important role in the response of the composite structure, especially in the failure mechanisms. In general, composite materials exhibit a brittle fracture which is difficult to predict and monitor. Typically, the cause of failure is the coalescence of many intralaminar microcracks and fiber debonds, which lead to delamination and, then, ply failure. Figure 1.2 shows a crack propagating inwards in a tensile coupon which is failing due to the free-edge effects [129]. In order to be able to predict such responses, the structural analysis must be capable of giving an accurate approximation of the strain and

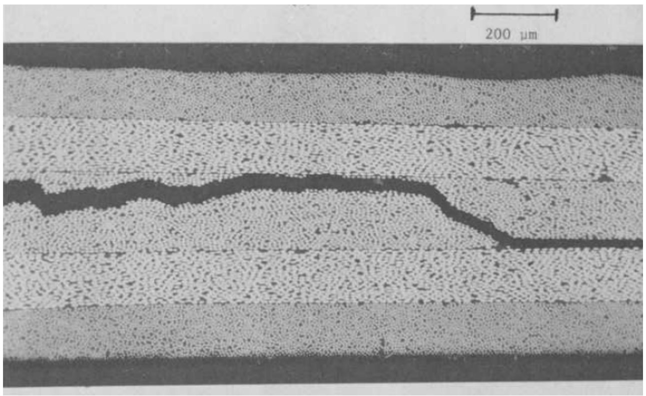

Fig. 1.2 X-radiograph of a $[25,-25,90]_s$ tensile specimen from [54].

stress fields at the ply level. Indeed, the capabilities of any damage model of composites must be deeply questioned if the correct stress distributions are not appropriately included.

Although the knowledge of composite materials has increased exponentially during the last few decades, its application in the large aerospace market is considerably recent and, therefore, a constant monitoring of the structure is demanded. In this line, the field of structural health monitoring (SHM) is gaining importance, in particular focusing on the implementation of on-line systems that inspect the structure during service. The goal of SHM is twofold: first, to assess the nature and severity of eventual structural flaws, allowing it for a rapid response before catastrophic failure; and, also, to optimize the inspection schedules and reduce the maintenance cost.

One of the most popular techniques under investigation for the on-line monitoring of composite structures is the use of ultrasonic guided waves, a.k.a Lamb waves. The concept is based on the deployment of a network of sensor/actuators in the structural parts of interest in such a manner that the eventual scattering of the waves determines the location and type of damage, as illustrated in Fig. 1.3. Given the high frequencies involved in the dynamic problem, the numerical modeling of these systems is a very demanding task from the computational point of view, especially in composite structures.

1.2 Objectives

In view of the aforementioned issues in composite modeling, the present thesis represents an advance towards the efficient implementation of numerical solutions for composite problems. The structural analysis of composites constitutes a broad research topic and it is not the intention here to introduce a new multiscale theory. The focus is on the implementation of a novel modeling framework, based on a unified formulation of structural theories and the

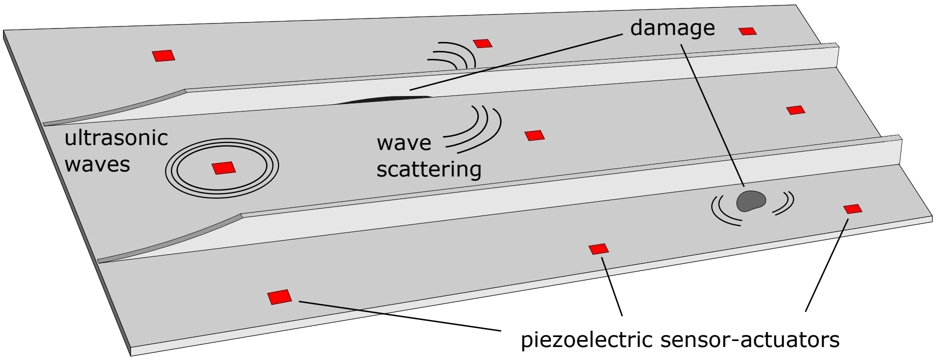

Fig. 1.3 Illustration of the operation of Lamb wave-based SHM systems.

FEM, that is convenient for the solution of composite problems at different scales. The main objectives can be summarized in:

1. Development of a new class of hierarchical models based on a computationally-efficient one-dimensional formulation and the FEM.
2. Computation of the 3D stress fields in generic composite problems with acceptable computational efforts.
3. Simulation of Lamb waves in metallic and composite thin-walled structures for SHM purposes.

1.3 Outline

The thesis is organized in three parts, each of one addresses one of the objectives mentioned previously. The content of the thesis is described in the following.

1.3.1 Part I

Chapter 2 discusses the topic of structural theories for beams and introduces the Carrera unified formulation (CUF) as a generator of 1D models. Based on the latter formulation, a hierarchical beam theory, the hierarchical Legendre expansion (HLE) is presented and several mapping techniques for the cross-section surface are discussed, with particular attention to the blending function method.

Chapter 3 introduces the finite element framework which is used to solve the structural problem. The principle of virtual displacements is recalled and the weak form of the governing equations is obtained. Different polynomial basis are employed to interpolate the unknowns along the beam axis. The fundamental nucleus of the formulation is written, which acts as the building block of the stiffness matrix.

Chapter 4 presents the implementation of a locking-free beam element based on the mixed interpolation of tensorial components (MITC). The issue of shear locking in the FEM is reviewed and the geometrical and constitutive equations rewritten. The fundamental nucleus of the new beam element is obtained.

Chapter 5 extends the formulation of locking-free elements based on MITC to general curved beams. The topics of curved finite elements and membrane locking are briefly discussed. All the previous equations are written in the Frenet-Serret curvilinear system. The fundamental nucleus of the stiffness matrix is also computed in this frame.

1.3.2 Part II

Chapter 6 presents the application of HLE models for the accurate stress evaluation of composite structures. Equivalent single layer (ESL) and layer wise (LW) approaches are described for the analysis of laminates at the meso-scale. The component wise (CW) approach is introduced as an extension of the LW for the modeling of the different constituents of fiber-reinforced composites at lower scales.

Chapter 7 shows the implementation of the current modeling framework in the micromechanics field. The mechanics of structure genome (MSG) is employed to compute the homogenized properties of the composite material and the local stress fields over the microstructure. The CW approach and the HLE are used to introduced a p-refinement scheme in micromechanics models.

Chapter 8 introduces a mixed formulation of displacements and stresses for laminates based on the Reissner's mixed variational theorem (RMVT). The fulfillment of the compatibility and equilibrium conditions at the interfaces is imposed a priori. Both the displacement and stresses are assumed via HLE and the fundamental nuclei of the mixed beam elements are obtained straightforwardly by following the same statements of displacement-based formulations.

Chapter 9 applies the proposed models to the computation of the 3D stress fields at the free edges of laminated structures. It shows the potential of refined beam theories to reduce drastically the computational costs of the simulation of real composite problems without compromising the accuracy. The onset of failure is approximated using the Hashin 3D criteria for the plies and the mixed mode quadratic criteria for the interfaces.

1.3.3 Part III

Chapter 10 discusses the topics of Lamb wave-based SHM and the propagation of ultrasonic waves in thin-walled media. Higher-order beam elements are employed to evaluate the time signals directly at all points of the structure. The time integration scheme, based on the Newmark's solver, is presented. The quality of the numerical solutions is assessed via benchmark tests.

Chapter 11 deals with the simulation of ultrasonic waves in composite laminates. A 2D finite element framework based on the CUF and HLE is introduced and different multi-layered theories are tested. The simultaneous computation of all the Lamb modes is attained. A novel model for the analysis of multi-component structures is derived by mixing ESL and LW theories in the thickness expansion.

Part I

Hierarchical one-dimensional finite elements

Chapter 2

Hierarchical beam theories based on the unified formulation

One-dimensional models, a.k.a. beam models, are widely employed in the design and analysis of slender structures. These dimensionally reduced models exploit the geometry of the structure to assume simple deformations of the cross-section, thus reducing the number of unknowns in the structural problem. In few words, it is assumed that the contribution of the deformation of the cross-section to the global response of the structure is reduced. Therefore, these classical assumptions are valid when the structure is considerably slender and may incur in high errors for medium to short beams. Moreover, the stress analysis of the structure requires more refined tools if non-homogeneous, thin-walled structures are considered.

This chapter provides a brief overview of the most relevant beam theories that are used by engineers and researchers in their structural analysis, paying especial attention to the ability of the different kinematics to capture the deformation of the beam's cross-section. Subsequently, a unified formulation of structural theories, known as the Carrera unified formulation (CUF), is presented as a tool to overcome the insufficiencies of the classical models. In order to improve the existing higher-order models implemented in the CUF framework, a hierarchical beam theory is presented which includes some interesting features for the structural modeling: p-refinement, exact mapping of the cross-section and non-local kinematics. The capabilities of this novel model are demonstrated through a few numerical examples of compact and thin-walled beams.

The contents of the present chapter can be found partially in journal papers [31, 145].

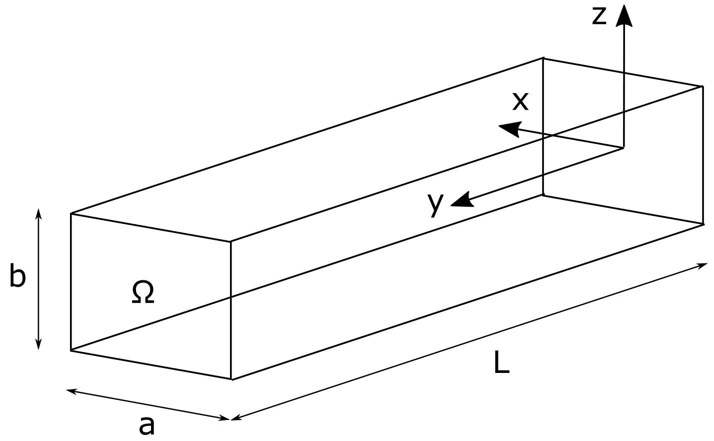

Fig. 2.1 Cartesian coordinate system used for a beam structure.

2.1 Preliminaries

Consider the beam structure of Fig. 2.1, whose length is L and cross-section surface $\Omega = a \times b$. The Cartesian reference system is defined in such a manner that the longitudinal direction corresponds to the y axis, whereas the cross-section lies on the xz plane. The displacements of any point of the structure can be written as:

$$\boldsymbol{u}(x,y,z) = \left\{ \begin{array}{c} u_x(x,y,z) \\ u_y(x,y,z) \\ u_z(x,y,z) \end{array} \right\}. \tag{2.1}$$

According to the present nomenclature, the second component, u_y, correspond to the longitudinal displacements, whereas u_x and u_z are the transverse displacements. Note that the dynamic effects are not included in this discussion, i.e. the time dependency is neglected.

Assuming small deformations, the strain-displacement relations are provided by the Cauchy strain tensor:

$$\varepsilon_{ij} = \frac{1}{2}\left(u_{i,j} + u_{j,i}\right), \tag{2.2}$$

where ε_{ij} is a second order tensor. According to classical elasticity, by exploiting the symmetry of the strain tensor the deformations can be expressed in vectorial form, as follows:

$$\boldsymbol{\varepsilon}^T = \left\{ \begin{array}{cccccc} \varepsilon_{yy} & \varepsilon_{xx} & \varepsilon_{zz} & \varepsilon_{xz} & \varepsilon_{yz} & \varepsilon_{xy} \end{array} \right\}. \tag{2.3}$$

Subsequently, the 3D geometrical relations can be written in matrix form as

$$\left\{\begin{array}{c}\varepsilon_{yy}\\ \varepsilon_{xx}\\ \varepsilon_{zz}\\ \varepsilon_{xz}\\ \varepsilon_{yz}\\ \varepsilon_{xy}\end{array}\right\}=\begin{bmatrix}0 & \frac{\partial}{\partial y} & 0\\ \frac{\partial}{\partial x} & 0 & 0\\ 0 & 0 & \frac{\partial}{\partial z}\\ \frac{\partial}{\partial z} & 0 & \frac{\partial}{\partial x}\\ 0 & \frac{\partial}{\partial z} & \frac{\partial}{\partial y}\\ \frac{\partial}{\partial y} & \frac{\partial}{\partial x} & 0\end{bmatrix}\left\{\begin{array}{c}u_x\\ u_y\\ u_z\end{array}\right\}, \tag{2.4}$$

or, in short:

$$\boldsymbol{\varepsilon}=\mathbf{D}\boldsymbol{u}, \tag{2.5}$$

where **D** is the linear differential operator.

2.2 Classical beam theories

Among the classical beam models, the simplest one corresponds to the Euler-Bernoulli beam theory (EBBT) [73]. The EBBT assumes that the cross-section of the beam remains always undeformed and orthogonal to the beam axis. Mathematically, the kinematic field of the EBBT can be expressed as:

$$\begin{aligned}u_x(x,y,z)=&u_{x_1}(y),\\ u_y(x,y,z)=&u_{y_1}(y)-x\frac{\partial u_{x_1}(y)}{\partial y}-z\frac{\partial u_{z_1}(y)}{\partial y},\\ u_z(x,y,z)=&u_{z_1}(y),\end{aligned} \tag{2.6}$$

where u_x, u_y and u_z are the components of the displacement vector and u_{x_1}, u_{y_1} and u_{z_1} are the unknowns of the problem, which correspond to the displacements of the beam axis. According to the definition of the beam kinematics in Eq. 2.6, all the shear deformations are null. For instance, considering the shear deformation ε_{yz} and according to the Cauchy definition (Eq. (2.2)), we have:

$$\varepsilon_{yz}=\frac{1}{2}\left(u_{y,z}+u_{z,y}\right)=\frac{1}{2}\left(\frac{\partial u_{z_1}}{\partial y}-\frac{\partial u_{z_1}}{\partial y}\right)=0. \tag{2.7}$$

The Timoshenko beam theory (TBT) [196] overcomes this inconsistency of the EBBT model by adding the rotations of the cross-section around x and z, leading to the following displacement field:

$$\begin{aligned} u_x(x,y,z) =& u_{x_1}(y), \\ u_y(x,y,z) =& u_{y_1}(y) + x\phi_z(y) - z\phi_x(y), \\ u_z(x,y,z) =& u_{z_1}(y), \end{aligned} \tag{2.8}$$

being now 5 the number of unknowns: 3 displacements (u_{x_1}, u_{y_1} and u_{z_1}) and 2 rotations (ϕ_z and ϕ_x).

The TBT beam model is suitable for the analysis of slender compact beams under shear and bending, but it cannot foresee with torsional effects. To achieve this, the Saint Venant theory (SVT) considers a long prismatic bar under torsion and defines the following displacement field:

$$\begin{aligned} u_x(x,y,z) =& z\phi_y(y), \\ u_y(x,y,z) =& \psi(x,z), \\ u_z(x,y,z) =& -x\phi_y(y), \end{aligned} \tag{2.9}$$

where ϕ_y is the twist angle around the beam axis and $\psi(x,z)$ is the warping function. The SVT assumes a constant rate of twist, i.e. $\frac{\partial \phi_y}{y} = c$, and accounts for the primary warping of the cross-section, which does not vary along the beam axis.

However, this description of the cross-section deformations is not suitable for the structural analysis of thin-walled beams, which undergo more complex deformations that cannot be described mathematically by Eq. (2.9). On this behalf, Vlasov [203] introduced a torsion theory that accounts for restrained warping. In his theory, the twist angle is not constant anymore along the beam axis, but fulfills the following differential equation:

$$EJ_\omega \frac{d^4\phi_y}{dy^4} - GJ_t \frac{d^2\phi_y}{dy^2} = m_y, \tag{2.10}$$

where EJ_ω and GJ_t are the warping and torsion stiffnesses, respectively, and m_y is the moment along y. In order to account for the secondary warping and the stress fields over the thin-walled section described by Vlasov, the kinematics of the beam must include higher-order terms, as it follows:

$$\begin{aligned} u_x(x,y,z) =& u_{x_1}(y) + z\phi_y(y), \\ u_y(x,y,z) =& u_{y_1}(y) + f_1(x)\phi_z(y) + g_1(x)\frac{\partial u_{x_1}(y)}{\partial y} + f_2(z)\phi_x(y) + g_2(z)\frac{\partial u_{z_1}(y)}{\partial y}, \\ u_z(x,y,z) =& u_{z_1}(y) - x\phi_y(y), \end{aligned} \tag{2.11}$$

where $f_1(x)$, $g_1(x)$, $f_2(z)$ and $g_2(z)$ are third-order functions. A similar higher-order theory was introduced by Reddy [165] for plates. This kind of theories are able to provide a parabolic distribution of the transverse shear deformations, therefore the homogeneous conditions at the free edges of the section can be fulfilled, diversely from the TBT and SVT theories, as shown in Fig. 2.2

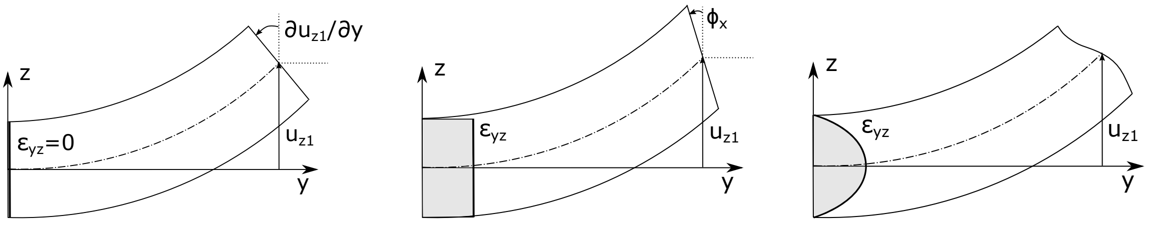

(a) EBBT (b) TBT (c) Vlasov-Reddy

Fig. 2.2 Possible displacements and shear deformations that can be predicted by the different classical theories.

To this point, the classical theories can be used to obtain a fair approximation of the mechanical response of beams for a limited range of structural problems that include slender beams under axial, bending and torsional loads. However, in many structural applications it is indeed necessary to apply more generic boundary conditions and, therefore, engineers are forced to rely on more computationally-expensive plate and solid formulations to perform their numerical analysis. Another issue arises when the in-plane deformations over the cross-sections are of interest, for instance in composite problems or short beams. In fact, if we use the kinematics described in Eq. (2.11):

$$\varepsilon_{xx} = u_{x,x} = 0, \tag{2.12}$$

$$\varepsilon_{zz} = u_{z,z} = 0, \tag{2.13}$$

$$\varepsilon_{xz} = \frac{1}{2}\left(u_{x,z} + u_{z,x}\right) = \frac{1}{2}\left(\phi_y - \phi_y\right) = 0, \tag{2.14}$$

which reflects that the SVT torsional terms alone cannot capture any deformation of the cross-section, local or global, in its own plane. Additional higher-order terms are to be added to include these mechanical responses in the model. In this regard, Prof. Washizu wisely stated [207]: '*For a complete removal of the inconsistency and an improvement of the accuracy of the beam theory,*' we may assume a generic expansion of the cross-sectional terms, whose number '*should be chosen properly*'.

2.3 Carrera unified formulation

The introduction of advanced beam models which are able to deal with different structural problems has been a topic of interest in the structural community for decades, specially in the analysis of composite structures. Addressing some of the aforementioned issues of classical theories, the Carrera unified formulation (CUF) was introduced as a generator of structural theories for plates by Carrera [28], then extended to 1D formulations [34]. In 1D problems, the CUF defines the kinematics of the beam theory in a compact form, as follows:

$$\boldsymbol{u}(x,y,z) = F_\tau(x,z)\,\boldsymbol{u}_\tau(y) \qquad \tau = 1,2,...,M, \tag{2.15}$$

that is a generic expansion of the displacement unknowns over the cross-section. In this expression, $\boldsymbol{u}_\tau(y)$ are the generalized displacement unknowns, $F_\tau(x,z)$ are arbitrary functions of the cross-section coordinates and M is the maximum number of terms in the expansion, which is an input of the analysis. The Einsten notation is used hereinafter, thus the repeated τ means summation. Making use of this form of kinematics, the accuracy of the beam model is dictated by the type of function used as expansion, which is chosen axiomatically, and the enrichment of the displacement field, which is represented by M. In the last decade, many beam theories have been implemented in the framework of CUF, such as trigonometric, polynomial, exponential and zig-zag, see [70]. Due to their versatility, polynomial expansions are the most commonly used in the CUF analyses.

2.3.1 Taylor expansion

Beam models based on the Taylor expansion (TE) are created using a 2D series of expansion of the type $F_\tau(x,z) = x^p z^q$, with p and q taking values from 0 to the maximum polynomial order, N, according to the Pascal triangle shown in Table 2.1.

Table 2.1 Pascal triangle.

order	M	F_τ
0	1	$F_1 = 1$
1	3	$F_2 = x\ F_3 = z$
2	6	$F_4 = x^2\ F_5 = xz\ F_6 = z^2$
3	10	$F_7 = x^3\ F_8 = x^2z\ F_9 = xz^2\ F_{10} = z^3$
$\vdots$	$\vdots$	$\vdots$
N	$\frac{(N+1)(N+2)}{2}$	$F_{(N^2+N+2)/2} = x^N\ F_{(N^2+N+4)/2} = x^{N-1}\ \dots\ F_{N(N+3)/2} = xz^{N-1}\ F_{(N+1)(N+2)/2} = z^N$

For instance, a TE third-order model ($N = 3$) can be written as

$$\begin{aligned}
u_x &= u_{x_1} + x\, u_{x_2} + z\, u_{x_3} + x^2\, u_{x_4} + xz\, u_{x_5} + z^2\, u_{x_6} + x^3\, u_{x_7} + x^2 z\, u_{x_8} + xz^2\, u_{x_9} + z^3\, u_{x_{10}},\\
u_y &= u_{y_1} + x\, u_{y_2} + z\, u_{y_3} + x^2\, u_{y_4} + xz\, u_{y_5} + z^2\, u_{y_6} + x^3\, u_{y_7} + x^2 z\, u_{y_8} + xz^2\, u_{y_9} + z^3\, u_{y_{10}},\\
u_z &= u_{z_1} + x\, u_{z_2} + z\, u_{z_3} + x^2\, u_{z_4} + xz\, u_{z_5} + z^2\, u_{z_6} + x^3\, u_{z_7} + x^2 z\, u_{z_8} + xz^2\, u_{z_9} + z^3\, u_{z_{10}},
\end{aligned} \tag{2.16}$$

including a total of 30 generalized unknowns over the cross-section. Note that the kinematics defined via TE are hierarchical, that is the polynomial order of the transverse approximation is increased by adding higher-order functions to the existing set. Consequently, the kinematics of Eq. (2.16) accounts for constant, linear, quadratic and cubic terms. Also, it is worth mentioning that the classical beam theories can be generated by truncating the kinematic field of a TE. For instance, the TBT model is obtained using the expansion terms of the following unknowns: u_{x_1}, u_{y_1}, u_{y_2}, u_{y_3} and u_{z_1}.

2.3.2 Lagrange expansion

The Lagrange expansion (LE) makes use of Lagrangian polynomials to interpolate the unknowns over the cross-section domain. Different Lagrangian domains have been implemented in the framework of CUF [41], including three-noded (L3), four-noded (L4), nine-noded (L9) and sixteen-noded (L16). For example, the expansion functions of a bilinear L4 domain are:

$$F_\tau = \frac{1}{4}(1 - r_\tau r)(1 - s_\tau s) \qquad \tau = 1,2,3,4, \tag{2.17}$$

where r and s are defined in the interval [-1, 1] and r_τ and s_τ are the roots of these polynomials, a.k.a nodes. It is worth mentioning that in LE a Jacobian transformation is required between the natural coordinates (r, s) and the cross-sectional domain defined in (x, z). In the case of a biquadratic L9, these F_τ functions are:

$$\begin{gathered}
F_\tau = \tfrac{1}{4}(r^2 + r\, r_\tau)(s^2 + s\, s_\tau), \qquad \tau = 1,3,5,7,\\
F_\tau = \tfrac{1}{2} s_\tau^2 (s^2 + s\, s_\tau)(1 - r^2) + \tfrac{1}{2} r_\tau^2 (r^2 + r\, r_\tau)(1 - s^2), \qquad \tau = 2,4,6,8,\\
F_\tau = (1 - r^2)(1 - s^2) \qquad \tau = 9,
\end{gathered} \tag{2.18}$$

Subsequently, the displacement field of a L9 domain can be written as:

$$\begin{aligned}
u_x &= F_1\, u_{x_1} + F_2\, u_{x_2} + F_3\, u_{x_3} + \ldots + F_9\, u_{x_9},\\
u_y &= F_1\, u_{y_1} + F_2\, u_{y_2} + F_3\, u_{y_3} + \ldots + F_9\, u_{y_9},\\
u_z &= F_1\, u_{z_1} + F_2\, u_{z_2} + F_3\, u_{z_3} + \ldots + F_9\, u_{z_9}.
\end{aligned} \tag{2.19}$$

Note that the unknowns of the mechanical problem represent pure displacements over the 3D beam. LE beam models possess some interesting features for the analysis of beam structures. Since nodal unknowns are placed over the edges of the cross-section domain, the application of the loads can be done in a 3D sense as for solid finite elements. Moreover, any geometry of the cross-section can be discretized with a number of Lagrangian domains, making LE appropriated for the analysis of thin-walled beams and civil structures, see for instance [39, 36].

2.4 Hierarchical Legendre expansion

A non-local hierarchical theory is generated by using the 2D set of Legendre polynomials as expansion functions of the cross-section coordinates. This set of interpolation functions, defined by Szabó and Babuška [189] for the *p*-version of the finite element method (FEM), exhibit some interesting properties for the generation of interpolation functions. They are based on a orthogonal basis and form a fully hierarchical set. Also, the number of functions with non-zero value at the edges of the domain is minimum.

The Legendre polynomials can be obtained from a recurrent definition:

$$L_0 = 1, \tag{2.20}$$

$$L_1 = \varsigma, \tag{2.21}$$

$$L_k = \frac{2k-1}{k}\varsigma L_{k-1}(\varsigma) - \frac{k-1}{k}L_{k-2}(\varsigma), \quad k = 2,3,... \tag{2.22}$$

The roots of L_k coincide with the Gauss points and the resultant polynomial set constitutes an orthonormal basis. The set of interpolating functions in a 1D space can be written as

$$\tilde{L}_1(r) = \frac{1}{2}(1-r), \tag{2.23}$$

$$\tilde{L}_2(r) = \frac{1}{2}(1+r), \tag{2.24}$$

$$\tilde{L}_i(r) = \phi_{i-1}(r), \quad i = 3,4,...,p+1, \tag{2.25}$$

where $\phi_j(r)$ are the normalized integrals of L_k:

$$\phi_j(r) = \sqrt{\frac{2j-1}{j}}\int_{-1}^{r} L_{j-1}(\varsigma)\,d\varsigma, \quad j = 2,3,4,... \tag{2.26}$$

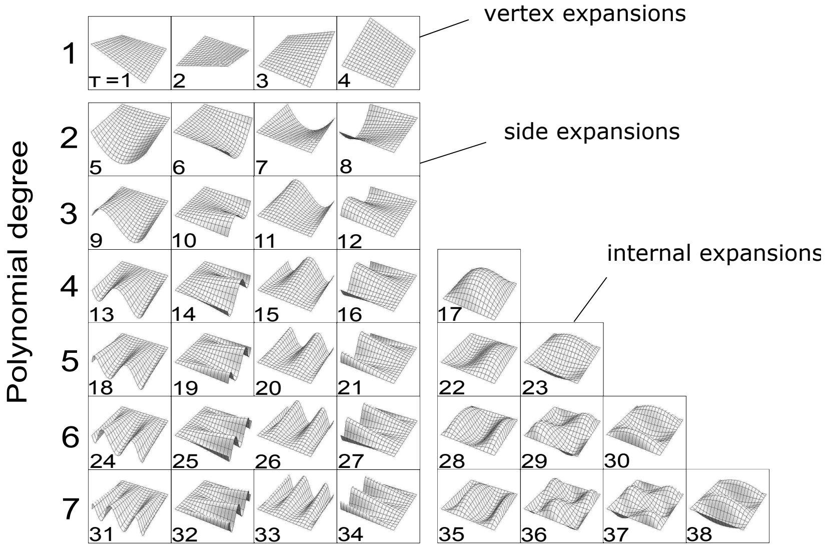
vertex expansions
side expansions
internal expansions
Polynomial degree
1
2
3
4
5
6
7
τ =1
2
3
4
5
6
7
8
9
10
11
12
13
14
15
16
17
18
19
20
21
22
23
24
25
26
27
28
29
30
31
32
33
34
35
36
37
38

Fig. 2.3 Hierarchical set of F_τ 2D functions used to generate HLE.

Eqs. (2.23) and (2.24) are linear functions that vary between 0 and 1 along the domain [-1, 1], thus they are known as *nodal modes*. The higher-order functions of Eq. (2.25) are denominated *internal modes* and they vanish at the edges of the interval.

The orthogonality of the Legendre set of functions is defined by:

$$\int_{-1}^{1} \frac{d\tilde{L}_i}{dr}\frac{d\tilde{L}_j}{dr}\,dx = \delta_{ij}, \quad \text{for } i \geq 3 \,\text{and}\, j \geq 1 \,\text{or}\, i \geq 3 \,\text{and}\, j \geq 1, \tag{2.27}$$

δ_{ij} being:

$$\delta_{ij} = 1 \qquad\qquad if\ i = j, \tag{2.28}$$

$$\delta_{ij} = 0 \qquad\qquad otherwise. \tag{2.29}$$

A 2D set of interpolating polynomials is defined by expanding the above procedure to quadrilateral domains in the [-1, 1] × [-1, 1] domain. Accordingly, in a 2D domain it is possible to defined three classes of expansions, *nodal*, *side* and *internal*, which are built from the products of the 1D Legendre polynomials.

Nodal expansions The nodal expansions are the same of the linear Lagrangian shape functions for quadrilateral domains, also used for linear LE models (L4):

$$F_\tau = \frac{1}{4}(1 - r_\tau r)(1 - s_\tau s) \qquad \tau = 1, 2, 3, 4 \tag{2.30}$$

Side expansions The side modes are defined for $p \geq 2$ and correspond to the following functions

$$F_\tau(r,s) = \frac{1}{2}(1-s)\phi_p(r) \qquad \tau = 5,9,13,18,... \tag{2.31}$$

$$F_\tau(r,s) = \frac{1}{2}(1+r)\phi_p(s) \qquad \tau = 6,10,14,19,... \tag{2.32}$$

$$F_\tau(r,s) = \frac{1}{2}(1+s)\phi_p(r) \qquad \tau = 7,11,15,20,... \tag{2.33}$$

$$F_\tau(r,s) = \frac{1}{2}(1-r)\phi_p(s) \qquad \tau = 8,14,16,21,... \tag{2.34}$$

For each polynomial order p, there are 4 functions (one per side) which vanish at all edges but one.

Internal expansions The internal modes are defined for $p \geq 4$ and for a given polynomial order the set includes $(p-2)(p-3)/2$ functions. They are obtained as from product of the 1D Legendre modes (Eq. (2.25)):

$$F_\tau(r,s) = \phi_{p_1}(r)\phi_{p_2}(s), \qquad p_1, p_2 = 2,3,4,... \; and \; p = p_1 + p_2. \tag{2.35}$$

For instance, the internal functions of the 6^{th} order are

$$F_{28}(r,s) = \phi_4(r)\phi_2(s) \tag{2.36}$$

$$F_{29}(r,s) = \phi_3(r)\phi_3(s) \tag{2.37}$$

$$F_{30}(r,s) = \phi_2(r)\phi_4(s) \tag{2.38}$$

Figure 2.3 shows the HLE from order $p = 1$ to $p = 7$. The hierarchical properties of the 1D polynomial set are maintained, i.e. the functions of lower-order are a subset of the higher-order model. For instance, for a 6^{th} order model the kinematics of the beam include all the expansion terms from $\tau = 1$ to $\tau = 30$. The explicit expressions all the Legendre functions until the 8^{th} order can be found in Appendix A.

HLE beam models include some of the features of other refined structural theories. The displacement field is enriched hierarchically, as for TE models. On the other hand, the cross-section of the beam can be discretized in a number of domains, as for LE models. From the modeling point of view, the main advantage of HLE theories is that the cross-section can be discretized just once, and the convergence of the solutions is attained by systematically changing the input parameter of the polynomial order, p, with no need for re-meshing

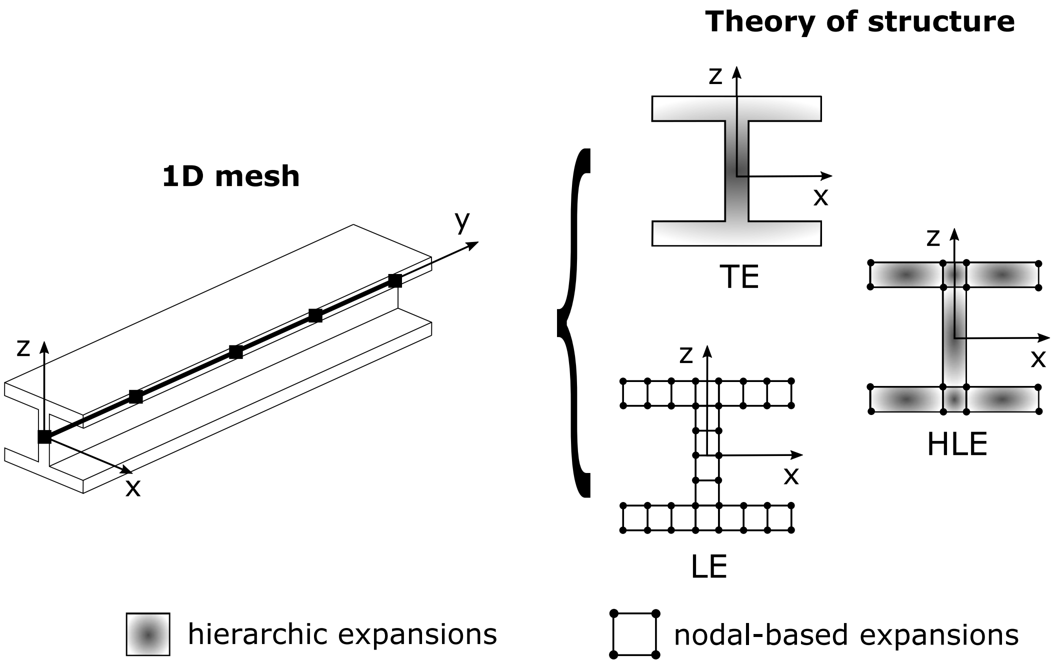

Fig. 2.4 Differences between various refined 1D CUF finite elements

procedures. Figure 2.4 illustrates the differences among the higher-order theories discussed here.

2.5 Cross-section mapping

The higher-order polynomials used in HLE theories call for the generation of coarse discretizations based on large quadrilateral domains, as shown in Fig. 2.4. When dealing with curved geometries, standard isoparametric elements represent the boundaries of the domain using the same set of interpolating functions. Therefore a numerical error is introduced when performing the integrals of the stiffness matrices due to the inability of the elements to capture the exact geometry of curved boundaries. In the case of large domains, this error may be unacceptably high and it becomes necessary to represent curved boundaries via non-isoparametric techniques.

Consider the Jacobian transformation of a quadrilaterial domain defined in (r, s) into the global coordinates (x, z) shown in Fig. 2.5, in which one of the sides is curved. The mapping functions, $\boldsymbol{Q}$, can be written as:

$$x = Q_x(r,s), \tag{2.39}$$

$$z = Q_z(r,s). \tag{2.40}$$

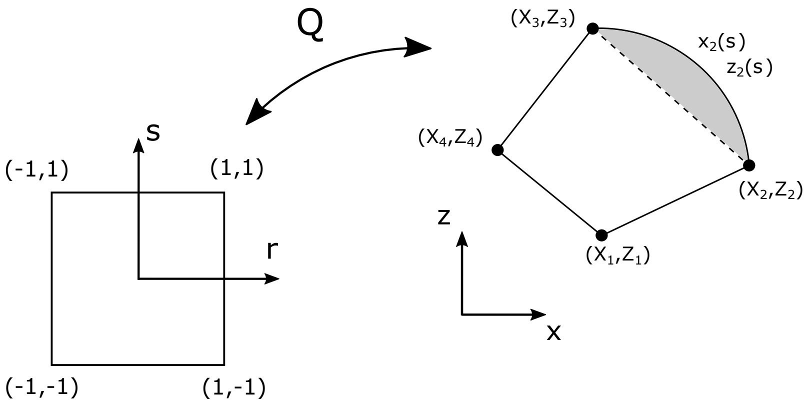

Fig. 2.5 Jacobian transformation of the quadrilateral domains of the cross-section, based on [189].

A brief description of the possible definitions of these mapping functions are included in the following.

2.5.1 First-order mapping

In the case of isoparametric mapping with linear expansions, for instance L4, the boundaries of the cross-section are approximated by piece-wise linear curves. The mapping functions are built from the linear expansion functions, as follows:

$$
\begin{aligned}
x = Q_x(r,s) = \; & \tfrac{1}{4}(1-r)(1-s)X_1 + \tfrac{1}{4}(1+r)(1-s)X_2 \\
& + \tfrac{1}{4}(1+r)(1+s)X_3 + \tfrac{1}{4}(1-r)(1+s)X_4,
\end{aligned}
\tag{2.41}
$$

$$
\begin{aligned}
z = Q_z(r,s) = \; & \tfrac{1}{4}(1-r)(1-s)Z_1 + \tfrac{1}{4}(1+r)(1-s)Z_2 \\
& + \tfrac{1}{4}(1+r)(1+s)Z_3 + \tfrac{1}{4}(1-r)(1+s)Z_4,
\end{aligned}
\tag{2.42}
$$

or in compact form:

$$
\mathbf{x} = F_\tau(r,s)\,\mathbf{X}_\tau \quad \tau = 1,...,4, \tag{2.43}
$$

where $\mathbf{x} = \{x\ z\}^T$ are the positions over the cross-section plane and $\mathbf{X}_\tau = \{X_\tau\ Z_\tau\}^T$ correspond to the vertex of the quadrilateral domain. F_τ are exactly the same linear functions as used in the description of the kinematics of the L4 beam model. It is clear that this kind of mapping is not able to represent the curved boundary and just represents a straight side (dashed line).

2.5.2 Second-order mapping

A similar procedure can be followed for the mapping of quadratic expansions like the L9. Now the mapping functions are described by the Lagrangian polynomials included in Eq. (2.18), as:

$$\mathbf{x} = F_\tau(r,s)\,\mathbf{X}_\tau \quad \tau = 1,...,9, \tag{2.44}$$

This isoparametric expansion allows one to represent curved geometries by a piece-wise parabolic approximation, thus reducing the error with respect to the linear mapping.

2.5.3 The blending function method

If the exact geometry is to be captured, a parametric representation of the curved edges must be generated. The blending function method (BFM), introduced by Gordon and Hall [81], makes it possible to describe the actual geometry of the analyzed domain in the mapping functions, ensuring that the exact domain is integrated in the energy terms. The BFM is employed here to generate non-isoparametric HLE domains which are able to represent very accurately the surface of arbitrary curved cross-sections.

Considering the quadrilateral domain of Fig. 2.5, the curved edge can be described mathematically in the 2D space by a pair of parametric function of the type $x = x_2(s)$ and $z = z_2(s)$. For instance, if cubic polynomials are employed to represent the geometry, we can write the following functions:

$$x_2(s) = a_x + b_x s + c_x s^2 + d_x s^3 \tag{2.45}$$

$$z_2(s) = a_z + b_z s + c_z s^2 + d_z s^3. \tag{2.46}$$

which fulfill the following conditions:

$$x_2(-1) = X_2, \quad x_2(1) = X_3, \tag{2.47}$$

$$z_2(-1) = Z_2, \quad z_2(1) = Z_3. \tag{2.48}$$

Subsequently, the mapping functions are expressed as follows:

$$x = Q_x(r,s) = F_\tau(r,s)X_\tau + \Big(x_2(s) - \big(\frac{1-s}{2}X_2 + \frac{1+s}{2}X_3\big)\Big)\frac{1+r}{2}, \tag{2.49}$$

$$z = Q_z(r,s) = F_\tau(r,s)Z_\tau + \Big(z_2(s) - \big(\frac{1-s}{2}Z_2 + \frac{1+s}{2}Z_3\big)\Big)\frac{1+r}{2}, \tag{2.50}$$

where $\tau = 1,...,4$. The first term of the right-hand side of these expressions corresponds to the first-order mapping. The second adds the section between $\boldsymbol{x}_2(s)$ and the straight line between

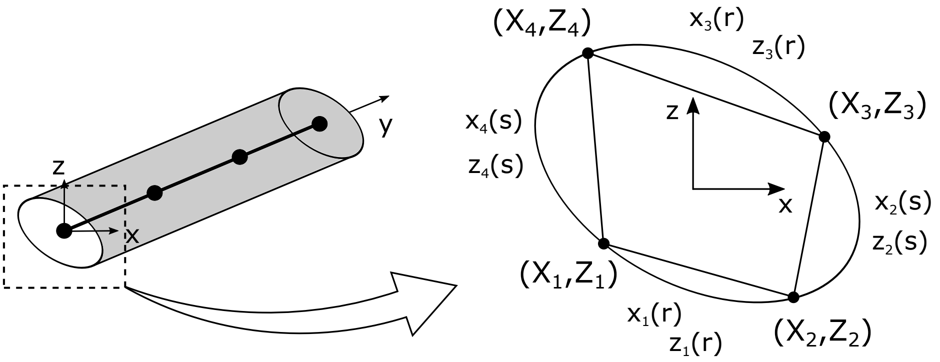

Fig. 2.6 Mapping of the cross-section domain by the BFM.

vertexes 2 and 3, highlighted in grey in Fig. 2.5. Finally, the term $\frac{1+r}{2}$ is denominated as blending function and it is added to vanish the transformation at the opposite edge of the quadrilateral domain.

If this operation is extended to all 4 sides of the quadrilateral domain, we obtain

$$\begin{aligned} x = Q_x(r,s) = {} & \tfrac{1}{2}(1-s)x_1(r) + \tfrac{1}{2}(1+r)x_2(s) + \tfrac{1}{2}(1+s)x_3(r) \\ & + \tfrac{1}{2}(1-r)x_4(s) - F_\tau(r,s)X_\tau, \\ z = Q_z(r,s) = {} & \tfrac{1}{2}(1-s)z_1(r) + \tfrac{1}{2}(1+r)z_2(s) + \tfrac{1}{2}(1+s)z_3(r) \\ & + \tfrac{1}{2}(1-r)z_4(s) - F_\tau(r,s)Z_\tau, \end{aligned} \tag{2.51}$$

being every side of the domain represented by parametric functions x_i and z_i, $i = 1,2,3,4$, as shown in Fig. 2.6. The main advantage of this approach in the context of beam modeling lies on the ability to separate the discretization of the cross-section from the quality of the numerical approximation. In this manner, the surface of any curved section, such as thin-walled or composite, can be modeled a priory and the polynomial order can be chosen according to the level of accuracy desired, with no need to waste computational resources to capture the exact geometry.

2.6 Examples

This section shows the potential of HLE theories through two numerical cases. The first example is a simple assessment by comparison against classical and higher-order beam theories, whereas the second shows the use of HLE to analyze curved thin-walled structures. The solutions are obtained by means of the FEM, which is described in the next chapter (3).

2.6.1 Square beam

The first case is a square beam similar to that of Fig. 2.1. The geometrical features are described in [41], being the length $L = 2$ m and the cross-section dimensions $a = b = 0.2$ m. The resulting slenderness ratio is then $L/b = 10$. The beam is clamped at one end ($y = 0$) and two point forces of magnitude $P = 25$ N are applied downwards on the lower corners of the other end ($y = L$), see Fig. 2.7. The properties of the material are those of an Aluminum alloy: Young modulus, E, equal to 75 GPa and Poisson ratio, ν, equal to 0.33. A convergent mesh of Lagrangian 1D elements is used along the beam axis.

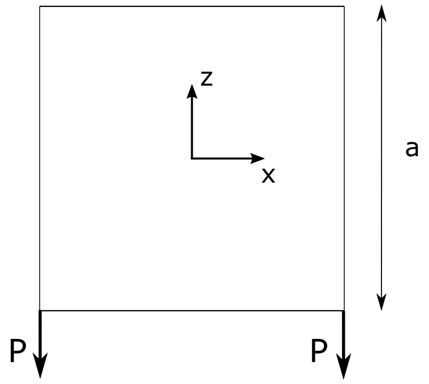

Fig. 2.7 Geometry and loading case of the squared beam example.

The assessment is done modeling the cross-section using only one HLE domain. Polynomial orders until $p = 8$ are tested. Table 2.2 shows the number of degrees of freedom (DOF) and the total number of expansions over the cross-section (M) for the HLE model here developed and the reference TE and LE solutions from [41]. Table 2.3 includes the values of displacements, longitudinal stresses and shear stresses at different locations of the beam structure. Reference solutions are added, including those of a 3D model generated in Nastran [51]. Figures 2.8 and 2.9 show graphs of the distributions of displacements and stresses at $y = L$ and $y = L/2$, respectively. The following remarks can be stated:

- In HLE models, the number of DOF and the expansion terms grows as the polynomial order p increases.
- The HLE solutions of the displacements evaluated at the loading points of the structure tend monotonically to those of the refined solid model used as reference. Also, in Fig. 2.8 is it possible to observe that higher-order polynomial expansions are able to capture the local peaks of the vertical displacements at the loading points.
- The computation of the longitudinal stresses is not challenging from the modeling point of view (the linear model HL1 is enough). On the other hand, the evaluation

of the transverse stresses is more troublesome and requires at least a third-order HL3 model to obtained satisfactory results, see Fig. 2.9 (b). The second order model HL2 provides similar results as the nine-noded LE.

Table 2.2 Model features: degrees of freedom and expansion terms.

model	DOF	M
SOLID [41]	18150	–
TE [41]		
N=1	279	3
N=2	558	6
N=3	930	10
N=4	1395	15
LE [41]		
L4	372	4
L9	837	9
HLE		
HL1	372	4
HL2	744	8
HL3	1116	12
HL4	1581	17
HL5	2139	23
HL6	2790	30
HL7	3534	38
HL8	4371	47

2.6.2 Wing structure

The second example deals with a monocoque wing structure, which is illustrated in Fig. 2.10. The airfoil corresponds to the NACA 2415 with a chord of 1 m and a total span of 6 m. The material is the same of the previous example ($E = 75$ GPa and $\nu = 0.33$) and clamped-free boundary conditions are considered. A point load of magnitude $P = 3000$ N is applied at $1/4$ of the chord in the lower wall at $2/3$ of the total span.

Figure 2.11 shows the discretization of the airfoil via HLE. To demonstrate the capabilities of the proposed approach for the efficient modeling of beam structures, only 5 curved domains are used to represent the cross-section. Cubic polynomials are used to parametrize the curved boundaries. The assembly of the different domains is carried out by merging the corresponding nodal and edge DOF in the stiffness matrix of the structural problem. It is worth pointing out that in case of distorted meshes like this one, the sign of the antisymmetric

Table 2.3 Solutions of displacements and stresses of the square beam example.

model	$u_z \times 10^5$	$\sigma_{yy} \times 10^{-4}$	$\sigma_{yz} \times 10^{-3}$
	$[-b/2, L, -h/2]$	$[0, L/2, h/2]$	$[0, L/2, 0]$
SOLID[41]	-1.340	3.750	-1.708
	Classical and higher-order TE [41]		
EBBT	-1.333	-	-
TBT	-1.343	-	-
N=1	-1.343	-	-
N=2	-1.327	-	-
N=3	-1.329	-	-
N=4	-1.330	-	-
	LE		
L4[41]	-1.115	-	-
L9	-1.331	3.750	-1.198
	HLE		
HL1	-1.115	3.750	-1.250
HL2	-1.329	3.750	-1.198
HL3	-1.332	3.750	-1.746
HL4	-1.335	3.750	-1.761
HL5	-1.336	3.750	-1.734
HL6	-1.337	3.751	-1.734
HL7	-1.339	3.743	-1.741
HL8	-1.340	3.745	-1.738

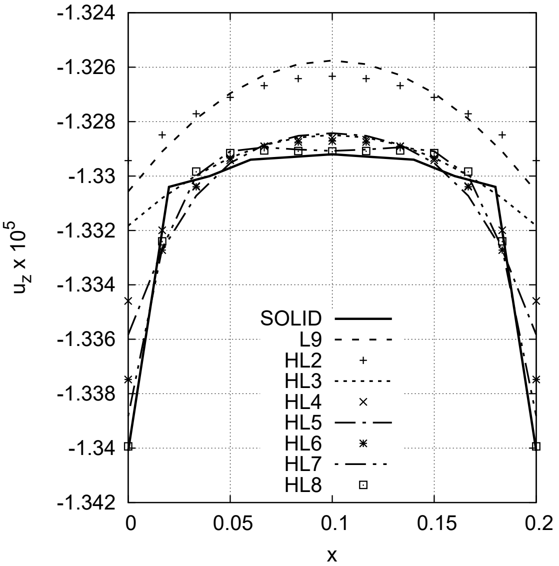

Fig. 2.8 Vertical displacement, u_z, along the bottom edge of the loaded section, $[:, L, -h/2]$.

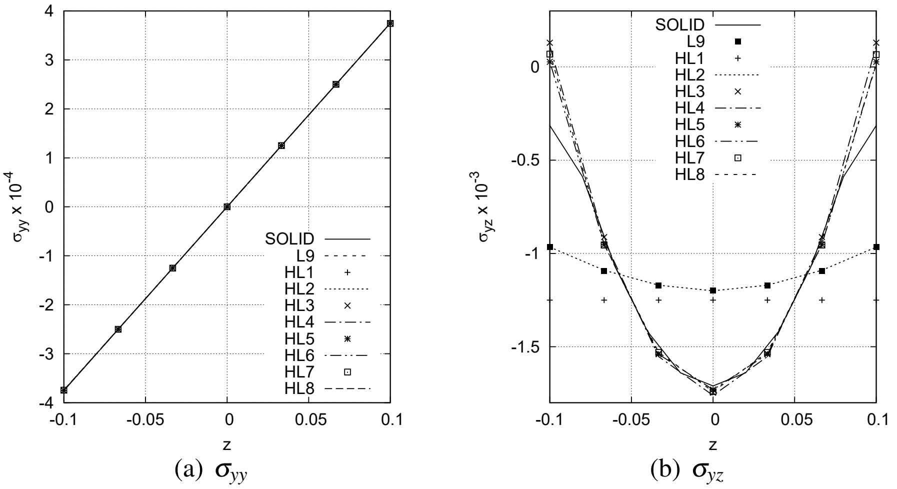

(a) σ_{yy} (b) σ_{yz}

Fig. 2.9 Longitudinal, σ_{yy}, and shear, σ_{yz}, stresses through the thickness at the center of the beam structure, $[0, L/2, :]$.

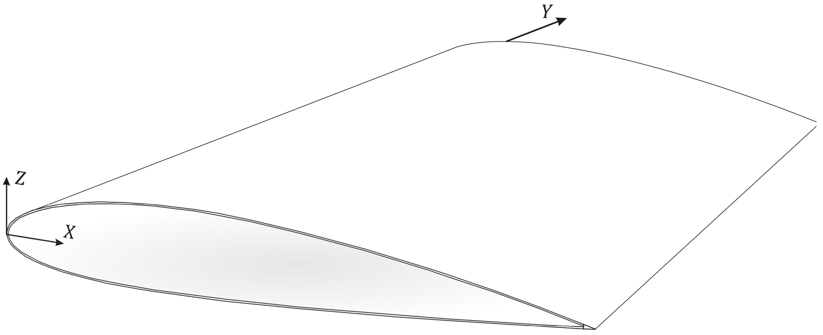

Fig. 2.10 Illustration of the monocoque wing structure.

Legendre side modes (odd p orders) has to be checked when assembling the domains to ensure C^0 displacement solutions over the section. Regarding the longitudinal mesh, 10 cubic 1D elements are employed.

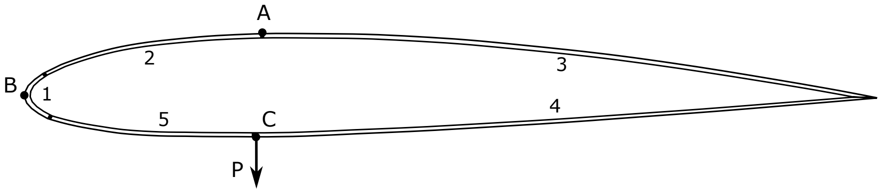

Fig. 2.11 HLE discretization of the wing profile and loading.

The solutions of displacements and stresses are evaluated in points A and B of Fig. 2.11 at different span coordinates. In particular, point A is located in coordinates [0.282394, 0.093267] of the section, whereas point B coincides with the leading edge [0, 0]. The results are shown in Table 2.4. A 3D FEM model is generated in Nastran for reference purposes. The convergence the solutions with respect to the polynomial order is rather fast, being the third-order HL3 model already acceptable. The second-order HL2 model fails for such a coarse mesh. All the solutions of $p > 3$ agree well with the 3D model, showing remarkable reductions in the computational costs. Finally, Fig. 2.12 includes the final configuration of the section at $y = 4$ m, where it is possible to observe the in-plane deformation of the airfoil caused by the application of the point load at the lower skin.

Table 2.4 Displacement and stress results of the wing with point load.

Model	$u_z \times 10^3$ [m] Point A, $y = L$	$\sigma_{yy} \times 10^{-6}$ [Pa] Point A, $y = 1$ m	$\sigma_{yz} \times 10^{-6}$ [Pa] Point B, $y = 1$ m	DOF
		MSC Nastran solid model		
HEXA8	-85.52	38.40	-43.46	395280
		Hierarchical Legendre Expansions, 10 B4		
HL2	-33.06	16.54	-60.38	2325
HL3	-83.38	37.68	-41.98	3720
HL4	-84.15	38.50	-43.81	5580
HL5	-84.76	38.55	-44.98	7905
HL6	-84.46	38.47	-44.38	10695
HL7	-84.29	38.44	-41.82	13950
HL8	-84.26	38.50	-41.81	17670

A second loadcase is generated by applying a distributed line load over the span of the wing in correspondence with point A. The magnitude of the loading is $L = 1766$ N/m. Figure 2.13 shows an illustration of the loading configuration (a) and a plot of the resulting

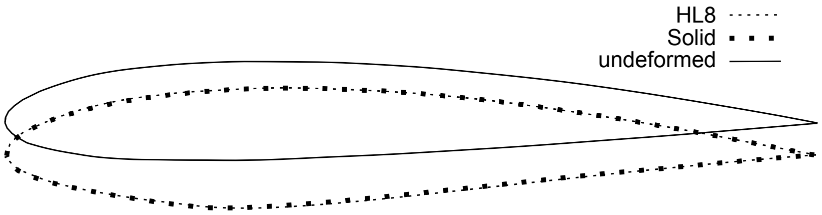

Fig. 2.12 Deformations of the loaded section of the monocoque wing.

deformation of the structure (b). Table 2.5 reports the numerical results of the HL8 beam in comparison to the 3D model of Nastran, which exhibit remarkable agreement as well.

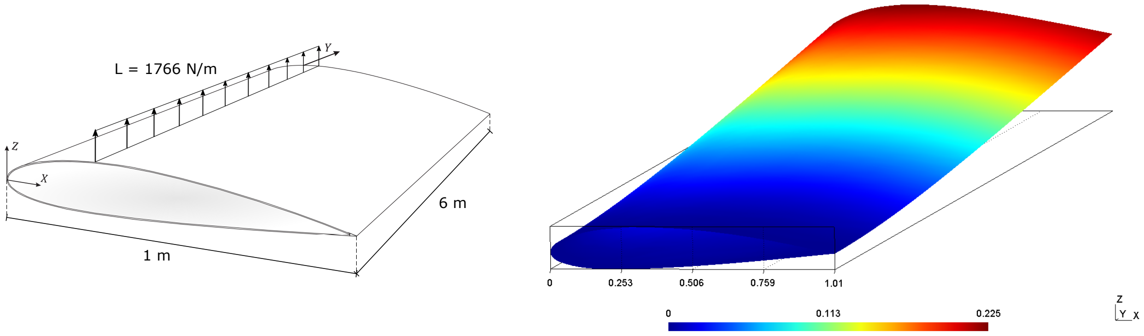

(a) Loading

(b) Deformed

Fig. 2.13 Monocoque wing under distributed line load.

Table 2.5 Displacement and stress results of the wing with distributed loading.

Model	u_z [m]	σ_{yy} [MPa]	σ_{yz} [MPa]	DOF
	Point A, $y = L$	Point A, $y = L/2$	Point B, $y = L/2$ m	
MSC Nastran	0.225	32.301	8.761	395280
HL8	0.223	32.000	8.839	17670

Chapter 3

Finite element method

The finite element method (FEM) is selected to solve the structural problem due to its superior versatility in comparison to other analytical and numerical approaches. This chapter presents the main theoretical formulations which are necessary for the implementation of the FEM code based on the CUF theories. First, the constitutive equations are discussed for different material types. Subsequently, a brief discussion of the development of the finite element formulation from the weak form of the governing equations is presented and the shape functions which are used to interpolate the generalized unknowns along the beam axis are described. From the principle of virtual displacements, the fundamental nucleus of the stiffness matrix is derived. This building block of the model represents one of the pillars of the current formulation, as it allows the user to generate any class of structural theory using the same formal statements.

Some of the contents presented in this chapter were included in [145].

3.1 Constitutive equations

As it is done previously for the strain tensor in Section 2.1, the symmetry of the stress tensor can be exploited to write it in the form of a six-term vector:

$$\boldsymbol{\sigma}^T = \left\{ \begin{array}{cccccc} \sigma_{yy} & \sigma_{xx} & \sigma_{zz} & \sigma_{xz} & \sigma_{yz} & \sigma_{xy} \end{array} \right\}, \tag{3.1}$$

where the components σ_{ij} correspond to the stress values at a certain point (x,y,z) expressed in the global coordinates.

Consider the material system illustrated in Fig. 3.1. In the most general case, a second coordinate system must be created to represent the material principal directions. Here, a system $(1,2,3)_m$ is defined being the axis 3 parallel to the fiber direction and the axis 1

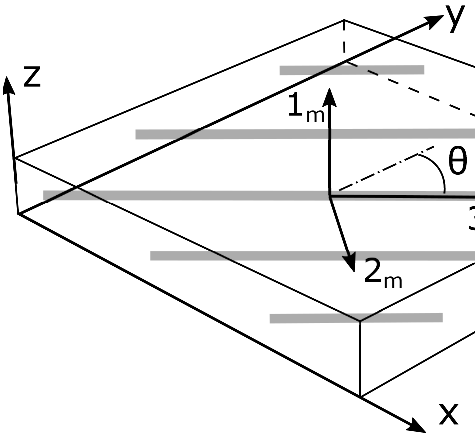

Fig. 3.1 Global and material reference systems.

orthogonal to the ply. Accordingly, the stress and strain vectors can be written in the material systems as:

$$\begin{aligned} \boldsymbol{\sigma}_m^T &= \left\{ \begin{array}{cccccc} \sigma_3 & \sigma_2 & \sigma_1 & \sigma_4 & \sigma_5 & \sigma_6 \end{array} \right\}, \\ \boldsymbol{\varepsilon}_m^T &= \left\{ \begin{array}{cccccc} \varepsilon_3 & \varepsilon_2 & \varepsilon_1 & \varepsilon_4 & \varepsilon_5 & \varepsilon_6 \end{array} \right\}. \end{aligned} \tag{3.2}$$

The stress-strain relations are given by the Hooke's law, which states:

$$\boldsymbol{\sigma}_m = \mathbf{C}\boldsymbol{\varepsilon}_m, \tag{3.3}$$

where **C** is the 6 × 6 stiffness matrix of the material. The coefficients of **C** are expressed in the material system $(1,2,3)_m$ and, in general, are a function of the position over the volume of the body. For anisotropic materials, the Hooke's law results:

$$\left\{ \begin{array}{c} \sigma_3 \\ \sigma_2 \\ \sigma_1 \\ \sigma_4 \\ \sigma_5 \\ \sigma_6 \end{array} \right\} = \left[\begin{array}{cccccc} C_{33} & C_{32} & C_{31} & C_{34} & C_{35} & C_{36} \\ C_{23} & C_{22} & C_{21} & C_{24} & C_{25} & C_{26} \\ C_{13} & C_{12} & C_{11} & C_{14} & C_{15} & C_{16} \\ C_{43} & C_{42} & C_{41} & C_{44} & C_{45} & C_{46} \\ C_{53} & C_{52} & C_{51} & C_{54} & C_{55} & C_{56} \\ C_{63} & C_{62} & C_{61} & C_{64} & C_{65} & C_{66} \end{array} \right] \left\{ \begin{array}{c} \varepsilon_3 \\ \varepsilon_2 \\ \varepsilon_1 \\ \varepsilon_4 \\ \varepsilon_5 \\ \varepsilon_6 \end{array} \right\}. \tag{3.4}$$

Due to the symmetry of the material matrix ($C_{ij} = C_{ji}$) the independent coefficients are not 36, but 21. When the material is anisotropic, its elastic properties vary over the three directions. However, most of the materials employed for engineering purposes exhibit certain symmetries, allowing for the use of a reduced set of independent constants. Some of the most common material definitions are explained in the following.

Isotropic materials A material is consider isotropic if its elastic properties are directionally independent. Classical examples of materials that fall under this category are the metals, for instance steel and aluminum. In this case, the stress-strain relations can be written as:

$$\begin{Bmatrix} \sigma_3 \\ \sigma_2 \\ \sigma_1 \\ \sigma_4 \\ \sigma_5 \\ \sigma_6 \end{Bmatrix} = \begin{bmatrix} C_{33} & C_{32} & C_{31} & 0 & 0 & 0 \\ C_{23} & C_{22} & C_{21} & 0 & 0 & 0 \\ C_{13} & C_{12} & C_{11} & 0 & 0 & 0 \\ 0 & 0 & 0 & C_{44} & 0 & 0 \\ 0 & 0 & 0 & 0 & C_{55} & 0 \\ 0 & 0 & 0 & 0 & 0 & C_{66} \end{bmatrix} \begin{Bmatrix} \varepsilon_3 \\ \varepsilon_2 \\ \varepsilon_1 \\ \varepsilon_4 \\ \varepsilon_5 \\ \varepsilon_6 \end{Bmatrix} \tag{3.5}$$

where the coefficients of **C** depend only on two elastic constants, usually: the Young's modulus, E, and the Poisson ratio, ν, as follows:

$$\begin{gathered} C_{11} = C_{22} = C_{33} = \frac{(1-\nu)E}{(1+\nu)(1-2\nu)}, \\ C_{12} = C_{13} = C_{23} = C_{21} = C_{31} = C_{32} = \frac{\nu E}{(1+\nu)(1-2\nu)}, \\ C_{44} = C_{55} = C_{66} = \frac{E}{2(1+\nu)}. \end{gathered} \tag{3.6}$$

Orthotropic materials An orthotropic material exhibits two planes of symmetry where the properties do not vary, resulting in 9 independent constants. These are commonly provided in the form of the engineering moduli: Young's moduli E_1, E_2, E_3; shear moduli G_{12}, G_{13}, G_{23}; and Poisson ratios ν_{12}, ν_{13}, ν_{23}. These constant are defined as:

$$E_i = \frac{\sigma_i}{\varepsilon_i}, \quad G_{ij} = \frac{\sigma_{ij}}{\varepsilon_{ij}}, \quad \nu_{ij} = -\frac{\varepsilon_j}{\varepsilon_i}. \tag{3.7}$$

The Hooke's law for orthotropic materials has the same form of that of isotropic materials, Eq. (3.5), but the coefficients of **C** are now expressed as:

$$\begin{aligned}
&C_{11} = \tfrac{E_1(1-\nu_{23}\nu_{32})}{\beta}, \quad C_{12} = \tfrac{E_1(\nu_{21}+\nu_{23}\nu_{31})}{\beta}, \quad C_{13} = \tfrac{E_1(\nu_{31}+\nu_{21}\nu_{32})}{\beta},\\
&C_{21} = \tfrac{E_2(\nu_{12}+\nu_{13}\nu_{32})}{\beta}, \quad C_{22} = \tfrac{E_2(1-\nu_{13}\nu_{31})}{\beta}, \quad C_{23} = \tfrac{E_2(\nu_{32}+\nu_{12}\nu_{31})}{\beta},\\
&C_{31} = \tfrac{E_3(\nu_{13}+\nu_{12}\nu_{23})}{\beta}, \quad C_{32} = \tfrac{E_3(\nu_{23}+\nu_{13}\nu_{21})}{\beta}, \quad C_{33} = \tfrac{E_3(1-\nu_{12}\nu_{21})}{\beta},\\
&C_{44} = G_{21}, \qquad C_{55} = G_{31}, \qquad C_{66} = G_{23},
\end{aligned} \tag{3.8}$$

where

$$\beta = 1 - \nu_{12}\nu_{21} - \nu_{12}\nu_{21} - \nu_{12}\nu_{21} - \nu_{12}\nu_{21}\nu_{31} - \nu_{12}\nu_{21}\nu_{31}. \tag{3.9}$$

Note that due to the symmetry of the stiffness matrix of the material, the following relations are satisfied:

$$\frac{\nu_{ij}}{E_i} = \frac{\nu_{ji}}{E_j}, \tag{3.10}$$

thus $C_{12} = C_{21}$, $C_{13} = C_{31}$ and $C_{23} = C_{32}$.

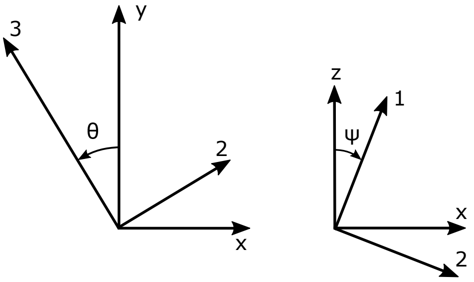

Fig. 3.2 Material rotation angles.

The Hooke's law reported in Eq. (3.5) is written in the material coordinate system. The orientation of the orthotropic material has to be included in the constitutive relations of the physical system. For that, the stress and strain vectors are written in the global coordinate system via a coordinate transformation, as follows:

$$\begin{aligned}
\boldsymbol{\sigma} &= \mathbf{T}\boldsymbol{\sigma}_m,\\
\boldsymbol{\varepsilon} &= \mathbf{T}\boldsymbol{\varepsilon}_m,
\end{aligned} \tag{3.11}$$

where **T** is the transformation matrix. If we consider the material rotations depicted in Fig. 3.2, the components of the **T** matrix depend on θ and ψ, which are the angles around the z

and y axis, respectively. Subsequently, the Hooke's law can be written in the global frame as

$$\boldsymbol{\sigma} = \mathbf{T}\,\mathbf{C}_m\,\mathbf{T}^T\,\boldsymbol{\varepsilon} = \tilde{\mathbf{C}}\boldsymbol{\varepsilon}, \tag{3.12}$$

or explicitly,

$$\begin{Bmatrix} \sigma_{yy} \\ \sigma_{xx} \\ \sigma_{zz} \\ \sigma_{xz} \\ \sigma_{yz} \\ \sigma_{xy} \end{Bmatrix} = \begin{bmatrix} \tilde{C}_{33} & \tilde{C}_{23} & \tilde{C}_{13} & 0 & 0 & \tilde{C}_{36} \\ \tilde{C}_{23} & \tilde{C}_{22} & \tilde{C}_{12} & 0 & 0 & \tilde{C}_{26} \\ \tilde{C}_{13} & \tilde{C}_{12} & \tilde{C}_{11} & 0 & 0 & \tilde{C}_{16} \\ 0 & 0 & 0 & \tilde{C}_{44} & \tilde{C}_{45} & 0 \\ 0 & 0 & 0 & \tilde{C}_{45} & \tilde{C}_{55} & 0 \\ \tilde{C}_{36} & \tilde{C}_{26} & \tilde{C}_{16} & 0 & 0 & \tilde{C}_{66} \end{bmatrix} \begin{Bmatrix} \varepsilon_{yy} \\ \varepsilon_{xx} \\ \varepsilon_{zz} \\ \varepsilon_{xz} \\ \varepsilon_{yz} \\ \varepsilon_{xy} \end{Bmatrix}. \tag{3.13}$$

The components $\tilde{C}_{ij}$ are a function of the 9 orthotropic constants included in Eq. (3.7), and the rotation angles of $(1,2,3)_m$ in (x,y,z). For the sake of brevity, the explicit expressions of C_{ij} are not enlisted here, but they can be found in [33].

When the elastic properties of the material are the same over one plane and vary only in the orthogonal direction, the material is said to be transverse isotropic. In this particular case, 5 material constants are enough to define the material matrix **C**. A classical example of this type of material are the fiber-reinforced composites, in which the properties of the material do not change over the plane normal to the fiber axis.

3.2 Finite element formulation

In the past years, several methods were employed to solve the structural problem in the CUF framework. Several analytical approaches for beam problems can be found in the literature, such as close-form Navier solutions [79], radial basis functions [176], dynamic stiffness method [143]. These models present the advantage of a minimum computational expense and, in most cases, do not suffer from convergence issues, making them appropriate for benchmarking. However, analytical models are suitable only for certain problems and can only deal with limited boundary conditions and geometry, which make them less attractive for generic purposes.

In order to overcome this limitations, a finite element formulation is adopted in this thesis. To apply the FEM, the system of partial differential equations that describe the problem is transformed into the weak form, that is expressing the equilibrium equations in integral form. The domain of integration is divided into a number of small portions, the *finite elements*, in which the fundamental variables are interpolated through shape functions. For more interest, some of the classical books of the FEM are those of Zienkiewicz and Taylor [224] and Bathe [13], among others. The implementation of the FEM to solve beams, plates and shell problems in the framework of CUF can be found in the book of Carrera et al. [29].

In FEM problems, the accuracy of the numerical model is controlled by the refinement of the discretization of the domain of analysis. Ideally, convergent studies should be carried out systematically to ensure the quality of the solutions. On the other hand, the high versatility of the FEM in dealing with arbitrary geometries and loadings makes it the most well-known method in structural analysis. Here, the FEM is employed to discretize the beam axis with 1D elements, interpolating in this manner the generalized unknowns of the cross-section over the longitudinal axis.

3.2.1 Interpolation of the generalized displacements

In beam problems, the cross-section unknowns are interpolated over the beam axis via 1D shape functions. In other words, the value of the generalized displacements at any point along the beam is a weighted combination of their values in certain axial locations, denoted to as beam nodes. In such manner, one can write:

$$\boldsymbol{u}_\tau(y) = N_i(y)\boldsymbol{u}_{\tau i}, \qquad i = 1,2,...,n_n, \tag{3.14}$$

where

$$\boldsymbol{u}_{\tau i} = \left\{ \begin{array}{ccc} u_{x\tau i} & u_{y_{\tau i}} & u_{z\tau i} \end{array} \right\}^T \tag{3.15}$$

is the displacement nodal vector and N_i is the corresponding shape function. n_n is the number of nodes per element. Two classes of elements are implemented using different polynomial sets: Lagrange and Legendre.

Lagrange beam elements Lagrange interpolation polynomials are the most extended choice in the h-version of FEM. In this approach the accuracy of the numerical solutions is incremented via refinement of the number of elements. The Lagrange polynomial basis is obtained from the following formula:

$$N_i(\xi) = \prod_{i=1, i\neq j}^{p_b} \frac{\xi - \xi_i}{\xi_j - \xi_i}, \qquad j = 1,...,n_n, \tag{3.16}$$

where p_b is the polynomial order of the shape functions. Note that N_i are defined in the interval $-1 \leq \xi \leq 1$ and the roots of the polynomials are chosen equidistant. For the sake of completeness, the Lagrange shape functions of two-noded (B2), three-noded (B3) and four-noded (B4) elements are included in the following:

- Linear element

$$N_1 = \tfrac{1}{2}(1-\xi),\;\; N_2 = \tfrac{1}{2}(1+\xi),\quad \begin{cases} \xi_1 = -1 \\ \xi_2 = +1 \end{cases} \tag{3.17}$$

- Quadratic element

$$N_1 = \tfrac{1}{2}\xi(\xi-1),\;\; N_2 = \tfrac{1}{2}\xi(\xi+1),\;\; N_3 = -(1+\xi)(1-\xi),\quad \begin{cases} \xi_1 = -1 \\ \xi_2 = +1 \\ \xi_3 = 0 \end{cases} \tag{3.18}$$

- Cubic element

$$\begin{matrix} N_1 = -\tfrac{9}{16}(\xi+\tfrac{1}{3})(\xi-\tfrac{1}{3})(\xi-1),\;\; N_2 = \tfrac{9}{16}(\xi+\tfrac{1}{3})(\xi-\tfrac{1}{3})(\xi+1), \\ \\ N_3 = +\tfrac{27}{16}(\xi+1)(\xi-\tfrac{1}{3})(\xi-1),\;\; N_4 = -\tfrac{27}{16}(\xi+1)(r+\tfrac{1}{3})(\xi-1), \end{matrix} \quad \begin{cases} \xi_1 = -1 \\ \xi_2 = +1 \\ \xi_3 = -\tfrac{1}{3} \\ \xi_4 = +\tfrac{1}{3} \end{cases} \tag{3.19}$$

Figure 3.3 (a) shows the distribution of these functions over the natural domain of the beam element.

Legendre beam elements The interpolation of the displacements is performed using a hierarchical set of 1D Legendre-based polynomials. This set is typical of the p-version of FEM, in which the numerical error is reduced via increment of the polynomial order of the element. A hierarchical set can be implemented using the following shape functions:

$$N_1(\xi) = \frac{1}{2}(1-\xi) \tag{3.20}$$

$$N_2(\xi) = \frac{1}{2}(1+\xi) \tag{3.21}$$

$$N_i(\xi) = \phi_{i-1}(\xi), \quad i = 3,4,...,n_n, \tag{3.22}$$

with

$$\phi_i(\xi) = \sqrt{\frac{2i-1}{i}} \int_{-1}^{\xi} L_{i-1}(\varsigma)\, d\varsigma, \quad i = 2,3,4,... \tag{3.23}$$

In this manner, the displacement approximation is enriched by adding shape functions of higher-order to the finite element. Figure 3.3 (b) shows the first three polynomial sets. One

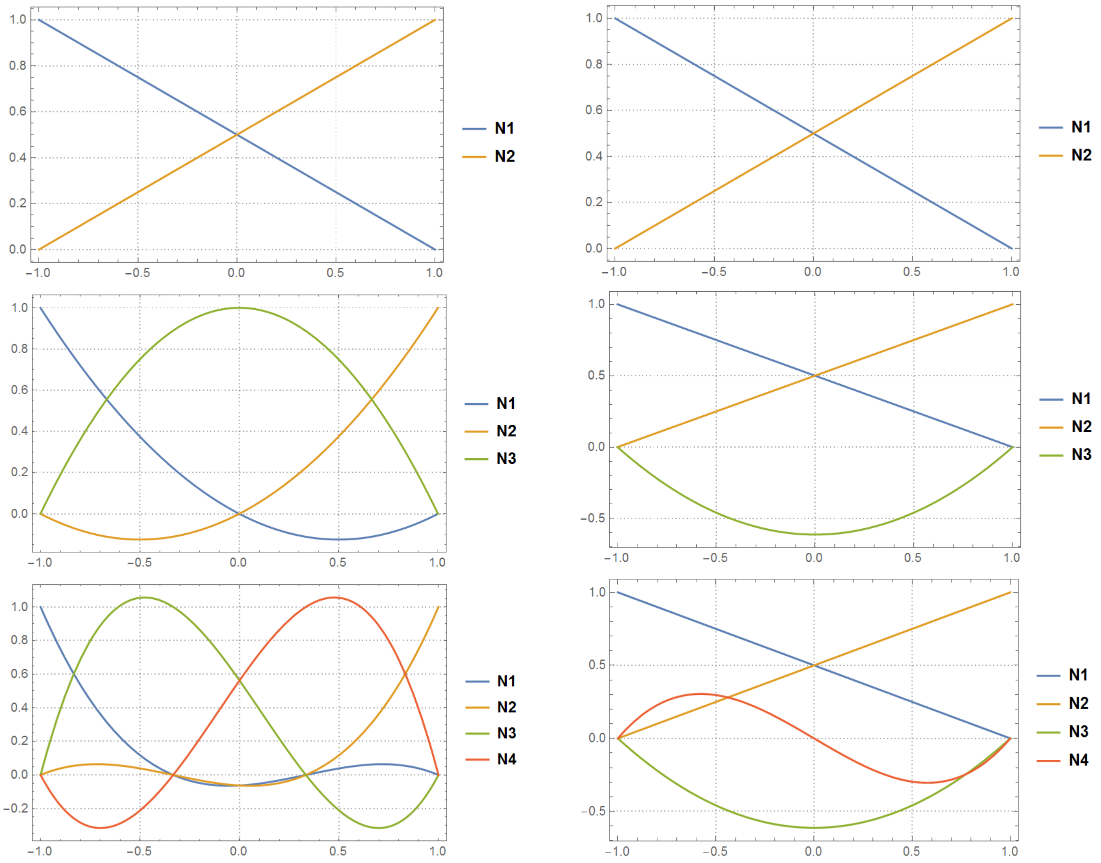

(a) Lagrange (b) Legendre

Fig. 3.3 Lagrange and Legendre interpolation polynomials.

can observe that, similarly to HLE theories, the higher-order functions do not reach the unitary value throughout the interval [-1, 1], therefore they are denoted as modes instead of nodal shape functions.

3.2.2 Principle of virtual displacements

According to the calculus of variations, a variational statement is formulated to find the stationary solutions of an integral problem. In solid mechanics, the variational formulation is that of minimizing the total potential energy of the structure, which sums the contributions of the internal and external energies. Taking virtual variations of the displacements, the Principle of Virtual Displacements (PVD) states that for all kinematically admissible virtual displacements, a body is in equilibrium if the virtual work done by the internal stresses equals the work done by the external loads:

$$\delta L_{\mathrm{int}} = \delta L_{\mathrm{ext}}. \tag{3.24}$$

The internal work L_{int} corresponds to the elastic strain energy, which is defined as

$$\delta L_{int} = \int_V \delta \boldsymbol{\varepsilon}^T \boldsymbol{\sigma} \, dV, \tag{3.25}$$

where V is volume of the body. On the other hand, according to d'Alembert principle the external work includes the contribution of the surface external loads L_s, point loads L_P and the volume inertial loads L_{ine},

$$\delta L_{\mathrm{ext}} = \delta L_{\mathrm{S}} + \delta L_{\mathrm{P}} - \delta L_{\mathrm{ine}} = \int_S \delta \boldsymbol{u}^T \mathbf{P}_S \, dS + \delta \boldsymbol{u}^T \mathbf{P} - \int_V \delta \boldsymbol{u}^T \rho \, \ddot{\boldsymbol{u}} \, dV, \tag{3.26}$$

where P_s is a surface load acting on the boundary S, ρ is the density of the material and $\ddot{\boldsymbol{u}}$ is the acceleration vector. As a result, the PVD of the problem can be written as

$$\int_V \delta \boldsymbol{u}^T \rho \, \ddot{\boldsymbol{u}} \, dV + \int_V \delta \boldsymbol{\varepsilon}^T \boldsymbol{\sigma} \, dV = \int_S \delta \boldsymbol{u}^T \mathbf{P}_S \, dS + \delta \boldsymbol{u}^T \mathbf{P}. \tag{3.27}$$

In the following discussion, for the sake of simplicity only the static case is considered, therefore the first term of Eq. (3.27) is dropped. The obtention of the equations of motion for dynamic problems is presented in Chapter 10.

3.2.3 Fundamental nucleus

By including the CUF kinematics of Eq. (2.15) into the expression of the FEM interpolation along the beam axis, Eq. (3.14), the displacement field can be written as:

$$\boldsymbol{u}(x,y,z) = N_i(y)F_\tau(x,z)\boldsymbol{u}_{\tau i}, \qquad \tau = 1,2,...,M, \qquad i = 1,2,...,n_n, \tag{3.28}$$

Subsequently, the strain fields are defined as

$$\boldsymbol{\varepsilon} = (\mathbf{D}\,F_\tau N_i)\,\boldsymbol{u}_{\tau i}, \tag{3.29}$$

where $\boldsymbol{\varepsilon}$ is the strain vector defined in Eq. (2.3) and $\mathbf{D}$ is the differential operator of Eq. (2.4). For the sake of clarity, the 6×3 operator resulting from the product of the differential operator and the kinematic functions is provided in the following:

$$\mathbf{D}\,F_\tau N_i = \begin{bmatrix} 0 & F_\tau N_{i,y} & 0 \\ F_{\tau,x} N_i & 0 & 0 \\ 0 & 0 & F_{\tau,z} N_i \\ F_{\tau,z} N_i & 0 & F_{\tau,x} N_i \\ 0 & F_{\tau,z} N_i & F_\tau N_{i,y} \\ F_\tau N_{i,y} & F_{\tau,x} N_i & 0 \end{bmatrix} \tag{3.30}$$

Then, according to the Hooke's law, the stress field results:

$$\boldsymbol{\sigma} = \mathbf{C}\,(\mathbf{D}\,F_\tau N_i)\,\boldsymbol{u}_{\tau i}, \tag{3.31}$$

Introducing the expressions of Eqs. (3.28), (3.29) and (3.31) into the PVD (Eq. ()3.27)), and considering the virtual displacements as $\delta\boldsymbol{u} = F_s N_j \boldsymbol{u}_{sj}$, the governing equations of the static problem read:

$$\int_L \int_\Omega \delta\boldsymbol{u}_{sj}^T\,(\mathbf{D}\,F_s\,N_j)^T\,\mathbf{C}\,\mathbf{D}\,F_\tau\,N_i\,\delta\boldsymbol{u}_{\tau i}\,dy\,d\Omega = \int_S \delta\boldsymbol{u}_{sj}^T\,F_s\,N_j\,P_S\,dS + \delta\boldsymbol{u}_{sj}^T\,F_s\,N_j\,\mathbf{P}. \tag{3.32}$$

This expression can be written in a compact form as

$$\delta\boldsymbol{u}_{sj}^T\,\mathbf{K}^{\tau sij}\,\delta\boldsymbol{u}_{\tau i} = \delta\boldsymbol{u}_{sj}^T\,\mathbf{P}^{sj}, \tag{3.33}$$

where

$$\mathbf{K}^{ij\tau s} = \int_L \int_\Omega (\mathbf{D}\, F_s N_j)^T\, \mathbf{C}\, \mathbf{D}\, F_\tau N_i \, dy\, d\Omega, \tag{3.34}$$

$$\mathbf{P}^{sj} = \int_S F_s N_j P_S \, dS + F_s N_j \mathbf{P}. \tag{3.35}$$

$\mathbf{K}^{ij\tau s}$ is a 3×3 matrix denoted to as *fundamental nucleus*, whose formal expression remains invariable with respect of the structural theory or FE scheme chosen. This definition is indeed one of the major strengths of CUF as a generator of structural models. From the coding standpoint, by simply looping on the indexes τ, s, i and j, any structural model can be created. Note that for beam problems, the domain of integration is decoupled into the cross-section surface, Ω, and the longitudinal dimension, L. The explicit form of the fundamental nucleus for orthotropic materials is included in the following:

$$\begin{aligned}
K^{\tau s i j}_{xx} &= \widetilde{C}_{22} I_{ij} E_{\tau_{,x} s_{,x}} + \widetilde{C}_{44} I_{ij} E_{\tau_{,z} s_{,z}} + \widetilde{C}_{26} I_{ij_{,y}} E_{\tau_{,x} s} + \widetilde{C}_{26} I_{i_{,y} j} E_{\tau s_{,x}} + \widetilde{C}_{66} I_{i_{,y} j_{,y}} E_{\tau s} \\
K^{\tau s i j}_{xy} &= \widetilde{C}_{23} I_{ij_{,y}} E_{\tau_{,x} s} + \widetilde{C}_{45} I_{ij} E_{\tau_{,z} s_{,z}} + \widetilde{C}_{26} I_{ij} E_{\tau_{,x} s_{,x}} + \widetilde{C}_{36} I_{i_{,y} j_{,y}} E_{\tau s} + \widetilde{C}_{66} I_{i_{,y} j} E_{\tau s_{,x}} \\
K^{\tau s i j}_{xz} &= \widetilde{C}_{12} I_{ij} E_{\tau_{,x} s_{,z}} + \widetilde{C}_{44} I_{ij} E_{\tau_{,z} s_{,x}} + \widetilde{C}_{45} I_{ij_{,y}} E_{\tau_{,z} s} + \widetilde{C}_{16} I_{i_{,y} j} E_{\tau s_{,z}} \\
K^{\tau s i j}_{yx} &= \widetilde{C}_{23} I_{i_{,y} j} E_{\tau s_{,x}} + \widetilde{C}_{45} I_{ij} E_{\tau_{,z} s_{,z}} + \widetilde{C}_{26} I_{ij} E_{\tau_{,x} s_{,x}} + \widetilde{C}_{36} I_{i_{,y} j_{,y}} E_{\tau s} + \widetilde{C}_{66} I_{ij_{,y}} E_{\tau_{,x} s} \\
K^{\tau s i j}_{yy} &= \widetilde{C}_{33} I_{i_{,y} j_{,y}} E_{\tau s} + \widetilde{C}_{55} I_{ij} E_{\tau_{,z} s_{,z}} + \widetilde{C}_{36} I_{ij_{,y}} E_{\tau_{,x} s} + \widetilde{C}_{36} I_{i_{,y} j} E_{\tau s_{,x}} + \widetilde{C}_{66} I_{ij} E_{\tau_{,x} s_{,x}} \\
K^{\tau s i j}_{yz} &= \widetilde{C}_{13} I_{i_{,y} j} E_{\tau s_{,z}} + \widetilde{C}_{55} I_{ij_{,y}} E_{\tau_{,z} s} + \widetilde{C}_{45} I_{ij} E_{\tau_{,z} s_{,x}} + \widetilde{C}_{16} I_{ij} E_{\tau_{,x} s_{,z}} \\
K^{\tau s i j}_{zx} &= \widetilde{C}_{12} I_{ij} E_{\tau_{,z} s_{,x}} + \widetilde{C}_{44} I_{ij} E_{\tau_{,x} s_{,z}} + \widetilde{C}_{45} I_{i_{,y} j} E_{\tau s_{,z}} + \widetilde{C}_{16} I_{ij_{,y}} E_{\tau_{,z} s} \\
K^{\tau s i j}_{zy} &= \widetilde{C}_{13} I_{ij_{,y}} E_{\tau_{,z} s} + \widetilde{C}_{55} I_{i_{,y} j} E_{\tau s_{,z}} + \widetilde{C}_{45} I_{ij} E_{\tau_{,x} s_{,z}} + \widetilde{C}_{16} I_{ij} E_{\tau_{,z} s_{,x}} \\
K^{\tau s i j}_{zz} &= \widetilde{C}_{11} I_{ij} E_{\tau_{,z} s_{,z}} + \widetilde{C}_{44} I_{ij} E_{\tau_{,x} s_{,x}} + \widetilde{C}_{55} I_{i_{,y} j_{,y}} E_{\tau s} + \widetilde{C}_{45} I_{ij_{,y}} E_{\tau_{,x} s} + \widetilde{C}_{45} I_{i_{,y} j} E_{\tau s_{,x}}
\end{aligned} \tag{3.36}$$

where the terms $E_{\tau_{(,x)(,z)} s_{(,x)(,z)}}$ and $I_{i_{(,y)} j_{(,y)}}$ correspond to the section and longitudinal integrals. The integrals of the cross-section expansions are defined as:

$$\begin{aligned}
E_{\tau_{,x} s_{,x}} &= \int_\Omega F_{\tau_{,x}} F_{s_{,x}} \, d\Omega, & E_{\tau_{,z} s_{,z}} &= \int_\Omega F_{\tau_{,z}} F_{s_{,z}} \, d\Omega, & E_{\tau s} &= \int_\Omega F_\tau F_s \, d\Omega, \\
E_{\tau_{,x} s_{,z}} &= \int_\Omega F_{\tau_{,x}} F_{s_{,z}} \, d\Omega, & E_{\tau_{,z} s_{,x}} &= \int_\Omega F_{\tau_{,z}} F_{s_{,x}} \, d\Omega, & E_{\tau_{,x} s} &= \int_\Omega F_{\tau_{,x}} F_s \, d\Omega, \\
E_{\tau s_{,x}} &= \int_\Omega F_\tau F_{s_{,x}} \, d\Omega, & E_{\tau_{,z} s} &= \int_\Omega F_{\tau_{,z}} F_s \, d\Omega, & E_{\tau s_{,z}} &= \int_\Omega F_\tau F_{s_{,z}} \, d\Omega,
\end{aligned} \tag{3.37}$$

whereas the integrals of the shape functions along the beam axis are:

$$\begin{aligned} I_{ij} &= \int_L N_i N_j \,\mathrm{d}y \qquad I_{ij_{,y}} = \int_L N_i N_{j_{,y}} \,\mathrm{d}y \\ I_{i_{,y}j} &= \int_L N_{i_{,y}} N_j \,\mathrm{d}y \quad I_{i_{,y}j_{,y}} = \int_L N_{i_{,y}} N_{j_{,y}} \,\mathrm{d}y \end{aligned} \tag{3.38}$$

Note that since the shape functions, Ni, are defined in the natural interval [-1, 1], a Jacobian transformation is performed in the computation of these integrals, as

$$I_{i_{(,y)}j_{(,y)}} = \int_{-1}^{1} N_{i_{(,\xi)}} N_{j_{(,\xi)}} |\boldsymbol{J}_y| d\xi \tag{3.39}$$

where $\boldsymbol{J}_y$ is the Jacobian matrix of the beam element.

Similarly, when non-local beam theories are implemented, such as LE or HLE, a Jacobian transformation is also required to compute the $E_{\tau_{(,x)(,z)}s_{(,x)(,z)}}$ terms, as follows:

$$E_{\tau_{(,x)(,z)}s_{(,x)(,z)}} = \int_{-1}^{1}\int_{-1}^{1} F_{\tau_{(,r)(,s)}} F_{s_{(,r)(,s)}} |\boldsymbol{J}_\Omega| dr\, ds \tag{3.40}$$

$\boldsymbol{J}_\Omega$ being the Jacobian matrix of the transformation between the (r, s) and (x, z) planes. All the integrals here displayed are computed by means of standard Gauss-Legendre quadrature. In the case of curved domains in the cross-section, as introduced in Sec. 2.5, the $\boldsymbol{J}_\Omega$ is defined from the mapping functions $\mathbf{Q}$ of Eq. (2.51).

Loads and constraints

Regarding the computation of the loading vector, some considerations can be made when dealing with surface loads. Two cases can be identified:

1. The load is distributed over a surface boundary parallel to the beam axis, for instance the top surface of Fig. 2.1, located at $z = b/2$ with dimension $a \times L$. In this case, the components of the loading vector are calculated as:

$$\mathbf{P}^{sj} = \int_L \int_a F_\tau(x, b/2)\, N_i(y)\, P_s \,dx\, dy \tag{3.41}$$

2. The surface load is applied over the cross-section, Ω. The computation of the load components is performed as:

$$\mathbf{P}^{sj} = N_i(y) \int_\Omega F_\tau(x,z)\, P_s \,dx\, dz \tag{3.42}$$

Obviously, in a FEM framework these loads are applied element-wise, making is possible to define arbitrary loaded zones over the boundaries of the body.

The imposition of displacement constraints on the beam structure is carried out via standard FEM techniques, for instance the penalty method. Consider that in non-local theories, such as HLE and LE, the displacement unknowns are distributed over the cross-section, thus the application of local constraints is straightforward.

3.2.4 Assembly of the stiffness matrix

The expressions of the components of the fundamental nucleus of Eq. (3.36) are independent of the choice of transverse expansions, F_τ, and shape functions, N_i. Indeed, in the CUF framework, the structural theory becomes an input of the analysis, which can be appropriately selected for each problem. For instance, for compact slender bodies a low-order TE may be sufficient, whereas for short or thin-walled beams a HLE model may be more suitable to get accurate solutions. All this capabilities can be implemented in the same code by only expanding the fundamental nucleus over τ, s, i, and j.

Figure 3.4 shows a diagram of the construction of the global stiffness matrix of the structural problem via expansion of the 3×3 fundamental nucleus. The assembly of the nodal stiffness matrix for hierarchical theories, e.g. TE or HLE, is done by adding more components in correspondence to the higher-order DOF (p=2,3,...). The assembly of all the elements to conform the global stiffness matrix is done via standard FEM techniques. Note that an extra loop over, el, has to be added when more than one element is used along the beam axis. Another loop is also included in the case of multi-domain discretizations of the cross-section. It is worth noting that this arrangement of the DOF leads to a concentration of the non-zero components of the stiffness matrix around the diagonal, which is advantageous from the computational point of view.

3.3 Example

A well-known benchmark test, the Scordelis-Lo roof, is chosen to assess the capabilities of the advanced HLE models with different FE interpolations along the beam axis. This numerical case, also known as the barrel vault, was presented by Belytschko et al. [17] and it is considered one of the shell obstacle course problems. This test can be found in many works in the literature and it is usually employed quantify the capabilities of novel shell formulations in dealing with membrane-like stress states, see Bathe and Dvorkin [14],

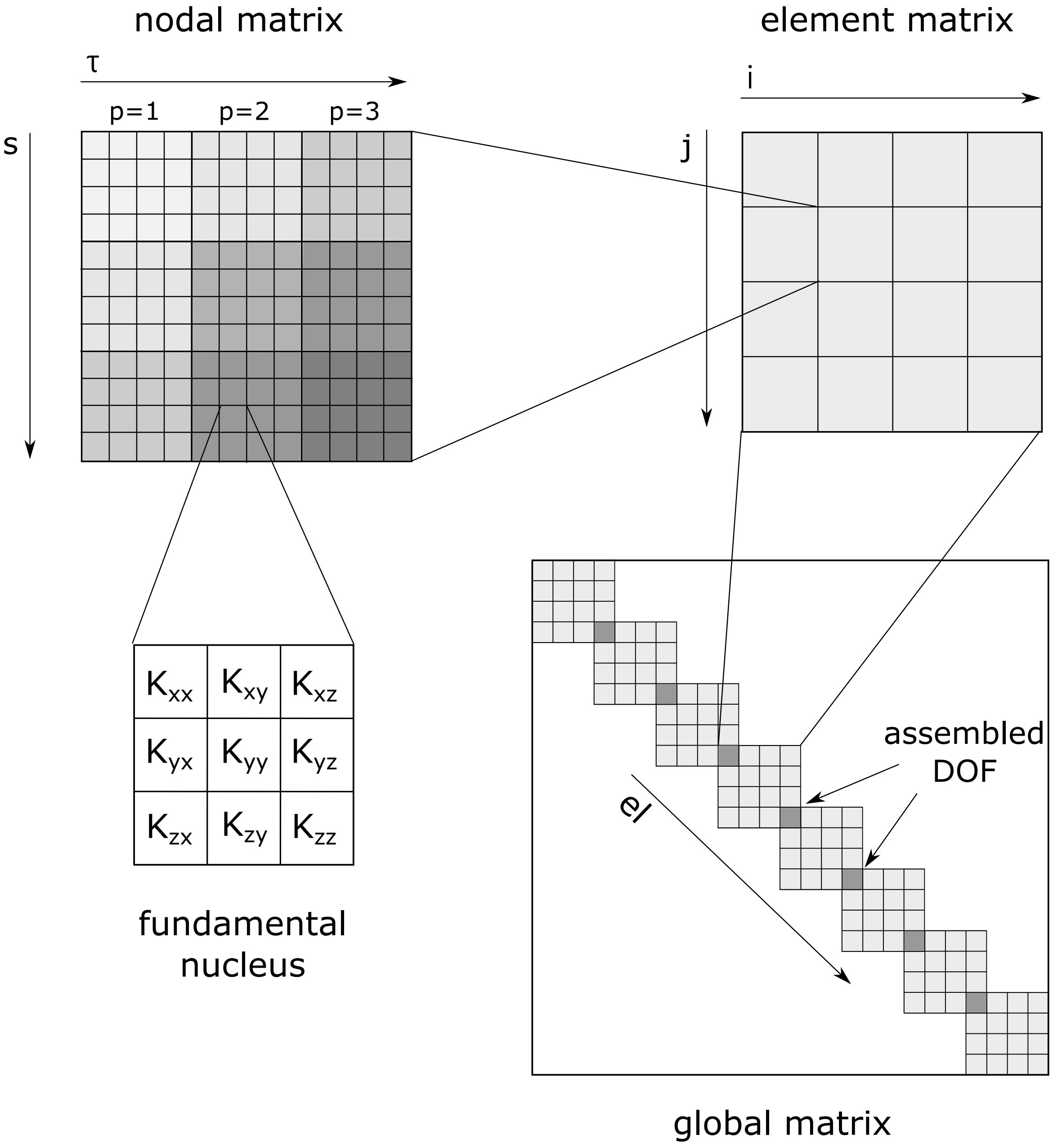
nodal matrix
τ
p=1
p=2
p=3
s
element matrix
i
j
K_{xx}
K_{xy}
K_{xz}
K_{yx}
K_{yy}
K_{yz}
K_{zx}
K_{zy}
K_{zz}
fundamental nucleus
assembled DOF
el
global matrix

Fig. 3.4 Construction of the stiffness matrix of CUF-based beam elements. The model shown includes 1 HLE domain of third-order and 8 four-noded beam elements.

Zienkiewi and Taylor [225] and McNeal and Harder [124], among others. Here the scope is to assess the convergence properties of the proposed higher-order beam elements.

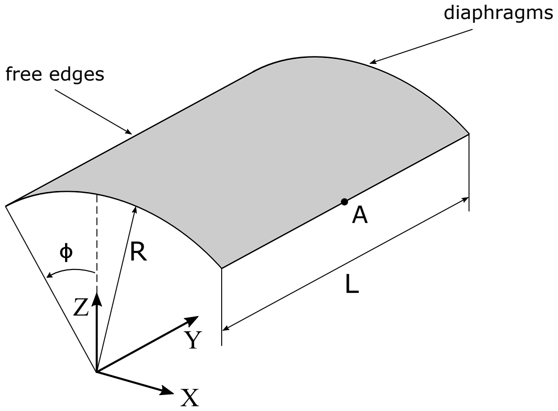

$E = 4.32 \times 10^8$ Pa
$\nu = 0.0$
$g = 90$ N/m^2
$R = 25$ m
$L = 50$ m
$t = 0.25$ m
$\phi = 40°$

Fig. 3.5 Scordelis–Lo problem features.

The characteristics of the problem are shown in Fig. 3.5. The roof is 50 m long, 0.25 m thick and the radius of curvature is $R = 25$ m. The curved edges lean on diaphragms, i.e. the displacements in x and z are constrained, and the longitudinal edges are free. The loading conditions correspond to the roof's own weight, here modeled as a surface load of 90 N/m^2 applied towards the negative z direction. The vertical displacement at midspan of the free-edge (point A) is used as benchmark value to assess the numerical model. The analytical solution provided by Scordelis and Lo [180] was $u_{ref} = -0.3086$ m, although the majority of the elements available in the literature converge to a lower value.

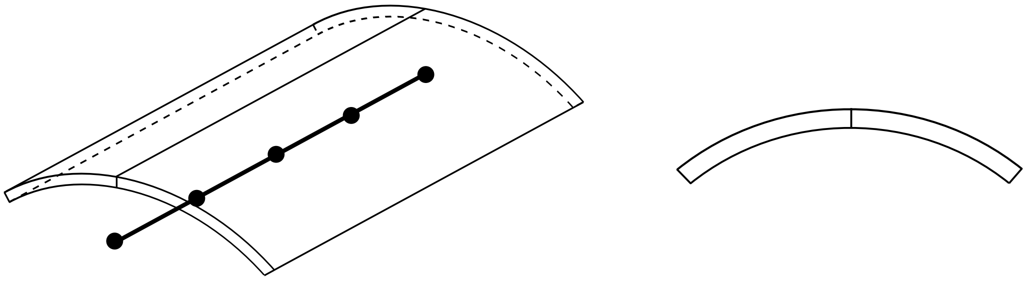

(a) Model

(b) Cross-section discretization. Not in scale.

Fig. 3.6 HLE beam model for the Scordelis-Lo roof.

The proposed model is featured in Fig. 3.6. As previously mentioned, one advantage for the efficient analysis of structures is that the discretization of the cross-section (b) is independent of the finite element mesh along the beam axis (a), thus no aspect ratio constraints apply between these two domains. Also, the curved geometry of the roof section can be represented exactly using a minimum number of HLE domains with BFM mapping. In particular, only 2 cross-section domains are employed here. Third-order polynomials are employed as parametric functions of the curved edges. Regarding the FEM discretization along the y axis, both Lagrange and Legendre 1D elements are tested. The following refinements of the model are studied:

- p-refinement of the cross-section assumptions via HLE: the cross-section discretization remains unaltered and the order of the kinematics is increased from second (HL2) to eighth (HL8).
- hp-refinement of the 1D mesh via Lagrange beam elements: both the number of elements (2,4,6 and 10) and the polynomial order of the shape functions (two-noded B2, three-noded B3 and four-noded B4) are varied.
- p-refinement of the 1D mesh via Legendre beam elements: only 1 element is placed on the beam axis and the order is increased hierarchically from second (P2) to sixth (P6).

Figure 3.7 shows the deformation of the structure predicted by a convergent model made of 10 B4 elements and HL5 section domains. One may observe how the cross-section of the thin-walled structure curves inwards due to the weight. Classical beam models cannot capture this type of response and, consequently, shell or solid elements are usually employed for this problem. Indeed, given the coarse discretizations which are tested, the first-order models based on Legendre functions are discarded in this study.

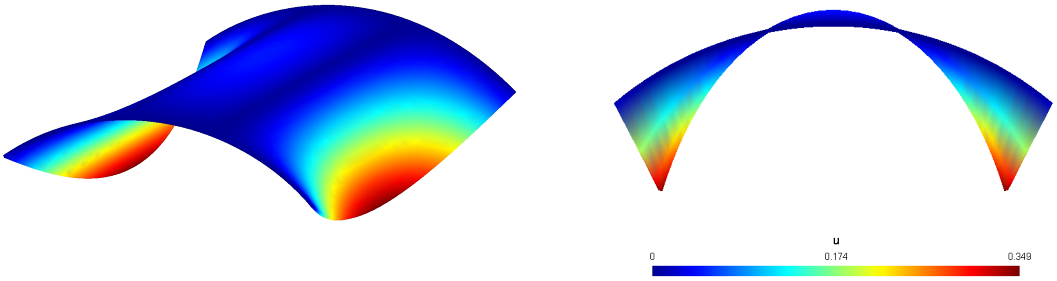

(a) 3D

(b) Front view

Fig. 3.7 Deformation of the Scordelis-Lo roof.

The results of vertical displacements at point A (see Fig. 3.5) are shown in tabular form in Tables 3.1 and 3.2 for Lagrange and Legendre 1D interpolations, respectively. It is possible to state that the numerical solutions tend in all cases to a value of $u_{z_A} \sim -0.3079$.

For a given FEM discretization, the behavior of the solutions is fairly monotonic as the HLE order increases. Figures 3.8 and 3.9 include the convergence curves based on the error in energy norm, which is computed with respect to a numerical overkill solution. There are two contributions to the total numerical error: the approximation of the beam theory and the FEM discretization. One can observe from the graph of Fig. 3.8 how for each 1D mesh the error diminishes fast with respect to the polynomial order of the HLE until a certain 'locked' solution. This means that the longitudinal approximation cannot capture the actual variation of the displacements along the y axis. Vice-versa, for a fixed polynomial order of HLE, both h and p refinements of the 1D mesh reduce systematically the error. The graphs included in Fig. 3.9 show the convergence of the different FE schemes tested here. Two conclusions can be highlighted:

- For a given order of the HLE, the numerical error is reduced monotonically for all mesh refinements.
- The convergence rates are faster for a p-refinement in comparison to a h-refinement, both for Lagrange and Legendre elements. Indeed, for a certain number of DOF (N DOFs) in 3.9 (a), the B4 solutions are more accurate than those of lower order (B3 and B2). Also, the slope of the curve in Fig. 3.9 (b) is steeper.

Table 3.1 Vertical displacement solutions obtained at point A using Lagrange beam elements for all HLE orders.

	# of B2 elements				# of B3 elements				# of B4 elements			
1D model	2	4	6	10	2	4	6	10	2	4	6	10
	Scordelis-Lo [180] u_z = -0.3086 m											
HL2	-0.0218	-0.0274	-0.0285	-0.0292	-0.0293	-0.0296	-0.0295	-0.0295	-0.0295	-0.0219	-0.0295	-0.0295
HL3	-0.2263	-0.2495	-0.2502	-0.2505	-0.2545	-0.2509	-0.2507	-0.2506	-0.2504	-0.2506	-0.2506	-0.2506
HL4	-0.2695	-0.3039	-0.3057	-0.3069	-0.3115	-0.3077	-0.3075	-0.3075	-0.3070	-0.3075	-0.3075	-0.3075
HL5	-0.2711	-0.3045	-0.3060	-0.3072	-0.3118	-0.3080	-0.3078	-0.3078	-0.3072	-0.3078	-0.3078	-0.3078
HL6	-0.2710	-0.3044	-0.3059	-0.3072	-0.3117	-0.3080	-0.3078	-0.3078	-0.3072	-0.3077	-0.3077	-0.3077
HL7	-0.2711	-0.3045	-0.3060	-0.3073	-0.3118	-0.3080	-0.3078	-0.3078	-0.3072	-0.3078	-0.3078	-0.3078
HL8	-0.2711	-0.3046	-0.3061	-0.3073	-0.3119	-0.3081	-0.3079	-0.3079	-0.3073	-0.3079	-0.3079	-0.3079

Finally, for the sake of completeness, the results obtained in this study are compared with those of the literature. These references include shell and solid elements implemented in the code Nastran by MacNeal and Harder [124], Koiter and Naghdi models from the work of Chinosi et al. [45] and refined locking-free shell elements from Cinefra et al. [50].

Table 3.2 Vertical displacement solutions obtained at point A using one Legendre element of increasing order for all HLE orders.

order:	P2	P3	P4	P5	P6
Scordelis-Lo [180] u_z = -0.3086 m					
HL2	-0.0256	-0.0292	-0.0295	-0.0294	-0.0295
HL3	-0.2342	-0.2470	-0.2517	-0.2510	-0.2506
HL4	-0.2849	-0.3030	-0.3086	-0.3078	-0.3073
HL5	-0.2859	-0.3038	-0.3090	-0.3082	-0.3076
HL6	-0.2858	-0.3038	-0.3089	-0.3081	-0.3075
HL7	-0.2859	-0.3038	-0.3090	-0.3082	-0.3076
HL8	-0.2860	-0.3039	-0.3091	-0.3082	-0.3077

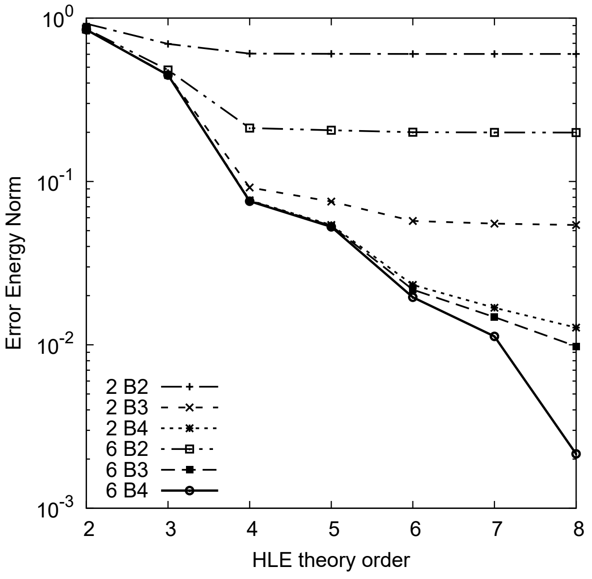

Fig. 3.8 Convergence of various Lagrange 1D meshes for increasing polynomial orders of the HLE.

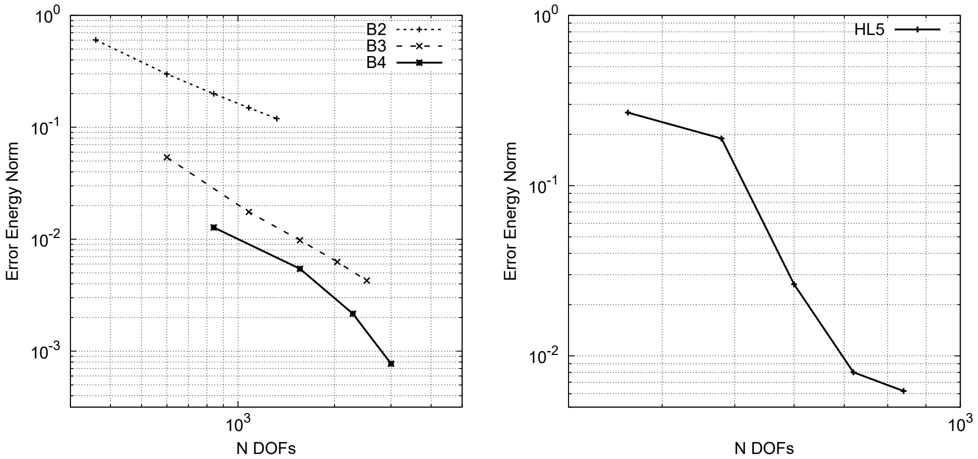

(a) Lagrange (b) Legendre

Fig. 3.9 Convergence analysis with respect to the number of DOF for a HL5 theory and all the discussed 1D meshes.

Table 3.3 Comparison of the normalized displacements, u_z/u_{ref}, against various results from the literature.

2D and 3D elements						1D HL5 model				
Mesh	4x4	6x6	8x8	10x10	13x13	Mesh	1	2	4	10
QUAD2 [124]	0.652	0.765	0.837	0.879	-	B2	-	0.879	0.987	0.996
QUAD4 [124]	1.029	0.998	0.988	0.984	-	B3	-	1.010	0.998	0.997
QUAD8 [124]	0.964	0.982	0.977	0.976	-	B4	-	0.995	0.997	0.997
HEXA8 [124]	1.007	0.992	0.985	-	-	P3	0.984	-	-	-
HEX20 [124]	0.253	0.577	0.796	-	-	P4	1.001	-	-	-
HEX20(R) [124]	0.948	0.983	0.979	-	-	P5	0.999	-	-	-
Koiter [45]	0.957	-	-	0.977	0.980					
Naghdi [45]	0.957	-	-	0.978	0.982					
MITC LD4 [50]	0.957	-	-	0.978	0.982					

Chapter 4

Mixed interpolation of tensorial components for beam elements

In the last decades, the finite element method has acquired a major importance in the computational mechanics field due to its high versatility and large adoption in commercial sofwares. In simple words, the FEM has made possible for engineers to foresee the mechanical response of complex systems from the design phase, resulting in massive reductions in the product development cost. However, one of the main limitations of the FEM stress analysis is related to the elevated computational expenses which are required for the study complex geometries. A vast amount of researches were dedicated to the introduction of new formulations based on less demanding 2D and 1D finite elements, which can provide satisfactory solutions minimizing the computational effort. In this context, there are still some challenges to be met in order to obtain effective and robust models. One of them is the shear locking that appears in finite elements when thin or slender structures are considered. This chapter is devoted to the introduction of a robust formulation, known as the mixed interpolation of tensorial components (MITC), to mitigate the shear locking in refined beam elements.

The main contents of this chapter were published in a journal paper [30].

4.1 Shear locking review

Displacement-based finite element formulations represent probably the most extended tool for the computational analysis of engineering structures. The versatility of FEM makes it possible for engineers and researchers to predict the mechanical response of structural components with few limitations in geometry or boundary conditions. Nevertheless, the users of FEM must be aware of the fact that, as for any numerical method, the solutions might be highly inaccurate under certain circumstances. In particular, in cases when thin structures are subjected to bending loadings, the numerical model may exhibit a sudden and uncontrollable increase of the shear stiffness, preventing the structure to deform. This issue, known as the *shear locking*, is considered one of the major deficiencies of the FEM. Indeed, in the last decades many have been the works proposing new formulations to mitigate this detrimental effect, see for instance [156, 164, 169, 17, 94, 53, 194, 184, 152, 222].

The shear locking appears in thin structures when, due to the finite element approximations, the shear strain energy results much higher than the real value, making the model to compute very small displacements, or in other words, to 'lock'. Since the numerical issue is a consequence of the overestimation of the shear stiffness of the finite element, it is of common use to employ certain numerical 'tricks' to diminish the computed value of the shear energies via reduced integration. Using this approach, first introduced by Zienkiewicz *et al.* [226], the order of the numerical quadrature of the stiffness matrix terms is decreased, leading to a softening of the numerical model. Other works discussing the implementation of reduced integrated schemes are [227, 160, 223]. A well-known variant of this method is known as the selective integration [66, 95, 126], which is based on the application of a reduced quadrature only in the shear terms of the stiffness matrix. The remaining terms are then computed via full integration. Although reduced elements show better convergence properties than full integrated elements, the reduction of the number of integration points in the quadrature of the stiffness terms may lead to undesired errors in the computation of the strain and stress fields and the appearance of spurious modes [124].

In order to overcome these issues, Dvorkin and Bathe [69] and MacNeal [123] proposed the use of a mixed interpolation of the strain fields in which the shear terms are approximated by means of reduced order functions. This method, commonly denoted to as Mixed Interpolation of Tensorial Components, or MITC, has been since successfully used to implement locking-free finite elements, showing remarkable levels of robustness for structural applications. Although the MITC method might be seen as selective integration of the finite element, it actually works as a full integration of the assumed strain fields. It is worth adding that a similar technique was presented before by Turner et al. [199] for the analysis of complex shell-type aeronautic structures. The use of assumed strain fields to mitigate the locking has received particular attention for the development of plate and shell elements, which due to their geometrical features are especially affected by locking issues. Some of the most renown contributions are those of Bucalem and Bathe [22], Huang and Hinton [93], Park and Stanley [153] and Jang and Pinsky [96], among others.

Although the MITC method mitigates the locking phenomena in an elegant and effective manner, its implementation in a 1D framework has not been yet fully addressed. The

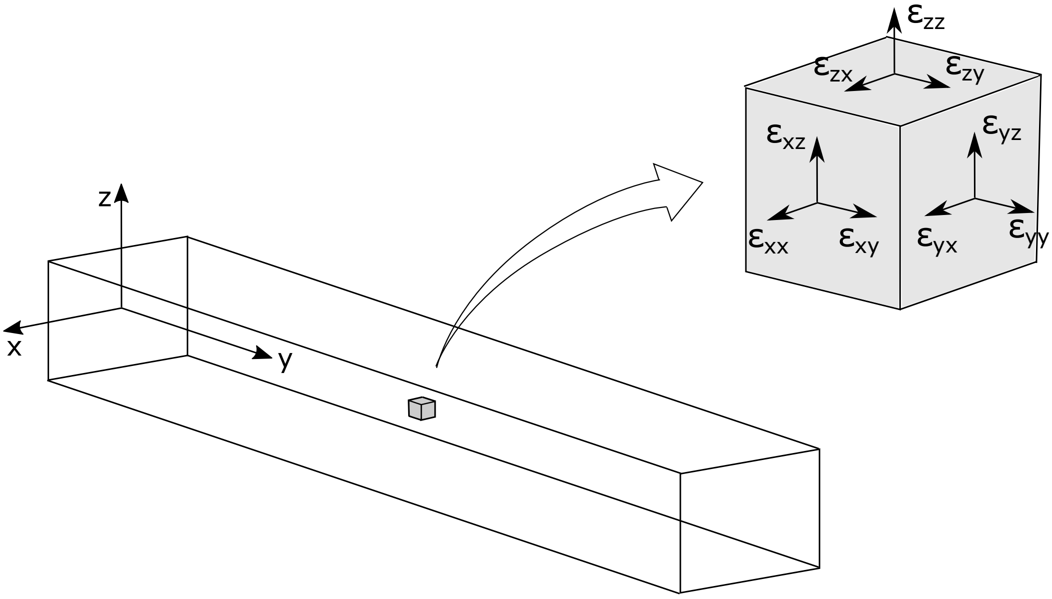

Fig. 4.1 Strain tensor in the current coordinate framework.

formulation of mixed interpolated 1D elements was initially proposed in the book of Bathe [13] for Timoshenko beams. In that text, the author demonstrates the necessity of adding assumed functions to interpolate the strains over a reduced set of points along the beam element: one point for two-noded elements, two points for three-noded elements and three points for four-noded elements. Lee et al. [113] introduced a geometry-dependent method to alleviate locking also in two-noded elements with tapered sections. More recently, Carrera and Pagani [38] assumed constant values of the shear strains in beam elements featuring variable kinematics. In the present development, the MITC method is extended to generic Lagrangian beam elements.

4.2 Geometrical and constitutive relations

For the purposes of the development of mixed interpolated elements, it is convenient to reformulate the geometrical and constitutive equations presented in the previous chapters. Let us consider the coordinate framework shown in Fig. 4.1. The strain vector can be decomposed into two separate sets of components, as follows:

$$\boldsymbol{\varepsilon}_B = \{\varepsilon_{yy}\ \varepsilon_{xx}\ \varepsilon_{zz}\ \varepsilon_{xz}\}^T \quad \boldsymbol{\varepsilon}_S = \{\varepsilon_{yz}\ \varepsilon_{xy}\}^T, \tag{4.1}$$

where $\boldsymbol{\varepsilon}_S$ contains the transverse shear components and $\boldsymbol{\varepsilon}_B$ the remaining four, including all the normal strains and the shear over the cross-section plane. Subsequently, the strain-displacement relations are written as:

$$\boldsymbol{\varepsilon}_B = \mathbf{D}_B \boldsymbol{u} = \mathbf{D}_{B_y} \boldsymbol{u} + \mathbf{D}_{B_\Omega} \boldsymbol{u}, \tag{4.2}$$

$$\boldsymbol{\varepsilon}_S = \mathbf{D}_S \boldsymbol{u} = \mathbf{D}_{S_y} \boldsymbol{u} + \mathbf{D}_{S_\Omega} \boldsymbol{u}, \tag{4.3}$$

where differential operators $\mathbf{D}_{B_y}$, $\mathbf{D}_{B_\Omega}$, $\mathbf{D}_{S_y}$ and $\mathbf{D}_{S_\Omega}$ are defined as

$$\begin{aligned} \mathbf{D}_{B_y} &= \begin{bmatrix} 0 & \frac{\partial}{\partial y} & 0 \\ 0 & 0 & 0 \\ 0 & 0 & 0 \\ 0 & 0 & 0 \end{bmatrix} \quad \mathbf{D}_{B_\Omega} = \begin{bmatrix} 0 & 0 & 0 \\ \frac{\partial}{\partial x} & 0 & 0 \\ 0 & 0 & \frac{\partial}{\partial z} \\ \frac{\partial}{\partial z} & 0 & \frac{\partial}{\partial x} \end{bmatrix} \\ \mathbf{D}_{S_y} &= \begin{bmatrix} 0 & 0 & \frac{\partial}{\partial y} \\ \frac{\partial}{\partial y} & 0 & 0 \end{bmatrix} \quad \mathbf{D}_{S_\Omega} = \begin{bmatrix} 0 & \frac{\partial}{\partial z} & 0 \\ 0 & \frac{\partial}{\partial x} & 0 \end{bmatrix} \end{aligned} \tag{4.4}$$

The stress vector is also reorganized by separating the transverse shear components from the rest, as follows:

$$\boldsymbol{\sigma}_B = \{\sigma_{yy} \ \sigma_{xx} \ \sigma_{zz} \ \sigma_{xz}\}^T \quad \boldsymbol{\sigma}_S = \{\sigma_{yz} \ \sigma_{xy}\}^T. \tag{4.5}$$

Therefore, the stress-strain relations can be rewritten accordingly

$$\left\{ \begin{array}{c} \boldsymbol{\sigma}_B \\ \boldsymbol{\sigma}_S \end{array} \right\} = \begin{bmatrix} \tilde{\mathbf{C}}_{BB} & \tilde{\mathbf{C}}_{BS} \\ \tilde{\mathbf{C}}_{SB} & \tilde{\mathbf{C}}_{SS} \end{bmatrix} \left\{ \begin{array}{c} \boldsymbol{\varepsilon}_B \\ \boldsymbol{\varepsilon}_S \end{array} \right\} \tag{4.6}$$

where the transformed material matrix $\tilde{\mathbf{C}}$, see Section 3.1, is expressed in the global reference system. Note that this matrix is also decomposed into several matrices accounting for the different terms. In the case of orthotropic materials, one can write:

$$\tilde{\mathbf{C}}_{BB} = \begin{bmatrix} \tilde{C}_{33} & \tilde{C}_{23} & \tilde{C}_{13} & 0 \\ \tilde{C}_{23} & \tilde{C}_{22} & \tilde{C}_{12} & 0 \\ \tilde{C}_{13} & \tilde{C}_{12} & \tilde{C}_{11} & 0 \\ 0 & 0 & 0 & \tilde{C}_{44} \end{bmatrix} \quad \tilde{\mathbf{C}}_{BS} = \tilde{\mathbf{C}}_{SB}^T = \begin{bmatrix} 0 & \tilde{C}_{36} \\ 0 & \tilde{C}_{26} \\ 0 & \tilde{C}_{16} \\ \tilde{C}_{45} & 0 \end{bmatrix} \quad \tilde{\mathbf{C}}_{SS} = \begin{bmatrix} \tilde{C}_{55} & 0 \\ 0 & \tilde{C}_{66} \end{bmatrix} \tag{4.7}$$

4.3 MITC beam elements

As shown in the previous chapter, the generalized unknowns of the cross-section are interpolated along the beam axis by means of 1D shape functions. Recalling Eq. (3.14), the complete displacement field can be written as

$$\boldsymbol{u}(x,y,x) = F_\tau(x,z)\,N_i(y)\,\boldsymbol{u}_{\tau i} \tag{4.8}$$

with $\tau = 1,2,...,M$ and $i = 1,2,...,n_n$. Lagrange two-node, three-node and four-node line elements are formulated here. The interpolation polynomials are depicted in Eqs. (3.17-3.19), respectively. Through the geometrical relations defined in Eq. (4.3), the strain components are computed from the derivatives of the expansion assumptions and the beam functions, as

$$\boldsymbol{\varepsilon}_B = F_\tau(\mathbf{D}_{B_y} N_i \mathbf{I}_3)\boldsymbol{u}_{\tau i} + (\mathbf{D}_{B_\Omega} F_\tau \mathbf{I}_3) N_i \boldsymbol{u}_{\tau i} \tag{4.9}$$

$$\boldsymbol{\varepsilon}_S = F_\tau(\mathbf{D}_{S_y} N_i \mathbf{I}_3)\boldsymbol{u}_{\tau i} + (\mathbf{D}_{S_\Omega} F_\tau \mathbf{I}_3) N_i \boldsymbol{u}_{\tau i} \tag{4.10}$$

where $\mathbf{I}_3$ is the 3×3 identity matrix. Note that by virtue of this expression, it is possible to split the interpolation of the transverse shear strain components from the rest. To this point, all the element strains are obtained directly from the same displacement approximations, N_i. As it is known, this standard approach is not physically consistent for bending problems, in which the distribution of shear strains should be of one order less than that of normal strains. As a consequence, the finite element can be too stiff in cases of beams with high slenderness ratios, in which the contribution of the transverse shear deformation should be negligible. The MITC method overcomes this issue of standard finite elements through an independent, lower-order interpolation of the transverse shear strains. Therefore, the shear strains of a MITC beam element are formulated as:

$$\bar{\boldsymbol{\varepsilon}}_S = \bar{N}_m\,\boldsymbol{\varepsilon}_{S_m} \qquad m = 1,...,n_n - 1 \tag{4.11}$$

where $\bar{N}_m$ are the assumed interpolations and $\boldsymbol{\varepsilon}_{S_m}$ are the shear strain values computed from the displacement derivatives in a reduced set of $n_n - 1$ points along the beam element. These points are known as tying points, T_m, and they are used to tie the displacement approximations with the strain assumptions. There is one tying point in a linear element, two in a quadratic element and three in a cubic element. For these MITC beam elements, the assumed strains are constant, linear and quadratic, respectively. Figure 4.2 illustrates the nodes and tying points for each element and the assumed strain distributions along the element.

The assumed functions for the strains, $\bar{N}_m$, are derived using a Lagrange polynomial basis, in such a way that

$$\bar{N}_m(T_n) = 1 \qquad\qquad if\ m = n \tag{4.12}$$

$$\bar{N}_m(T_n) = 0 \qquad\qquad otherwise \tag{4.13}$$

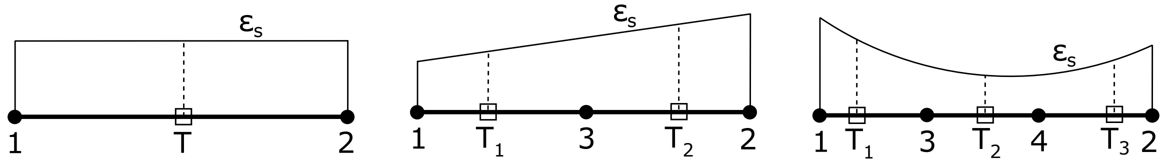

(a) 2-node (b) 3-node (c) 4-node

Fig. 4.2 MITC element interpolations of shear strains.

For the sake of completeness, the assumed interpolation functions are included in the following:

- two-node element:

$$\bar{N}_1 = 1, \qquad \xi_T = 0 \tag{4.14}$$

- three-node element:

$$\bar{N}_1 = -\tfrac{1}{2}\sqrt{3}(\xi - \tfrac{1}{\sqrt{3}}),\ \bar{N}_2 = \tfrac{1}{2}\sqrt{3}(\xi + \tfrac{1}{\sqrt{3}}),\ \begin{cases} \xi_{T_1} = -\frac{1}{\sqrt{3}} \\ \xi_{T_2} = \frac{1}{\sqrt{3}} \end{cases} \tag{4.15}$$

- four-node element:

$$\bar{N}_1 = \tfrac{5}{6}\xi(\xi - \sqrt{\tfrac{3}{5}}),\ \bar{N}_2 = -\tfrac{5}{3}(\xi - \sqrt{\tfrac{3}{5}})(\xi + \sqrt{\tfrac{3}{5}}), \bar{N}_3 = \tfrac{5}{6}\xi(\xi + \sqrt{\tfrac{3}{5}}),\ \begin{cases} \xi_{T_1} = -\sqrt{\frac{3}{5}} \\ \xi_{T_2} = 0 \\ \xi_{T_3} = \sqrt{\frac{3}{5}} \end{cases} \tag{4.16}$$

ξ_{T_m} are the locations of the tying points in the interval [-1, 1] of the beam element. One can notice that these coordinates correspond to the locations of the Gauss points. Indeed, these set of points are also denoted to as Barlow points [11], which are known for providing the highest accuracy in the computation of the strains within the finite element.

Subsequently, introducing Eq. (4.10) into Eq. (4.11), the element shear strains are written as:

$$\bar{\boldsymbol{\varepsilon}}_S = \bar{N}_m F_\tau (\mathbf{D}_{S_y} N_i \mathbf{I})_m \boldsymbol{u}_{\tau i} + \bar{N}_m (\mathbf{D}_{S_\Omega} F_\tau \mathbf{I}) N_{i_m} \boldsymbol{u}_{\tau i} \tag{4.17}$$

Note that N_{i_m} is the value of the shape function N_i at the tying point, or $N_i(T_m)$. For the sake of clarity, the explicit expressions of the differential operators are included in matrix form:

$$(\mathbf{D}_{S_y} N_i \mathbf{I})_m = \begin{bmatrix} 0 & 0 & N_{i,y}(T_m) \\ N_{i,y}(T_m) & 0 & 0 \end{bmatrix}, \quad \mathbf{D}_{S_\Omega} F_\tau \mathbf{I} = \begin{bmatrix} 0 & F_{\tau,z} & 0 \\ 0 & F_{\tau,x} & 0 \end{bmatrix} \tag{4.18}$$

The first matrix is composed of the values of the derivatives of the shape functions evaluated at the tying points, whereas the second array accounts for the derivatives of the expansions over the cross-section.

By substituting the assumed strains in the Hooke's law, Eq. (4.6), the stress-strain relations now read:

$$\left\{ \begin{array}{c} \bar{\boldsymbol{\sigma}}_B \\ \bar{\boldsymbol{\sigma}}_S \end{array} \right\} = \left[\begin{array}{cc} \tilde{\mathbf{C}}_{BB} & \tilde{\mathbf{C}}_{BS} \\ \tilde{\mathbf{C}}_{SB} & \tilde{\mathbf{C}}_{SS} \end{array} \right] \left\{ \begin{array}{c} \boldsymbol{\varepsilon}_B \\ \bar{\boldsymbol{\varepsilon}}_S \end{array} \right\} \tag{4.19}$$

Accordingly, the stress fields in the MITC element are computed as

$$\begin{aligned} \bar{\boldsymbol{\sigma}}_B = \;& \tilde{\mathbf{C}}_{BB}\left[F_\tau(\mathbf{D}_{B_y}N_i\mathbf{I})\boldsymbol{u}_{\tau i} + (\mathbf{D}_{B_\Omega}F_\tau\mathbf{I})N_i\boldsymbol{u}_{\tau i}\right] \\ & + \tilde{\mathbf{C}}_{BS}\left[\bar{N}_m F_\tau(\mathbf{D}_{S_y}N_i\mathbf{I})_m\boldsymbol{u}_{\tau i} + \bar{N}_m(\mathbf{D}_{S_\Omega}F_\tau\mathbf{I})N_{i_m}\boldsymbol{u}_{\tau i}\right] \\ \bar{\boldsymbol{\sigma}}_S = \;& \tilde{\mathbf{C}}_{SB}\left[F_\tau(\mathbf{D}_{B_y}N_i\mathbf{I})\boldsymbol{u}_{\tau i} + (\mathbf{D}_{B_\Omega}F_\tau\mathbf{I})N_i\boldsymbol{u}_{\tau i}\right] \\ & + \tilde{\mathbf{C}}_{SS}\left[\bar{N}_m F_\tau(\mathbf{D}_{S_y}N_i\mathbf{I})_m\boldsymbol{u}_{\tau i} + \bar{N}_m(\mathbf{D}_{S_\Omega}F_\tau\mathbf{I})N_{i_m}\boldsymbol{u}_{\tau i}\right] \end{aligned} \tag{4.20}$$

Note that the unknowns of the MITC element remain those related to the displacements of the standard CUF element, $\boldsymbol{u}_{\tau i}$. No extra degrees of freedom are added, which is advantageous from the computational expense standpoint.

4.3.1 Fundamental nucleus

For the purposes of the implementation of MITC elements and recalling the PVD, the virtual variation of the internal work, introduced in Eq. (3.25), can be written as

$$\delta L_{int} = \int_L \int_\Omega \delta\boldsymbol{\varepsilon}^T \boldsymbol{\sigma}\, d\Omega\, dy = \int_L \int_\Omega (\delta\boldsymbol{\varepsilon}_B^T\, \bar{\boldsymbol{\sigma}}_B + \delta\bar{\boldsymbol{\varepsilon}}_S^T\, \bar{\boldsymbol{\sigma}}_S)\, d\Omega\, dy \tag{4.21}$$

Ω and L being the cross-section domain and the length of the beam element, respectively. According to the definitions of the element stresses (Eq. (4.20)) and strains (Eqs. (4.10) and (4.17)), the elastic strain energy results:

$$\begin{aligned} &\delta L_{int} = \\ &\int_L \int_\Omega \Big([\delta\boldsymbol{u}_{sj}F_s(\mathbf{D}_{B_y}N_j\mathbf{I}) + \delta\boldsymbol{u}_{sj}\,(\mathbf{D}_{B_\Omega}F_s\mathbf{I})N_j]\,\tilde{\mathbf{C}}_{BB}\left[F_\tau(\mathbf{D}_{B_y}N_i\mathbf{I})\boldsymbol{u}_{\tau i} + (\mathbf{D}_{B_\Omega}F_\tau\mathbf{I})N_i\boldsymbol{u}_{\tau i}\right] + \\ &[\delta\boldsymbol{u}_{sj}F_s(\mathbf{D}_{B_y}N_j\mathbf{I}) + \delta\boldsymbol{u}_{sj}\,(\mathbf{D}_{B_\Omega}F_s\mathbf{I})N_j]\,\tilde{\mathbf{C}}_{BS}\,[\bar{N}_m F_\tau(\mathbf{D}_{S_y}N_i\mathbf{I})_m\boldsymbol{u}_{\tau i} + \bar{N}_m(\mathbf{D}_{S_\Omega}F_\tau\mathbf{I})N_{i_m}\boldsymbol{u}_{\tau i}] + \\ &[\delta\boldsymbol{u}_{sj}\bar{N}_n F_s(\mathbf{D}_{S_y}N_j\mathbf{I})_n + \delta\boldsymbol{u}_{sj}\,\bar{N}_n(\mathbf{D}_{S_\Omega}F_s\mathbf{I})N_{j_n}]\,\tilde{\mathbf{C}}_{SB}\left[F_\tau(\mathbf{D}_{B_y}N_i\mathbf{I})\boldsymbol{u}_{\tau i} + (\mathbf{D}_{B_\Omega}F_\tau\mathbf{I})N_i\boldsymbol{u}_{\tau i}\right] + \\ &[\delta\boldsymbol{u}_{sj}\bar{N}_n F_s(\mathbf{D}_{S_y}N_j\mathbf{I})_n + \delta\boldsymbol{u}_{sj}\,\bar{N}_n(\mathbf{D}_{S_\Omega}F_s\mathbf{I})N_{j_n}]\tilde{\mathbf{C}}_{SS}\,[\bar{N}_m F_\tau(\mathbf{D}_{S_y}N_i\mathbf{I})_m\boldsymbol{u}_{\tau i} + \bar{N}_m(\mathbf{D}_{S_\Omega}F_\tau\mathbf{I})N_{i_m}\boldsymbol{u}_{\tau i}] \\ &\Big)\, d\Omega\, dy \end{aligned} \tag{4.22}$$

As in the previous chapter, this expression can be compacted into:

$$\delta L_{\text{int}} = \delta \boldsymbol{u}_{sj}^{T} \mathbf{K}^{\tau sij} \boldsymbol{u}_{\tau i} \tag{4.23}$$

where $\mathbf{K}^{\tau sij}$ is the fundamental nucleus of the MITC beam element. Same as for standard beam elements, the fundamental nucleus is a 3×3 matrix that acts as the smallest building block of the model. The formal expressions of its nine components are included here:

$$\begin{aligned} K_{xx}^{\tau sij} = {} & \widetilde{C}_{22} \int_L N_i N_j \, dy \, E_{\tau_{,x} s_{,x}} + \widetilde{C}_{44} \int_L N_i N_j \, dy \, E_{\tau_{,z} s_{,z}} + \widetilde{C}_{26} \int_L N_i (N_n N_{(j_{,y})_n}) \, dy \, E_{\tau_{,x} s} \\ & + \widetilde{C}_{26} \int_L (N_m N_{(i_{,y})_m}) N_j \, dy \, E_{\tau s_{,x}} + \widetilde{C}_{66} \int_L (N_m N_{(i_{,y})_m}) (N_n N_{(j_{,y})_n}) \, dy \, E_{\tau s} \end{aligned} \tag{4.24}$$

$$\begin{aligned} K_{xy}^{\tau sij} = {} & \widetilde{C}_{23} \int_L N_i N_{j_{,y}} \, dy \, E_{\tau_{,x} s} + \widetilde{C}_{45} \int_L N_i (N_n N_{j_n}) \, dy \, E_{\tau_{,z} s_{,z}} + \widetilde{C}_{26} \int_L N_i (N_n N_{j_n}) \, dy \, E_{\tau_{,x} s_{,x}} \\ & + \widetilde{C}_{36} \int_L (N_m N_{(i_{,y})_m}) N_j \, dy \, E_{\tau s} + \widetilde{C}_{66} \int_L (N_m N_{(i_{,y})_m}) (N_n N_{j_n}) \, E_{\tau s_{,x}} \end{aligned} \tag{4.25}$$

$$\begin{aligned} K_{xz}^{\tau sij} = {} & \widetilde{C}_{12} \int_L N_i N_j \, dy \, E_{\tau_{,x} s_{,z}} + \widetilde{C}_{44} \int_L N_i N_j \, dy \, E_{\tau_{,z} s_{,x}} + \widetilde{C}_{45} \int_L N_i (N_n N_{(j_{,y})_n}) \, E_{\tau_{,z} s} \\ & + \widetilde{C}_{16} \int_L (N_m N_{(i_{,y})_m}) N_j \, E_{\tau s_{,z}} \end{aligned} \tag{4.26}$$

$$\begin{aligned} K_{yx}^{\tau sij} = {} & \widetilde{C}_{23} \int_L N_{i_{,y}} N_j \, dy \, E_{\tau s_{,x}} + \widetilde{C}_{45} \int_L (N_m N_{i_m}) N_j \, dy \, E_{\tau_{,z} s_{,z}} + \widetilde{C}_{26} \int_L (N_m N_{i_m}) N_j \, dy \, E_{\tau_{,x} s_{,x}} \\ & + \widetilde{C}_{36} \int_L N_{i_{,y}} (N_n N_{(j_{,y})_n}) \, dy \, E_{\tau s} + \widetilde{C}_{66} \int_L (N_m N_{i_m}) (N_n N_{(j_{,y})_n}) \, dy \, E_{\tau_{,x} s} \end{aligned} \tag{4.27}$$

$$\begin{aligned} K_{yy}^{\tau sij} = {} & \widetilde{C}_{33} \int_L N_{i_{,y}} N_{j_{,y}} \, dy \, E_{\tau s} + \widetilde{C}_{36} \int_L (N_m N_{i_m}) N_{j_{,y}} \, dy \, E_{\tau_{,x} s} + \widetilde{C}_{36} \int_L N_{i_{,y}} (N_n N_{j_n}) \, E_{\tau s_{,x}} \\ & + \widetilde{C}_{55} \int_L (N_m N_{i_m}) (N_n N_{j_n}) \, dy \, E_{\tau_{,z} s_{,z}} + \widetilde{C}_{66} \int_L (N_m N_{i_m}) (N_n N_{j_n}) \, dy \, E_{\tau_{,x} s_{,x}} \end{aligned} \tag{4.28}$$

$$\begin{aligned} K_{yz}^{\tau sij} = {} & \widetilde{C}_{13} \int_L N_{i_{,y}} N_j \, dy \, E_{\tau s_{,z}} + \widetilde{C}_{55} \int_L (N_m N_{i_m}) (N_n N_{(j_{,y})_n}) \, dy \, E_{\tau_{,z} s} \\ & + \widetilde{C}_{45} \int_L (N_m N_{i_m}) N_j \, dy \, E_{\tau_{,z} s_{,x}} + \widetilde{C}_{16} \int_L (N_m N_{i_m}) N_j \, dy \, E_{\tau_{,x} s_{,z}} \end{aligned} \tag{4.29}$$

$$\begin{aligned} K_{zx}^{\tau sij} = {} & \widetilde{C}_{12} \int_L N_i N_j \, dy \, E_{\tau_{,z} s_{,x}} + \widetilde{C}_{44} \int_L N_i N_j \, dy \, E_{\tau_{,x} s_{,z}} + \widetilde{C}_{45} \int_L (N_m N_{(i_{,y})_m}) N_j \, dy \, E_{\tau s_{,z}} \\ & + \widetilde{C}_{16} \int_L N_i (N_n N_{(j_{,y})_n}) \, dy \, E_{\tau_{,z} s} \end{aligned} \tag{4.30}$$

$$\begin{aligned} K_{zy}^{\tau sij} = {} & \widetilde{C}_{13} \int_L N_i N_j \, dy \, E_{\tau_{,z} s} + \widetilde{C}_{55} \int_L (N_m N_{(i_{,y})_m}) (N_n N_{j_n}) \, dy \, E_{\tau s_{,z}} \\ & + \widetilde{C}_{45} \int_L N_i (N_n N_{(j_{,y})_n}) \, dy \, E_{\tau_{,x} s_{,z}} + \widetilde{C}_{16} \int_L N_i (N_n N_{(j_{,y})_n}) \, dy \, E_{\tau_{,z} s_{,x}} \end{aligned} \tag{4.31}$$

$$\begin{aligned}K_{zz}^{\tau s i j} = {} & \widetilde{C}_{11}\int_L N_i N_j \, dy E_{\tau_{,z}s_{,z}} + \widetilde{C}_{44}\int_L N_i N_j \, dy E_{\tau_{,x}s_{,x}} + \widetilde{C}_{45}\int_L N_i (N_n N_{(j_{,y})_n}) \, dy E_{\tau_{,x}s} \\ & + \widetilde{C}_{55}\int_L (N_m N_{(i_{,y})_m})(N_n N_{(j_{,y})_n}) \, dy E_{\tau s} + \widetilde{C}_{45}\int_L (N_m N_{(i_{,y})_m}) N_j \, dy E_{\tau s_{,x}}\end{aligned} \tag{4.32}$$

The subscripts i and j are the loops on the FE nodes, whereas τ and s are those of the expansion terms over the cross-section (see Chapter 2). The subscripts m and n refer to the loops over the typing points. Note that while N_m is the m-th interpolation function for the assumed strains, $N_{(i_{,y})_m}$ is the derivative y of the displacement shape function, N_i, evaluated at the tying point m, or $N_{i_{,y}}(T_m)$. The $E_{\tau_{(,x)(,z)}s_{(,x)(,z)}}$ terms correspond to the integrals of the expansion functions, F_τ, over the cross-section surface, Ω, see Eq. (3.37).

As a result of this formulation, the integrals of the shear terms of the stiffness matrix are computed using a set of assumed interpolations N_m and N_n, which are always one order less than the interpolation of the displacement unknowns. A full Gaussian quadrature is used for all the integrals, which prevents the appearance of unexpected spurious effects. The MITC method in the CUF framework provides a class of advanced beam elements which are robust and do not lock when slender structures are considered. These elements are computationally similar to the standard ones in that the unknowns of the problem remain the same and the assembly of the stiffness matrix is done by means of the same statements, see Fig. 3.4. Moreover, MITC elements compute more accurate strain and stress fields than reduced integrated elements, as it is shown in the next section.

4.4 Example

A numerical example is included here to show the capabilities of the proposed locking-free beam elements in comparison with standard full and reduced integrated elements. The problem case is illustrated in Fig. 4.3 and considers a cantilever beam of square section loaded at the free end with a point load. The length of the beam is $L = 1$ m whereas the cross-section dimension is $b = 0.1$ m. The magnitude of the vertical load is $F = 100$. The material corresponds to an Aluminum alloy of $E = 75$ GPa and $\nu = 0.33$.

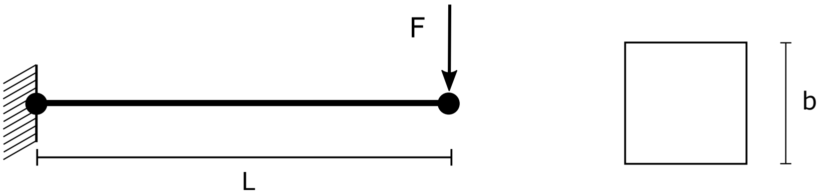

Fig. 4.3 Cantilever beam under shear-bending loading. The beam is modeled using a single 1D element.

An analytical solution of the problem can be obtained making use of the Timoshenko's theory, according to which the vertical displacement at the tip is equal to:

$$u = u_{z_b} + u_{z_s} = \frac{F_z L^3}{3EI} + \frac{F_z L}{AG} = -5.369 \times 10^{-5}\, m, \tag{4.33}$$

where u_{z_b} and u_{z_s} are the contributions from the bending and shear effects, respectively. Assuming constant shear over the cross-section, a first approximation of the shear stresses over the beam is given by:

$$\sigma_{yz} = -\frac{F_z}{\Omega} = -1.0 \times 10^4 \text{ Pa}. \tag{4.34}$$

where $\Omega = b^2$. Furthermore, a second approximation of the shear stresses can be obtained by taking into consideration the first momentum of area, $S_x(z) = \int_\Omega z d\Omega$, and the intertia of the section, I_x. In this case, the distribution of shear stresses over the thickness of the cross-section is given by:

$$\sigma_{yz}(z) = -\frac{F_z S_x(z)}{Ib}, \tag{4.35}$$

Accordingly, the maximum shear stress at the center of the cross-section is equal to:

$$\sigma_{yz}(z=0) = -\frac{3F_z}{2A} = -1.500 \times 10^4 \text{ Pa}. \tag{4.36}$$

Table 4.1 Displacements and shear stresses computed by the different beam elements.

		L4 model					L9 model				
		$u_z \times 10^5$ m	$\sigma_{yz} \times 10^{-4}$ Pa				$u_z \times 10^5$ m	$\sigma_{yz} \times 10^{-4}$ Pa			
		y = L	Node 1	Node 2	Node 3	Node 4	y = L	Node 1	Node 2	Node 3	Node 4
B2	Full	-0.138	-3.902	1.902	-	-	-0.139	-3.915	1.910	-	-
	Reduced	-3.382	-95.367	93.367	-	-	-4.035	-113.770	111.684	-	-
	Selective	-3.193	-90.037	88.037	-	-	-3.606	-101.664	99.605	-	-
	MITC	-3.193	-1.000	-1.000	-	-	-3.606	-1.029	-1.029	-	-
B3	Full	-3.424	-4.935	0.967	-4.935	-	-3.942	-4.667	0.810	-4.603	-
	Reduced	-4.492	-32.355	14.678	-32.355	-	-5.363	-38.485	17.687	-38.056	-
	Selective	-4.175	-27.889	12.445	-27.889	-	-4.663	-28.628	12.771	-28.431	-
	MITC	-4.175	-1.000	-1.000	-1.000	-	-4.663	-1.094	-0.996	-0.898	-
B4	Full	-4.311	-0.289	-1.290	-0.710	-1.711	-4.950	0.386	-1.582	-0.357	-2.581
	Reduced	-4.488	-0.841	-1.065	-0.935	-1.159	-5.359	-0.849	-1.135	-0.694	-2.005
	Selective	-4.319	1.497	-2.017	0.017	-3.497	-4.988	4.334	-3.248	1.327	6.659
	MITC	-4.319	-1.000	-1.000	-1.000	-1.000	-4.988	-1.228	-0.982	-0.939	-1.097

The present study focuses on the effects shear locking in linear, quadratic and cubic beam elements. Different integration schemes and the MITC method are considered. Only one beam element is employed. Two beam models are tested: a bilinear L4 and a biquadratic L9, see Section 2.3.2. Table 4.1 displays the solutions of tip displacements and shear stresses for all the possible combinations of elements, integrations and section expansions. Note that B2, B3 and B4 refer to two-noded, three-noded and four-noded beam elements, respectively. All the solutions are evaluated at the center of the cross-section. The distribution of shear stresses along the center of the beam, $0 \leq y \leq 1$, is displayed in Fig. 4.4 for elements featuring L4 kinematics. Finally, Fig. 4.5 shows the convergence of the displacement solutions for a increasing number of linear elements (B2) and the different integration schemes. Some remarks can be made out of the results:

- Standard full integrated elements exhibit shear locking. The displacements solutions are in all cases lower than the other elements. Indeed, the two-noded elements gives almost zero value for the displacements.
- Higher-order beam elements are less affected by locking issues. The reason being that the numerical overestimation of the shear energies is less dramatic than in linear elements.
- From Fig. 4.5, it can be observed that the convergence behavior in terms of displacements of MITC elements is equivalent to that of the selective integration for the problem case considered here.
- Although reduced and selective integrations perform well for the computation of the displacement solutions, the stress fields of the element are not accurate and exhibit large oscillations around the exact solution. This numerical deficiency prevent the use of reduced integrations if a good approximation of the shear stresses is required from the analysis. On the other hand, the shear stresses of the MITC elements show very low (or none) oscillations along the beam axis.

Equation (4.35) suggests that the shear stresses are quadratic across the thickness of the beam. In order to capture this distribution the kinematics of the cross-section must be enriched. Using HLE, the polynomial order of the F_τ set of cross-section functions is increased hierarchically allowing the model to capture highly complex distributions of the stress fields. Figure 4.6 includes the graph of the transverse shear stresses along the z axis for a four-node MITC element at the second node ($y = L/3$) and various HLE orders. The analytical solution is also included for comparison. As expected, at least a third-order model (HL3) is required to represent the parabolic distribution of these solutions.

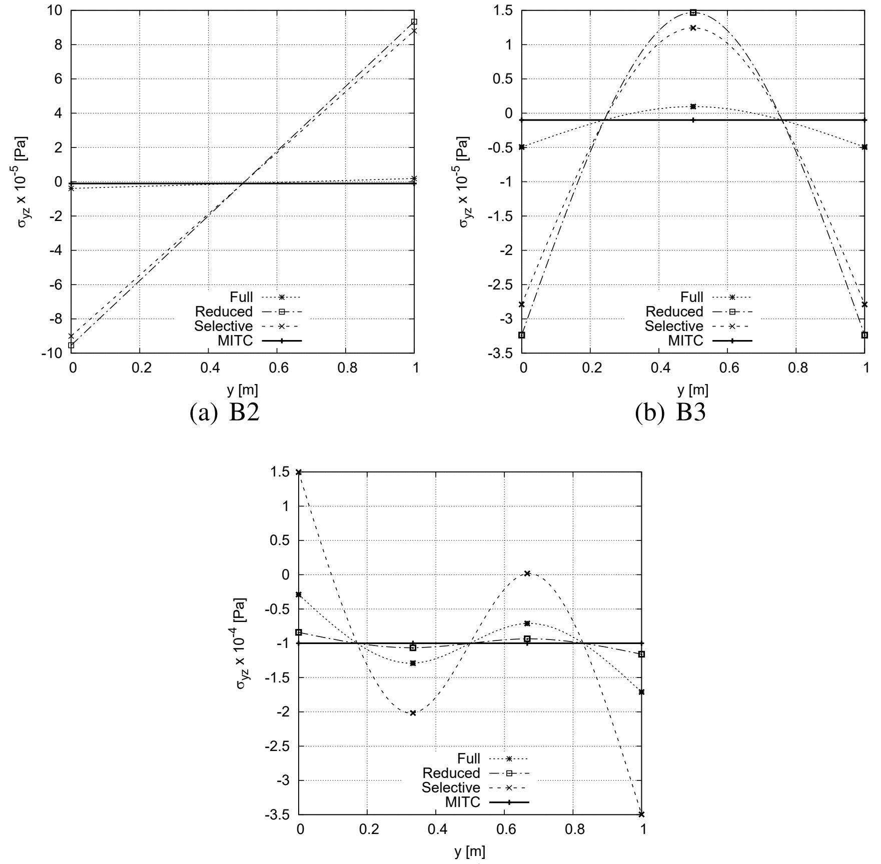

(a) B2 (b) B3

(c) B4

Fig. 4.4 Distribution of shear stresses, σ_{yz}, over the beam's length for L4 expansion. The Timoshenko's analytical solution is $\sigma_{yz} = -1.0 \times 10^4$ Pa.

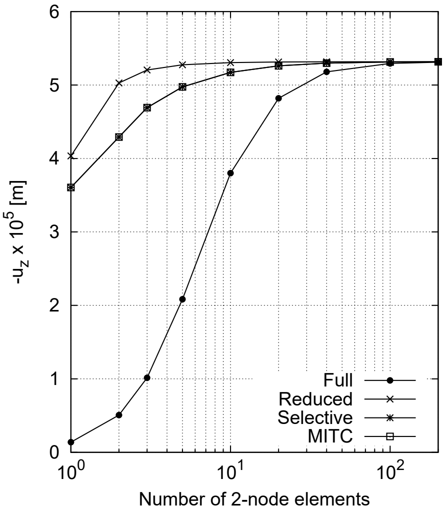

Fig. 4.5 Convergence of the vertical displacement, u_z, at the tip for linear elements with different integration schemes.

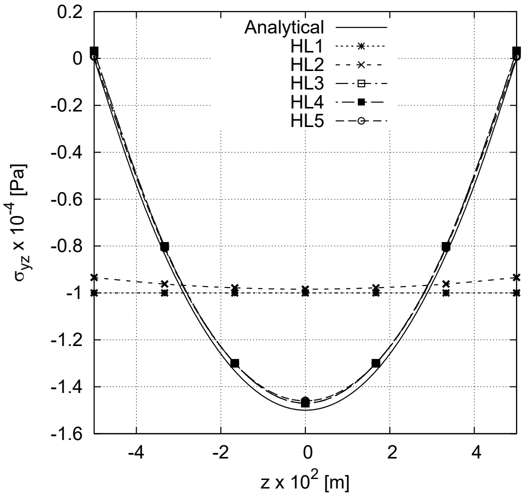

Fig. 4.6 Distribution of shear stresses, σ_{yz}, across the thickness of the beam for a single B4 MITC element at $y = L/3$.

Chapter 5

Locking-free curved beam elements

This chapter is an extension of the previous formulation of locking-free elements for curved beam structures. A new kind of locking appears in the finite elements when a curved geometry is considered: the membrane locking. This numerical effect arises due to the axial-membrane coupling and must be appropriately mitigated for the generation of robust FEM models. An overview of curved finite elements is provided and the MITC method is implemented to overcome all kinds of locking.

The theoretical developments and numerical results were published in [61].

5.1 Curved finite elements and membrane locking

The analysis of curved structures adds some complexities to the FEM modeling. First, the geometrical approximation of curved paths and boundaries is definitely more complicated than that of straight bodies, often leading to the introduction of numerical errors due to the inability of the model to represent the exact geometry. In addition, the mechanical response is dominated by the coupling between axial and bending deformations, which must be captured by the model. This effect is illustrated in a simple example in Fig. 5.1, which shows the bending deformation of an arch when loaded axially. Despite these difficulties and given the fact that many of the structures that surround us exhibit curved geometries, the implementation of reliable computational models for curved bodies is of paramount importance and, therefore, has been addressed since the early years of FEM.

Some of the initial studies on curved elastic theories were carried out by Love [121] and Lamb [109]. Since then, many advances on the modeling of curved structures have been discussed in the literature, for instance in Ericksen and Truesdell [72], Washizu [205], Reissner [172], Ashwell and Gallagher [7], Banan [10] and Tufekci and Arpaci [198]. It is well-known in the FEM community that the coupling between membrane and bending

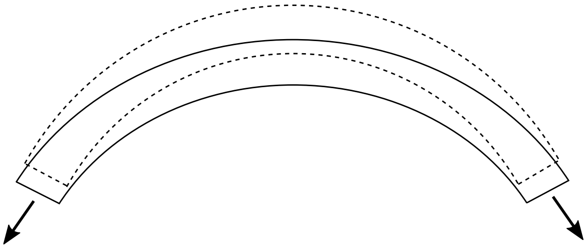

Fig. 5.1 Illustration of the membrane-bending coupling in curved structures.

effects in curved finite elements leads to numerical inconsistencies in the computation of the stiffness integrals that make the elements too stiff. This detrimental issue is known as *membrane locking*, and, together with the shear locking (see Section 4.1), poses a major threat for the robustness of the FEM model. As a consequence, huge efforts have been made to mitigate this stiffening behavior. Several remarkable contributions are depicted in the following.

The implementation of reduced and selective reduced integration schemes for the evaluation of the stiffness terms is one of the most adopted techniques against locking in FEM. Its application in curved shells and beams was done by Noor and Peters [141] and Stolarski and Belytschko [185]. A set of higher-order polynomials for curved arch elements was proposed by Dawe [57], concluding that a quintic models provided the best solutions for thin and thick structures. Babu and Prathap [9] and Alturi *et al.* [8] introduced a family of locking-free elements making use of field-consistent membrane and shear interpolations accounting for their constrained physical limits. Earlier, Fried [78] suggested the use of specific shape functions obtained from the integration of the polynomial expressions, avoiding in this manner the inconsistencies in the interpolation of the strains. Tessler and Spiridigliozzi [195] presented an anisoparametric beam element using a local penalty-relaxation method. More recently, Kim and Kim [104] proposed a hybrid-mixed formulation in which higher-order interpolations are used to generate finite elements featuring nodeless degrees of freedom to mitigate locking.

As a continuation of the previous chapter, the aim here is to devise locking-free curved beam elements by means of the mixed interpolation of tensorial components (MITC) method [69, 123]. Accordingly, a mixed interpolation of the element deformation is performed by reducing the order of both membrane and shear assumed strains. Similar approaches based on MITC can be found in Bucalem and Bathe [22], Huang and Hinton [93], Jang and Pinsky [96], Park and Stanley [153] and Cinefra *et al.* [50]. The main advantage of this method is that the inconsistencies in the strain interpolations are eliminated while performing a full integration of the energy terms of the stiffness matrix of the element. Moreover, no extra

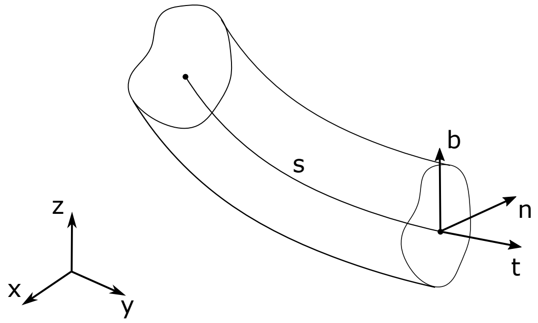

Fig. 5.2 Frenet-Serret coordinate system of a reference beam.

degrees of freedom are added to the problem and the prediction of membrane and shear strains and stresses is superior to that of reduced integrated elements.

5.2 Curved beams: the general framework

Let us consider a general curve expressed by the vector **r**(s), with s being the curvilinear abscissa of the beam. The components of $\mathbf{r}(s)$ correspond to the Cartesian coordinates of the line of centers of the beam section, i.e. the beam axis, see Fig. 5.2. This curvilinear system is represented by the Frenet-Serret frame, which is defined by an orthonormal vector basis $\{\mathbf{t},\mathbf{b},\mathbf{n}\}$, being:

$$\mathbf{t}(s) = \frac{\frac{d\mathbf{r}(s)}{ds}}{\left\|\frac{d\mathbf{r}(s)}{ds}\right\|}, \qquad \mathbf{n}(s) = \frac{\frac{d^2\mathbf{r}(s)}{ds^2}}{\left\|\frac{d^2\mathbf{r}(s)}{ds^2}\right\|}, \qquad \mathbf{b}(s) = \mathbf{t}\times\mathbf{n}. \tag{5.1}$$

t is the tangent versor of the curve at a given coordinate s, **n** is the normal versor oriented towards the center of the curve, and **b** is the binormal versor. This reference system is used to express all the variables of the beam problem hereinafter.

Subsequently, a generic curve in the 3D space can be defined by two parameters, known as the curvature κ and torsion T, respectively:

$$\kappa(s) = \left\|\frac{d^2\mathbf{r}(s)}{ds^2}\right\|, \qquad \mathrm{T}(s) = \frac{d\mathbf{n}(s)}{ds}\cdot\mathbf{b}. \tag{5.2}$$

Accordingly, the Frenet-Serret formulas provide the expressions for the derivatives of the versors $\{\mathbf{t},\mathbf{n},\mathbf{b}\}$ as:

$$\frac{d}{ds}\begin{Bmatrix}\mathbf{t}\\ \mathbf{n}\\ \mathbf{b}\end{Bmatrix} = \begin{bmatrix}0 & \kappa & 0\\ -\kappa & 0 & \mathrm{T}\\ 0 & -\mathrm{T} & 0\end{bmatrix}\begin{Bmatrix}\mathbf{t}\\ \mathbf{n}\\ \mathbf{b}\end{Bmatrix}. \tag{5.3}$$

It is pointed out that in the present formulation the torsion of the curve is not considered, thus T is set as zero. As a consequence, the undeformed curved beam lies on a plane.

Let $\{s, \xi, \eta\}$ be the curvilinear coordinate system associated to the Frenet-Serret reference frame, therefore the position of a generic point P over the 3D beam can be expressed as:

$$\boldsymbol{r}_P = \boldsymbol{r}(s_P) + \xi_P \boldsymbol{n} + \eta_P \boldsymbol{b}. \tag{5.4}$$

Finally, the determinant of the metric tensor in this system is defined as [205]

$$g = (1 - \kappa \xi)^2. \tag{5.5}$$

Therefore, the infinitesimal volume in the curved beam must be calculated as

$$dV = \sqrt{g}\, ds\, d\xi\, d\eta, \tag{5.6}$$

which accounts for the deformation of the infinitesimal parallelepiped due to the curvature of the longitudinal direction, s.

5.3 Geometrical and constitutive relations

According to the aforementioned formulation, the displacements of the deformed beam are now expressed in the local coordinate system:

$$\boldsymbol{u} = u_s \mathbf{t} + u_\xi \mathbf{n} + u_\eta \mathbf{b}, \tag{5.7}$$

or $\boldsymbol{u} = \{u_s \; u_\xi \; u_\eta\}^T$ in vectorial form. Subsequently, the linear relation between displacements and strains is written as:

$$\varepsilon_{ss} = \frac{1}{H}\left(\frac{\partial u_s}{\partial s} - \kappa u_\xi\right), \tag{5.8}$$

$$\varepsilon_{\xi\xi} = \frac{\partial u_\xi}{\partial \xi}, \tag{5.9}$$

$$\varepsilon_{\eta\eta} = \frac{\partial u_\eta}{\partial \eta}, \tag{5.10}$$

$$\varepsilon_{\xi\eta} = \frac{\partial u_\xi}{\partial \eta} + \frac{\partial u_\eta}{\partial \xi}, \tag{5.11}$$

$$\varepsilon_{s\eta} = \frac{1}{H}\left(\frac{\partial u_\eta}{\partial s}\right) + \frac{\partial u_s}{\partial \eta}, \tag{5.12}$$

$$\varepsilon_{s\xi} = \frac{1}{H}\left(\frac{\partial u_\xi}{\partial s} + \kappa u_s\right) + \frac{\partial u_s}{\partial \xi}, \tag{5.13}$$

where $H = \sqrt{g}$ and $\boldsymbol{\varepsilon} = \{\varepsilon_{ss}\ \varepsilon_{\xi\xi}\ \varepsilon_{\eta\eta}\ \varepsilon_{\xi\eta}\ \varepsilon_{s\eta}\ \varepsilon_{s\xi}\}^T$ is the vector of the deformations.

For the purposes of the implementation of a mixed interpolated element, it is appropriate to split the strain vector in membrane and shear components (ε_{ss}, $\varepsilon_{s\xi}$ and $\varepsilon_{s\eta}$) on one side, and transverse components ($\varepsilon_{\xi\xi}$, $\varepsilon_{\eta\eta}$ and $\varepsilon_{\xi\eta}$) on the other, as follows:

$$\boldsymbol{\varepsilon}_C = \{\varepsilon_{ss}\ \varepsilon_{s\eta}\ \varepsilon_{s\xi}\}^T, \tag{5.14}$$

$$\boldsymbol{\varepsilon}_\Omega = \{\varepsilon_{\xi\xi}\ \varepsilon_{\eta\eta}\ \varepsilon_{\xi\eta}\}^T. \tag{5.15}$$

Note that the assumptions over the cross-section remain the same as those of straight beams (see Chapter 2) although now they are expressed in the $\xi\eta$-plane. Therefore, the transverse deformations, $\boldsymbol{\varepsilon}_\Omega$, will be distinct from zero for generic problems. Subsequently, the geometrical relations can be written in matrix form as:

$$\boldsymbol{\varepsilon}_C = (\mathbf{D}_M + \mathbf{D}_S)\boldsymbol{u}, \tag{5.16}$$

$$\boldsymbol{\varepsilon}_\Omega = \mathbf{D}_\Omega \boldsymbol{u}, \tag{5.17}$$

where :

$$\begin{gathered}
\mathbf{D}_M = \begin{bmatrix} \frac{1}{H}\frac{\partial}{\partial s} & -\frac{1}{H}\kappa & 0 \\ 0 & 0 & 0 \\ \frac{1}{H}\kappa & 0 & 0 \end{bmatrix}, \quad \mathbf{D}_S = \begin{bmatrix} 0 & 0 & 0 \\ \frac{\partial}{\partial \eta} & 0 & \frac{1}{H}\frac{\partial}{\partial s} \\ \frac{\partial}{\partial \xi} & \frac{1}{H}\frac{\partial}{\partial s} & 0 \end{bmatrix}, \\
\mathbf{D}_\Omega = \begin{bmatrix} 0 & \frac{\partial}{\partial \xi} & 0 \\ 0 & 0 & \frac{\partial}{\partial \eta} \\ 0 & \frac{\partial}{\partial \eta} & \frac{\partial}{\partial \xi} \end{bmatrix}.
\end{gathered} \tag{5.18}$$

$\mathbf{D}_M$ is the differential operator that includes the membrane terms, $\mathbf{D}_S$ includes the shear terms and $\mathbf{D}_\Omega$ is the cross-sectional operator. The shear operator can be rewritten as:

$$\mathbf{D}_S = \mathbf{D}_{S_\parallel} + \mathbf{D}_{S_\perp}, \tag{5.19}$$

where

$$\mathbf{D}_{S_\parallel} = \begin{bmatrix} 0 & 0 & 0 \\ 0 & 0 & \frac{1}{H}\frac{\partial}{\partial s} \\ 0 & \frac{1}{H}\frac{\partial}{\partial s} & 0 \end{bmatrix}, \quad \mathbf{D}_{S_\perp} = \begin{bmatrix} 0 & 0 & 0 \\ \frac{\partial}{\partial \eta} & 0 & 0 \\ \frac{\partial}{\partial \xi} & 0 & 0 \end{bmatrix}. \tag{5.20}$$

Note that in this manner the derivatives on s are separated from those over the cross-section.

Accordingly, the stress-strain relations are written as:

$$\left\{ \begin{array}{c} \boldsymbol{\sigma}_C \\ \boldsymbol{\sigma}_\Omega \end{array} \right\} = \left[\begin{array}{cc} \mathbf{C}_{CC} & \mathbf{C}_{C\Omega} \\ \mathbf{C}_{\Omega C} & \mathbf{C}_{\Omega\Omega} \end{array} \right] \left\{ \begin{array}{c} \boldsymbol{\varepsilon}_C \\ \boldsymbol{\varepsilon}_\Omega \end{array} \right\}, \qquad (5.21)$$

where $\boldsymbol{\sigma}_C = \{\sigma_{ss}\ \sigma_{s\xi}\ \sigma_{s\eta}\}^T$ includes the membrane and shear components, and $\boldsymbol{\sigma}_\Omega = \{\sigma_{\xi\xi}\ \sigma_{\eta\eta}\ \sigma_{\xi\eta}\}^T$ the transverse ones. In the case orthotropic materials, the material submatrices, $\mathbf{C}_{CC}$, $\mathbf{C}_{C\Omega}$, $\mathbf{C}_{\Omega C}$ and $\mathbf{C}_{\Omega\Omega}$, are written as:

$$\begin{gathered} \mathbf{C}_{CC} = \left[\begin{array}{ccc} C_{11} & 0 & 0 \\ 0 & C_{55} & 0 \\ 0 & 0 & C_{66} \end{array} \right], \quad \mathbf{C}_{\Omega\Omega} = \left[\begin{array}{ccc} C_{22} & C_{23} & 0 \\ C_{23} & C_{33} & 0 \\ 0 & 0 & C_{44} \end{array} \right], \\ \mathbf{C}_{C\Omega} = \mathbf{C}_{\Omega C}^T = \left[\begin{array}{ccc} C_{12} & C_{13} & 0 \\ 0 & 0 & 0 \\ 0 & 0 & 0 \end{array} \right]. \end{gathered} \qquad (5.22)$$

Note that the material coefficients C_{ij} are expressed in the material coordinates, for which the subindex 1 lies on the versor **t**, 2 on **n** and 3 on **b**. This is a clear advantage for the modeling of curved laminates and fibers, as it will be shown further on in this thesis. In the case of different angle plies, the material transformations depicted in Section 3.1 must be applied.

5.4 Locking-free beam elements

As introduced in the previous chapters, in the CUF framework the deformation of the cross-section of the beam is assumed via arbitrary functions. Therefore, the displacement field of the curved beam can be expressed as:

$$\boldsymbol{u}(s,\xi,\eta) = F_\tau(\xi,\eta)\boldsymbol{u}_\tau(s), \quad \tau = 1,...,M, \qquad (5.23)$$

where $\boldsymbol{u}_\tau = \{u_{s_\tau}\ u_{\xi_\tau}\ u_{\eta_\tau}\}^T$ is the vector of the generalized displacements and M is the total number of expansion terms in the kinematic field. Then, in order to formulate the beam finite element, the unknowns are interpolated using shape functions, N_i, as shown in Section 3.2.1. Accordingly:

$$\boldsymbol{u}_\tau(s) = N_i(s)\boldsymbol{u}_{\tau i} \qquad i = 1,...,n_n, \qquad (5.24)$$

n_n being the number of nodes. Lagrangian interpolation functions are used in the present formulation.

Introducing Eqs. (5.23) and (5.24) into Eqs. (5.16) and (5.17), the element strains are computed as

$$\boldsymbol{\varepsilon}_C = F_\tau(\mathbf{D}_M N_i \mathbf{I}_3)\boldsymbol{u}_{\tau i} + F_\tau(\mathbf{D}_{S_\parallel} N_i \mathbf{I}_3)\boldsymbol{u}_{\tau i} + (\mathbf{D}_{S_\perp} F_\tau \mathbf{I}_3) N_i \boldsymbol{u}_{\tau i}, \tag{5.25}$$

$$\boldsymbol{\varepsilon}_\Omega = (\mathbf{D}_\Omega F_\tau \mathbf{I}_3) N_i \boldsymbol{u}_{\tau i}\ , \tag{5.26}$$

where $\mathbf{I}_3$ is the 3×3 identity matrix.

The mitigation of the shear locking in thin beams is presented in the previous chapter. In the case of curved beams, the axial strains generated by the curvature terms may provoke an uncontrollable increment of the bending stiffness [185], known as membrane locking. This effect is caused by the physical inconsistencies that arise when the same shape functions are used to interpolate all the strain terms along the beam axis, as in Eqs. 5.25 and 5.26. To solve this numerical issue, a vector containing the membrane and shear strains is defined as:

$$\bar{\boldsymbol{\varepsilon}}_C = \bar{N}_m \boldsymbol{\varepsilon}_{C_m} \qquad m = 1, ..., n-1, \tag{5.27}$$

where $\bar{\boldsymbol{\varepsilon}}_C$ are the assumed membrane and shear deformations. In such manner, a lower-order set of functions, $\bar{N}_m$, is employed to interpolate the membrane and shear strains computed from the displacements, ε_{C_m}. The set of assumed functions are the Lagrangian polynomials with roots at the tying points, T_m, which were introduced in Section 4.3. For the sake of clarity, the locations of the tying points in the local interval [-1, 1] are included here:

$$\begin{array}{lc} B2: & r_{T_1} = 0, \\ B3: & r_{T_1} = -\frac{1}{\sqrt{3}},\ r_{T_2} = \frac{1}{\sqrt{3}}, \\ B4: & r_{T_1} = -\sqrt{\frac{3}{5}},\ r_{T_2} = 0,\ r_{T_3} = \sqrt{\frac{3}{5}}\ , \end{array} \tag{5.28}$$

r being the natural coordinate of the beam element.

Now evaluating the strains of Eq. (5.25) at the tying points, Eq. (5.27) can be rewritten in the following form:

$$\bar{\boldsymbol{\varepsilon}}_C = \bar{N}_m F_\tau(\mathbf{D}_M N_i \mathbf{I}_3)_m \boldsymbol{u}_{\tau i} + \bar{N}_m F_\tau(\mathbf{D}_{S_\parallel} N_i \mathbf{I}_3)_m \boldsymbol{u}_{\tau i} + \bar{N}_m(\mathbf{D}_{S_\perp} F_\tau \mathbf{I}_3) N_{i_m} \boldsymbol{u}_{\tau i}\ . \tag{5.29}$$

Subsequently, making use of Eq. (5.21), the stresses over the curved beam element are expressed as:

$$\begin{aligned} \bar{\boldsymbol{\sigma}}_C = \ & \mathbf{C}_{CC}\left[\bar{N}_m F_\tau(\mathbf{D}_M N_i \mathbf{I}_3)_m \boldsymbol{u}_{\tau i} + \bar{N}_m F_\tau(\mathbf{D}_{S_\parallel} N_i \mathbf{I}_3)_m \boldsymbol{u}_{\tau i} \right. \\ & \left. + \bar{N}_m(\mathbf{D}_{S_\perp} F_\tau \mathbf{I}_3) N_{i_m} \boldsymbol{u}_{\tau i}\right] + \mathbf{C}_{C\Omega}\left[(\mathbf{D}_\Omega F_\tau \mathbf{I}_3) N_i \boldsymbol{u}_{\tau i}\right] \end{aligned} \tag{5.30}$$

$$\begin{aligned}\bar{\boldsymbol{\sigma}}_{\Omega} = \;& \mathbf{C}_{\Omega C}\left[\bar{N}_m F_\tau(\mathbf{D}_M N_i \mathbf{I}_3)_m \boldsymbol{u}_{\tau i} + \bar{N}_m F_\tau(\mathbf{D}_{S_\parallel} N_i \mathbf{I}_3)_m \boldsymbol{u}_{\tau i}\right. \\ & \left. + \bar{N}_m(\mathbf{D}_{S_\perp} F_\tau \mathbf{I}_3) N_{i_m} \boldsymbol{u}_{\tau i}\right] + \mathbf{C}_{\Omega\Omega}\left[(\mathbf{D}_\Omega F_\tau \mathbf{I}_3) N_i \boldsymbol{u}_{\tau i}\right].\end{aligned} \tag{5.31}$$

Note that in the current formulation the assumed functions appear in the definitions of both stress vectors.

5.4.1 Fundamental nucleus

The system of governing equations are obtained via the PVD, see Section 3.2.2. The virtual variation of the internal work, δL_{int}, can be split into the contributions of the membrane and shear strains, δL_{int_C}, one the one hand, and the transverse deformations, δL_{int_Ω}, on the other. Thus using Eq. (3.25) and the definition of the infinitesimal volume in curved beams, Eq. (5.6), one can write:

$$\delta L_{int_C} = \int_L \int_\Omega \delta \bar{\boldsymbol{\varepsilon}}_C^T \bar{\boldsymbol{\sigma}}_C H d\Omega ds = \int_L \int_\Omega (\delta \bar{\boldsymbol{\varepsilon}}_C^T \bar{\boldsymbol{C}}_{CC} \bar{\boldsymbol{\varepsilon}}_C + \delta \bar{\boldsymbol{\varepsilon}}_C^T \bar{\boldsymbol{C}}_{C\Omega} \boldsymbol{\varepsilon}_\Omega) H d\Omega ds, \tag{5.32}$$

$$\delta L_{int_\Omega} = \int_L \int_\Omega \delta \boldsymbol{\varepsilon}_\Omega^T \bar{\boldsymbol{\sigma}}_\Omega H d\Omega ds = \int_L \int_\Omega (\delta \boldsymbol{\varepsilon}_\Omega^T \bar{\boldsymbol{C}}_{\Omega C} \bar{\boldsymbol{\varepsilon}}_C + \delta \boldsymbol{\varepsilon}_\Omega^T \bar{\boldsymbol{C}}_{\Omega\Omega} \boldsymbol{\varepsilon}_\Omega) H \, d\Omega ds, \tag{5.33}$$

where L is the length of the curve defined by s and Ω is the surface of the cross-section. Making use of the geometrical relations, Eq. (5.26) and (5.29), and the constituent equations, Eq. (5.31), the total internal work can be expressed as:

$$\delta L_{\text{int}} = \delta L_{int_C} + \delta L_{int_\Omega} = \delta \boldsymbol{u}_{\tau i}^T (\mathbf{K}_{CC}^{\tau\varsigma ij} + \mathbf{K}_{C\Omega}^{\tau\varsigma ij} + \mathbf{K}_{\Omega C}^{\tau\varsigma ij} + \mathbf{K}_{\Omega\Omega}^{\tau\varsigma ij}) \boldsymbol{u}_{\varsigma j} \,, \tag{5.34}$$

where $\mathbf{K}^{\tau\varsigma ij}$ are the 3×3 fundamental nuclei of the stiffness matrix of the curved beam. In this development, τ and ς are the indexes of the transverse expansions, whereas i and j are those of the FEM interpolations. Note that although the inclusion of the curvature terms in the geometrical relations provokes the appearance of new terms in the stiffness matrix, the formal derivation of the fundamental nuclei remains the same. Any desired class of FE approximation and tranverse expansion can be implemented without modifying these core expressions. For the sake of completeness, the explicit form of each fundamental nucleus is included here:

$$\begin{aligned}
&K_{CC}^{\tau\varsigma ij}(1,1)=I_{\bar{i}_{,s}\bar{j}_{,s}}E^{11}_{\tau\varsigma\frac{1}{H}}+I_{\overline{ij}}\left(E^{55}_{\tau_{,\eta}\varsigma_{,\eta}H}+E^{66}_{\tau_{,\xi}\varsigma_{,\xi}H}\right)+\kappa I_{\overline{ij}}\left(E^{66}_{\tau\varsigma_{,\xi}}+E^{66}_{\tau_{,\xi}\varsigma}\right)+\kappa^2 I_{\overline{ij}}E^{66}_{\tau\varsigma\frac{1}{H}},\\
&K_{CC}^{\tau\varsigma ij}(1,2)=I_{\bar{i}_{,s}\bar{j}}E^{66}_{\tau\varsigma_{,\xi}}+\kappa\left(I_{\bar{i}_{,s}\bar{j}}E^{66}_{\tau\varsigma\frac{1}{H}}-I_{\overline{ij}_{,s}}E^{11}_{\tau\varsigma\frac{1}{H}}\right)\\
&K_{CC}^{\tau\varsigma ij}(1,3)=I_{\bar{i}_{,s}\bar{j}}E^{55}_{\tau\varsigma_{,\eta}},\\
&K_{CC}^{\tau\varsigma ij}(2,1)=+I_{\overline{ij}_{,s}}E^{66}_{\tau_{,\xi}\varsigma}+\kappa\left(I_{\overline{ij}_{,s}}E^{66}_{\tau\varsigma\frac{1}{H}}-I_{\bar{i}_{,s}\bar{j}}E^{11}_{\tau\varsigma\frac{1}{H}}\right),\\
&K_{CC}^{\tau\varsigma ij}(2,2)=I_{\bar{i}_{,s}\bar{j}_{,s}}E^{66}_{\tau\varsigma\frac{1}{H}}+\kappa^2 I_{\overline{ij}}E^{11}_{\tau\varsigma\frac{1}{H}}, \qquad K_{CC}^{\tau\varsigma ij}(2,3)=0,\\
&K_{CC}^{\tau\varsigma ij}(3,1)=I_{\overline{ij}_{,s}}E^{55}_{\tau_{,\eta}\varsigma}, \qquad K_{CC}^{\tau\varsigma ij}(3,2)=0, \qquad K_{CC}^{\tau\varsigma ij}(3,3)=I_{\bar{i}_{,s}\bar{j}_{,s}}E^{55}_{\tau\varsigma\frac{1}{H}}
\end{aligned} \tag{5.35}$$

$$\begin{aligned}
&K_{C\Omega}^{\tau\varsigma ij}(1,1)=0, && K_{C\Omega}^{\tau\varsigma ij}(1,2)=I_{\overline{ij}_{,s}}E^{12}_{\tau_{,\xi}\varsigma}, && K_{C\Omega}^{\tau\varsigma ij}(1,3)=I_{\overline{ij}_{,s}}E^{13}_{\tau_{,\eta}\varsigma},\\
&K_{C\Omega}^{\tau\varsigma ij}(2,1)=0, && K_{C\Omega}^{\tau\varsigma ij}(2,2)=-\kappa I_{\bar{i}j}E^{12}_{\tau\varsigma_{,\xi}}, && K_{C\Omega}^{\tau\varsigma ij}(2,3)=-\kappa I_{\overline{ij}}E^{13}_{\tau_{,\eta}\varsigma},\\
&K_{C\Omega}^{\tau\varsigma ij}(3,1)=0, && K_{C\Omega}^{\tau\varsigma ij}(3,2)=0, && K_{C\Omega}^{\tau\varsigma ij}(3,3)=0
\end{aligned} \tag{5.36}$$

$$\begin{aligned}
&K_{\Omega C}^{\tau\varsigma ij}(1,1)=0, && K_{\Omega C}^{\tau\varsigma ij}(1,2)=0, && K_{\Omega C}^{\tau\varsigma ij}(1,3)=0,\\
&K_{\Omega C}^{\tau\varsigma ij}(2,1)=I_{\bar{i}_{,s}j}E^{12}_{\tau\varsigma_{,\xi}}, && K_{\Omega C}^{\tau\varsigma ij}(2,2)=-\kappa I_{\overline{ij}}E^{12}_{\tau_{,\xi}\varsigma}, && K_{\Omega C}^{\tau\varsigma ij}(2,3)=0,\\
&K_{\Omega C}^{\tau\varsigma ij}(3,1)=I_{\bar{i}_{,s}j}E^{13}_{\tau\varsigma_{,\eta}}, && K_{\Omega C}^{\tau\varsigma ij}(3,2)=-\kappa I_{\bar{i}j}E^{13}_{\tau\varsigma_{,\eta}}, && K_{\Omega C}^{\tau\varsigma ij}(3,3)=0,
\end{aligned} \tag{5.37}$$

$$\begin{aligned}
&K_{\Omega\Omega}^{\tau\varsigma ij}(1,1)=0, \qquad K_{\Omega\Omega}^{\tau\varsigma ij}(1,2)=0, \qquad K_{\Omega\Omega}^{\tau\varsigma ij}(1,3)=0, \qquad K_{\Omega\Omega}^{\tau\varsigma ij}(2,1)=0,\\
&K_{\Omega\Omega}^{\tau\varsigma ij}(2,2)=I_{ij}\left(E^{22}_{\tau_{,\xi}\varsigma_{,\xi}H}+E^{44}_{\tau_{,\eta}\varsigma_{,\eta}H}\right),\\
&K_{\Omega\Omega}^{\tau\varsigma ij}(2,3)=I_{ij}\left(E^{23}_{\tau_{,\eta}\varsigma_{,\xi}H}+E^{44}_{\tau_{,\xi}\varsigma_{,\eta}H}\right),\\
&K_{\Omega\Omega}^{\tau\varsigma ij}(3,1)=0,\\
&K_{\Omega\Omega}^{\tau\varsigma ij}(3,2)=I_{ij}\left(E^{23}_{\tau_{,\xi}\varsigma_{,\eta}H}+E^{44}_{\tau_{,\eta}\varsigma_{,\xi}H}\right),\\
&K_{\Omega\Omega}^{\tau\varsigma ij}(3,3)=I_{ij}\left(E^{33}_{\tau_{,\eta}\varsigma_{,\eta}H}+E^{44}_{\tau_{,\xi}\varsigma_{,\xi}H}\right),
\end{aligned} \tag{5.38}$$

In these equations, the integrals of the shape functions are included in the I terms, which are defined as:

$$
\begin{aligned}
I_{i_{(,s)}j_{(,s)}} &= \int_L N_{i_{(,s)}} N_{j_{(,s)}} \, ds, \\
I_{\bar{i}_{(,s)}j_{(,s)}} &= \int_L \overline{N}_m N_{i_{(,s)m}} N_{j_{(,s)}} \, ds, \\
I_{i_{(,s)}\bar{j}_{(,s)}} &= \int_L N_{i_{(,s)}} \overline{N}_n N_{j_{(,s)n}} \, ds, \\
I_{\bar{i}_{(,s)}\bar{j}_{(,s)}} &= \int_L \overline{N}_m N_{i_{(,s)m}} \overline{N}_n N_{j_{(,s)n}} \, ds.
\end{aligned}
\tag{5.39}
$$

where the subscripts i and j correspond to the 1D shape functions, and m and n to the assumed strains. Note that $N^m_{i_{(,s)}}$ refers to the i-th function (or its derivative on s) evaluated at the m-th tying point T_m, or:

$$
N_{i_{(,s)m}} = N_{i_{(,s)}}\left(T_m\right). \tag{5.40}
$$

On the other hand, the E terms are the integrals of the expansion functions over the beam's section. The subscripts H and $\frac{1}{H}$ mean application of the metric tensor in the computation of the integral. The nomenclature works as follows:

$$
\begin{aligned}
E^{12}_{\tau_{,\xi}\varsigma} &= \int_\Omega C_{12} \, F_{\tau_{,\xi}} F_\varsigma \; d\xi \; d\eta, \\
E^{44}_{\tau_{,\eta}\varsigma_{,\eta}H} &= \int_\Omega C_{44} \, F_{\tau_{,\eta}} F_{\varsigma_{,\eta}} \; H \; d\xi \; d\eta, \\
E^{11}_{\tau\varsigma\frac{1}{H}} &= \int_\Omega C_{11} \, F_\tau F_\varsigma \; \frac{1}{H} \; d\xi \; d\eta.
\end{aligned}
\tag{5.41}
$$

The numerical integrals are computed in all cases via full Gaussian quadrature. It is worthy noting that for the computation of the term H solely in the cross-sectional integrals it is assumed that the curvature, κ, is constant along the beam element, see Eq. (5.5). In the case of non-constant curvatures along s, i.e. $\kappa(s)$, 3D integrals must be defined over the volume of the beam.

The beam element proposed here adds some interesting features to the structural analysis of curved structures. It overcomes membrane and shear locking with no need of extra DOF. It also provides a better approximation of the 3D stress and strain fields over the volume of the beam. Due to the well-known robustness of the MITC method, it avoids the arise of unexpected spurious modes, which are typical of reduced integrations [124]. The implementation of HLE in this framework allows it to study any complex structure in a 3D sense, while maintaining the advantages on the aspect ratio of the beam elements. Moreover, the non-local capabilities and the BFM, see Section 2.5, make it possible to generate very

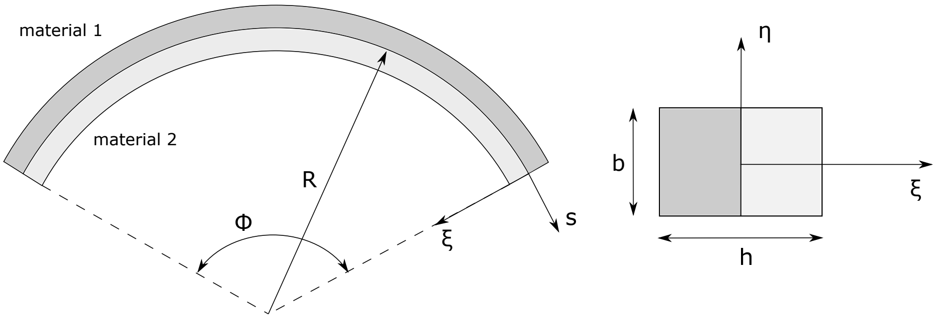

Fig. 5.3 Characteristics of the arch under study.

accurate models of composite materials with a reduced impact in the computational costs, as it will be shown in the next chapters.

5.5 Examples

This section includes the assessment of the proposed curved beam elements with HLE sections. The first example shows the effects of locking in curved structures and the convergence rates of the displacements solutions. A second example shows the verification of the quality of the stress solutions via analytical and numerical solutions from the literature.

5.5.1 Circular arch

A simply-supported arch is considered first, the focus being on the study of the effects of the order of the shape functions for different slenderness ratios of the structure. The geometrical features are included in Figure 5.3. The section exhibits a rectangular shape, with $h = 0.6$ m and $b = 0.4$ m. The opening angle is in all cases $\Phi = 2/3\pi$. The arch is made of two materials with a surface ratio 1:1 over the section. The material properties are enlisted in Table 5.1. Two slenderness ratios are considered in this study: $L/h = 5$ and $L/h = 500$. The loading corresponds to a concentrated force $P = 1000$ N applied upwards at midspan in $\xi = 0.0$ and $\eta = 0.0$.

Table 5.1 Elastic properties of the materials. $E_2 = 1$ GPa.

	$\frac{E_1}{E_2}$	$\frac{E_3}{E_2}$	$\frac{G_{12},G_{13},G_{23}}{E_2}$	ν_{12}, ν_{13}, ν_{23}
material 1	30	1	0.5	0.25
material 2	5	1	0.5	0.25

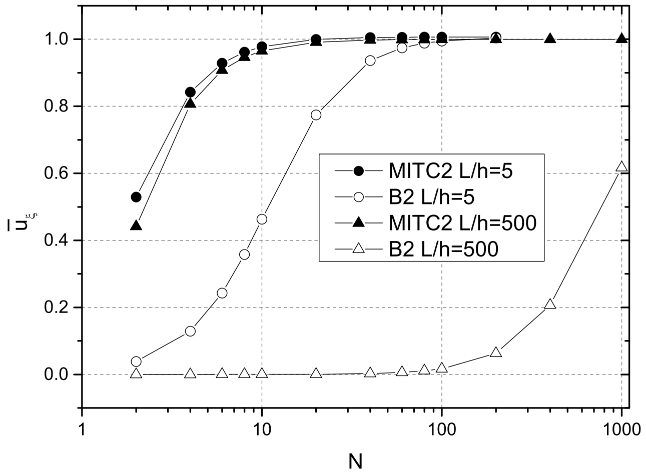

Fig. 5.4 Radial displacement, $\bar{u}_\xi$, against the number of two-noded curved elements. Slenderness ratios $L/h = 5$ and $L/h = 500$.

Analytical solutions can be obtained for the given geometry and boundary conditions. The derivation of strong-form solutions of in the current framework was done in [62] and it is used here to produce exact references to assess the beam elements proposed. A first-order HL1 expansion is used in all cases. The Navier solutions of this problem are:

$$u_\xi^{Nav} = 4.735 \times 10^{-5} \text{ m} \qquad for\, L/h = 5 \tag{5.42}$$

$$u_\xi^{Nav} = 23.169 \text{ m} \qquad for\, L/h = 500 \tag{5.43}$$

Figures 5.4, 5.5 and 5.6 show the convergence of the normalized radial displacements, $\bar{u}_\xi = u_\xi / u_\xi^{Nav}$, for a growing number of beam elements, N. The solutions of obtained via full integration (B*) and the MITC method (MITC*) are compared. From the convergence analysis, it is possible to state that:

- Due to its exactness, Navier-type solutions represent a highly reliable reference to assess the finite element solution. The results shown here were obtained using 200 half waves. For more details of this formulation, the reader is referred to [71].
- As expected, the locking phenomena is more evident in low order elements and leads to disastrous effects when thin beams are analyzed.
- Higher-order elements alleviate the stiffening response at the expense of extra nodes.
- Curved elements based on MITC are able to mitigate the locking issues independently of the thickness of the structure, even for two-noded elements as shown in Fig. 5.4. As a consequence, the efficiency of the analysis is highly improved.

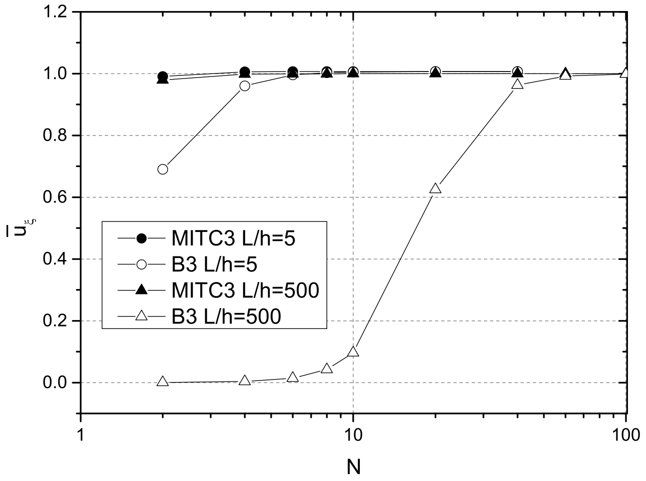

Fig. 5.5 Radial displacement, $\bar{u}_\xi$, against the number of three-noded curved elements. Slenderness ratios $L/h = 5$ and $L/h = 500$.

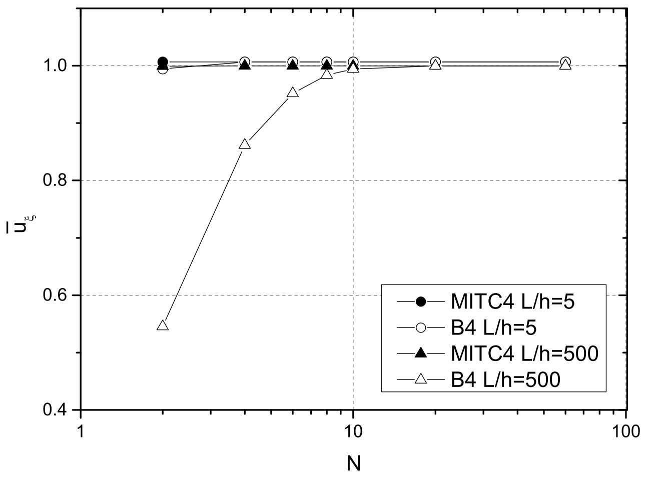

Fig. 5.6 Radial displacement, $\bar{u}_\xi$, against the number of four-noded curved elements. Slenderness ratios $L/h = 5$ and $L/h = 500$.

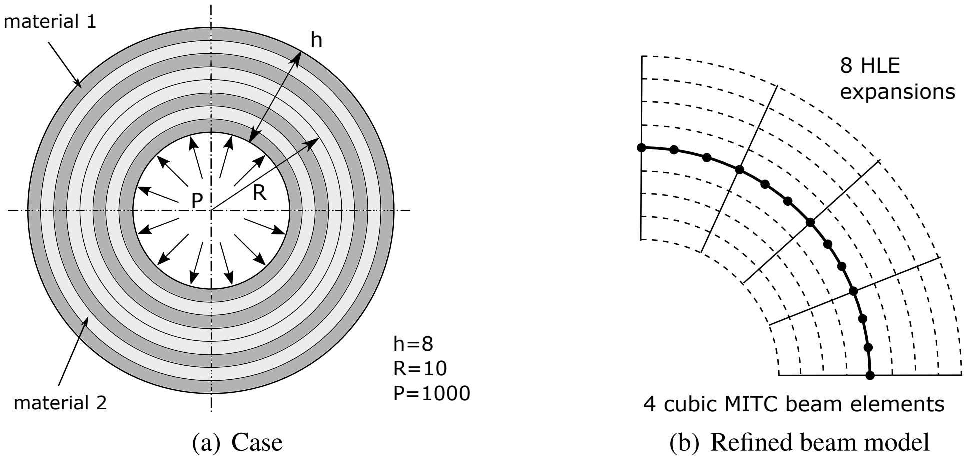

(a) Case

(b) Refined beam model

Fig. 5.7 Features of the hollow laminated disk and proposed beam model.

5.5.2 Laminated circular disk

A circular laminate is employed to assess the solutions of stresses in the thickness direction of the curved beam. The accurate structural analysis of laminated materials demands the inclusion of certain physical effects in the model, such as the shear deformations and layer-wise kinematics, which increase considerably the number of variables of the problem. As a consequence, classical elasticity solutions such as those of Lekhniskii [114], Pagano [146] or Varadan and Bhaskar [200] are still used by engineers and researchers in the design of composite structures.

The benchmark case is a cylindrical disk with internal pressure, for which analytical (Lekhnitskii [114]) and numerical solutions (Surana and Nguyen [187]) are available. The features of the problem are presented in Fig. 5.7 (a). To be consistent with the latter reference, plane stress conditions are applied and no conversion is performed in the model, leading to dimensionless solutions. The laminated structure is made of a symmetric stack of eight layers of two materials. The elastic properties of these materials are those Table 5.1, although now $E_2 = 1 \times 10^6$. An internal pressure of magnitude $P = 1000$ is applied over the inner wall of the disk. Due to the double symmetry of the problem, only quarter of structure is studied, as shown in Fig. 5.7 (b). The beam model is generated using 4 curved MITC beam elements and a HLE domain per layer.

Figures 5.8 and 5.9 include the solutions of radial displacements, radial stresses and circumferential stresses, respectively, over the thickness of the laminate. The reference results [187] were obtained using a 2D beam based on Lagrangian assumptions over the thickness and 45 quadratic beam elements along the center line of the laminate. In the graphs, $p = 1$, $p = 2$ and $p = 4$ correspond to the polynomial order of the thickness functions. On the other hand, the proposed HLE solutions are obtained for polynomial orders from 1 (HL1) to 8 (HL8). It is possible to observe that the HL1 model fails in capturing the exact distribution of the displacements of Lekhniskii, although the convergence is reached already for the HL2 model. Regarding the stress fields, the HLE beam models of higher-order are able to capture the layer wise distribution of the stress field showing an excellent agreement with the analytical stresses. Finally, the contour plots of the stress fields over the disk are included in Fig. 5.10 for the HL3 model.

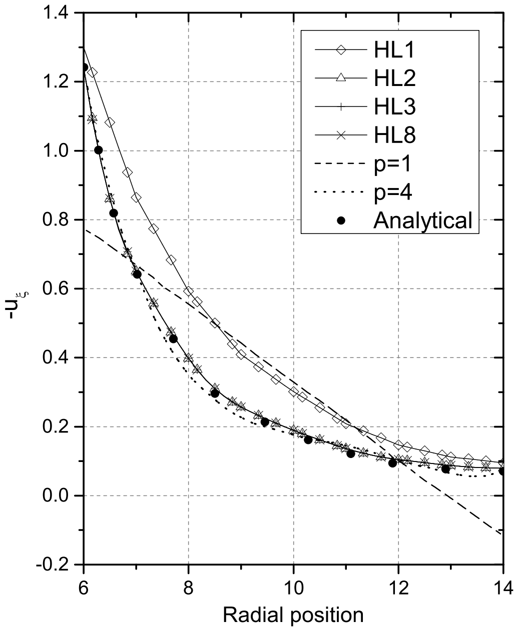

Fig. 5.8 Radial displacement, u_ξ, through the thickness of the laminated disk. References from [187].

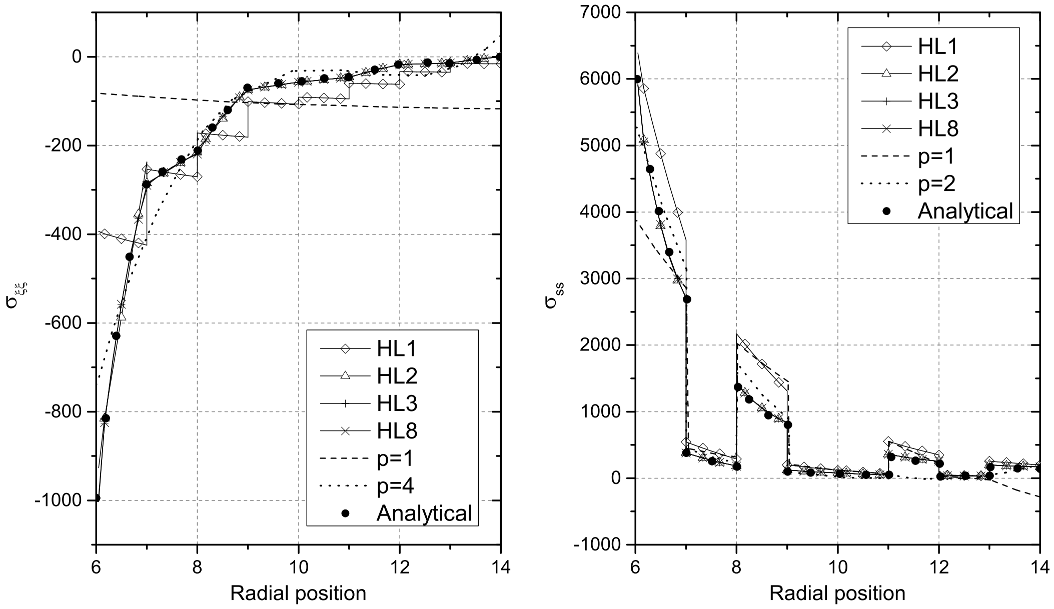

(a) Radial stress (b) Circumferential stress

Fig. 5.9 Radial, $\sigma_{\xi\xi}$, and circumferential, σ_{ss}, stress fields through the thickness of the laminated disk. References from [187].

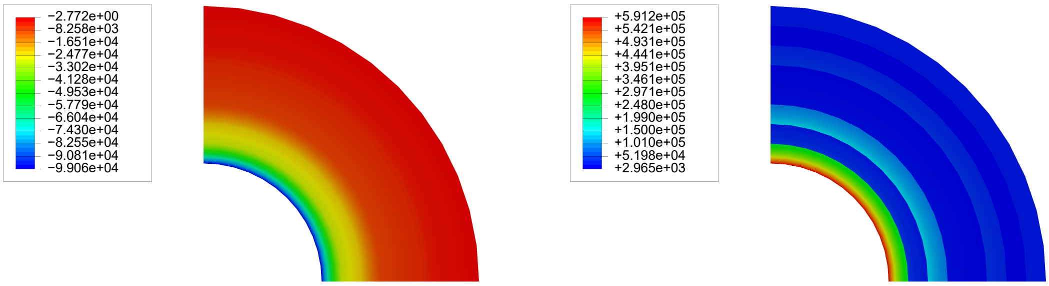

(a) Radial stresses (b) Circumferential stresses

Fig. 5.10 Stress fields over the eight-layer curved beam for the third order HL3 model.

Part II

Analysis of composite structures via hierarchical beam models

Chapter 6

HLE for composite simulation

The analysis of composite structures demands the introduction of more computationally-efficient numerical tools which must overcome the limitations of metallic-oriented FEM codes that are nowadays available. Until today, the separation of scales that characterizes the composite materials has made the stress analysis of these structures often an unreliable support tool for the structural design, leading to the need of higher safety margins in the industrial product. The present chapter focuses on the application of the numerical developments hereinbefore presented for the modeling of composite materials at different scales. The focus is on maintaining the highest levels of resolution in the stress fields while cutting down the computational costs by orders of magnitude if possible. For that, some standard methods used in the literature are recalled and redefined in a hierarchical framework based on HLE beam theories.

Some of the numerical results included in this chapter for assessment purposes were published in [144] and [61].

6.1 Introduction

The introduction of composite materials for structural applications has become a common solution in many engineering fields such as aerospace, automotive, energy and naval. The advantages of composite structures in comparison with their metallic counterparts are many, including better specific stiffness and strength mechanical properties, see [170, 97], and the emerging of new design variables which lead to a better optimization of the final product, such as the number of plies and the orientation in laminated structures. Due to these interesting features, aerospace companies nowadays make use of these materials not only in secondary parts, but in primary structures such as the wing and fuselage, see for instance the B 787 and the A 350 widebody aircraft. Nevertheless, in order to fully exploit the advanced capabilities of composite structures while ensuring the maximum levels of safety, the physical phenomena involved in the damage of composites must be investigated deeper. Computational models are useful for this purpose and must be used as a support to experimental test to acquire all the knowledge necessary to produce better and safer structures.

It is well-known in the research community that a good approximation of the 3D stress and strain fields is necessary to predict accurately the different failure modes of composite structures. For this reason, most of researchers base their damage models of laminated structures in 3D finite elements, which are able to capture the full stress state. However, due to the limitations in the aspect ratio constraints, the dimension of the solid element is defined by the thickness of the composite layer, making the computational model too expensive and limiting these approach to structures not bigger than coupons. As a solution to this issue, in the last decades a large research effort has been dedicated to the development of efficient models for the accurate analysis of multi-layered structures. Dimensionally reduced beam and plate formulations allow it to overcome the aspect ratio constraints thus reducing the computational size of the problem, see the review series of Kapania and Raciti [100, 101]. Among the most well-known models for laminate analysis one finds: higher-order models [99, 151, 197, 166, 128, 34], trigonometric theories [75], zig-zag models [115, 6, 202], mixed variational theories [174, 163] and layer-wise methods [168, 182, 147, 188, 190, 117, 42]. In this works, different kinematic and/or variational methods are used to represent the distribution of stresses in the thickness direction. Regarding the kinematic approach, multi-layered theories are usually classified into equivalent single layer (ESL), in which the number of unknowns is independent of the number of layers, and layer wise (LW), in which independent assumptions are taken for each layer of the laminate. A detailed description of these two approaches is provided in this chapter and the following.

In many cases, the initiation and propagation of damage in composites can be only understood if the physics at the micro-scale are accounted. For instance, the appearance of delaminated areas in fiber-reinforced composites is usually a consequence of the coalescence of microcracks and fiber debondings, which propagate towards the interply region. If one aims to include these physical effects into the composite model, multiscale approaches must be implemented. According to this approach, the composite problem is divided into different spatial scales, usually macro-scale for the structural component, meso-scale for the laminate coupon, and micro-scale for the material constituents. Two flows of information through the scales are usually defined: bottom-up and top-down. The former is based on the computation of the homogenized properties of the smaller scales, which are applied as constitutive information in the upper scales; whereas the latter addresses the computation of the local solutions within the structure and is carried out via application of the correspondent boundary conditions from the results of the global model.

This chapter introduces the HLE beam models in the analysis of composite structures at different scales. Hierarchical LW models are generated by discretizing the stack of plies as mathematical layers based on Legendre polynomials. For the analysis of micro-models accounting for different constituents (fiber, matrix, plies,...), the *component wise* (CW) approach is recalled. CW models can be seen as an extension of LW models that allows it to predict the deformation of each component of the structure via dedicated kinematics. A similar methodology was previously employed for the analysis of reinforced aerospace structures [35] and civil structures [36]. This approach can be straightforwardly implemented in the framework of CUF using non-local theories such as HLE and LE, which allow for a discretization of the cross-section surface into smaller expansions domains.

6.2 Composite modeling

In this section, a detailed description of the application of HLE models for meso-scale and micro-scale analyses. A selected number of examples is included showing the capabilities and computational advantages of the theoretical developments included in Chapters 2, 3, 4 and 5 for the analysis of composites. It is shown that the possibility of decoupling the numerical approximation over the 3D volume into longitudinal and section domains represent a clear advantage for the modeling of composite structures in terms of accuracy and effectiveness. Further applications to more interesting composite problems, including micromechanics, free-edge analysis and mixed variational models, are presented in the next chapters.

6.2.1 Meso-scale

Consider the coordinate frame shown in Fig 5.2. The longitudinal direction of the composite beam lies on the y axis, whereas the cross-section Ω is defined on x and z. For simple laminates, the stacking direction coincides with the vertical axis z. Note that the cross-section total domain is obtained as the sum of the layer surfaces as

$$\Omega = \sum_{k=1}^{n_l} \Omega_k \tag{6.1}$$

where k is the layer counter and n_l is the total number of layers. In the CUF framework, the definition of the stiffness matrix for beam problems is formally independent of the multi-layered theory selected. In other words, the user may appropriately choose the most convenient model on the basis of the accuracy requirements for the solutions. This means that for problems governed by global effects, such as the modal response, models accounting for ESL kinematics may be sufficiently accurate. On the other hand, for accurate stress analyses, LW approaches provide a better approximation of the interlaminar stresses throughout the stack of plies.

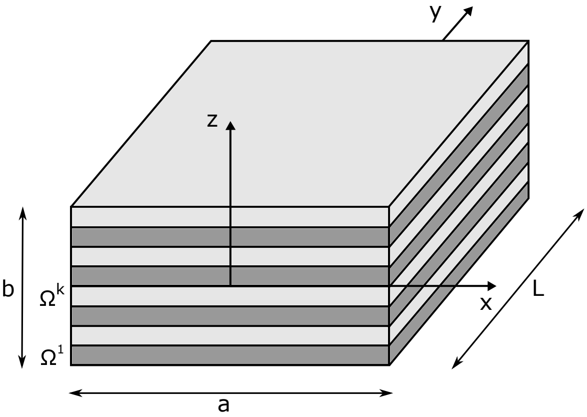

Fig. 6.1 Reference system of the current frame for meso-scale analysis.

In this section, the application of TE, LE and HLE kinematics to generate ESL and LW models for laminates is discussed, showing the suitability and advantages of each method. The focus remains the introduction of HLE for the implementation of hierarchical models for composite structures, in which the accuracy/cost is controlled by the user through the polynomial order parameter.

Equivalent Single Layer

In ESL models, the contribution of each expansion term to the nodal stiffness matrix is obtained by summation of the integrals of the F_τ functions over each layer, represented by the domain Ω_k. In this manner, the moments of the expansion terms at each layer are included in the equivalent homogenized layer. For this purpose, the expressions of the fundamental nucleus of Eq. (3.36) must be modified to include the material coefficients inside the transverse integrals, $E_{\tau_{(,x)(,z)}s_{(,x)(,z)}}$, defined in Eq. (3.37). Accordingly, we obtain

$$E_{\tau_{(,x)(,z)}s_{(,x)(,z)}} = \sum_{k=1}^{n_l} \tilde{C}^k_{\alpha\beta} \int_a \int_{z_b^k}^{z_t^k} F_{\tau_{(,x)(,z)}} F_{s_{(,x)(,z)}} \, dz\, dx \qquad (6.2)$$

where $\tilde{C}^k$ are the rotated material coefficients described in Section 3.1, a is the width of the laminated beam, and z_b^k and z_t^k are the bottom and top z-coordinates of layer k, respectively. The subindexes between brackets refer to eventual partial derivatives.

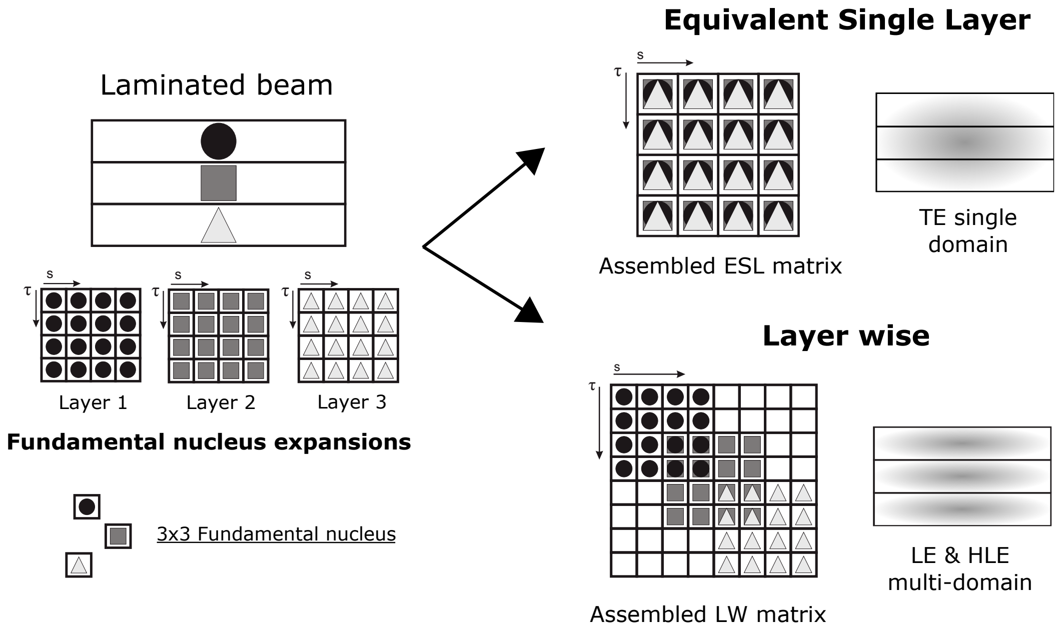
Laminated beam
s
τ
Layer 1
Layer 2
Layer 3
Fundamental nucleus expansions
3x3 Fundamental nucleus
Equivalent Single Layer
Assembled ESL matrix
TE single domain
Layer wise
Assembled LW matrix
LE & HLE multi-domain

Fig. 6.2 Assembly procedure of the stiffness matrix through ESL and LW approaches

In principle, this approach can be adopted using any of the expansions here discussed (TE, LE and HLE). However, usually in the literature ESL models are generated through local theories which are based on a centered expansion. Particular attention was dedicated to the introduction of zig-zag terms into the kinematic field which allow it to represent the sudden changes in the solutions at the interfaces between layers. The discussion of these theories is out of the scope of this thesis, but the reader can refer to the review of Carrera [27] if interested. An interesting ESL approach based on HLE theories for plates is implemented in Chapter 11 for the study of dynamic problems.

Layer wise

LW models account for the deformation of each layer independently, thus they are able to provide a 3D distribution of the solutions over the laminate body. The drawback with respect to ESL is that the computational costs increase proportionally to the number of layers, therefore in most cases this kind of analysis are allocated for the study of simple laminates and composite coupons. Indeed, although LW theories were introduced several decades ago [168] and despite the computational advantages, still nowadays most researchers rely on 3D finite elements for their stress-based damage analyses and the introduction of LW models in commercial softwares is limited. Some of the reasons for this are the complexities related to the management of the model inputs and the imposition of arbitrary boundary conditions, which are addressed here.

Figure 6.2 illustrate how the nodal stiffness matrix is generated in ESL and LW beams. The implementation of LW models can be done straightforward by employing non local theories such as LE or HLE which enable it to represent the different layers via discretization of the cross-section surface. As opposed to ESL, in which a single expansion domain accounts for the whole section of the laminate, now each layer is discretized using one, or more, expansion domains. The continuity of the displacements at the interfaces between the plies is imposed through the assembly of the coincident degrees of freedom, as illustrated in Fig. 6.2. It should be mentioned that LW models can also be implemented using local theories such as TE, but the fulfillment of the C^0 conditions is more tricky [40, 37]. Considering again the expressions of the transverse integrals (Eq. (3.37)), one can write:

$$E^k_{\tau_{(,x)(,z)}s_{(,x)(,z)}} = \tilde{C}^k_{\alpha\beta} \int_{-1}^{1} \int_{-1}^{1} F_{\tau_{(,r)(,s)}} F_{s_{(,r)(,s)}} \, |\boldsymbol{J}_{\Omega_k}| \, dr \, ds. \tag{6.3}$$

where $\boldsymbol{J}_{\Omega_k}$ is the Jacobian matrix of the transformation between the natural coordinates of the expansion (r, s) to the section plane defined in (x, z). Note that in case of functionally graded materials the material coefficients must be moved inside the integrals.

In previous works based on LE [42] the convergence of the displacement and stress solutions was sough via h-refinement, i.e. augmenting the number of mathematical domains per layer. On the contrary, by virtue of the hierarchical properties of HLE, the accuracy of the stress solutions is improved by only changing the input parameter of the polynomial order. In this manner, the section can be discretized a priori using a coarse mesh, and the convergence of the solutions can be checked faster with no need of remeshing. This capability is especially interesting in composite analysis, where in many problems the stress distributions adopt complex shapes which require very high resolutions of the model. Moreover, using the blending function method, any curvature of the laminate can be exactly represented without adding degrees of freedom, as it will be shown in the numerical examples.

To this point one may ask: LW shell models can do the same, isn't it?. Yes, but again the aspect ratio constraints of the finite elements give HLE beam models an advantage when slender laminates are analyzed, such as stringers or composite tubes. Using the proposed method, no matter how many layers and details are present over the cross-section surface, the convergence of the 1D discretization along the longitudinal axis remains independent, as it is shown in Section 3.3, and can be usually obtained using long beam elements leading to huge savings in DOF.

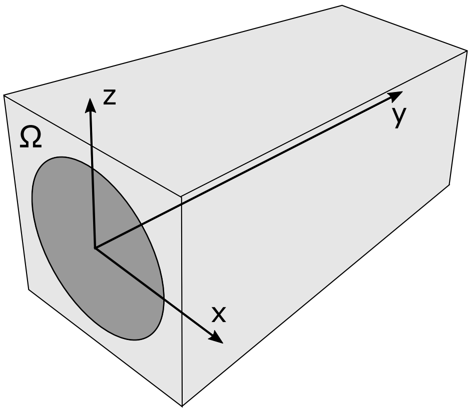

Fig. 6.3 Reference system of the current frame for micro-scale analysis.

6.2.2 Micro-scale

Given the geometrical and multi-phase characteristics of composite materials, the numerical analysis of composites at the micro-scale is usually carried out using in most cases 3D elements. Only if plain strain is assumed 2D elements can be employed to capture all the heterogeneities of the microstructure. Therefore in general, a detailed stress analysis at this scale is associated to large discretizations which can be prohibitive in a multi-scale framework. In order to tackle this issue, by exploiting the aforementioned features of non-local beam theories, it is possible to extend the LW approach to generate models that account for the deformations of each component of the microstructure independently. For this purpose, the total surface of the section is defined as

$$\Omega = \sum_{k=1}^{n_c} \Omega_k \tag{6.4}$$

where now n_c refers to the total number of constituents in the microstructure. This approach is denoted to as component wise (CW) and its implementation using HLE models is to be discussed here.

Component wise

Consider the coordinate frame illustrated in Fig. 6.3. According to this reference system, the heterogeneities of the composite material are allocated over the cross-section plane, xz, whereas the direction of the fibers is parallel to the y axis. In CW models, the section of the microstructure is discretized to represent all the constituents of the composite and the material properties of each one are applied conveniently for each expansion domain as in Eq. (6.3). This technique was first applied in the framework of the CUF for the stress analysis of composite laminates made of thick fibers [35] and more recently for the evaluation of accurate failure parameters [125].

HLE theories can be used to model the different phases of fiber-reinforced composites using large expansion domains and hierarchical kinematics. Using the blending function method, the curvature of the fibers can be exactly represented through a non-isoparametric Jacobian transformation, as it is described in Section 2.5.3. In this manner, for sufficiently high polynomial orders, only one HLE domain is enough to represent the section of the fiber. Composite structures exhibiting variations or discontinuities along the longitudinal can be modeled by generating an appropriate finite element model, e.g. using curved beams or defining different properties along the 1D mesh.

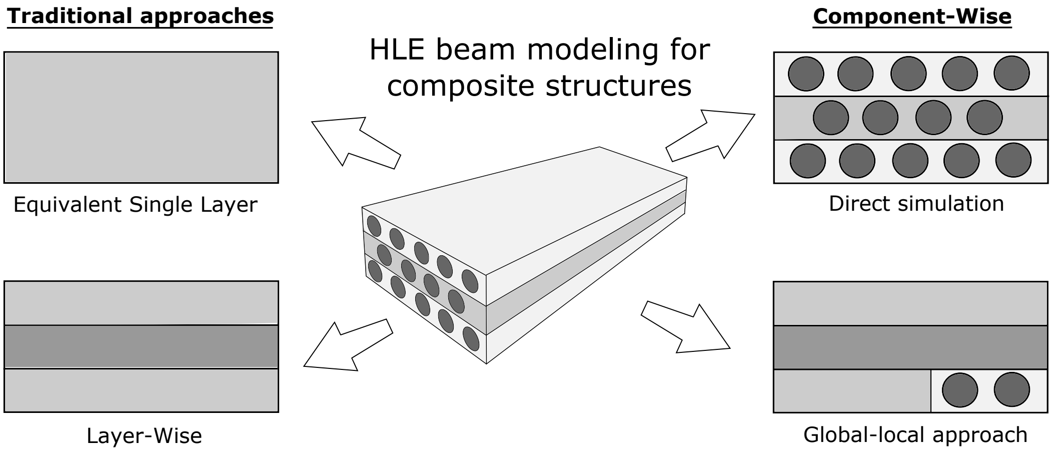

Fig. 6.4 Different approaches available via HLE modeling.

The CW approach together with the hierarchical theories here proposed allows it study the same structural problem from a different perspective. Indeed, note that in the current framework, ESL and LW approaches can be considered as particular cases of the CW approach. By means of the same fundamental statements, it is possible generate models that aim at different resolutions in terms of stress and strain solutions. Briefly, ESL models can be adopted for global analyses, LW models for accurate failure evaluation of multi-layered structures, and CW models for the analysis of microstructures for homogenization and recovery purposes. Figure 6.4 illustrates the different approaches that can be adopted using HLE theories.

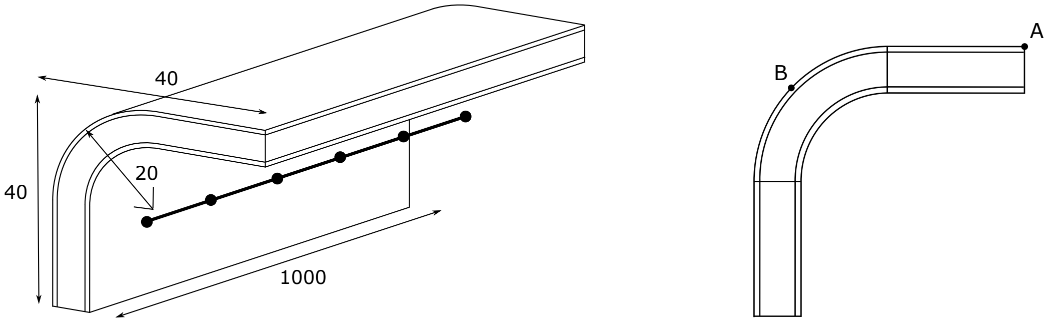

(a) Model (units in mm) (b) Cross-section discretization

Fig. 6.5 HLE model of the curved sandwich.

6.3 Examples

In the following, some numerical examples showing the main features of the proposed modeling technique are included. The focus is on the stress evaluation at the meso and micro-scales.

6.3.1 Curved sandwich beam

The first case deals with the meso-scale analysis of a cantilever L-angle beam of sandwich material. The sandwich is made of two Aluminum skins, 1 mm thick each, and a foam core of 5 mm. The materials are considered isotropic: $E_{Al} = 75$ GPa, $\nu_{Al} = 0.33$; $E_{foam} = 0.1063$ GPa, $\nu_{foam} = 0.32$. The total length of the beam is equal to 1 m, whereas the width and height are equal to 40 mm, resulting in a slenderness ratio of 25. Figure 6.5 shows (a) the geometrical features of the model and (b) the discretization of the cross-section. One can see that the entire surface of the section is modeled using only 9 HLE domains, 3 of which are mapped using the BFM to capture the curvature of the corner. As for the 1D mesh, 10 MITC beam element of third order are employed, ensuring locking-free solutions.

The beam is clampled in one end, $y = 0$, and a pressure of 10 kN/m^2 is applied on the upper flat section of the structure. The deformed of the sandwich beam under the pressure is shown in Fig. 6.6, where it is possible to notice the bending-torsion coupling due to the geometry of the cross-section. Table 6.1 shows the numerical results for the displacements and stresses for polynomial orders from 2 to 8. The 2D and 3D FEM solutions obtained from the commercial software Nastran are also included for comparison purposes. The position of the evaluation points A and B is indicated in Fig. 6.5 (b). Note that the vertical displacements, u_z, are computed at the tip of the beam, whereas the longitudinal and shear stresses, σ_{yy} and σ_{yz} respectively, are evaluated at the middle section and represented in the global coordinate

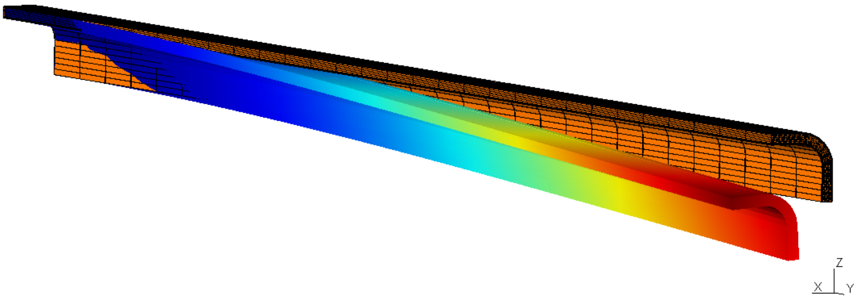

Fig. 6.6 Deformed of the sandwich beam.

Table 6.1 Displacements and stress values of the curved sandwich at the evaluating points.

model	$u_z \times 10^2$ m	$\sigma_{yy} \times 10^{-7}$ Pa	$\sigma_{yz} \times 10^{-6}$ Pa	DOF
	Point A, tip	Point B, midspan		
		Nastran		
Solid	-3.715	3.353	4.324	166617
Shell	-3.900	3.496	2.721	71000
		HLE beam		
HL2	-3.032	3.421	-6.551	3720
HL3	-3.711	3.307	4.484	5952
HL4	-3.712	3.293	4.466	9021
HL5	-3.712	3.288	4.276	12927
HL6	-3.712	3.290	4.256	17670
HL7	-3.712	3.298	4.308	23250
HL8	-3.712	3.297	4.321	29667

frame. Figure 6.7 shows the stress distributions across the thickness point B for the reference FEM models and the HLE beams of odd order. Finally, Fig. 6.8 includes a contour plot of the stress solutions over the cross-section at midspan. It can be concluded that:

1. In the case of thick sandwich structures, the use of plate elements based on the FSDT can lead to poor results, especially for the out-of-plane shear stresses. Indeed, the results differ substantially with respect to those obtained from the solid model of the same code, which is taken as benchmark herein.
2. The LW solutions computed via HLE models converge fast to similar values of the 3D model. Indeed, a 3^{rd} order expansion (HL3) is accurate enough.
3. Obviously, as the polynomial order of the HLE domains augments, the number of DOF increases. However, due to the advantages in the aspect ratio of the beam elements, the computational cost is reduced at least by one order of magnitude.
4. By virtue of the enriched kinematics of HLE beam elements, the 3D stress fields over the whole cross-section are obtained from the structural analysis, as shown in Fig. 6.8.

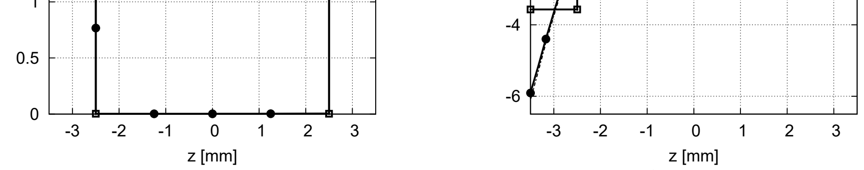

(a) σ_{yy} (b) σ_{yz}

Fig. 6.7 Stress distributions across the thickness at point B and $y = L/2$.

6.3.2 Fiber-reinforced structures

The second assessment considers a representative example of a fiber-reinforced composite structure at the micro-scale. The geometry of the structure is depicted in Fig. 6.9. It accounts for three different material phases: fibers, matrix and homogenized inner layer.

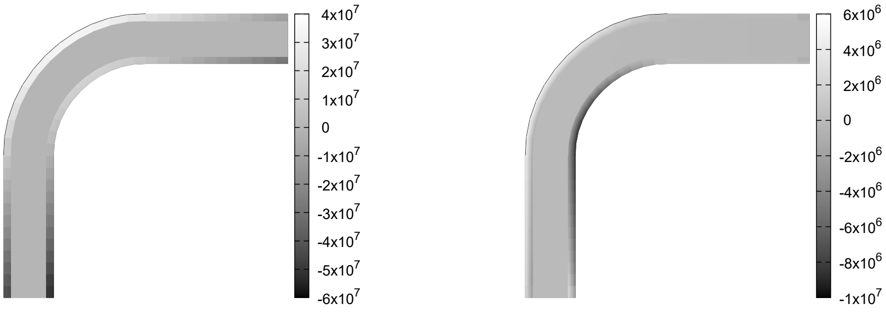

(a) σ_{yy} (b) σ_{yz}

Fig. 6.8 Longitudinal and shear stress fields at midspan.

The mechanical properties of the composite resemble those of a carbon/epoxy system, see Table 6.2. The properties of the homogenized layer are computed using the classical rule of mixtures. The length of the structure is $L = 40$ mm, the height is $h = 0.6$ mm and the width is $b = 0.8$ mm. The diameter of the fibers is $d = 0.016$ mm. A clamped-free configuration is applied and a point load of magnitude $F_z = -1$ N is applied at the coordinates [b/2, L ,0].

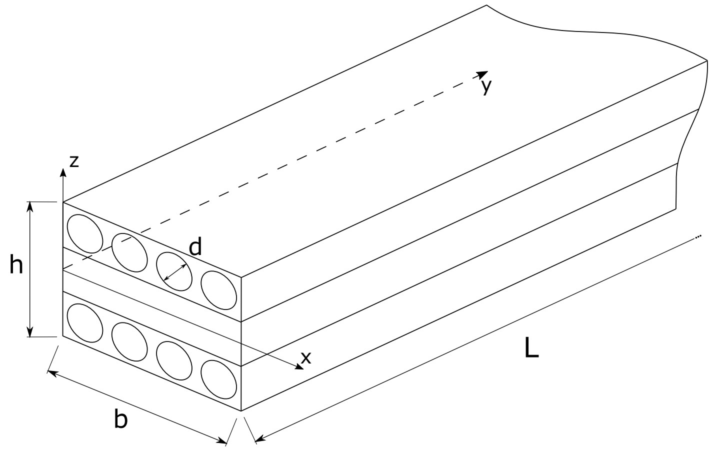

Fig. 6.9 Geometry of the cross-ply beam.

The CW approach is employed here to tune the accuracy of the stress analysis from the homogenized layers to micro-models accounting for the fibers and matrix. Three different approaches are presented:

1. Full LW: the composite beam is modeled as a $[0°, 90°, 0°]$ laminate using the homogenized properties of the fiber/matrix system. Only three HLE domains are enough to represent the cross-section, as shown in Fig. 6.10 (a).

Table 6.2 Material properties of the carbon/epoxy composite.

Component	E_1 [GPa]	E_2 [GPa]	E_3 [GPa]	G_{12} [GPa]	G_{13} [GPa]	G_{23} [GPa]	ν_{12}	ν_{13}	ν_{23}
Fiber	202.038	12.134	12.134	8.358	8.358	47.756	0.2128	0.2128	0.2704
Layer	103.173	5.145	5.145	2.107	2.107	2.353	0.2835	0.2835	0.3124
Matrix	3.252	3.252	3.252	1.200	1.200	1.200	0.355	0.355	0.355

2. Full CW: all the fibers are included in the cross-section discretization. The middle ply is modeled using the homogenized properties and orientation of 90°, see Fig. 6.10 (b).

3. Mixed LW-CW: a global/local model is created by accounting for only a single fiber-matrix cell. Homogenized properties are employed elsewhere in correspondence to the 0° and 90° plies. The cross-section discretization for this case is shown in Fig. 6.10 (c).

Note that the fiber-matrix cells are modeled using 5 HLE curved domains, including only one domain for the fiber. Third-order polynomials are used to parametrize the curved geometry intro the mapping functions.

Figure 6.10 illustrates the computed stress fields obtained from the three proposed approaches. It is possible to observe that the CW model (h) shows that the most critical zone of the shear stresses are the interfaces between the fibers and the matrix in the top and bottom layer, not the middle layer (g). The numerical assessment is shown in Table 6.3, including the convergence analysis in terms of displacements and stresses for all models considered. The number of DOF of each model depicted in the last column. A Nastran solid model is included as reference. The displacements are evaluated at the loading point, whereas the stress values are taken at the center point of the fiber included in the mixed LW-CW model, Fig. 6.10 (c)), at the midspan section. Finally, Fig. 6.11 shows the stress distributions across the thickness the HL6 models and the Nastran reference model. The results show that:

- The convergence of the HLE solutions is already reached for the third-order model (HL3). The HL2 model provides good displacement and longitudinal stresses, however also a third-order expansion is needed to compute accurate shear stresses.

- The displacement results converge to slightly different values depending on the approach selected (LW, CW or mixed). This response can be explained by the error induced from the homogenization of the fiber/matrix cell. Indeed, the full CW model is the closest to the refined solid model.

- The inefficacy of 3D models for the study of composite materials is highlighted. In this example, the maximum difference between the numerical solutions of the full

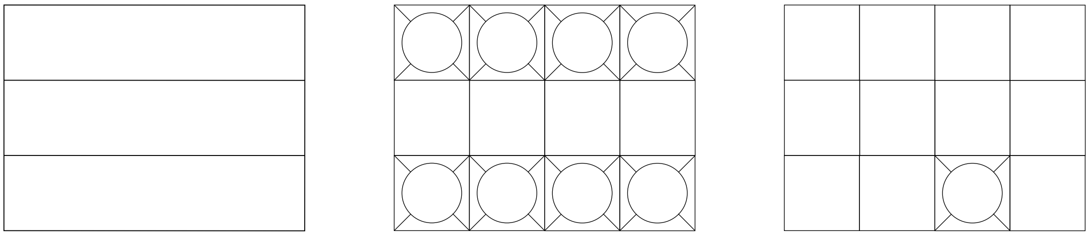

(a) LW (b) CW (c) LW-CW

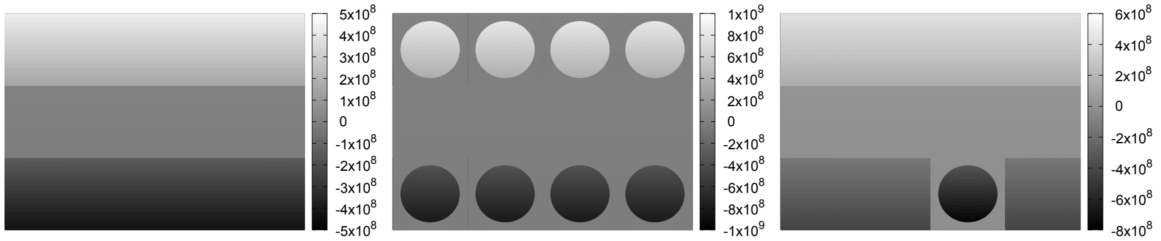

(d) σ_{yy} (e) σ_{yy} (f) σ_{yy}

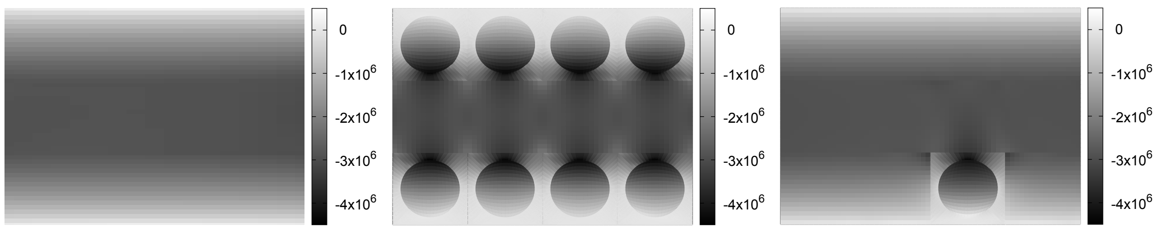

(g) σ_{yz} (h) σ_{yz} (i) σ_{yz}

Fig. 6.10 Discretizations and stress fields computed using different approaches: LW (a), (d) and (g); CW (b), (e) and (h); and mixed LW-CW (c), (f) and (i).

CW and the Nastran model is in all cases lower than 3.5 % (HL2 excluded), while the computational costs in terms of DOF are at least 50 times smaller.

- An interesting feature of the CW approach is that it enables one to perform global/local stress analysis in which only certain regions of the section are modeled with high resolution accounting for fibers and matrix. This procedure reduces considerably the amount of DOF used in the analysis with no repercussion in the quality of the stress fields in the local zone. This is demonstrated in Fig. 6.11, where it is possible to observe the transition between the real stresses in the CW cell and the homogenized LW zone.

Table 6.3 Displacements and stresses of the cross-ply beam for the different models.

	$u_z \times 10^2$ m [b/2, L, 0]	$\sigma_{yy} \times 10^{-8}$ Pa [5b/8, L/2, -0.2]	$\sigma_{yz} \times 10^{-6}$ Pa [5b/8, L/2, -0.2]	DOFs
		Nastran		
HEXA8	-1.569	-5.928	-2.147	1579653
		HLE LW		
HL2	-1.491	-2.880	-1.577	1674
HL3	-1.491	-2.880	-1.710	2604
HL4	-1.491	-2.879	-1.712	3813
HL5	-1.491	-2.879	-1.655	5031
HL6	-1.491	-2.880	-1.654	7068
		HLE CW		
HL2	-0.348	-0.838	-43.008	13671
HL3	-1.547	-5.849	-2.142	22506
HL4	-1.548	-5.848	-2.169	35433
HL5	-1.548	-5.848	-2.211	52452
HL6	-1.548	-5.848	-2.212	73563
		HLE CW-LW		
HL2	-1.046	-3.717	-124.390	5859
HL3	-1.498	-5.661	-2.384	9486
HL4	-1.498	-5.659	-2.381	14601
HL5	-1.498	-5.659	-2.412	21204
HL6	-1.498	-5.659	-2.408	29295

6.3.3 Curved microstructure

A final example is included to show the capabilities of HLE beams for the analysis of curved fibers. The features of the problem are illustrated in Fig. 6.12. The material system is a

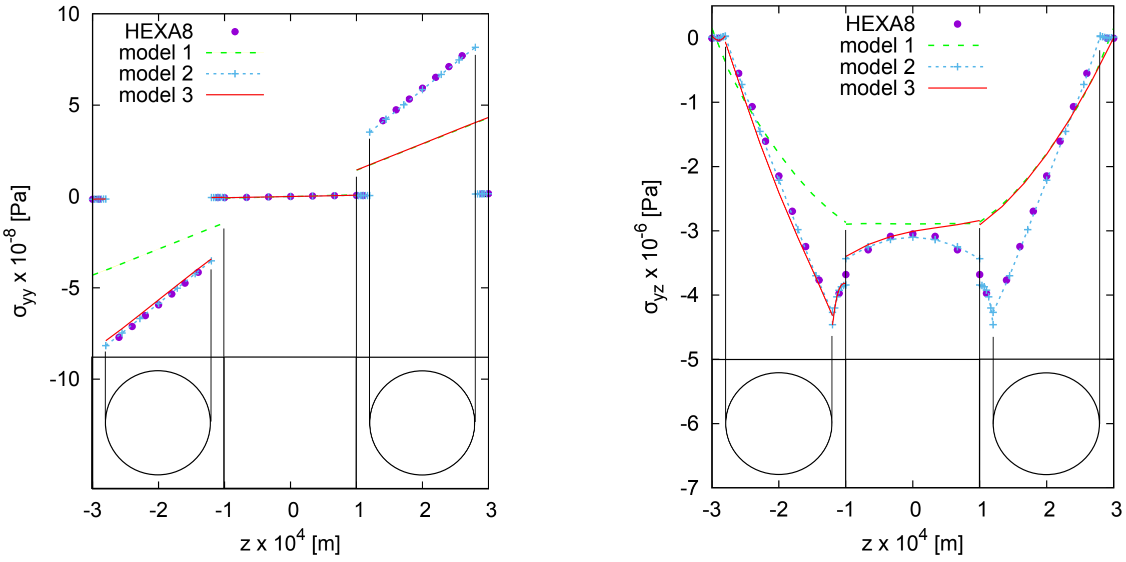

(a) σ_{yy} (b) σ_{yz}

Fig. 6.11 Stresses distributions through the thickness at [5b/8,L/2,:] computed by the HL6 model. The figure attached to the bottom of the graphs represent a vertical strip of the composite structure and the vertical black lines are added to indicate the domains of the fiber, matrix and layer in the model. Note: HEXA8 = solid, model 1 = LW, model 2 = CW, model 3 = mixed CW-LW.

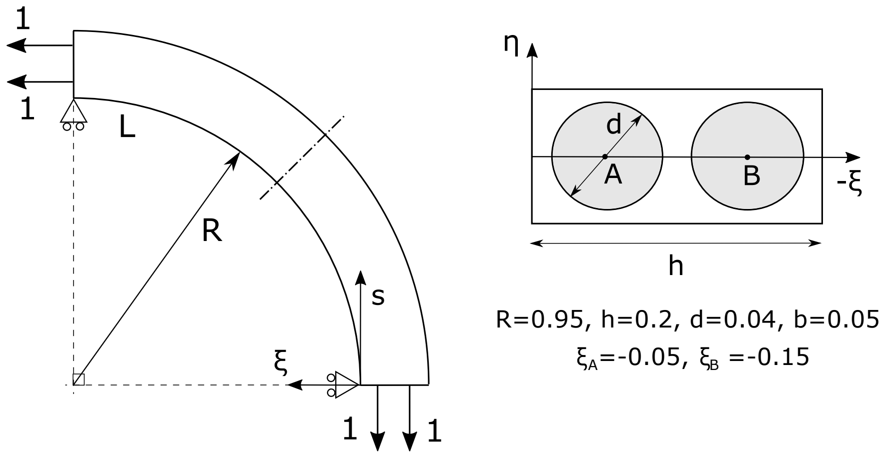

Fig. 6.12 Geometry and section of the fiber-matrix microstructure. Distances in mm and forces in N.

IM7/8551-7 carbon/epoxy and the elastic properties of the constituents are included in 6.4. A fiber volume fraction of 0.5027 is considered. This kind of micro-models are typically generated to investigate the onset of kinking due to misalignments of the fibers. The model accounts for two fibers and a curvature equal to a quarter of a circle. The Frenet-Serret reference system is used to express the variables of the structural problem, see Chapter 5.2. The beam is simply supported at both ends, i.e. $u_\xi = u_\eta = 0$ at $s = 0$ and $s = L$, and symmetry conditions are applied at the center of the microstructure, i.e. $u_s = 0$ at $s = L/2$. The loading case proposed is a pull-out of the fibers of a magnitude of 1 N at each edge, modeled as a distributed pressure over the section of the fibers, see Eq. (3.42).

Table 6.4 Material properties of the carbon/epoxy composite, taken from [98].

	E_1 [GPa]	E_2, E_3 [GPa]	G_{12}, G_{13} [GPa]	G_{23} [GPa]	ν_{12}, ν_{13}	ν_{23}
IM7 fiber	276	19	27	7	0.2	0.2
8551-7 matrix	4.08	4.08	1.478	1.478	0.38	0.38

A convergence study is carried out for both HLE beam elements and 3D finite elements. The proposed HLE model includes a mesh of MITC curved beam elements along the longitudinal path and a total of 16 HL4 curved domains for the cross-section. The solid model is generated in the FEM software Abaqus [183] using C3D8 linear elements. Table 6.5 shows maximum displacements in absolute value for increasing mesh refinements of both types of elements. In particular, three solid models of increasing mesh density are created. Due to the aspect ratio limitations, the computational cost of this approach grows rapidly. It is worth noting that the Abaqus model converges from above, which can be explained by the imprecision of the straight elements to correctly represent the actual volume of curved structures. On the other hand, the cross-section discretization of the HLE beam model is fixed and the convergence of the 1D mesh is achieved already for 4 cubic (MITC4) curved elements. Figure 6.13 includes the contour plots of the total displacements, showing a remarkable agreement.

Table 6.5 Maximum deflection, u_{max}, of the curved microstructure. DOF between brackets.

MITC beam - HL4					
mesh	2 B2 (1,413)	2 B3 (2,355)	2 B4 (3,297)	4 B4 (6,123)	14 B4 (20,253)
$u_{max} \times 10^5$	2.775	4.918	4.940	4.942	4.942
ABAQUS - C3D8					
mesh	(54,417)	(245,979)	(575,667)		
$u_{max} \times 10^5$	5.150	5.115	4.965		

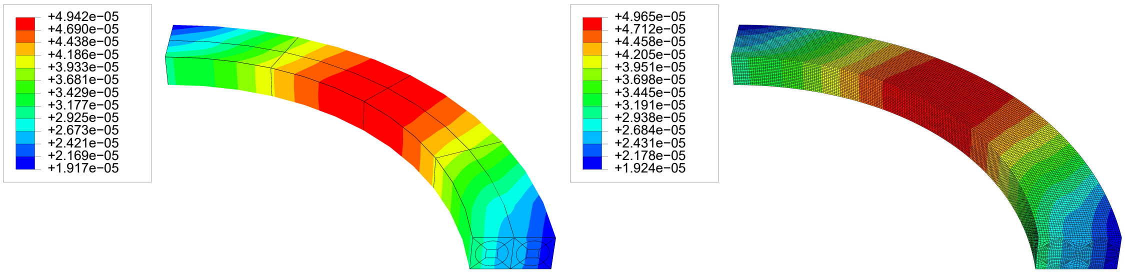

(a) 4 MITC4-HL4 (b) ABAQUS refined

Fig. 6.13 Contour plots of the displacements (m).

Finally, Fig. 6.14, 6.15 and 6.16 exhibit the longitudinal, radial and shear stress fields over the naked fibers. It can be stated that both models compute very similar solutions in all cases. The dimension of the numerical models which is required in this kind of problems is a limiting factor for the modeling of microstructures with high-resolution. These results demonstrate the high effectiveness of locking-free beam elements and HLE theories for the stress analysis of composite materials.

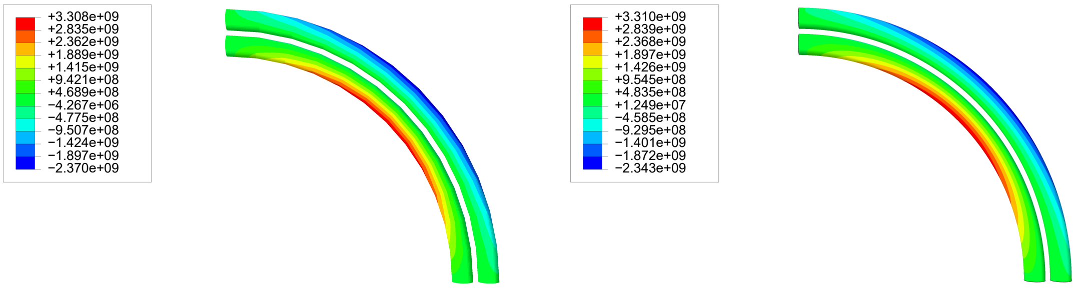

(a) 4 MITC4-HL4 (b) ABAQUS refined

Fig. 6.14 Longitudinal stresses (Pa) over the naked fibers.

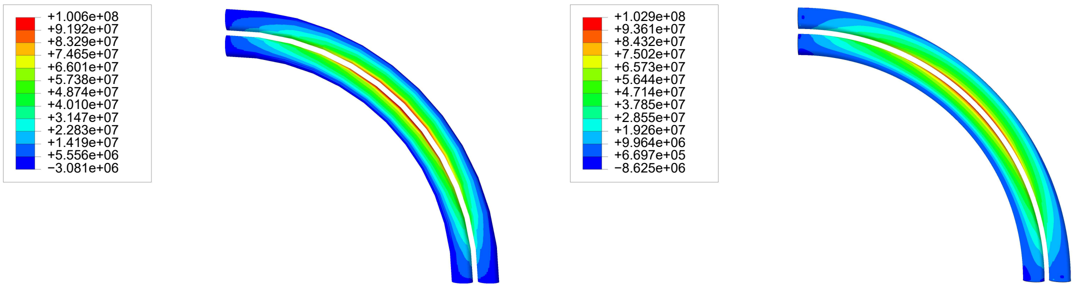

(a) 4 MITC4-HL4 (b) ABAQUS refined

Fig. 6.15 Radial stresses (Pa) over the naked fibers.

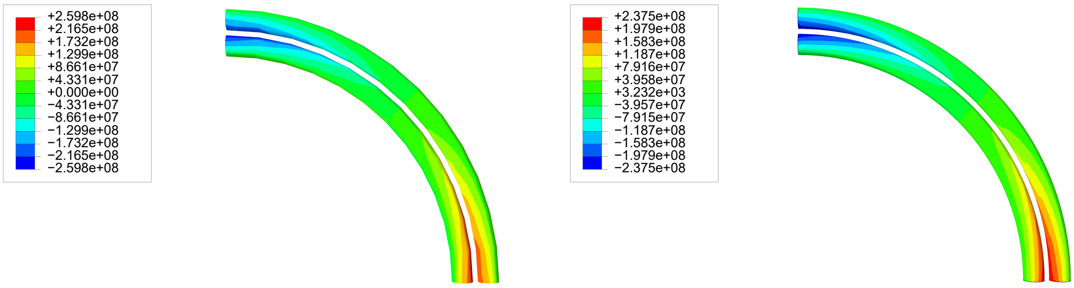

(a) 4 MITC4-HL4 (b) ABAQUS refined

Fig. 6.16 Shear stresses, $\sigma_{s\xi}$, (Pa) over the naked fibersl.

Chapter 7

Micromechanics: mechanics of structure genome

The proposed modeling approach is applied to model the microstructure of fiber-reinforced composites in a micromechanics framework. The objective is twofold: the homogenization of the composite material to obtain the equivalent elastic properties; and the computation of the local stress fields over the microstructure from the global response of the structure. The micromechanics theory selected is the mechanics of structure genome (MSG), which presents some interesting features for the efficient resolution of the unit cell problem. This theory makes it possible to decouple the multiscale problem into global and local analyses with no need of ad hoc assumptions or multiple loading steps, providing the 3D constitutive information and the local fields in a single run.

The present development was carried out in collaboration with Porf. W. Yu of Purdue University and the results were published in a journal paper [60].

7.1 Micromechanics

The micromechanics analysis of composites is essential to understand how the microscopic details, such as fiber arrangement or volume fraction, affect the global response of the structural component. This research field is receiving much attention in the last years and several analytical and numerical methods are available in the literature. Comprehensive reviews of these methods can be found in [137, 88, 4]. Most of the micromechanics approaches make use of the assumption that the arrangement of the fibers and particles follows a regular and periodic pattern, which makes it possible to identify a so-called *unit cell* (UC). The UC is defined as the minimum geometrical entity that can be periodically repeated over the media to conform the global structure. Some of the most well-known analytical methods for the UC problem are the various rules of mixtures [90], the Mori-Tanaka method [130], the Hashin-Shtrikman bounds [87], the generalized self-consistent method [49] and the elasticity-based cell method [214, 213]. Semi-analytical and numerical formulations have also been introduced to deal with more generic microstructures, among these the method of cells [3], the generalized method of cells [150], the mathematical homogenization theory [18, 134] and the high-fidelity method of cells [5]. A wide-spread method among researchers is known as the *representative volume element* (RVE), which is based on the averaging of the local solutions under periodic boundary conditions to compute the equivalent elastic properties [186]. In the end, all the aforementioned methods pursue the same goals:

- To obtain the effective properties of heterogeneous materials from the UC, which can be then used as constitutive information of an equivalent homogeneous material for the macro-scale model.
- To recover the local displacement, strain and stress fields over the UC volume for a given set of outputs of the global analysis.

In this chapter, the multiscale problem is solved by means of the mechanics of structure genome (MSG), introduced by Yu [217], and hierarchical CW beam models. In the MSG framework, the concept of the *structure genome* (SG) is presented as the smallest mathematical building block of the structure. Accordingly, the SG may be a line representing the stack of plies in a laminate, a surface that accounts for the different constituents in fiber-reinforced composites, or, in the most generic case, a 3D cell whose phases vary over the three spatial coordinates. In order to solve all these cases in a unified manner, the MSG applies the variational asymptotic method (VAM) for problems involving smaller parameters and separation of scales [19]. This method was successfully employed as a micromechanics tool for composite simulation in many works [219, 218, 221], showing excellent levels of accuracy and efficiency.

7.1.1 The unit cell problem

Consider a composite media wherein the microstructure is periodically repeated over the volume. The UC is then defined as the smallest building block of that structure which contains all the necessary information to identify the material properties at the macro-scale. Figure 7.1 shows an illustration of periodic array of heterogeneous material and the correspondent UC. The following reference systems are used for the material: the macroscopic properties are defined in a global coordinate system, $\boldsymbol{x} = \{x_1, x_2, x_3\}$, whereas the local reference system of the UC corresponds to $\boldsymbol{y} = \{y_1, y_2, y_3\}$.

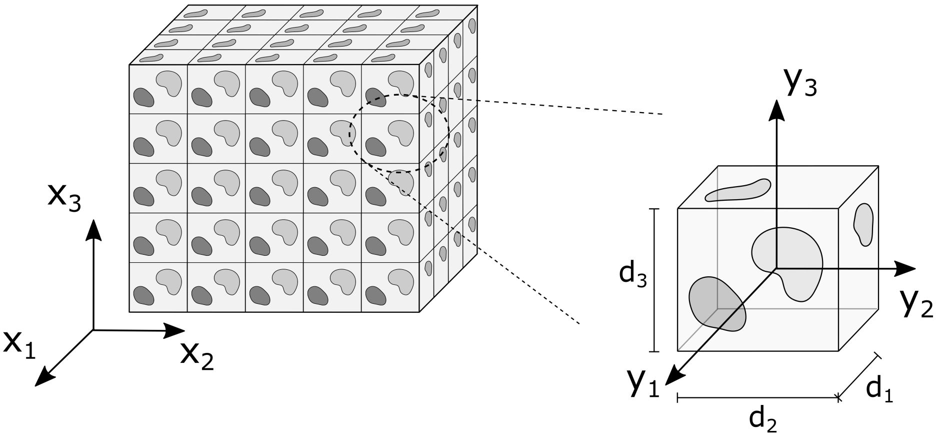

Fig. 7.1 Coordinate reference systems of a periodic heterogeneous material and its UC.

In order to derive a multiscale framework, the starting point is the assumption of scale separation, i.e. the UC must be smaller than the macrostructure. This is mathematically achieved imposing that

$$y_i = x_i/\delta \tag{7.1}$$

where δ is defined as a scaling parameter which characterizes the dimension of the UC. As a consequence, the constitutive information extracted from the UC remains always independent of the macrostructural problem, which is characterized by the geometry, boundary conditions and loadings.

Also, an average value of the local solutions over the UC volume must exist and is equal to the global solution of the structural problem. For example, for the displacement solutions it is possible to state that

$$\frac{1}{V}\int_V u_i(\boldsymbol{x},\boldsymbol{y})\,dV = \bar{u}_i(\boldsymbol{x}) \qquad i = 1,2,3, \tag{7.2}$$

where V is the volume of the cell, u_i are the local displacements and $\bar{u}_i$ are the averaged displacements. Note that the local variables depend on both the global and the local systems, $\boldsymbol{x}$ and $\boldsymbol{y}$, whereas the averaged values are only function of the global coordinates.

The compatibility of the displacements with neighboring UCs is typically imposed via periodic boundary conditions (PBC). The PBC can be written mathematically as:

$$\begin{aligned} u_i(x_1,x_2,x_3;\frac{d_1}{2},y_2,y_3) &= u_i(x_1+d_1,x_2,x_3;-\frac{d_1}{2},y_2,y_3), \\ u_i(x_1,x_2,x_3;y_1,\frac{d_2}{2},y_3) &= u_i(x_1,x_2+d_2,x_3;y_1,-\frac{d_2}{2},y_3), \\ u_i(x_1,x_2,x_3;y_1,y_2,\frac{d_3}{2}) &= u_i(x_1,x_2,x_3+d_3;y_1,y_2,-\frac{d_3}{2}), \end{aligned} \tag{7.3}$$

where d_1, d_2 and d_3 are the dimensions of the UC, as shown in Fig. 7.1. In the practice, these equations establish that the displacements at a certain point located at the boundary of the UC are equal to those of the corresponding point in the opposed boundary.

7.2 Variational Asymptotic Method for UCs

The VAM was introduced by Berdichevskly [19] to provide efficient solutions for structural problems. This method can be applied to stationary value problems in which some terms are smaller than others. Given a certain variational statement, the VAM provides the stationary points of the functional via asymptotic expansions of the small parameters. This method can be exploited in mechanical problems that feature high differences in the spatial dimensions. For instance, in beams the cross-section is smaller than the length, or in plate structures the thickness is usually negligible in comparison to the in-plane dimensions. Moreover, the VAM can be considered a natural approach for the implementation of multiscale models for composite problems, given the several geometrical scales that are involved.

In many multiscale problems, such as the one represented in Fig. 7.1, the SG is equivalent to the UC. In MSG, the functional Π of the stationary value problem that is to be minimized corresponds to the difference between the strain energies of the SG and the equivalent homogeneous material. It is written as:

$$\Pi = \left\langle \frac{1}{2} C_{ijkl}\, \varepsilon_{ij}\, \varepsilon_{kl} \right\rangle - \frac{1}{2} C^*_{ijkl}\, \bar{\varepsilon}_{ij}\, \bar{\varepsilon}_{kl}, \tag{7.4}$$

where $\langle \bullet \rangle = \frac{1}{V}\int_V \bullet\, dV$ denotes volume average. The first term of the Π is the averaged strain energy of the heterogeneous microstructure, whereas the second is the strain energy of the equivalent homogeneous material. C_{ijkl} and C^*_{ijkl} are fourth-order elastic tensors, and ε_{ij} and ε_{kl} are second-order strain tensors. $\bar{\varepsilon}_{ij}$ and $\bar{\varepsilon}_{kl}$ are the global strains.

The local displacements over the UC can be defined as the sum of the global displacements and the local fluctuations, as follows

$$u_i(\boldsymbol{x};\boldsymbol{y}) = \bar{u}_i(\boldsymbol{x}) + \delta\, \chi_i(\boldsymbol{x};\boldsymbol{y}), \tag{7.5}$$

where χ_i are the fluctuation functions, which are multiplied by the scaling parameter δ. Subsequently, it is necessary to define the derivative of a field of the type $f(\boldsymbol{x};\boldsymbol{y})$ in the multiscale framework:

$$\frac{\partial f}{\partial x_j} + \frac{1}{\delta}\frac{\partial f}{\partial y_j}. \tag{7.6}$$

Applying Eq. (7.6) to Eq. (7.5), and after discarding the smallest terms, see [19], the local strains can be written as

$$\varepsilon_{ij}(\boldsymbol{x};\boldsymbol{y}) = \bar{\varepsilon}_{ij}(\boldsymbol{x}) + \chi_{(i,j)}(\boldsymbol{x};\boldsymbol{y}), \tag{7.7}$$

where the global strains, $\bar{\varepsilon}_{ij}$, are defined as

$$\bar{\varepsilon}_{ij}(\boldsymbol{x}) = \frac{1}{2}\Big(\frac{\partial \bar{u}_i(\boldsymbol{x})}{\partial x_j} + \frac{\partial \bar{u}_j(\boldsymbol{x})}{\partial x_i}\Big), \tag{7.8}$$

and the fluctuation derivatives, $\chi_{(i,j)}$, are

$$\chi_{(i,j)}(\boldsymbol{x};\boldsymbol{y}) = \frac{1}{2}\Big(\frac{\partial \chi_i(\boldsymbol{x};\boldsymbol{y})}{\partial y_j} + \frac{\partial \chi_j(\boldsymbol{x};\boldsymbol{y})}{\partial y_i}\Big). \tag{7.9}$$

Now recalling Eq. (7.2), one can write

$$\bar{u}_i = \langle u_i \rangle, \qquad \bar{\varepsilon}_{ij} = \langle \varepsilon \rangle, \tag{7.10}$$

which imply the following constraints to the fluctuation unknowns:

$$\langle \chi_i \rangle = 0, \qquad \langle \chi_{(i,j)} \rangle = 0. \tag{7.11}$$

Meaning that the local solutions do not have an effect on the macrostructure.

Finally, using Eqs. (7.5) and (7.7), and considering that the global strain energy (second term of Eq. (7.4)) is invariable, the micromechanics problem via MSG is finding the fluctuation unknowns, χ_i, which minimize the functional

$$\Pi_1 = \frac{1}{2}\Big\langle C_{ijkl}\,(\bar{\varepsilon}_{ij} + \chi_{(i,j)})\,(\bar{\varepsilon}_{kl} + \chi_{(k,l)})\Big\rangle \tag{7.12}$$

with the constrains written in Eq. (7.11).

7.3 Refined beam models for unit cells

Although closed-form solutions are very useful in micromechanics, they are only available in a few simple problems. The UC problem is usually solved by means of the FEM. This approach is indeed used in the multiscale code SwiftComp^{TM} [220]. In the present research, the governing equations of 3D SGs are solved via HLE-CW models.

The local coordinate system chosen for the UC is shown in Fig. 7.2. For illustrative purposes, the microstructure is that of a fiber-reinforced composite material, although more

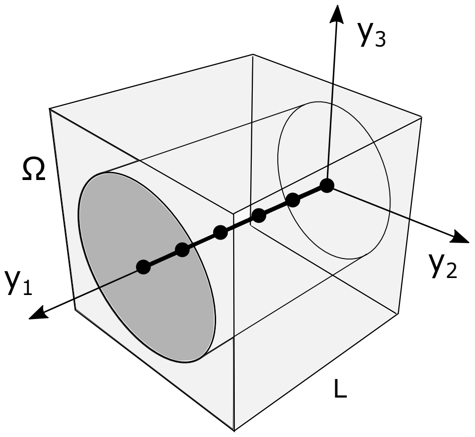

Fig. 7.2 Reference system for the beam modeling of the UC.

generic cases can be accounted for. The beam axis, y_1, is defined along the fiber direction, whereas the cross-section of the beam, Ω, accounts for the heterogeneous phases and lies on $y_2 y_3$. In this framework, the fluctuation unknowns can be expanded over the cross-section via arbitrary functions of the y_2 and y_3 coordinates, as follows

$$\boldsymbol{\chi}(\boldsymbol{x};y_1,y_2,y_3) = F_\tau(y_2,y_3)\,\boldsymbol{\chi}_\tau(\boldsymbol{x};y_1) \quad \tau = 1,2,...,M, \tag{7.13}$$

where $\boldsymbol{\chi}$ is the vector of the fluctuations, F_τ are the expansion functions and $\boldsymbol{\chi}_\tau$ is the vector of the generalized unknowns along the fibre-direction. Using the CW approach, each constituent represented over the cross-section, e.g. fiber and matrix in Fig. 7.2, is modeled via independent kinematics. Also, since the $y_2 y_3$ plane is discretized via HLE domains, the application of the PBC can be straightforwardly done selecting the appropriate DOF over the cross-section boundaries.

As in the previous chapter, the fiber direction is meshed using Lagrangian beam elements. Accordingly, the generalized fluctuation unknowns, $\boldsymbol{\chi}_\tau$, are interpolated along the y_1 coordinate as follows:

$$\boldsymbol{\chi}_\tau(\boldsymbol{x};y_1) = N_i(y_1)\,\boldsymbol{\chi}_{\tau i}(\boldsymbol{x}) \quad i = 1,2,...,n \tag{7.14}$$

where $\boldsymbol{\chi}_{\tau i}(\boldsymbol{x})$ is the nodal unknown vector and n is the total number of beam nodes.

The geometrical relations of the beam element read:

$$\boldsymbol{\varepsilon} = \bar{\boldsymbol{\varepsilon}} + \mathbf{D}\boldsymbol{\chi}. \tag{7.15}$$

Following the usual notation of micromechanics formulations, the vector of the global strains, $\bar{\boldsymbol{\varepsilon}}$, is written as

$$\bar{\boldsymbol{\varepsilon}}^T = \left\{ \begin{array}{cccccc} \bar{\varepsilon}_{11} & \bar{\varepsilon}_{22} & \bar{\varepsilon}_{33} & 2\bar{\varepsilon}_{23} & 2\bar{\varepsilon}_{13} & 2\bar{\varepsilon}_{12} \end{array} \right\} \tag{7.16}$$

and the differential operator, $\mathbf{D}$, is defined as:

$$\mathbf{D} = \begin{bmatrix} \frac{\partial}{\partial y_1} & 0 & 0 \\ 0 & \frac{\partial}{\partial y_2} & 0 \\ 0 & 0 & \frac{\partial}{\partial y_3} \\ 0 & \frac{\partial}{\partial y_3} & \frac{\partial}{\partial y_2} \\ \frac{\partial}{\partial y_3} & 0 & \frac{\partial}{\partial y_1} \\ \frac{\partial}{\partial y_2} & \frac{\partial}{\partial y_1} & 0 \end{bmatrix} \tag{7.17}$$

Subsequently, the functional Π_1 of Eq. (7.12) can be rewritten as

$$\Pi_1^* = \frac{1}{2} \int_V (\bar{\boldsymbol{\varepsilon}} + \mathbf{D}\boldsymbol{\chi})^T \,\tilde{\mathbf{C}}\, (\bar{\boldsymbol{\varepsilon}} + \mathbf{D}\boldsymbol{\chi})\, dV, \tag{7.18}$$

and the PBC are also applied in the fiber direction:

$$\boldsymbol{\chi}_{\tau 1} = \boldsymbol{\chi}_{\tau n} \qquad \tau = 1,2,...,M, \tag{7.19}$$

where 1 and n are the first and last nodes. The master-slave method is employed to impose Eq. (7.19) in the numerical model. It is worth noting that in the case of fiber-reinforced composites, the solutions do not vary along the beam axis thus a single B2 element can be placed with no loss of accuracy. After the application of Eq. (7.19), the remaining DOF are those of a single section. As noted in [221], the volume constrains of Eq. (7.11) do not affect the variation of Π_1^*, although they reduce the admissible solutions of the fluctuations to a unique vector $\boldsymbol{\chi}_{\tau i}$.

Finally, using Eqs. (7.14), (7.13) and (7.18), the functional Π_1^* reads

$$\Pi_1^* = \frac{1}{2} (\boldsymbol{\chi}_{sj}^T \boldsymbol{E}^{\tau sij} \boldsymbol{\chi}_{\tau i} + 2\boldsymbol{\chi}_{sj}^T \boldsymbol{D}_{h\varepsilon}^{sj} \bar{\boldsymbol{\varepsilon}} + \bar{\boldsymbol{\varepsilon}}^T \boldsymbol{D}_{\varepsilon\varepsilon} \bar{\boldsymbol{\varepsilon}}) \tag{7.20}$$

where

$$\begin{aligned}
\boldsymbol{E}^{\tau sij} =& \int_L \int_\Omega (\mathbf{D}(F_\tau N_i \boldsymbol{I}_3))^T \, \tilde{\mathbf{C}} \, \mathbf{D}(F_s N_j \boldsymbol{I}_3) \, d\Omega \, dy_1 \\
\boldsymbol{D}_{h\varepsilon}^{\tau i} =& \int_L \int_\Omega (\mathbf{D}(F_\tau N_i \boldsymbol{I}_3))^T \, \tilde{\mathbf{C}} \, d\Omega \, dy_1 \\
\boldsymbol{D}_{\varepsilon\varepsilon} =& \int_L \int_\Omega \tilde{\mathbf{C}} \, d\Omega \, dy_1
\end{aligned} \tag{7.21}$$

$\boldsymbol{I}_3$ being the 3×3 identity matrix. $\boldsymbol{E}^{\tau sij}$ and $\boldsymbol{D}_{h\varepsilon}^{\tau i}$ are the fundamental nucleus of the UC problem. On the other hand, $\boldsymbol{D}_{\varepsilon\varepsilon}$ is the effective stiffness matrix of the material by volume average. Note that $\boldsymbol{E}^{\tau sij}$ is a 3×3 matrix, $\boldsymbol{D}_{h\varepsilon}^{\tau i}$ a 3×6 matrix and $\boldsymbol{D}_{\varepsilon\varepsilon}$ a 6×6 matrix. The meaning of the indexes τ, s, i and j is equivalent to previous chapters (see Chapter 3). The explicit expressions of the components of $\boldsymbol{E}^{\tau sij}$ are equivalent to those of the standard fundamental nucleus $\mathbf{K}^{\tau sij}$ for structural problems, which was introduced in Eq. (3.36). The expressions of the $\boldsymbol{D}_{h\varepsilon}^{\tau i}$ matrix are indicated here:

$$\begin{aligned}
D_{h\varepsilon 11}^{\tau i} &= \tilde{\mathrm{C}}_{11} \int_l N_{i,y_1} \mathrm{d}y_1 \int_\Omega F_\tau \, d\Omega & D_{h\varepsilon 12}^{\tau i} &= \tilde{\mathrm{C}}_{12} \int_l N_{i,y_1} \mathrm{d}y_1 \int_\Omega F_\tau \, d\Omega \\
D_{h\varepsilon 13}^{\tau i} &= \tilde{\mathrm{C}}_{13} \int_l N_{i,y_1} \mathrm{d}y_1 \int_\Omega F_\tau \, d\Omega & D_{h\varepsilon 14}^{\tau i} &= 0 \\
D_{h\varepsilon 15}^{\tau i} &= \tilde{\mathrm{C}}_{55} \int_l N_i \mathrm{d}y_1 \int_\Omega F_{\tau,z} \, d\Omega & D_{h\varepsilon 16}^{\tau i} &= \tilde{\mathrm{C}}_{66} \int_l N_i \mathrm{d}y_1 \int_\Omega F_{\tau,x} \, d\Omega \\
D_{h\varepsilon 21}^{\tau i} &= \tilde{\mathrm{C}}_{12} \int_l N_i \mathrm{d}y_1 \int_\Omega F_{\tau,x} \, d\Omega & D_{h\varepsilon 22}^{\tau i} &= \tilde{\mathrm{C}}_{22} \int_l N_i \mathrm{d}y_1 \int_\Omega F_{\tau,x} \, d\Omega \\
D_{h\varepsilon 23}^{\tau i} &= \tilde{\mathrm{C}}_{23} \int_l N_i \mathrm{d}y_1 \int_\Omega F_{\tau,x} \, d\Omega & D_{h\varepsilon 24}^{\tau i} &= \tilde{\mathrm{C}}_{44} \int_l N_i \mathrm{d}y_1 \int_\Omega F_{\tau,z} \, d\Omega \\
D_{h\varepsilon 25}^{\tau i} &= 0 & D_{h\varepsilon 26}^{\tau i} &= \tilde{\mathrm{C}}_{66} \int_l N_{i,y_1} \mathrm{d}y_1 \int_\Omega F_\tau \, d\Omega \\
D_{h\varepsilon 31}^{\tau i} &= \tilde{\mathrm{C}}_{13} \int_l N_i \mathrm{d}y_1 \int_\Omega F_{\tau,z} \, d\Omega & D_{h\varepsilon 32}^{\tau i} &= \tilde{\mathrm{C}}_{23} \int_l N_i \mathrm{d}y_1 \int_\Omega F_{\tau,z} \, d\Omega \\
D_{h\varepsilon 33}^{\tau i} &= \tilde{\mathrm{C}}_{33} \int_l N_i \mathrm{d}y_1 \int_\Omega F_{\tau,z} \, d\Omega & D_{h\varepsilon 34}^{\tau i} &= \tilde{\mathrm{C}}_{44} \int_l N_i \mathrm{d}y_1 \int_\Omega F_{\tau,x} \, d\Omega \\
D_{h\varepsilon 25}^{\tau i} &= \tilde{\mathrm{C}}_{55} \int_l N_{i,y_1} \mathrm{d}y_1 \int_\Omega F_\tau \, d\Omega & D_{h\varepsilon 26}^{\tau i} &= 0
\end{aligned} \tag{7.22}$$

Note that in this case the material subindexes are written with respect to the material system depicted in Fig. 7.2.

Performing the variation of Π_1^*, it is found that the minimum of the functional is provided by the following linear expression

$$\boldsymbol{E}^{\tau sij} \boldsymbol{\chi}_{\tau i} = -\boldsymbol{D}_{h\varepsilon}^{sj} \bar{\boldsymbol{\varepsilon}}. \tag{7.23}$$

Since $\boldsymbol{\chi}_{\tau i}$ is a linear function of $\bar{\boldsymbol{\varepsilon}}$, it can be state that

$$\boldsymbol{\chi}_{\tau i}(\boldsymbol{x}) = \boldsymbol{\chi}_{\tau i0}\,\bar{\boldsymbol{\varepsilon}}(\boldsymbol{x}) \tag{7.24}$$

Subsequently, the linear system of equations results in:

$$\boldsymbol{E}^{\tau sij}\boldsymbol{\chi}_{\tau i0} = -\boldsymbol{D}_{h\varepsilon}^{sj} \tag{7.25}$$

where $\boldsymbol{\chi}_{\tau i0}$ is a 3×6 matrix including the fluctuation solutions.

7.3.1 Effective properties and local fields

The equivalent homogeneous properties of the heterogeneous material are straightforwardly obtained from the solution of the linear system of Eq. (7.25). For this, we consider that the energy stored in the equivalent homogeneous material is equal to that of the heterogeneous material. Substituting Eq. (7.24) into Eq. (7.23), and then into the strain energy of Eq. (7.20); and making the energetic equivalence, the effective stiffness matrix is obtained as:

$$\tilde{\mathbf{C}}^{*} = \frac{1}{V}\,(\boldsymbol{\chi}_{sj0}^{T}\boldsymbol{D}_{h\varepsilon}^{sj} + \boldsymbol{D}_{\varepsilon\varepsilon}) \tag{7.26}$$

where $\tilde{\mathbf{C}}^{*}$ contains the material properties of the equivalent homogenized body.

The computation of the local fields is performed by simply introducing the fluctuation solutions obtained from Eq. (7.25) back into the geometrical and constitutive equations. In this manner, the local strains are defined as

$$\boldsymbol{\varepsilon} = \bar{\boldsymbol{\varepsilon}} + \mathbf{D}(F_{\tau}N_{i}\boldsymbol{\chi}_{\tau i0}\,\bar{\boldsymbol{\varepsilon}}) \tag{7.27}$$

and the local stresses are obtained from the Hooke's law:

$$\boldsymbol{\sigma} = \tilde{\mathbf{C}}\boldsymbol{\varepsilon}. \tag{7.28}$$

In MSG, the local fluctuations are obtained from the solution of the stationary value of the energy functional and, therefore, no external loads are required to compute the effective properties of the homogenized material. Furthermore, due to the decoupling between the fluctuation unknowns, $\boldsymbol{\chi}_{\tau i0}$, and the global strains, $\bar{\boldsymbol{\varepsilon}}$, the local solutions can be computed for arbitrary inputs with only a single run of the code.

7.4 Example

Benchmarking is essential in micromechanics to assess new formulations in a common framework. In this line, several worldwide projects were organized to present the capabilities of many different multiscale formulations, among these the *World Wide Failure Exercise* (WWFE) [91] and the *Micromechanics Simulation Challenge* (MSC) [181]. The numerical example included here was defined by Sertse *et al.* [181] in the framework of the latter project. It considers an hexagonal pack of carbon/epoxy material and both the effective properties and the local stress fields are requested. The model is assessed against the solutions provided by the participants in MSC, among them FVDAM [43, 44], GMC and HFGMC [16], DIGIMAT [1], Altair MDS [76], ESI-VPS [84], SwiftComp [220] and RVE analysis based on 3D FEM.

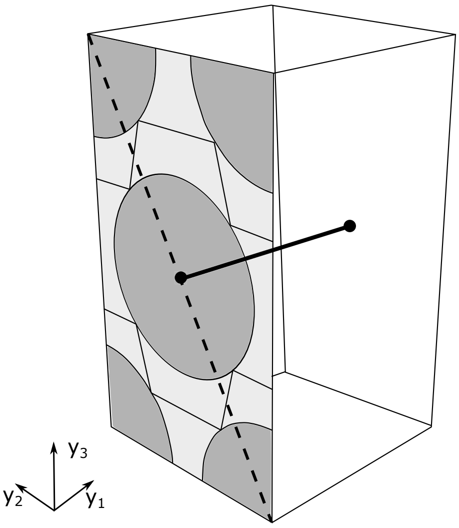

Fig. 7.3 HLE beam model of the hexagonal pack UC.

The fiber is modeled as transverse isotropic with the following elastic properties: $E_1 = 276$ GPa, $E_2 = 19.5$ GPa, $G_{12} = 70$ GPa, $G_{23} = 5.74$ GPa, $\nu_{12} = 0.28$ and $\nu_{23} = 0.7$; whereas the matrix is isotropic, with $E = 4.76$ GPa and $\nu = 0.37$. The fiber volume fraction is equal to 0.6. The CW model of the hexagonal pack is shown in Fig. 7.3. A discretization of 15 HLE domains is created for the cross-section surface, including one domain per fibre. The effective properties are shown in Table 7.1. The obtained solutions are in good agreement with those of the references. It can be observed that the most challenging results are those of the transverse properties, although the solutions converge to the values of SwiftComp and 3D FEM as the HLE order increases.

The computation of the local solutions can be very demanding due to the high gradients of the strain/stress fields over the heterogeneous body. Given the coarse domain distributions

Table 7.1 Effective properties of the hexagonal pack (E_i and G_{ij} in GPa). References from [181].

Model	E_1	E_2	E_3	G_{12}	G_{13}	G_{23}	ν_{12}	ν_{13}	ν_{23}
References									
FEA RVE	167.33	10.67	10.67	6.38	6.39	3.33	0.312	0.312	0.600
FVDAM	167.30	10.67	10.67	6.38	6.39	3.33	0.310	0.310	0.600
GMC	167.40	10.46	10.08	5.33	4.45	3.00	0.312	0.312	0.612
HFGMC	167.40	10.71	10.69	6.58	6.54	3.36	0.312	0.312	0.603
DIGIMAT-MF/MT	167.52	10.53	10.53	6.36	6.36	3.27	0.312	0.312	0.605
Altair MDS	167.40	10.71	10.71	6.45	6.44	3.35	0.312	0.312	0.600
ESI	166.71	10.67	10.67	6.35	6.38	3.33	0.312	0.312	0.599
SwiftComp	167.33	10.67	10.67	6.38	6.39	3.33	0.312	0.312	0.600
CW-HLE									
HL2	167.65	10.84	10.84	6.56	6.69	3.40	0.312	0.312	0.599
HL4	167.65	10.71	10.71	6.42	6.44	3.36	0.312	0.312	0.599
HL7	167.65	10.68	10.68	6.40	6.41	3.34	0.312	0.312	0.600

typically used in HLE models, high polynomial orders are needed. Figure 7.4 shows the longitudinal stress σ_{11} generated by a unitary longitudinal strain ε_{11}, Fig. 7.5 shows the shear stress σ_{13} under shear strain ε_{13}, Fig. 7.6 shows the shear stress σ_{23} under shear strain ε_{23} and Fig. 7.7 shows the shear stress σ_{12} under combined strains ε_{11} and ε_{13}. The left-hand side of the aforementioned figures includes the 3D plot of the correspondent stress solutions, whereas the right-hand side plots the distribution of stresses along the diagonal of the section of the hexagonal pack (dashed line in Fig. 7.3) for all the models considered. There is a remarkable agreement between the HLE solutions, and the 3D FEA and SwiftComp results.

It is obvious that HLE and SwiftComp should ideally converge to the same solutions for further refinements, since both are based on the same governing equations. The focus here is to assess the use of higher-order beam theories in a multiscale framework. The computational times of each micromechanical model can be found in Table 7.2. All the reference times are extracted from [181]. The proposed solutions were obtained in a Windows 7 64-bit OS, Intel(R) Core(TM) i7-5500U CPU @ 2.40GHz 16.0GB RAM.

Table 7.2 Computational time (s) of the homogenization and dehomogenization. Reference values from [181].

Model	FVDAM	GMC	HFGMC	DIGIMAT	MDS	ESI	SwiftComp	HL7	FEA
Homog.	4	-	-	0.03	4.58	-	0.26	0.19	-
Dehomog.	0.88	-	-	-	5.97	-	0.93	0.73	-
Total	4.88	0.292	1.151	-	10.55	29.00	1.19	0.92	42.00

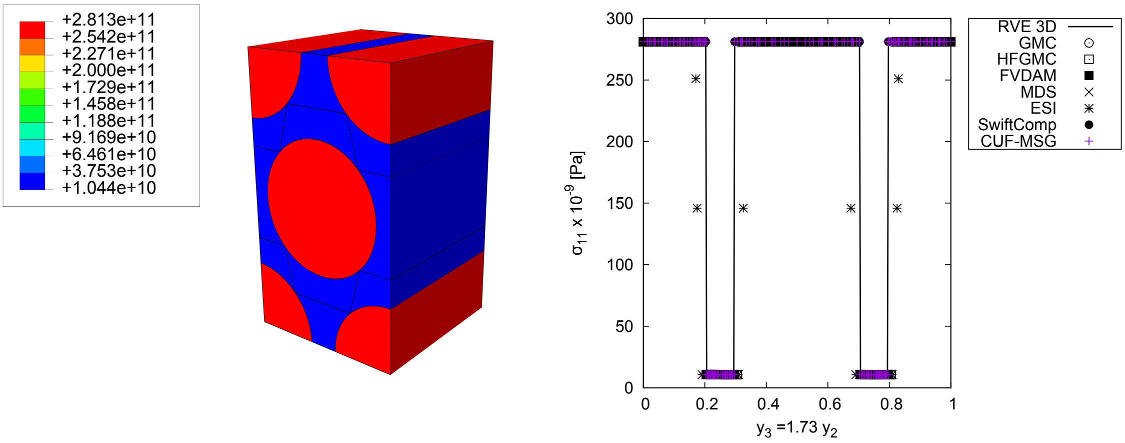

(a) σ_{11} (b) diagonal values

Fig. 7.4 Longitudinal stress σ_{11} generated by a unitary longitudinal strain ε_{11}. Reference values from [181].

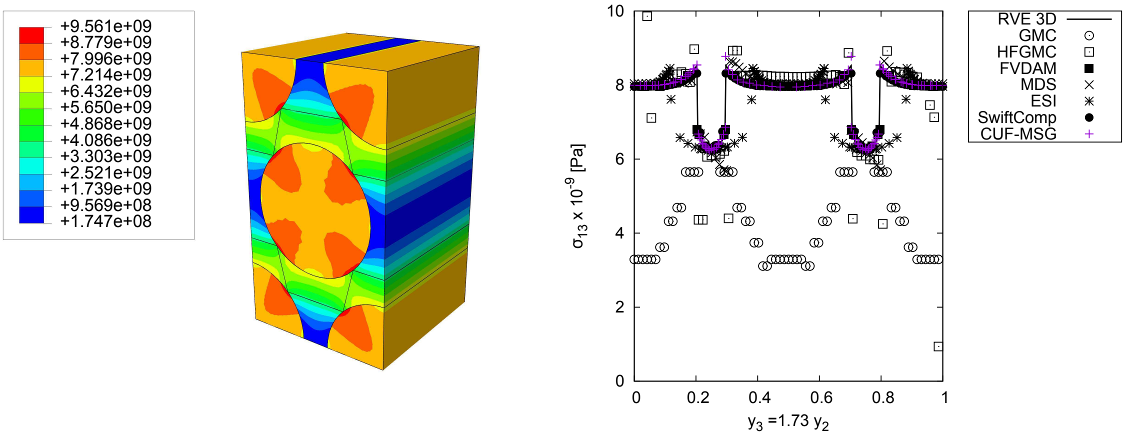

(a) σ_{13} (b) diagonal values

Fig. 7.5 Shear stress σ_{13} generated by a unitary shear strain ε_{13}. Reference values from [181].

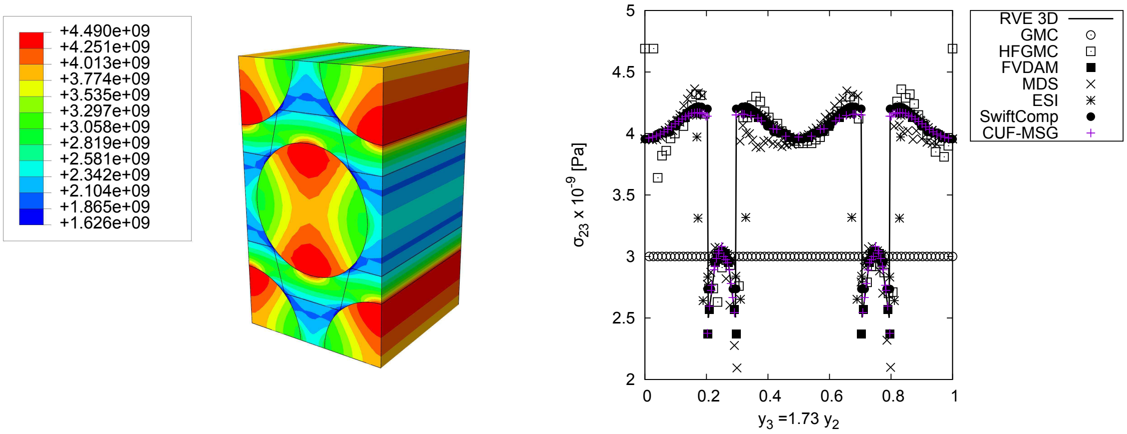

(a) σ_{23} (b) diagonal values

Fig. 7.6 Shear stress σ_{23} generated by a unitary shear strain ε_{23}. Reference values from [181].

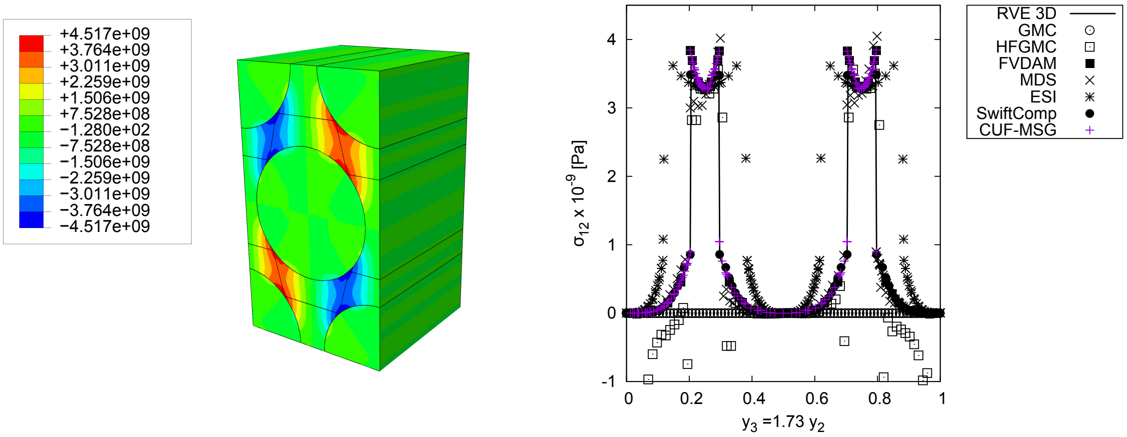

(a) σ_{12} (b) diagonal values

Fig. 7.7 Shear stress σ_{12} generated by combined strains ε_{11} and ε_{13}. Reference values from [181].

Chapter 8

Refined beam elements based on mixed assumptions

This chapter proposes the application of the Reissner's mixed variational theorem (RMVT) [173] for the correct computation of the transverse stresses in generic laminates. Using this mixed variational statement, both displacements and stresses are included in the solution vector, and, therefore, the compatibility and equilibrium conditions can be prescribed and satisfied exactly at the interfaces and boundaries of the laminate. A layer-wise (LW) approach is adopted for both fields and a p-refinement of the stress solutions is performed via hierarchical Legendre expansion (HLE) models.

The present development and results can be found in [58].

8.1 Laminate considerations

Differently from metallic plates, the transverse anisotropy exhibited by multilayered materials leads to complex distributions of displacements, strains and stresses over the stacking direction. Due to the heterogeneity of the laminate, the transverse deformations play a role in the mechanical response of the structure and, therefore, should not be neglected in the simulation. The compatibility and equilibrium conditions of the elastic problem requires continuous displacements (u_x, u_y, u_z) and transverse stresses (σ_{zz}, σ_{xz}, σ_{yz}), respectively, across the thickness of the laminate. This condition is known as interlaminar continuity (IC) and represents a major challenge in the modeling of composite laminates, as shown in book of Reddy [170], among others. The problem can be summarized as follows: in order to satisfy the equilibrium conditions, the transverse deformation must be distinct layer by layer and, therefore, the slope of displacement fields must exhibit sudden changes at the ply

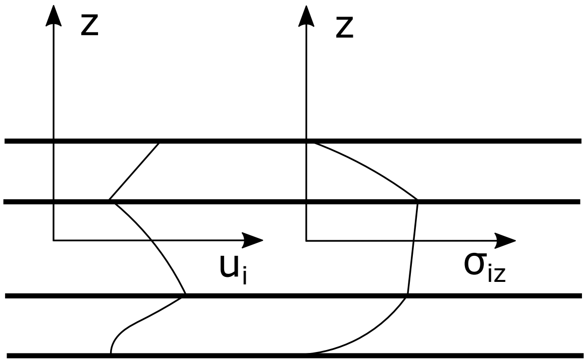

Fig. 8.1 Typical displacement and transverse stress fields across the thickness of multilayered structures.

interfaces. This well-known behavior is commonly known as the zig-zag effect (ZZ) and it is illustrated in Fig. 8.1, which shows the IC in multi-layered structures. Carrera [23] noted that the ZZ and IC conditions are strongly connected and must be modeled properly to obtain an accurate description of the laminate response. Mathematically speaking, the model should compute C^0 displacements and C^0 transverse stresses along the thickness direction. These conditions, which are denominated as the C^0_z-Requirements [24], are not fulfilled in the majority of multilayered theories available today in composite design.

8.2 Reissner's mixed variational theorem (RMVT)

The principle of virtual displacements (PVD) is probably the most commonly used variational statement for the development of displacement-based FEM formulations. It makes use of compatible displacement fields as variables and sets the equilibrium of the internal and external works. In static analyses, the PVD can be written as:

$$\int_V (\delta \boldsymbol{\varepsilon}_p^T \, \boldsymbol{\sigma}_p + \delta \boldsymbol{\varepsilon}_n^T \, \boldsymbol{\sigma}_n) \, dV = \delta L_e. \tag{8.1}$$

Note that the elastic energy has been decoupled into in-plane components (subscript p) and transverse components (subscript n), being $\boldsymbol{\sigma}_p = \{\sigma_{yy}, \sigma_{xx}, \sigma_{xy}\}$, $\boldsymbol{\varepsilon}_p = \{\varepsilon_{yy}, \varepsilon_{xx}, \varepsilon_{xy}\}$, $\boldsymbol{\sigma}_n = \{\sigma_{zz}, \sigma_{xz}, \sigma_{yz}\}$ and $\boldsymbol{\varepsilon}_n = \{\varepsilon_{zz}, \varepsilon_{xz}, \varepsilon_{yz}\}$. The geometrical and constitutive equations, Eqs. (2.2) and (3.12) respectively, are introduced in the PVD to derive the governing equations in terms of the displacement unknowns. As a consequence, the stress fields are computed *a posteriori* using the displacement derivatives back in the Hooke's law. Subsequently, the C^0_z-Requirements are never guaranteed *a priori* and can only be approximated via refinement of the model. A possible solution to this issue is the use of stress recovery methods, which allow it to satisfy the C_z^0-Requirements via integration of the 3D equilibrium equations, see Whitney [210], although this process is done also *a posteriori*.

The C_z^0-Requirements can be completely fulfilled *a priori* if both the displacements and stresses are taken as variables in the variational principle. This can be done via the Hu-Washizu principle [206], which imposes the compatibility conditions in the PVD through Lagrange multipliers, or the Hellinger-Reissner principle [171], which imposes the equilibrium of the stresses as a constraint to the principle of virtual forces. In these mixed variation principles, the Lagrange multipliers become a second set of variables, i.e. stresses in the Hu-Washizu principle and displacements in the Hellinger-Reissner principle.

In laminated plates, Reissner realized that it is enough to impose the equilibrium only in the transverse direction. Indeed, the RMVT establishes the C_z^0-Requirements *a priori* and completely through the use of independent fields for the displacements and transverse stresses. The IC is imposed in the PVD by adding and extra term to the internal energy:

$$\int_V (\delta \boldsymbol{\varepsilon}_{pG}^T \, \boldsymbol{\sigma}_{pH} + \delta \boldsymbol{\varepsilon}_{nG}^T \, \boldsymbol{\sigma}_{nM} + \delta \boldsymbol{\sigma}_{nM}^T (\boldsymbol{\varepsilon}_{nG} - \boldsymbol{\varepsilon}_{nH}))\, dV = \delta L_e, \tag{8.2}$$

where the subscript H denotes computation through the Hooke's law, subscript G denotes computation through the geometrical relations and subscript M denotes the use of assumed fields for the transverse stresses, $\boldsymbol{\sigma}_{nM}$. Note that the IC conditions are satisfied via the compatibility of transverse strains obtained independently from the geometrical relations and the constitutive laws, or

$$\boldsymbol{\varepsilon}_{nG} = \boldsymbol{\varepsilon}_{nH}. \tag{8.3}$$

By virtue of the RMVT principle, the transverse stresses, $\sigma_{zz}, \sigma_{xz}, \sigma_{yz}$, become unknowns of the mechanical problem an can be prescribed to be continuous through the laminate thickness. The in-plane stresses, $\sigma_{xx}, \sigma_{yy}, \sigma_{xy}$, which are discontinuous in the thickness direction, are computed *a posteriori* through the Hooke's law.

8.3 Constitutive and geometrical relations

For a generic k^{th}-lamina, the Hooke's law reads

$$\boldsymbol{\sigma}^k = \tilde{\mathbf{C}}^k \boldsymbol{\varepsilon}^k \tag{8.4}$$

Following the same notation of Eq. (8.1), the constitutive laws can be rewritten as

$$
\begin{aligned}
\boldsymbol{\sigma}^k_{pH} &= \tilde{\mathbf{C}}^k_{pp}\boldsymbol{\varepsilon}^k_{nG} + \tilde{\mathbf{C}}^k_{pn}\boldsymbol{\varepsilon}^k_{nG} \\
\boldsymbol{\sigma}^k_{nH} &= \tilde{\mathbf{C}}^k_{np}\boldsymbol{\varepsilon}^k_{pG} + \tilde{\mathbf{C}}^k_{nn}\boldsymbol{\varepsilon}^k_{nG}
\end{aligned}
\tag{8.5}
$$

where the stiffness matrices for an orthotropic lamina read:

$$
\begin{gathered}
\tilde{\mathbf{C}}_{pp} = \begin{bmatrix} \tilde{C}_{11} & \tilde{C}_{12} & \tilde{C}_{16} \\ \tilde{C}_{12} & \tilde{C}_{22} & \tilde{C}_{26} \\ \tilde{C}_{16} & \tilde{C}_{26} & \tilde{C}_{66} \end{bmatrix} \quad \tilde{\mathbf{C}}_{nn} = \begin{bmatrix} \tilde{C}_{33} & 0 & 0 \\ 0 & \tilde{C}_{44} & \tilde{C}_{45} \\ 0 & \tilde{C}_{45} & \tilde{C}_{55} \end{bmatrix} \\
\tilde{\mathbf{C}}_{pn} = \tilde{\mathbf{C}}^T_{np} = \begin{bmatrix} \tilde{C}_{13} & 0 & 0 \\ \tilde{C}_{23} & 0 & 0 \\ \tilde{C}_{36} & 0 & 0 \end{bmatrix} .
\end{gathered}
\tag{8.6}
$$

In order to obtain the transverse strains from the Hooke's law, ε_{nH}, it is possible to rewrite the constitutive relations as follows (see [26]):

$$
\begin{aligned}
\boldsymbol{\sigma}^k_{pH} &= \mathbf{C}^k_{pp}\boldsymbol{\varepsilon}^k_{nG} + \mathbf{C}^k_{pn}\boldsymbol{\sigma}^k_{nM} \\
\boldsymbol{\varepsilon}^k_{nH} &= \mathbf{C}^k_{np}\boldsymbol{\varepsilon}^k_{pG} + \mathbf{C}^k_{nn}\boldsymbol{\sigma}^k_{nM}
\end{aligned}
\tag{8.7}
$$

In these equations, the components of the constitutive matrices $\mathbf{C}^k_{pp}$, $\mathbf{C}^k_{pn}$, $\mathbf{C}^k_{np}$ and $\mathbf{C}^k_{nn}$ include both stiffness and compliance coefficients. They are obtained from the following relations:

$$
\begin{aligned}
\mathbf{C}^k_{pp} &= \tilde{\mathbf{C}}^k_{pp} - \tilde{\mathbf{C}}^k_{pn}{\tilde{\mathbf{C}}^k_{nn}}^{-1}\tilde{\mathbf{C}}^k_{np} \\
\mathbf{C}^k_{pn} &= \tilde{\mathbf{C}}^k_{pn}{\tilde{\mathbf{C}}^k_{nn}}^{-1} \\
\mathbf{C}^k_{np} &= -{\tilde{\mathbf{C}}^k_{nn}}^{-1}\tilde{\mathbf{C}}^k_{np} \\
\mathbf{C}^k_{nn} &= {\tilde{\mathbf{C}}^k_{nn}}^{-1}
\end{aligned}
\tag{8.8}
$$

where ${\tilde{\mathbf{C}}^k_{nn}}^{-1}$ is the compliance matrix related to the transverse terms.

8.3.1 Geometrical relations

In linear elasticity, the displacements and strains are related to each other through the following geometrical relations:

$$\begin{aligned}\boldsymbol{\varepsilon}_{pG} &= \mathbf{D}_p\,\boldsymbol{u}\\ \boldsymbol{\varepsilon}_{nG} &= \mathbf{D}_n\,\boldsymbol{u}\end{aligned} \tag{8.9}$$

where the differential operators $\mathbf{D}_p$ and $\mathbf{D}_n$ are written as

$$\mathbf{D}_p = \begin{bmatrix} 0 & \frac{\partial}{\partial y} & 0 \\ \frac{\partial}{\partial x} & 0 & 0 \\ \frac{\partial}{\partial y} & \frac{\partial}{\partial x} & 0 \end{bmatrix} \quad \mathbf{D}_n = \begin{bmatrix} 0 & 0 & \frac{\partial}{\partial z} \\ \frac{\partial}{\partial z} & 0 & \frac{\partial}{\partial x} \\ 0 & \frac{\partial}{\partial z} & \frac{\partial}{\partial y} \end{bmatrix}. \tag{8.10}$$

8.4 RMVT-based beam theories

Most RMVT-based models available in the literature are derived via plate/shell formulations, i.e. displacements and stresses are assumed only in the thickness direction. A few works focus on mixed beam formulations, such as Murakami *et al*. [133], Murakami and Yamakawa [135], and more recently Tessler [192], although they mostly deal with 2D beams. In the current framework, the kinematics of the 3D beam are written as:

$$\boldsymbol{u}^k(x,y,z) = F_\tau(x,z)\,\boldsymbol{u}^k_\tau(y) \qquad \tau = 1,2,...,M \tag{8.11}$$

as shown in Chapter 2. In order to formulate a mixed beam element, the stress variables must be also assumed over the cross-section, as follows:

$$\boldsymbol{\sigma}^k_{nM}(x,y,z) = G_\tau(x,z)\,\boldsymbol{\sigma}^k_{n\tau}(y) \qquad \tau = 1,2,...,M \tag{8.12}$$

A LW description of the transverse stresses is chosen for the sake of capturing the sudden changes of the derivatives of the solutions at the interfaces. Figure 8.2 shows an illustration of the LW mixed beam element. Using HLE theories, the C^0_z-Requirements are imposed simply as

$$\begin{aligned}\boldsymbol{u}^k_t &= \boldsymbol{u}^{k+1}_b\\ \boldsymbol{\sigma}^k_{nt} &= \boldsymbol{\sigma}^{k+1}_{nb},\end{aligned} \tag{8.13}$$

for $k = 1,...,n_l-1$. The subscripts t and b denote top and bottom of the layer, respectively. These conditions are introduced in the numerical model via assembly of the cross-section

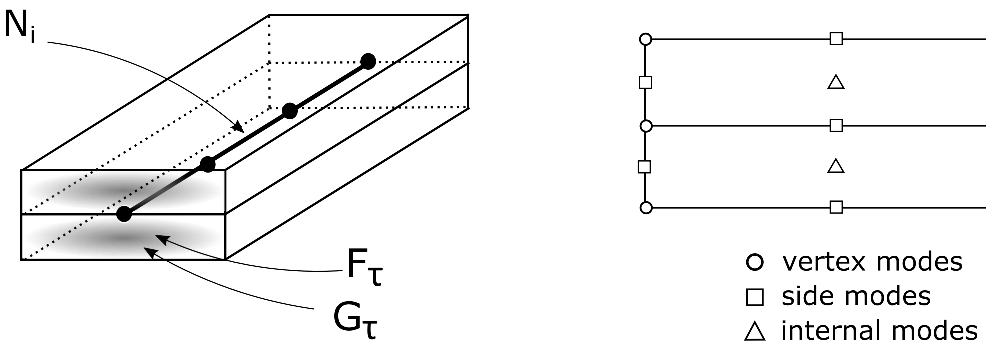

(a) Refined beam element (b) Cross-section

Fig. 8.2 Representation of the proposed refined beam element (a) and the distribution of the unknowns over the cross-section (b) in a two-layer laminate.

sub-matrices in the global stiffness matrix, see Fig. 3.4. Furthermore, the availability of cross-sectional unknowns over the boundaries of the section allows it to prescribe arbitrary transverse stresses at the faces of the structure, for instance at top and bottom:

$$\begin{aligned} \boldsymbol{\sigma}_{nt}^{N_l} &= \boldsymbol{\sigma}_{nt}^{*} \\ \boldsymbol{\sigma}_{nb}^{1} &= \boldsymbol{\sigma}_{nb}^{*} \end{aligned} \tag{8.14}$$

where the superscript $*$ denotes prescribed values. Accordingly, stress-free boundary conditions can be directly imposed in the analysis a priori.

8.5 Fundamental nucleus

As for previous developments, the displacement and transverse stress variables of the cross-section are interpolated over the beam axis via standard 1D shape functions:

$$\boldsymbol{u}_\tau^k(y) = N_i(y)\,\boldsymbol{u}_{\tau i}^k \qquad i = 1,...,n_n \tag{8.15}$$

$$\boldsymbol{\sigma}_\tau^k(y) = N_i(y)\,\boldsymbol{\sigma}_{\tau i}^k \qquad i = 1,...,n_n \tag{8.16}$$

where $\boldsymbol{u}_{\tau i}^k = \{u_{\tau i_x}^k, u_{\tau i_y}^k, u_{\tau i_z}^k\}$ and $\boldsymbol{\sigma}_{\tau i}^k = \{\sigma_{\tau i_x}^k, \sigma_{\tau i_y}^k, \sigma_{\tau i_z}^k\}$ are the displacement and transverse stress nodal unknowns, respectively.

Introducing the interpolations of Eq. (8.15) and Eq. (8.16), and transverse assumptions of Eq. (8.11) and Eq. (8.12), into the geometrical relations (Eq. (8.9)) and the mixed constitutive laws Eq. (8.7), the RMVT functional of Eq. (8.2) becomes

$$
\begin{aligned}
&\int_L\int_\Omega (\delta \boldsymbol{u}_{\tau i}^{kT}[\mathbf{D}_p^T(F_\tau N_i \boldsymbol{I}_3)\mathbf{C}_{pp}^k\mathbf{D}_p(F_sN_j\boldsymbol{I}_3)]\boldsymbol{u}_{sj}^k + \\
&\delta\boldsymbol{u}_{\tau i}^{kT}[\mathbf{D}_p^T(F_\tau N_i \boldsymbol{I}_3)\mathbf{C}^k_{pn}(G_sN_j\boldsymbol{I}_3)+(F_\tau N_i \boldsymbol{I}_3)\mathbf{D}_n^T(G_sN_j\boldsymbol{I}_3)]\boldsymbol{\sigma}^k_{sj}+ \\
&\delta\boldsymbol{\sigma}^{kT}_{\tau i}[(G_\tau N_i \boldsymbol{I}_3)\mathbf{D}_n(F_sN_j\boldsymbol{I}_3)-(G_\tau N_i \boldsymbol{I}_3)\mathbf{C}^k_{np}\mathbf{D}_p(F_sN_j\boldsymbol{I}_3)]\boldsymbol{u}^k_{sj}- \\
&\delta\boldsymbol{\sigma}^{kT}_{\tau i}[(G_\tau N_i \boldsymbol{I}_3)\mathbf{C}^k_{nn}(G_sN_j\boldsymbol{I}_3)]\boldsymbol{\sigma}^k_{sj})\,d\Omega\,dy = \delta\boldsymbol{u}^{kT}_{\tau i}\,\mathbf{P}^k_{\tau i}
\end{aligned}
\qquad (8.17)
$$

where $\boldsymbol{I}_3$ is the 3×3 identity matrix. The right-hand side of this equation is the virtual external work done by a generic load $\mathbf{P}^k_{\tau i} = (P_{x_{\tau i}}\ P_{y_{\tau i}}\ P_{z_{\tau i}})^k$. In compact form, Eq. (8.17) can be expressed as

$$
\delta\boldsymbol{u}^{kT}_{\tau i}[\mathbf{K}^{k\tau sij}_{uu}\boldsymbol{u}^k_{sj}+\mathbf{K}^{k\tau sij}_{u\sigma}\boldsymbol{\sigma}^k_{sj}]+\delta\boldsymbol{\sigma}^{kT}_{\tau i}[\mathbf{K}^{k\tau sij}_{\sigma u}\boldsymbol{u}^k_{sj}+\mathbf{K}^{k\tau sij}_{\sigma\sigma}\boldsymbol{\sigma}^k_{sj}] = \delta\boldsymbol{u}^{kT}_{\tau i}\,\mathbf{P}^k_{\tau i} \qquad (8.18)
$$

where $\mathbf{K}^{k\tau sij}_{uu}$, $\mathbf{K}^{k\tau sij}_{u\sigma}$, $\mathbf{K}^{k\tau sij}_{\sigma u}$ and $\mathbf{K}^{k\tau sij}_{\sigma\sigma}$ are the 3×3 fundamental nuclei of the stiffness matrix of the mixed beam element. The explicit expressions of the components of this arrays are included in the following:

$$
\begin{aligned}
K^{\tau sij}_{uu}(1,1) &= C_{22}I_{ij}\int_\Omega F_{\tau_{,x}}F_{s_{,x}}\,d\Omega + C_{26}I_{i_{,y}j}\int_\Omega F_\tau F_{s_{,x}}\,d\Omega + C_{26}I_{ij_{,y}}\int_\Omega F_{\tau_{,x}}F_s\,d\Omega + \\
&\quad C_{66}I_{i_{,y}j_{,y}}\int_\Omega F_\tau F_s\,d\Omega \\
K^{\tau sij}_{uu}(1,2) &= C_{26}I_{ij}\int_\Omega F_{\tau_{,x}}F_{s_{,x}}\,d\Omega + C_{66}I_{i_{,y}j}\int_\Omega F_\tau F_{s_{,x}}\,d\Omega + C_{12}I_{ij_{,y}}\int_\Omega F_{\tau_{,x}}F_s\,d\Omega + \\
&\quad C_{16}I_{i_{,y}j_{,y}}\int_\Omega F_\tau F_s\,d\Omega \\
K^{\tau sij}_{uu}(1,3) &= 0 \\
K^{\tau sij}_{uu}(2,1) &= C_{26}I_{ij}\int_\Omega F_{\tau_{,x}}F_{s_{,x}}\,d\Omega + C_{12}I_{i_{,y}j}\int_\Omega F_\tau F_{s_{,x}}\,d\Omega + C_{66}I_{ij_{,y}}\int_\Omega F_{\tau_{,x}}F_s\,d\Omega + \\
&\quad C_{16}I_{i_{,y}j_{,y}}\int_\Omega F_\tau F_s\,d\Omega \\
K^{\tau sij}_{uu}(2,2) &= C_{66}I_{ij}\int_\Omega F_{\tau_{,x}}F_{s_{,x}}\,d\Omega + C_{16}I_{i_{,y}j}\int_\Omega F_\tau F_{s_{,x}}\,d\Omega + C_{16}I_{ij_{,y}}\int_\Omega F_{\tau_{,x}}F_s\,d\Omega + \\
&\quad C_{11}I_{i_{,y}j_{,y}}\int_\Omega F_\tau F_s\,d\Omega \\
K^{\tau sij}_{uu}(2,3) &= 0 \\
K^{\tau sij}_{uu}(3,1) &= 0 \qquad K^{\tau sij}_{uu}(3,2) = 0 \qquad K^{\tau sij}_{uu}(3,3) = 0
\end{aligned}
\qquad (8.19)
$$

$$
\begin{aligned}
K_{u\sigma}^{\tau sij}(1,1) &= C_{23}\, I_{ij} \int_{\Omega} F_{\tau_{,x}}\, G_s\, d\Omega + C_{36}\, I_{i_{,y}j} \int_{\Omega} F_{\tau}\, G_s\, d\Omega \\
K_{u\sigma}^{\tau sij}(1,2) &= I_{ij} \int_{\Omega} F_{\tau}\, G_{s_{,z}}\, d\Omega \qquad\qquad K_{u\sigma}^{\tau sij}(1,3) = 0 \\
K_{u\sigma}^{\tau sij}(2,1) &= C_{36}\, I_{ij} \int_{\Omega} F_{\tau_{,x}}\, G_s\, d\Omega + C_{13}\, I_{i_{,y}j} \int_{\Omega} F_{\tau}\, G_s\, d\Omega \\
K_{u\sigma}^{\tau sij}(2,2) &= 0 \qquad\qquad K_{u\sigma}^{\tau sij}(2,3) = I_{ij} \int_{\Omega} F_{\tau_{,z}}\, G_s\, d\Omega \\
K_{u\sigma}^{\tau sij}(3,1) &= I_{ij} \int_{\Omega} F_{\tau_{,z}}\, G_s\, d\Omega \\
K_{u\sigma}^{\tau sij}(3,2) &= I_{ij} \int_{\Omega} F_{\tau_{,x}}\, G_s\, d\Omega \\
K_{u\sigma}^{\tau sij}(3,3) &= I_{i_{,y}j} \int_{\Omega} F_{\tau}\, G_s\, d\Omega
\end{aligned} \tag{8.20}
$$

$$
\begin{aligned}
K_{\sigma u}^{\tau sij}(1,1) &= -C_{23}\, I_{ij} \int_{\Omega} G_{\tau}\, F_{s_{,x}}\, d\Omega + -C_{36}\, I_{ij_{,y}} \int_{\Omega} G_{\tau}\, F_s\, d\Omega \\
K_{\sigma u}^{\tau sij}(1,2) &= -C_{36}\, I_{ij} \int_{\Omega} G_{\tau}\, F_{s_{,x}}\, d\Omega + -C_{13}\, I_{ij_{,y}} \int_{\Omega} G_{\tau}\, F_s\, d\Omega \\
K_{\sigma u}^{\tau sij}(1,3) &= I_{ij} \int_{\Omega} G_{\tau}\, F_{s_{,z}}\, d\Omega \\
K_{\sigma u}^{\tau sij}(2,1) &= I_{ij} \int_{\Omega} G_{\tau}\, F_{s_{,z}}\, d\Omega \\
K_{\sigma u}^{\tau sij}(2,2) &= 0 \\
K_{\sigma u}^{\tau sij}(2,3) &= I_{ij} \int_{\Omega} G_{\tau}\, F_{s_{,x}}\, d\Omega \\
K_{\sigma u}^{\tau sij}(3,1) &= 0 \\
K_{\sigma u}^{\tau sij}(3,2) &= I_{ij} \int_{\Omega} G_{\tau}\, F_{s_{,z}}\, d\Omega \\
K_{\sigma u}^{\tau sij}(3,3) &= I_{ij_{,y}} \int_{\Omega} G_{\tau}\, F_s\, d\Omega
\end{aligned} \tag{8.21}
$$

$$\begin{aligned}
K_{\sigma\sigma}^{\tau sij}(1,1) &= -C_{33} I_{ij} \int_{\Omega} G_\tau G_s d\Omega \\
K_{\sigma\sigma}^{\tau sij}(1,2) &= 0 \\
K_{\sigma\sigma}^{\tau sij}(1,3) &= 0 \\
K_{\sigma\sigma}^{\tau sij}(2,1) &= 0 \\
K_{\sigma\sigma}^{\tau sij}(2,2) &= -C_{44} I_{ij} \int_{\Omega} G_\tau G_s d\Omega \\
K_{\sigma\sigma}^{\tau sij}(2,3) &= -C_{45} I_{ij} \int_{\Omega} G_\tau G_s d\Omega \\
K_{\sigma\sigma}^{\tau sij}(3,1) &= 0 \\
K_{\sigma\sigma}^{\tau sij}(3,2) &= -C_{45} I_{ij} \int_{\Omega} G_\tau G_s d\Omega \\
K_{\sigma\sigma}^{\tau sij}(3,3) &= -C_{55} I_{ij} \int_{\Omega} G_\tau G_s d\Omega
\end{aligned} \tag{8.22}$$

where the $I_{i_{(,y)} j_{(,y)}}$ terms are the integrals of the interpolation functions defined in Eq. (3.38).

Finally, the linear system of the static problem is written as

$$\begin{aligned}
\delta \boldsymbol{u}_{\tau i}^{kT} &: \mathbf{K}_{uu}^{k\tau sij} \boldsymbol{u}_{sj}^{k} + \mathbf{K}_{u\sigma}^{k\tau sij} \boldsymbol{\sigma}_{sj}^{k} = \mathbf{P}_{\tau i}^{k} \\
\delta \boldsymbol{\sigma}_{\tau i}^{kT} &: \mathbf{K}_{\sigma u}^{k\tau sij} \boldsymbol{u}_{sj}^{k} + \mathbf{K}_{\sigma\sigma}^{k\tau sij} \boldsymbol{\sigma}_{sj}^{k} = 0.
\end{aligned} \tag{8.23}$$

8.6 Examples

The capabilities of the proposed beam elements are demonstrated through two numerical examples. The first correspond to the well-known benchmark of Pagano [147], who provided the exact solutions for thick laminates under cylindrical bending. The second considers a composite sandwich beam from the work of Groh and Weaver [83].

8.6.1 Thick laminates

Two thick laminates are chosen first to assess the stress solution. The results are compared against 3D exact solutions of Pagano [147, 148] and several LW and ESL models from the literature. Figure 8.3 shows the features of the numerical case for a thick laminate. The slenderness, L/h, is equal to 4 in all cases. A sinusoidal distributed load of magnitude q_0 is applied along the beam over the top face. The laminate is simply supported and

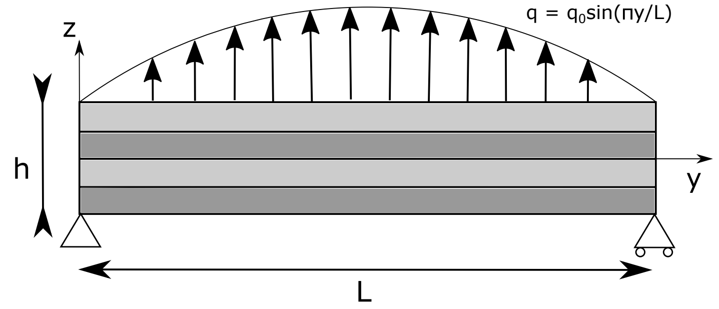

Fig. 8.3 Loading case of the laminates.

cylindrical bending is imposed. Three-layer [0°/90°/0°] and four-layer [0°/90°/0°/90°] stacking sequences are considered. The normalized properties of the ply are:

$$E_1/E_2 = 25,\ G_{12}/E_2 = 0.5,\ G_{23}/E_2 = 0.2,\ \nu_{12} = \nu_{23} = 0.25 \tag{8.24}$$

with $E_2 = 1$ MPa. A number of cubic beam elements are placed along the beam axis and a LW distribution of HLE domains is generated across the thickness.

Table 8.1 Convergence analysis of the beam element discretization based on the maximum transverse displacement $\bar{u}_z = u_z \frac{100 E_2 h^3}{q_0 L^4}$. Number of DOF between parentheses.

Laminate		[0°/90°/0°]			[0°/90°/0°/90°]	
No. elements	1	2	4	1	2	4
HL1	2.636 (96)	2.784 (168)	2.783 (312)	3.829 (120)	4.060 (210)	4.059 (390)
HL2	2.711 (216)	2.864 (378)	2.864 (702)	3.929 (276)	4.167 (483)	4.165 (897)
HL3	2.735 (336)	2.887 (588)	2.887 (1,092)	3.946 (432)	4.182 (756)	4.180 (1,404)
HLM1	2.645 (192)	2.776 (336)	2.790 (624)	4.460 (240)	4.686 (420)	4.709 (780)
HLM2	2.724 (432)	2.861 (756)	2.875 (1,404)	3.995 (552)	4.160 (966)	4.181(1,794)
HLM3	2.735 (672)	2.872 (1,176)	2.886 (2,184)	3.946 (864)	4.159 (1,502)	4.180(2,808)

Table 8.1 shows the convergence of the transverse displacements for an increasing number of beam elements and polynomial orders of the expansion. Solutions based on the PVD are also included. The verification with references from the literature is shown in Table 8.2. It is possible to conclude that the convergence in terms of the LW transverse approximation is rather fast, showing that the HLM2 and HLM3 models compute similar values. Figures 8.4, 8.5 and 8.6 show the solutions of longitudinal, transverse normal and transverse shear stresses, respectively, of the symmetric laminate. The reference solutions of these graphs are extracted from Carrera and Demasi [32] and are based on 2D finite elements. The results are presented in normalized form according to the following criteria:

$$\bar{u}_y = u_y \times E_2/(q_0 h) \quad \bar{\sigma}_{yy} = \sigma_{yy}/q_0 \quad \bar{\sigma}_{zz} = \sigma_{zz}/q_0 \quad \bar{\sigma}_{yz} = \sigma_{yz}/q_0 \tag{8.25}$$

Table 8.2 Maximum transverse displacement, $\bar{u}_z = u_z \frac{100E_2h^3}{q_0L^4}$, at $z = 0$ of the thick laminates considered.

Model	Description	[0/90/0]	[0/90/0/90]
Elasticity	Solutions from Pagano's theory [148]	2.887	4.181
HOT	Higher-order theory by Lo *etal*. [120]	2.687	3.587
EMZC1	First-order ESL mixed model with ZZ effects by Carrera [26]	2.904	3.300
EMZC2	Second-order ESL mixed model with ZZ effects by Carrera [26]	2.831	3.478
EMZC3	Third-order ESL mixed model with ZZ effects by Carrera [26]	2.881	4.102
LWM4	Fourth-order LW mixed model by Carrera [26]	2.887	4.181
ESLM1	Third-order ESL model by Cho and Parmerter [47]	-	4.083
M-p	Parabolic LW mixed model by Carrera [25]	2.891	4.181
D-p	Parabolic LW displacement-based model by Carrera [25]	2.870	4.164
	Proposed LW models (four cubic beam elements)		
HLM1	First-order HLE mixed model	2.790	4.709
HLM2	Second-order HLE mixed model	2.875	4.181
HLM3	Third-order HLE mixed model	2.886	4.180

The solutions of the anti-symmetric laminate are shown in Fig. 8.7, 8.8 and 8.9, accounting for normalized longitudinal displacements, transverse normal stresses and transverse shear stresses, respectively. The reference solutions are extracted from Carrera [25], where (M) refers to stresses computed *a priori*, (3D) corresponds to stresses obtained *a posteriori* through integration of the 3D elasticity equilibrium equations, and (H) refers to stresses obtained through the Hooke's law. The solutions of the first-order (HL1) and second-order (HL2) beam models based on the PVD, are also included in Fig. 8.9 (b) for comparison purposes.

The following observations can be made from these results:

- Both the ZZ and IC effects are fulfilled in all cases of mixed models, even when low-order expansions are employed. Indeed, one can notice that RMVT-based models provide always continuous solutions of the transverse stresses at the interface between layers independently of the accuracy of the stress fields.

- The PVD-based models cannot satisfy the C_z^0-Requirements and show highly discontinuous values of the interlaminar stresses, see Fig. 8.9 (b).

- The ESL models from the references (EMZC3 in Fig. 8.6 and ESLM1 in Fig. 8.9 (a)) provide a good global approximation of the transverse stresses but fail in capturing the actual distribution at the interfaces, which mostly depend on the sudden changes in the material properties. In particular, the EMZC3 model, which makes use of the Murakami's ZZ function [132], overestimates σ_{zz} towards the central ply of the

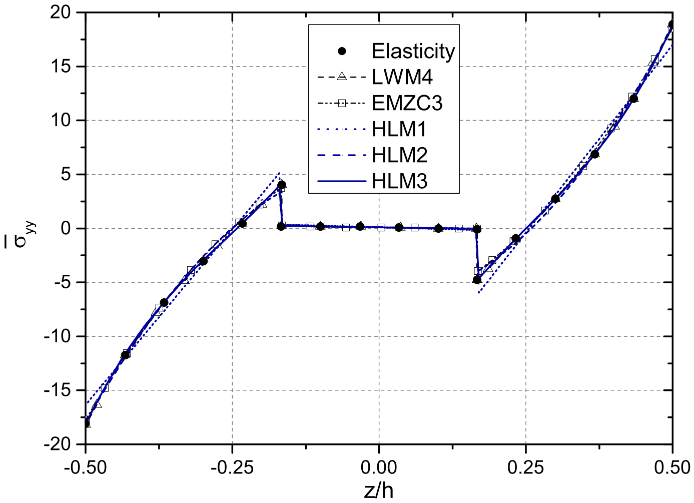

Fig. 8.4 Longitudinal stress of the symmetric 3 layer laminate at *y*=*L/2*. References from [32].

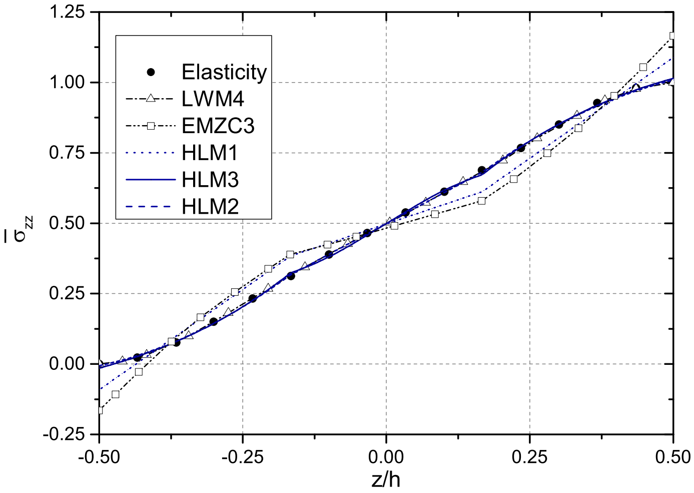

Fig. 8.5 Transverse normal stress of the symmetric 3 layer laminate at *y*=*L/2*. References from [32].

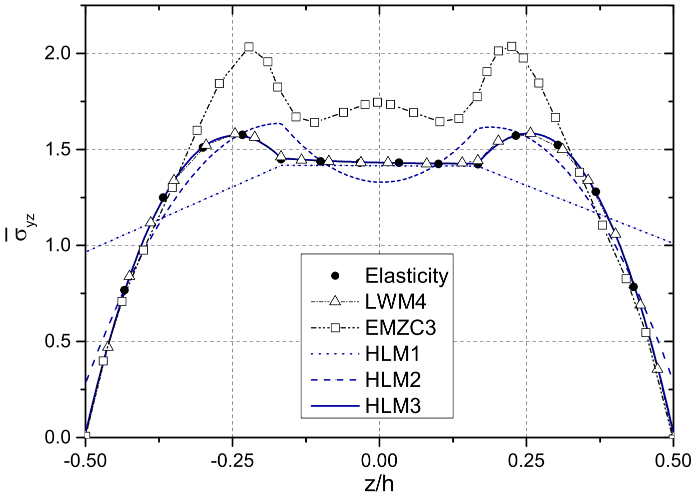

Fig. 8.6 Transverse shear stress of the symmetric 3 layer laminate at *y=0*. References from [32].

[0°/90°/0°] laminate, and ESLM1 does not capture the high gradients of the stresses in the 0° ply of the [0°/90°/0°/90°] beam.

- LW models are recommended when high levels of precision in the mechanical solutions are required at the meso-scale. One can observe that by increasing the polynomial order of the stress fields in the mixed models, the transverse stress solutions converge to the 3D elasticity solutions. The second-order mixed model (HLM2) provides acceptable results in terms of transverse stresses, although the stress boundary conditions at top and bottom faces are not fully satisfied, see Fig.8.6 for instance.

Finally, in order to fully exploit the features of the proposed model, the zero values of the transverse stresses at top and bottom faces are imposed via stress boundary conditions (SBC). The results are included in Fig. 8.10. Remarkably, a huge improvement can be observed for both the first and second-order models. The linear model (HLM1 SBC) provides fairly accurate transverse shear stresses, which are exactly zero at the free faces and piece-wise continuous through the stacking sequence. Moreover, the quadratic model (HLM2 SBC) shows now a very good agreement with respect to the elasticity solution.

8.6.2 Composite sandwich

The second example considers a symmetric sandwich beam with cross-ply skins. The features of the cases and the material properties are taken from the work of Groh and Weaver [83]. The skins are made of carbon-fiber (cf) and the core is made of a symmetric sequence of polyvinyl chloride foam (pvc) and honeycomb (hc). The stacking sequence of the sandwich

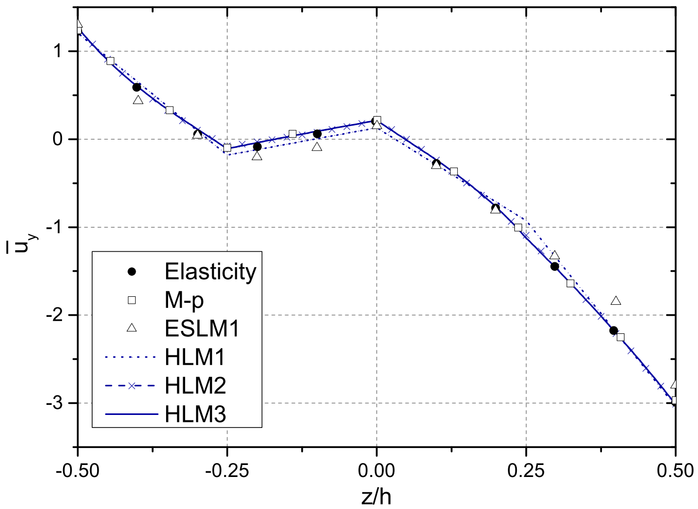

Fig. 8.7 Longitudinal displacements of the anti-symmetric laminate at *y=0*. References from [25].

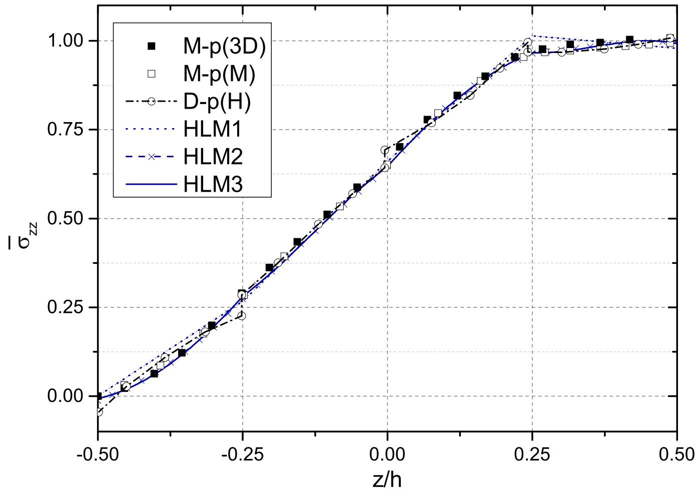

Fig. 8.8 Transverse normal stress of the anti-symmetric layer laminate at *y=L/2*. References from [25].

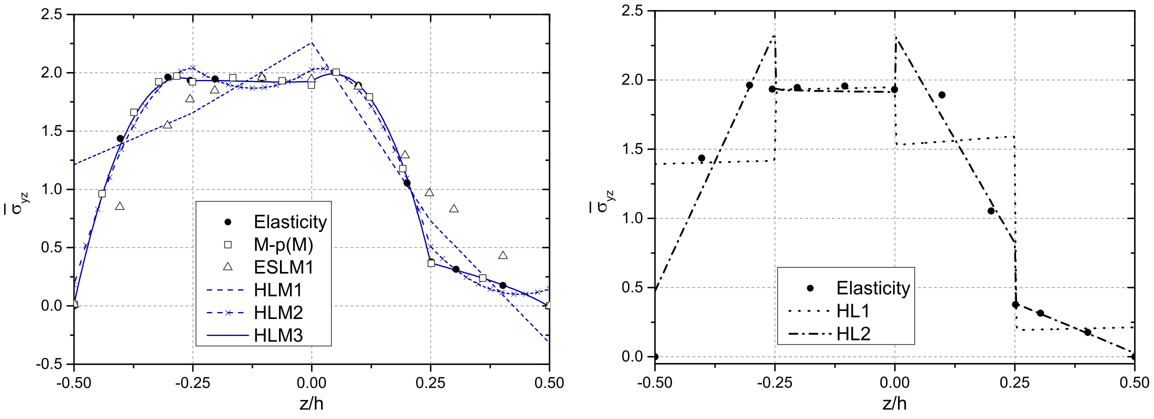

(a) RMVT (b) PVD

Fig. 8.9 Transverse shear stress of the anti-symmetric layer laminate at *y=0*. References from [25].

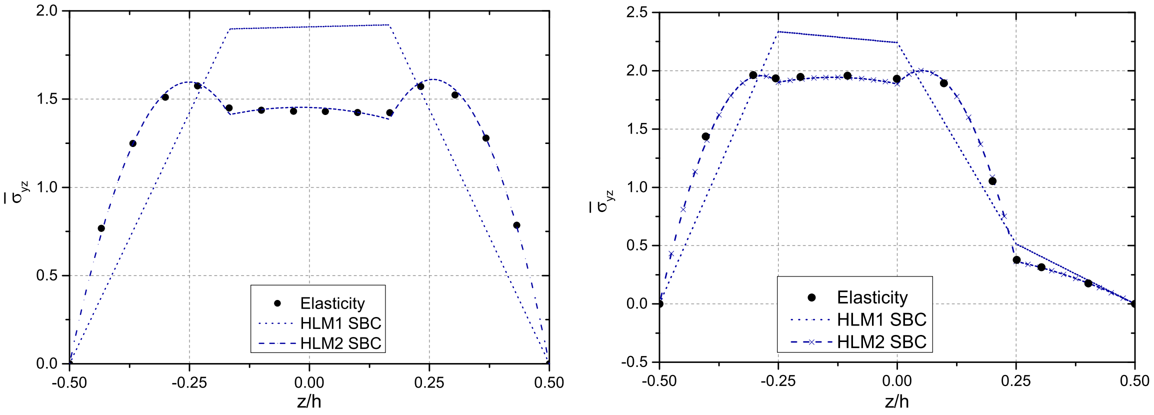

(a) Symmetric laminate (b) Anti-symmetric laminate

Fig. 8.10 Transverse shear stresses of the [0/90/0] and [0/90/0/90] laminates with imposed stress-free boundary conditions. References from [25].

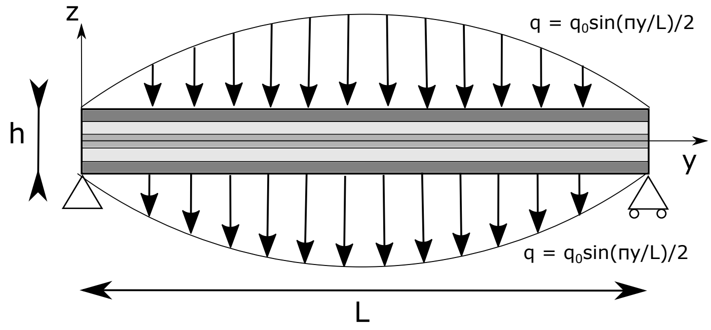

Fig. 8.11 Loading case of the composite sandwich.

is [cf$_{90}$/cf$_0$/pvc/hc/pvc/cf$_0$/cf$_{90}$], where the subindexes 0 and 90 refer to the fiber angle with respect to the y-axis. The geometry and loading case are illustrated in Fig. 8.11. Table 8.3 shows the material properties of the constituents normalized with respect to the shear moduli of the honeycomb, $G_{12}^{(hc)}$. The relative thickness of each layer is [0.1/0.1/0.2/0.2/0.2/0.1/0.1] and the slenderness ratio L/h is equal to 8. According to the authors of the original work [83], this particular numerical case represents a challenging test for structural models due to the high transverse anisotropy of the materials that compose the sandwich structure, which maximizes the ZZ effects, and the fact that externally weak layers (cf$_{90}$) are placed at top and bottom faces. Distributed sinusoidal loads of a single wave and magnitude $q_0/2$ are applied downwards in correspondence with the top and bottom faces and plane stress assumptions are imposed.

Table 8.3 Mechanical properties of the materials for the composite sandwich example. The values of Young's moduli and shear moduli are normalized with respect to G_{12} of the honeycomb (hc).

Material	E_1	E_2	E_3	G_{12}	G_{13}	G_{23}	ν_{12}	ν_{13}	ν_{23}
cf	25×10^6	1×10^6	1×10^6	5×10^5	5×10^5	2×10^5	0.25	0.25	0.25
pvc	25×10^4	25×10^4	25×10^4	9.62×10^6	9.62×10^6	9.62×10^6	0.3	0.3	0.3
hc	250	250	2500	1	875	1750	0.9	3×10^{-5}	3×10^{-5}

Figures 8.12, 8.13 and 8.14 show the distribution of stress fields across the thickness of the multilayered beam. The solutions from the reference paper correspond to a refined zig-zag theory inspired on the work of Tessler *et al.* [193] and are based upon the Hellinger-Reissner variational principle (HR-RZT), a modified third-order theory accounting for zig-zag effects (MRZZ) and RMVT-based zig-zag model (RMVT-RZT). The 3D elasticity solutions of Pagano [147] are also included. All the reference data has been extracted directly from the published graphs. As for the previous numerical examples, four cubic beam elements are

used along the longitudinal direction and each layer of the sandwich is represented by a single HLE domain.

Table 8.4 Normalized solutions of the maximum axial and transverse shear stresses. All the references are obtained from [83].

Model	Description	$\bar{\sigma}_{yy} \times \frac{h^2}{L^2}$	$\bar{\sigma}_{yz}$	DOF
Elasticity	Solutions from Pagano's theory	6.342	5.697	-
MRZZ	Modified Reddy's third-order theory with ZZ function	6.369	2.170	-
HR-RZT	Hellinger-Reissner principle with refined ZZ function	6.343	5.702	-
RMVT-RZT	RMVT principle with refined ZZ function	6.346	5.530	-
HLM1	First-order mixed HLE model	6.270	5.611	1,248
HLM2	Second-order mixed HLE model	6.352	5.639	2,964
HLM3	Third-order mixed HLE model	6.350	5.642	4,680

The results show that the proposed LW mixed beam model is able to provide acceptable solutions already for the second-order model (HLM2) and the converge to the 3D elasticity for the third-order model (HLM3). Although the HLM1 model computes accurate axial stress distributions, one can observe that the solutions for the transverse stresses oscillate around those of the elasticity theory, being this effect more evident towards the external layers. In view of the results, it is possible to state that the use of independent LW assumptions for displacements and stresses has proven to be a suitable choice for the accurate computation of the stress solutions in generic laminated structures, at the expense of extra degrees of freedom for the transverse stress fields.

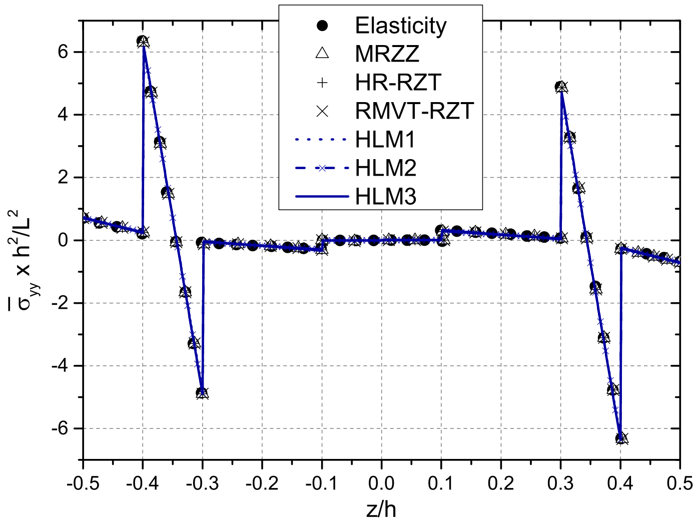

Fig. 8.12 Longitudinal stress of the composite sandwich at $y = L/2$. References from [83].

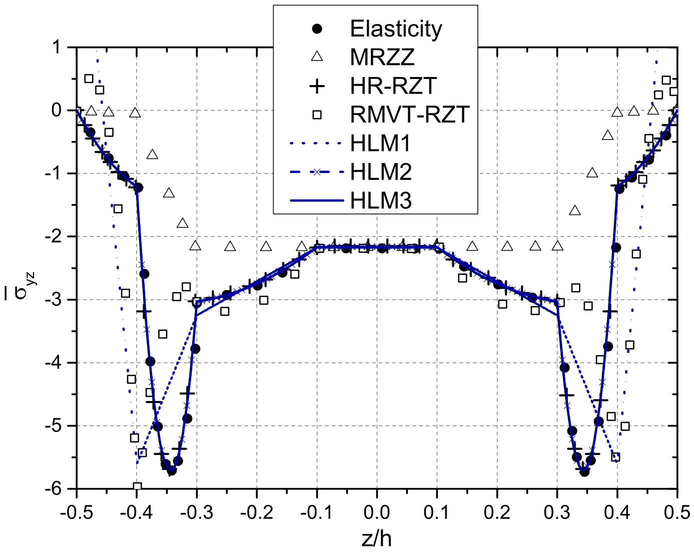

Fig. 8.13 Transverse shear stress of the composite sandwich at $y = 0$. References from [83].

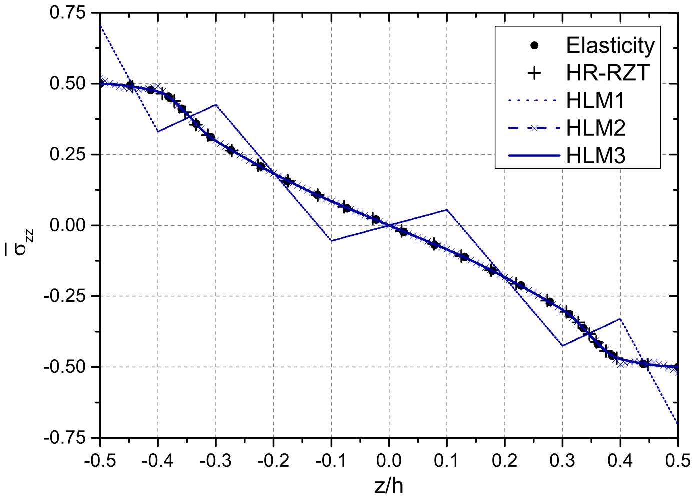

Fig. 8.14 Transverse normal stress of the composite sandwich at $y = 0$. References from [83].

Chapter 9

Free-edge analysis

The increasing adoption of composite laminates in the construction of new lightweight structures demands a comprehensive knowledge of their mechanical response at different scales. Unlike traditional thin-walled metallic structures, laminates are inherently heterogeneous and feature abrupt changes of the material properties through the thickness, see the book of Jones [97]. Although this allows for the optimization of the material to a desired performance, it also provokes some unwanted effects such as stress concentrations in holes, joints and free edges, that must be fully understood for the safe deployment of composite parts. The study of this phenomena demands a very high resolution from the numerical model, which usually is obtained in two manners: reducing the dimension of the problem by imposing strong physical constraints, such as plain strain assumptions, or increasing the computational expenses by refining the mesh in the critical areas. This chapter proposes the use of higher-order beam elements to reduce drastically the computational expenses of the free-edge analysis in generic laminated problems.

9.1 The free-edge problem in the literature

The so-called free-edge effects refer to singular stress states that arise at the interfaces between dissimilar layers in the vicinity of geometrical or mechanical discontinuities in the structure. An illustration of the free-edge effects in typical composite beams is shown in Fig. 9.1. The classical laminate theories cannot provide any useful information of the free-edge effects, therefore specific models continue to be developed for the understanding of the mechanics of this complex problem. The first studies addressing the topic were carried out by Hayashi [89] and Puppo and Evensen [161]. Then, in 1970 Pipes and Pagano [157] provided the first approximation of the 3D stress fields at the free edges. The latter work was followed by numerous studies, which have made the literature rich in analytic and numerical solutions

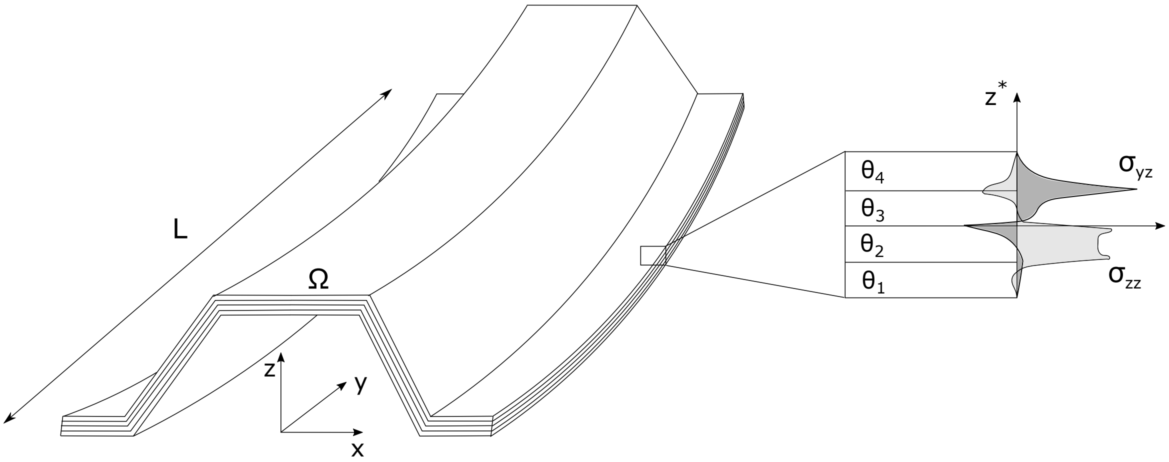

Fig. 9.1 Free-edge stresses in generic composite beams.

dedicated to the free-edge problem, see the review of Mittelstedt and Becker [129]. However, given the high complexity and singular nature of the interlaminar stress fields, no exact elasticity solution is available and there is an active interest on the development of robust tools that predict accurately these stress concentrations. In most studies, the benchmark example is that defined in [157], which addresses a symmetric cross-ply laminate of infinite length loaded under uniaxial extension. In that case, the solutions become independent of the longitudinal direction and the problem is reduced to the section domain.

Physically, the appearance of stress peaks in the free edge can be explained as follows: due to the Poisson effect and the diverse elastic moduli of the orthotropic material, the plies tend to behave differently in the in-plane direction. Subsequently, in order to satisfy the compatibility of the displacements at the interfaces, transverse shear stresses appear in a small zone near the free edge and, consequently, the fulfillment of the equilibrium conditions lead to the development of a full 3D state of stress, as illustrated in Fig 9.1. A correct evaluation of these stresses, which can lead to the onset of delamination, becomes then necessary for the design of composite structures. An overview of some of the most relevant solutions of the free-edge problem which are available in the literature is included in the following.

Since the initial investigations of the free edge problem, many close-form approaches have followed focusing on the accurate approximation of the stress fields. As an extension of their early research, Pipes and Pagano [158] proposed an approximate elasticity solution using a Fourier series for the displacements. Then, Pagano [149] employed a modified version of the higher-order theory of Whitney and Sun [209] to provide an analytic solution of the interlaminar normal stresses in symmetric composite laminates. Kassapoglou and Lagace [102] used the force balanced method and the principle of minimim complementary energy to solve the interlaminar stresses in angle-ply and cross-ply laminates. Becker [15] introduced a single-layer higher-order theory with a warping mode in the free-edge area. The stress functions of Lekhnitskii [114] were employed by Yin [216] to develop a stress-based layerwise model for the evaluation of the interlaminar stresses in a laminate strip under combinations of extension, bending and twisting. Tahani and Nosier [191] presented a displacement-based analytical solution of uniformly loaded composite laminates based on the layerwise theory of Reddy [167]. An approximate stress function was introduced by Flanagan [77] using an expansion of harmonic terms in the thickness direction and the principle of minimum complimentary energy. An iterative method to solve the free-edge stresses based on the extended Kantorovich method was employed by Cho and Yoon [48] for uniaxial extension. In a further development, Cho and Kim [46] extended the method to study also bending, twisting and thermal loads. More recently, Dhanesh et al. [65] introduced the mixed-field multiterm Kantorovich method using the Reissner's mixed variational theorem [173] to satisfy all boundary conditions at the free-edges and the interlaminar continuity.

Numerical approaches have also been introduced to provide the 3D stress solutions at the free edges. Among these, an special mention must be devoted to the pioneering work of Pipes and Pagano [157], who used the finite difference method (FDM) to compute the 3D displacements and stresses in symmetric laminates. In the following years, the FEM was employed in most of the works on free-edge due to its availability and versatility, commonly to generate 2D plane strain models. Wang and Crossman [204] made an study of the interlaminar singularities in symmetric laminates using three-node elements with a mesh refinement in the free-edge zone. Whitcomb et al. [208] performed an extensive study on the reliability of the FEM for the study of stress singularities using eight-node elements, reporting that the stress solutions obtained are accurate except for the two elements in the vicinity of the singularity. Although computationally more expensive, 3D solid elements have also been employed to solve the free-edge problem by Raju and Crews [162] and Lessard et al. [116], among others. Recenly, Martin et al. [127] compared the accuracy of 2D and 3D finite elements for the onset of delamination due to shear in angle-ply laminates.

Non-traditional FE models based on plate/beam theories of structures have also been used to obtain 3D stress fields at the free-edge. Robbins and Reddy [175] implemented a higher-order LW plate element to study 3D-like localized effects in composite laminates, showing interesting advantages in comparison to 3D solid models, such as faster element stiffness integration and simplified input requirements. D'Ottavio et al. [67] proposed a number of displacement-based and mixed plate elements with higher-order kinematics for the study of the interlaminar stresses at the free-edges. Vidal et al. [201] used the proper generalized method to split the problem in the 2D in-plane domain, modeled via eight-node elements, and a 1D analysis on the thickness direction, represented by a layerwise fourth-order expansion.

In a recent publication, Peng et al. [154] employed the mechanics of structure genome (MSG) to study the free-edge effects in composite beams featuring generic laminations via a refined cross-sectional analysis.

9.2 High-fidelity beam models for free-edge analysis

Many displacement-based theories of structure are available for the study of the mechanical response of laminated structures. As introduced in Chapter 6, the multi-layered theories are divided in equivalent-single layer (ESL), in which the displacement assumptions are taken for the whole thickness of the laminate, and layer wise (LW), in which independent assumptions are made for each layer. ESL theories are very attractive due to their lower computational costs and they are extensively employed by engineers to acquire information about the global response of the composite structure. However, these theories, which in most cases make use of C^1 kinematics across the stack of plies, are not suitable to provide accurate 3D stress fields at the ply level, specially in thick laminates, or in particularly complex zones, such as open holes or free-edges.

Despite the higher computational demands, LW models provide more information of the meso-scale effects by accounting for the deformation of each ply independently. In this class of theories, the C^0 continuity of the displacements is imposed at the interfaces between layers. By taking displacement assumptions at the ply-level, LW models are able to capture the zig-zag effect of the displacements in the thickness direction, which is strongly related to the complex distribution of transverse stresses in composite laminates, as noted by Carrera [23].

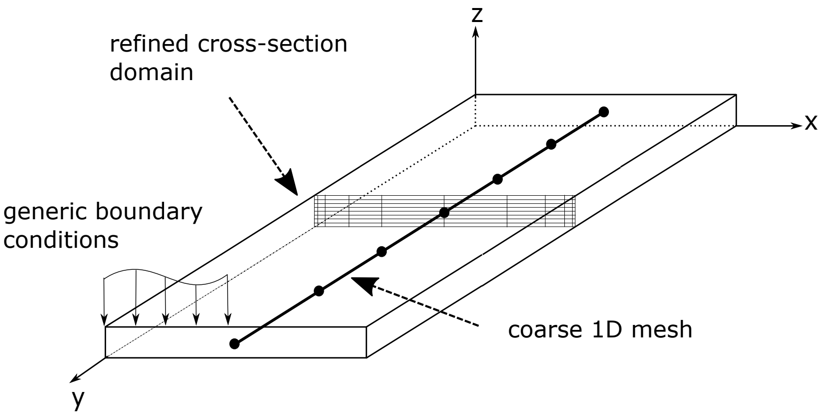

Fig. 9.2 Representation of the FEM modeling of composite laminates using CUF elements.

Free-edge effects in laminates are confined in a small zone whose size is directly proportional to the thickness of the laminate, as reported in the experimental work of Pipes

[159]. Subsequently, for the accurate damage analysis of laminated structures, a refinement of the model is required towards the free edge, see for instance the works of Wang and Crossman [204], Martin et al. [127] and Saeedi et al.[177]. Using CUF beam models, these refinements can be allocated to the cross-section domain without affecting the discretization along the longitudinal axis, which is generated to satisfy the global boundary conditions. In such manner, one has in hand a model which is based on the FEM and therefore can deal with generic boundary conditions, but is not affected by the aspect ratio constraints of the 3D elements. Figure 9.2 illustrates the modeling technique for the free-edge analysis of laminated coupons. Note that the cross-section is discretized with LE or HLE refinements towards the lateral edges, whereas the longitudinal mesh remains coarse.

9.3 Failure criteria

The possibility of obtaining the 3D stress fields over the whole laminate with reduced computational costs enables it to perform advanced failure evaluations of the structure very efficiently. In this manner, one can produce preliminary information about which are the most critical laminations regarding the free-edge stresses. In other words, for a given laminate, which are the stacking sequences that are most prone to delaminate. This kind of solutions might be extremely useful as a support for the testing campaigns in the design of composite structures, for instance allowing engineers to discard certain sequences for the experimental tests, thus saving time and cost in the research process.

The Hashin 3D criteria [86] is chosen here to compute the failure indexes in laminated coupons. This method was introduced as a 3D failure criteria for unidirectional fiber-reinforced laminates and is based on the use of quadratic stress functions and the allowables of transverse isotropic materials. Accordingly, four different failure modes are obtained:

- Fibre Tension:

$$\left(\frac{\sigma_{11}}{X_T}\right)^2 + \frac{\sigma_{12}^2 + \sigma_{13}^2}{S_{12}^2} \geq 1 \tag{9.1}$$

- Fibre Compression:

$$\left(\frac{\sigma_{11}}{X_C}\right)^2 \geq 1 \tag{9.2}$$

- Matrix Tension:

$$\frac{(\sigma_{22} + \sigma_{33})^2}{Y_T^2} + \frac{\sigma_{23}^2 - \sigma_{22}\sigma_{33}}{S_{23}^2} + \frac{\sigma_{12}^2 + \sigma_{13}^2}{S_{12}^2} \geq 1 \tag{9.3}$$

- Matrix Compression:

$$\left[\left(\frac{Y_C}{2S_{23}}\right)^2-1\right]\left(\frac{\sigma_{22}+\sigma_{33}}{Y_C}\right)+\frac{(\sigma_{22}+\sigma_{33})^2}{4S_{23}^2}+\frac{\sigma_{23}^2-\sigma_{22}\sigma_{33}}{S_{23}^2}+\frac{\sigma_{12}^2+\sigma_{13}^2}{S_{12}^2}\geq 1 \tag{9.4}$$

where σ_{ij} are the stress components expressed in the material coordinate system. Note that for clarity reasons, the classical notation is used here for the definition of the material directions, i.e. 1 for the fiber direction, 2 for the in-plane normal, and 3 for the out-of-plane direction. X and Y are the material allowances in the fiber and transverse directions, T under tension and C under compression. S_{ij} are the shear strengths.

On the other hand, the onset of delamination is computed using the mixed mode quadratic criterion [21], which reads:

$$\left(\frac{<\sigma_{33}>}{Z_T}\right)^2+\left(\frac{\sigma_{23}}{S_{23}}\right)^2+\left(\frac{\sigma_{13}}{S_{13}}\right)^2\geq 1 \tag{9.5}$$

where $<\sigma_{33}>$ is equal to $max(0,\sigma_{33})$ and Z_T is the interlaminar normal strength.

9.4 Examples

The numerical assessment is conducted via two examples. The first is the well-known benchmark case of Pipes and Pagano [157], which is included here to to verify the RMVT-based elements and to perform the convergence analyses. The second shows the application of displacement-based beam elements for the advanced failure indexing of generic laminates.

9.4.1 Pipes-Pagano problem

The numerical test considers an infinitely long symmetric laminate made loaded under tension. The stacking sequence is $[45,-45]_S$ with all the layers of equal thickness and material properties $E_1 = 137.9$ GPa, $E_2 = E_3 = 14.5$ GPa, $G_{12} = G_{13} = G_{23} = 5.9$ GPa and $\nu_{12} = \nu_{13} = \nu_{23} = 0.21$. The section is rectangular with the width-to-thickness ratio, $b/h = 4$, equal to 4. A global strain of magnitude $\varepsilon_{yy} = \varepsilon_0 = 0.01$ is applied. The model characteristics are illustrated in Fig. 9.3. Ten cubic mixed elements based on the RMVT (see Chapter 8) are employed for the finite element discretization along the beam axis and a slenderness ratio of $L/b = 20$ is considered in order to satisfy the length requirements.

The discretization of the cross-section is shown in the right side of Fig. 9.3. As mentioned throughout this thesis, one of the advantages of HLE models in composite simulation is that

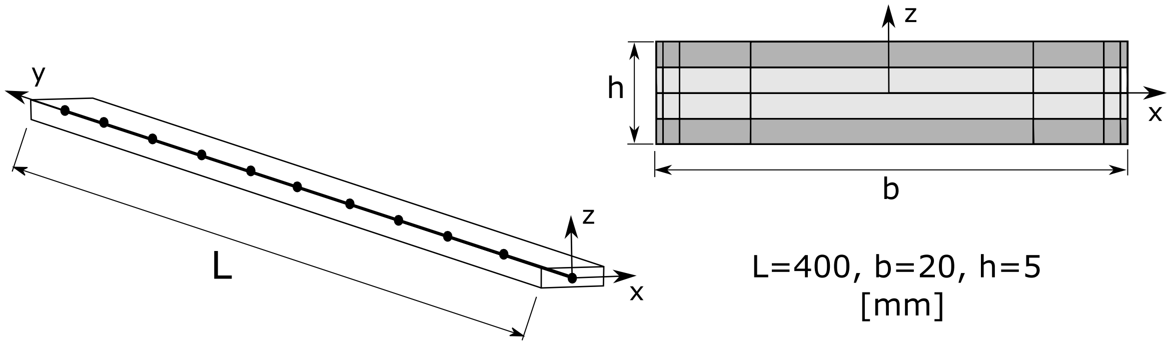

Fig. 9.3 Geometry and mesh of the laminated beam under axial extension.

an arbitrary distribution of the expansion domains can be selected to represent the cross-section surface, allowing the user to refine the kinematics of the beam model in the critical zones such as free-edges. The mesh of the model is fixed and the accuracy is improved via the polynomial order. The number of DOF of each model is enlisted in Table 9.1.

Table 9.1 Pipes and Pagano's problem: DOF of each HLE mixed model.

Model	DOF
HLM1	6,720
HLM2	17,976
HLM3	29,232
HLM4	45,192
HLM5	65,856

Figure 9.4 shows the interlaminar shear stresses at $y = L/2$. One can notice that the approximated elasticity solutions of Pipes and Pagano [158] are properly represented if a sufficiently high polynomial order is employed for the stress assumptions over the section (HLM4 and above). The free-edge stresses are also in good agreement with the FEM solution obtained by Wang and Crossman [204]. Figure 9.5 includes the shear stress distribution across the thickness of the laminate at the free edge for different mixed and displacement-based HLE models. The FEM solution of [204] and a close-form solution by Dhanesh *et al.* [65], based on the extended mixed-field Kantorovic method, are included for comparison. Finally, the dependency between the width of the free-edge zone with the thickness of the laminate is highlighted in Fig. 9.6. The fourth-order model (HLM4) is used for three different thicknesses, h, $h/2$ and $h/3$, showing how the width of the free-edge zone diminishes for thinner laminates. Indeed, it can be observed that the 3D stress fields appear in a zone of the same magnitude of the total thickness, as reported in [158].

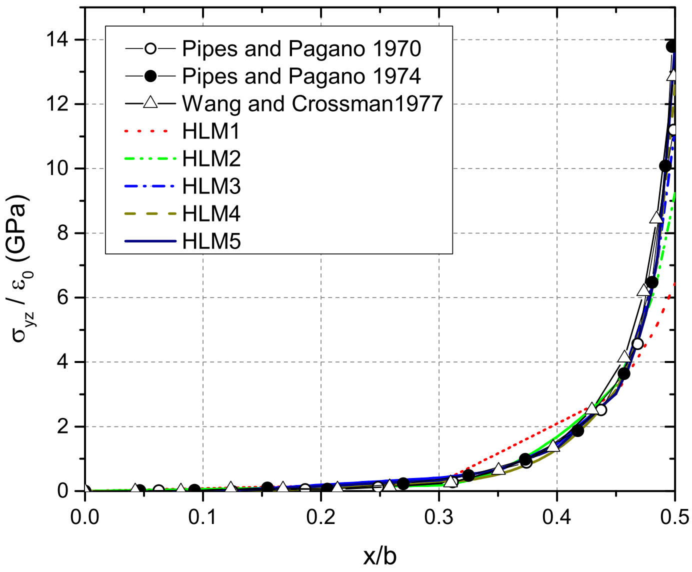

Fig. 9.4 Transverse shear stresses along x at $y = L/2$ and $z = h/4$ computed via HLE mixed models.

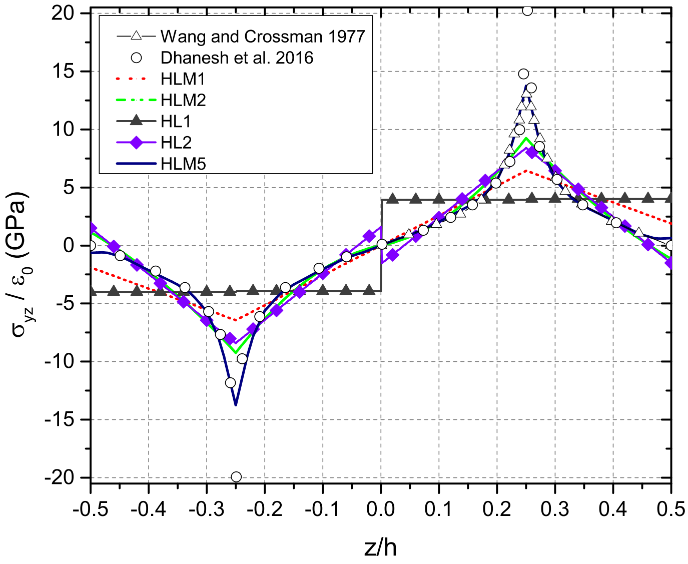

Fig. 9.5 Transverse shear stresses along z at $y = L/2$ and x=$b/2$ computed via HLE mixed models.

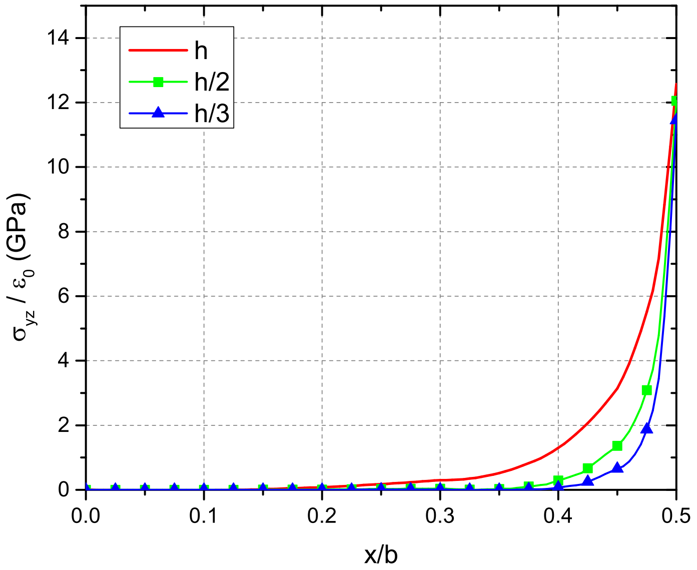

Fig. 9.6 Transverse shear stresses along x computed by the HLM4 model for different thicknesses computed via HLE mixed models.

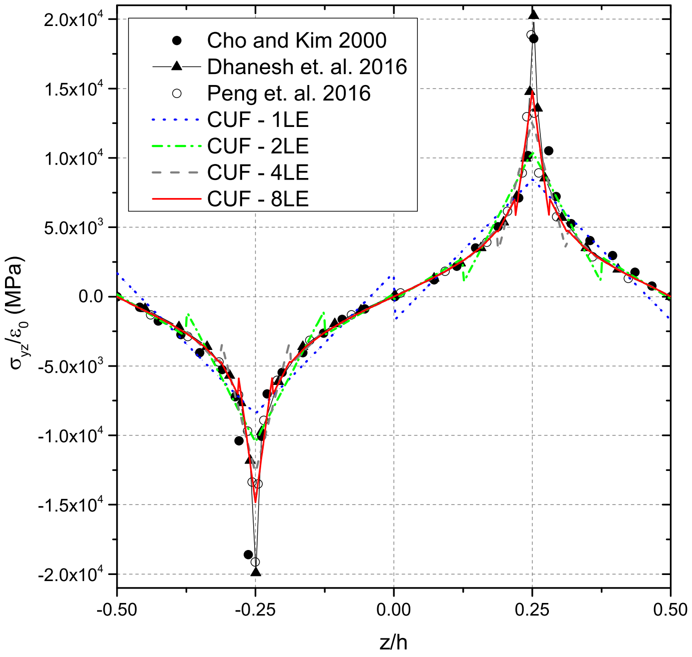

Fig. 9.7 Transverse shear stresses along z at $x = b/2$ computed via displacement-based LE models.

The same analysis is done employing displacement-based elements and LE quadratic theories. Therefore, the improvement of the stress fields is sough via *h*-refinement of the cross-section discretization. Figure 9.7 includes the solutions of the transverse shear stresses along *z* for an increasing number of mathematical layers per physical ply, from 1 to 8. It is possible to observe that the equilibrium conditions are not satisfy a priori, although the error diminishes as the model is refined.

9.4.2 Failure evaluation of tensile specimen

The failure index evaluation of a tensile specimen is carried out to show the capabilities of the formulation in more realistic applications. The studied laminate is a balanced and symmetric cross-ply based on the ASTM 3039 [2] recommendations. The material system is the IM7/8552, see Table 9.2, and the stacking sequence is [45°, -45°, 90°, 0°]$_s$. The dimensions of the model are: $L = 200$ mm, $b = 25$ mm and $h = 2.54$ mm, with the thickness of each lamina being equal to $h_0 = 0.3175$ mm. A schematic representation of the specimen and the boundary conditions are given in Fig. 9.8. On one end (y = 0), the displacements in the *y* and *z* directions were constrained, while in the other (y = L) simply-supported conditions were applied on the *z* direction.

Table 9.2 Mechanical properties of the IM7/8552 lamina.

Material	E_1 [GPa]	E_2 [GPa]	E_3 [GPa]	G_{12} [GPa]	G_{13} [GPa]	G_{23} [GPa]	ν_{12}	ν_{13}	ν_{23}
IM7/8552	165.0	9.0	9.0	5.6	5.6	2.8	0.34	0.34	0.5

Table 9.3 Material strength values of the IM7/8552 lamina.

Failure criteria	Z_t [MPa]	S_{13} [MPa]	S_{23} [MPa]	X_t [MPa]	Y_t [MPa]	S_{12} [MPa]
Mixed mode delamination	60.0	90.0	90.0			
Hashin 3D	73.0	90.0	57.0	2,560.0	73.0	90.0

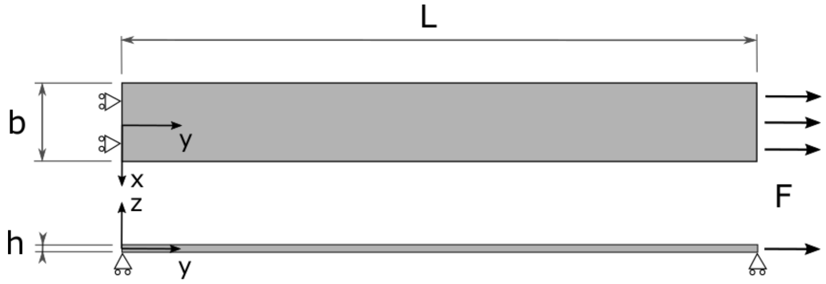

Fig. 9.8 Dimensions and loading conditions of the tensile specimen

The main aim of the present study is to demonstrate the efficiency LW beam models in comparison with solid models generated in ABAQUS. The stress solutions of the proposed model were evaluated at relevant points through the thickness within the structure, along with a mesh convergence study; center of the beam (x = 0.0, y = L/2), and free-edge at the mid-span (x = 12.5, y = L/2). In the analysis, attention was paid to the out-of-plane stress components, which directly influence the onset of failure in composite materials. The model data and computational times for both LW and solid models are tabulated in Table 9.4. Figure 9.9 shows the (a) normal and (b) shear stress distributions over the thickness at the free-edge for an axial force of magnitude $F = 6,350$ N. It is noticeable how the stress solutions computed via 3D elements evolve towards those of the LE models as the number of elements in the thickness increases.

Table 9.4 Model discretizations for the tensile specimen.

Model	Discretization*	DOF	CPU Time [s]
CUF-LW	320 L9 over the cross-section, 6 B4 along y.	77,805	82
ABQ3D-Coarse	30 x 8 x 200 linear elements, 1/layer.	168,237	27
ABQ3D-Medium	30 x 24 x 200 linear elements, 3/layer.	467,325	261
ABQ3D-Refined	70 x 40 x 400 linear elements, 5/layer.	3,501,933	3526

*All discretizations are graded towards the free-edges

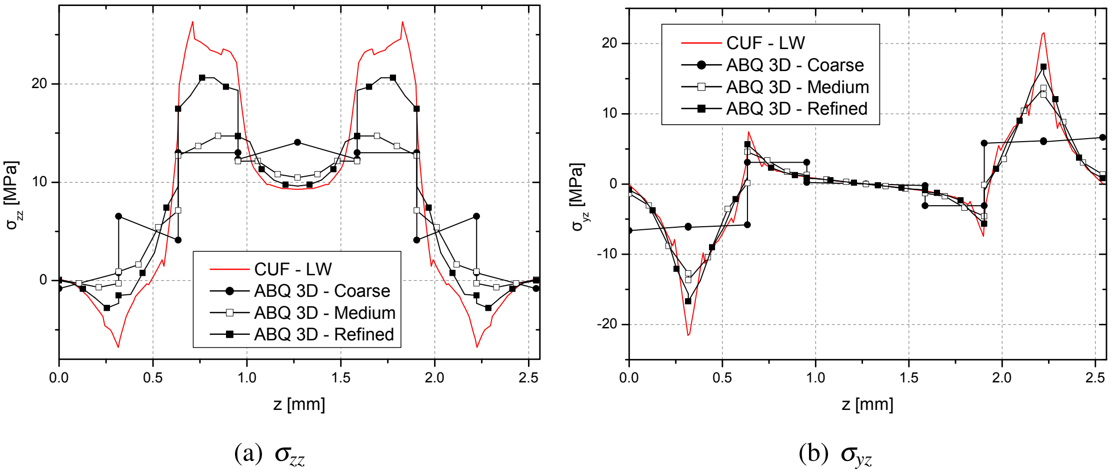

(a) σ_{zz} (b) σ_{yz}

Fig. 9.9 Out-of-plane stress components at the free-edge.

The three predominant failure modes which typically appear in tensile tests are investigated: delamination onset, matrix failure, and fiber failure. Tables 9.5 and 9.6 summarize the results of the present example. The former shows the failure indexes computed by the solid models for the onset load of the CUF-LW model, which is shown in the head. In other words, the failure indexes computed for those loads. The latter includes the tensile loads of the initial failure for each mode. Figures 9.10-9.13 show the contour plots of the failure indexes for the CUF-LW and the finest solid model. It is possible to note that in the fiber tension mode, Fig. 9.12, the model shows fiber failure at the interfaces towards in the free-edge. This non-physical result is due to the high interlaminar shear stresses shown in Fig. 9.9, which are included in the failure criteria, Eq. 9.1. In order to avoid this effect, the criterion is modified to neglect the transverse shear stresses, σ_{13}. The new results are shown in Fig. 9.13. It is also worth noting that all these solutions are computed in a linear framework, therefore all the failure onsets are independent of each other.

Table 9.5 Comparison of the failure indices computed by the different models considered under the same loading value

Mode		Delamination	Matrix Tension	Fibre Tension	Fiber Tension*
Load [N]		14,287.5	11,938.0	27,178.0	34,417.0
Model	DOF	Failure index value			
ABQ3D coarse	168,237	0.28	0.4	0.7	1.07
ABQ3D medium	467,325	0.31	0.45	0.71	0.94
ABQ3D refined	3,501,933	0.6	0.73	0.82	1.05
CUF-LW	77,805	1	1	1	1

*Modified Hashin 3D criteria with only in-plane components

Table 9.6 Values of the tensile load corresponding to the onset of failure of each mode considered

Mode	DOF	Delamination	Matrix Tension	Fibre Tension	Fiber Tension*
ABQ3D coarse	168,237	27,178.0	18,796.0	32,385.0	33,401.0
ABQ3D medium	467,325	25,717.5	17,843.5	32,258.0	35,433.0
ABQ3D refined	3,501,933	18,478.5	14,033.5	30,226.0	33,655.0
CUF-LW	77,805	14,287.5	11,938.0	27,178.0	34,417.0

*Modified Hashin 3D criteria with only in-plane components

9.5 Further developments

The capabilities of refined beam elements for the evaluation of stress concentrations in generic laminates are demonstrated. The approach offers a good compromise between accuracy and computational cost, and it is reliable in that it is based on the FEM. In fact, the current framework enables it to perform free-edge analysis in generic beam geometries and boundary

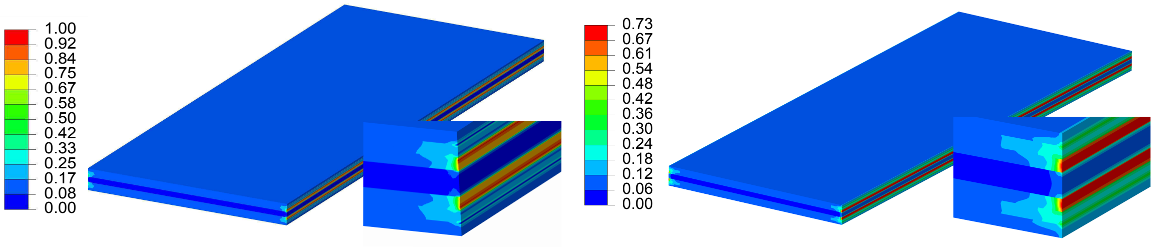
1.00
0.92
0.84
0.75
0.67
0.58
0.50
0.42
0.33
0.25
0.17
0.08
0.00
0.73
0.67
0.61
0.54
0.48
0.42
0.36
0.30
0.24
0.18
0.12
0.06
0.00

(a) CUF-LW (b) ABQ3D - refined

Fig. 9.10 Failure index for matrix tension

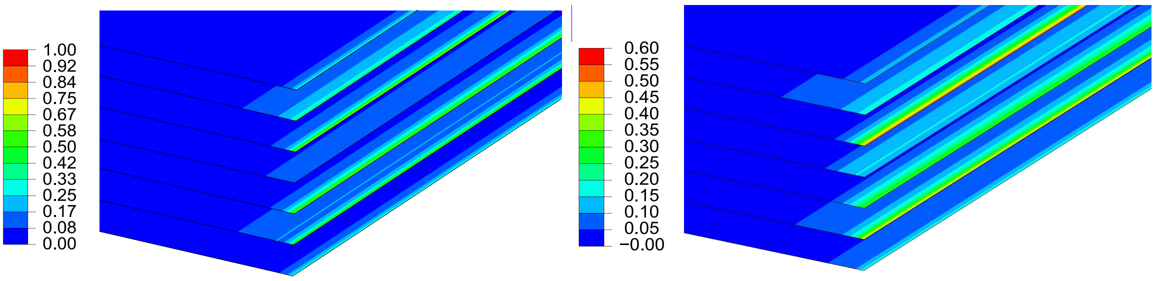
1.00
0.92
0.84
0.75
0.67
0.58
0.50
0.42
0.33
0.25
0.17
0.08
0.00
0.60
0.55
0.50
0.45
0.40
0.35
0.30
0.25
0.20
0.15
0.10
0.05
−0.00

(a) CUF-LW (b) ABQ3D - refined

Fig. 9.11 Failure index for delamination

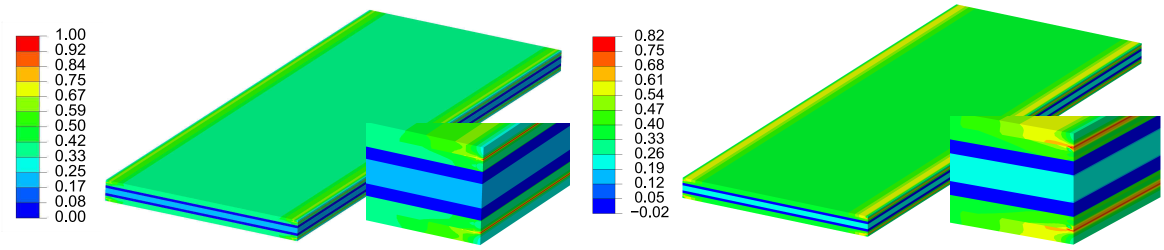
1.00
0.92
0.84
0.75
0.67
0.59
0.50
0.42
0.33
0.25
0.17
0.08
0.00
0.82
0.75
0.68
0.61
0.54
0.47
0.40
0.33
0.26
0.19
0.12
0.05
−0.02

(a) CUF-LW (b) ABQ3D - refined

Fig. 9.12 Failure index for fiber tension

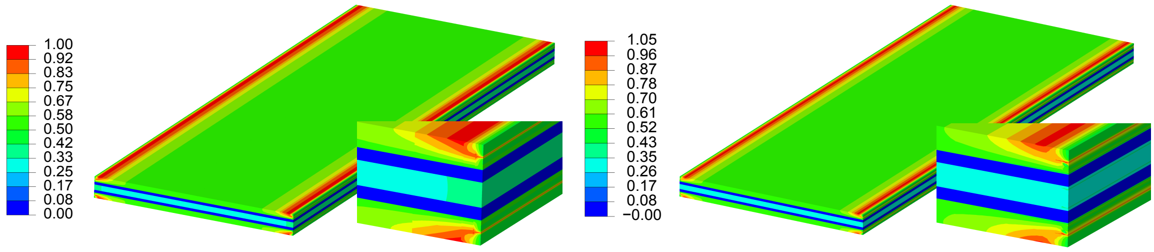
1.00
0.92
0.83
0.75
0.67
0.58
0.50
0.42
0.33
0.25
0.17
0.08
0.00
1.05
0.96
0.87
0.78
0.70
0.61
0.52
0.43
0.35
0.26
0.17
0.08
−0.00

(a) CUF-LW (b) ABQ3D - refined

Fig. 9.13 Failure index for fiber tension using the modified criteria

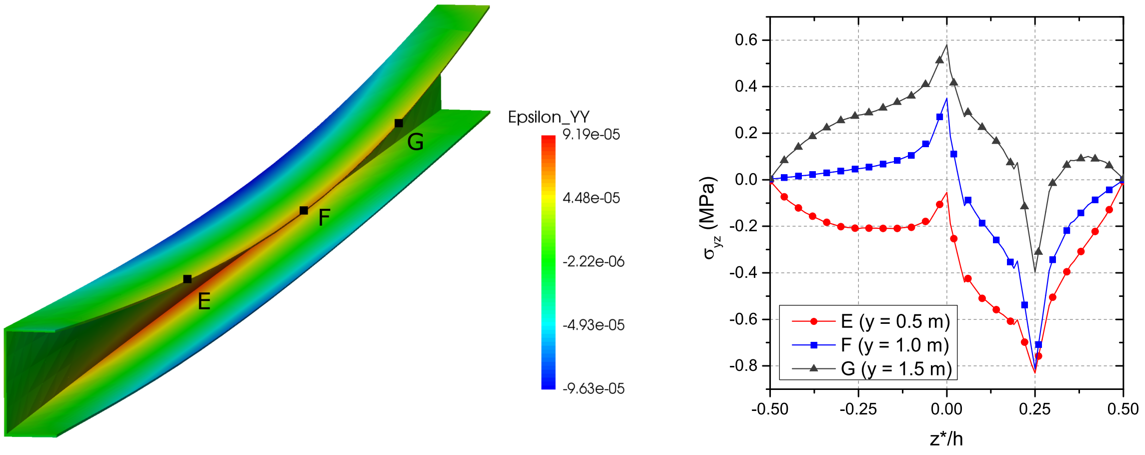

(a) Longitudinal strain contour (b) Shear stress at free edge

Fig. 9.14 Illustration of the capabilities of refined beam elements for free-edge analysis.

conditions. As an example, Fig. 9.14 shows the computation of free-edge stresses at different points in a C-section laminated beam loaded under vertical pressure. In this case, the stress fields at the free edges are not constant anymore along the beam axis and no analytical solution is available. Results like this one illustrate the potential of the proposed formulation to extend the meso-scale 3D stress analysis to the study of the whole structural components.

Part III

Simulation of Lamb waves for structural health monitoring

Chapter 10

Simulation of Lamb waves via higher-order beams

The deployment of structural health monitoring (SHM) systems for the on-line damage detection in aerospace structures is gaining much attention in the recent years. One of the most investigated methods is the use of guided ultrasonic waves, a.k.a. Lamb waves, generated by a system of actuator-sensors attached to the structure. The goal is to localize and quantify the damage trough the scattering of the waves. The design and deployment of such systems requires a profound knowledge of the mechanical behavior of ultrasonic waves in thin-walled structures, therefore numerical models are paramount. However, the simulation of this dynamic problem is extremely demanding due to the high computational refinements which are needed to study this phenomena. Analytical models are in most cases restricted to the computation of dispersion curves and traditional FEM models soon reach their limits in terms of computational cost. Addressing the need for computationally efficient numerical solutions, this chapter introduces the application of refined beam elements for the analysis of Lamb wave propagation in the time domain. An extensive study on the quality of different structural theories is carried out and the propagation in thin-walled beams, such as stringers in aerospace structures, is shown.

The formulation and some of the results included in the present chapter have been submitted for journal publication [59].

10.1 Introduction to Lamb waves

The term Lamb wave, given after his discoverer [110], refers to a class of guided ultrasonic waves (GUW) which propagate in plates with free boundaries. These waves appear as a consequence of the reflections of the longitudinal and transversal waves with the stress-free boundaries, which gives birth to an infinite range of new modes. Indeed, the displacements field of the Lamb waves is a summation of longitudinal and the transverse components, as shown in Fig. 10.1. These waves are highly dispersive and feature very short wavelengths, which means that they can travel long distances within the structural body while being sensitive to small defects. This characteristics make Lamb waves an optimal candidate for the implementation of SHM systems.

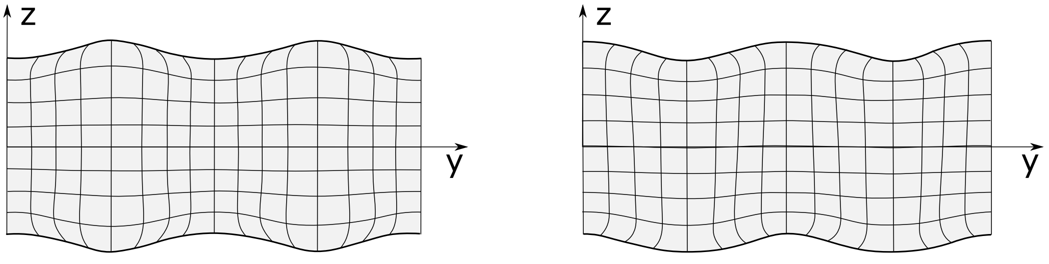

(a) S_0 (b) A_0

Fig. 10.1 Symmetric and antisymmetric first Lamb wave modes.

In the case of elastic isotropic materials, the Lamb waves can be analytically described making use of the Rayleigh-Lamb equations:

$$\frac{tan(\beta\frac{d}{2})}{tan(\alpha\frac{d}{2})} = -\left[\frac{4\alpha\beta k^2}{(k^2-\beta^2)^2}\right]^a. \tag{10.1}$$

with

$$\alpha^2 = \omega^2/c_1^2 - k^2, \qquad \beta^2 = \omega^2/c_2^2 - k^2 \tag{10.2}$$

where k is the wavenumber and ω the angular frequency. In Eq. 10.1, $a = 1$ describes the symmetric modes and $a = -1$ the antisymmetric modes. The solution of this equation provides the relation between wavenumber and the excited frequency. Subsequently, the phase velocity, c_p, is obtained as:

$$c_p = \omega/k. \tag{10.3}$$

This relation provides the dispersion curves of the different wave modes. As an example, the dispersion graph of an aluminum plate is shown in Fig. 10.2.

The group velocity, c_g, can be then derived from the phase velocity using the following relation [80]:

$$c_g = c_p^2\left(c_p - \omega\frac{\partial c_p}{\partial \omega}\right)^{-1}. \tag{10.4}$$

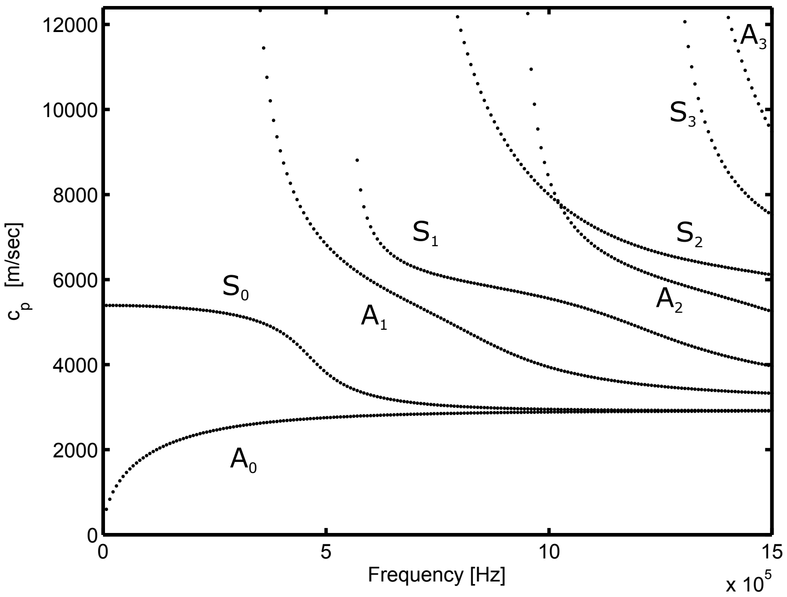

Fig. 10.2 Dispersion curves of a 5 mm thick aluminum plate. Data from GUIGUW software [20].

The computation of the phase and group velocities is necessary when dealing with Lamb wave problems, for instance to determine the traveling velocity of the wave packets in different materials. However, the Rayleigh-Lamb relations cannot be directly obtained for more complex materials, such as laminates. In order to study such cases, researchers usually make use of numerical models to obtain the dispersion curves. Some of the most well-known methods are: the transfer matrix method [122], the global matrix method [142], the mass-spring lattice method (MSLM) [215] and the local interaction simulation approach (LISA) [64, 112]. A semi-analytical finite element (SAFE) [55, 12] was also introduced to deal with generic waveguides. This method exploits the versatility of the finite element method (FEM) to describe complex material systems and cross-sections.

Although these methods provide useful information of the propagation of Lamb waves very efficiently, FEM-based methods are still necessary when it comes to study reflections, scattering and mode conversions [103, 139]. The simulation of GUW using the FEM results to be a major challenge for several reasons, among them:

- The domain of the analysis is usually large due to the low levels of attenuation of the Lamb waves. Also, engineers may need to simulate large parts to accurately capture the scattering caused by arbitrary defects.

- A very fine discretization is needed due to the short wavelengths involved. As a rule of thumb, the element must be small in comparison to the minimum wavelength. Ratios as low as $\frac{1}{20}$ have been suggested for linear elements [131].
- The time domain has to be also discretize accordingly to maximum frequency (smallest period).

As a consequence of these requirements, the simulation of SHM systems is computationally highly expensive. In order to increase the numerical efficiency, it is known that higher-order methods based on *hp*-refinement techniques present some advantages for the wave propagation analysis. Several FEM-based approaches are available in the literature, such as the spectral element method (SEM) [105, 108], the enriched finite element method [85], the isogeometric analysis (IGA) [63, 211], the spectral cell method [68] and the p-version of FEM [212]. An interesting study of some of these methods is included in the latter reference, which demonstrates the superior convergence rates of higher-order elements when compared to standard lower order elements.

This chapter introduces the use of refined structural theories for the accurate simulation of ultrasonic guided waves in thin-walled structures. The idea is to capture the displacement fields of the Lamb wave modes using higher-order expansions such as TE and HLE. In this manner, 3D spatial discretizations are avoided, reducing the complexity of the model and the computational expense.

10.2 Beam theories for Lamb waves

Exploiting the geometrical features of thin-walled solids, researchers usually make use of dimensionally reduced models, i.e. beams and shells, to simulate Lamb waves [107, 92]. These models enable it to reduce massively the computational needs by taking certain assumptions in the smallest dimension. Since the spatial discretization is only done in a 1D domain for beams or a 2D domain for shells, much bigger parts can be modeled. For the sake of clarity, the displacement field of the Timoshenko beam [196] is written:

$$\begin{aligned} u_x(x,y,z,t) &= u_{x_0}(y,t), \\ u_y(x,y,z,t) &= u_{y_0}(y,t) - z\,\phi_x(y,t) + x\,\phi_z(y,t), \\ u_z(x,y,z,t) &= u_{z_0}(y,t), \end{aligned} \tag{10.5}$$

where ϕ_x and ϕ_z are the shear unknowns. The mathematical assumptions of this model allow only displacements in the propagation direction, neglecting any deformation in the cross-section. This limitations of the classical theories are highly detrimental when studying Lamb waves. The most obvious consequence is that the symmetric modes are totally neglected, therefore only the A_0 waves are usually addressed. Also, taking a look into Fig. 10.1 (b), it is possible to see that the linear approximations in the thickness direction are not representative of the displacement distributions in the antisymmetric modes. Therefore, the quality of the analysis is compromised. In addition, the prediction of higher-order modes (A_1, A_2, ...) may be compromised.

The basic idea of the proposed methodology is to use hierarchical higher-order theories such that the dimensionally reduced FEM model can represent the complex displacement fields of the symmetric and antisymmetric modes. For instance, if TE are employed, the mathematical assumptions of the beam element are of the type

$$\boldsymbol{u}(x,y,z,t) = F_\tau(x,z)\, \boldsymbol{u}_\tau(y,t), \tag{10.6}$$

with $F_\tau = x^a\, z^b$, a and b being integers between 0 and the polynomial order p according to the Pascal triangle, see Table 2.1. Fig. 10.3 illustrates the possible deformations of classical and TE models. By adding the linear terms (b), the beam model is able to simulate stretching, therefore the symmetric mode S_0 can be approximated. By increasing the polynomial order p, the mathematical assumptions become rich enough to accurately represent the mode shapes of Lamb waves.

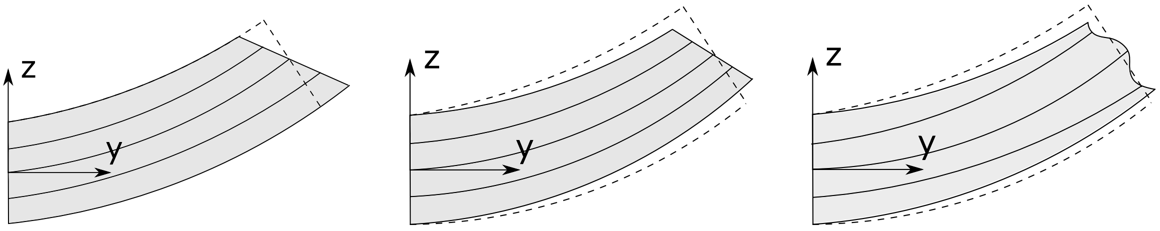

(a) Timoshenko (b) TE p=1 (c) TE p=N

Fig. 10.3 Possible deformations of the beam's section for various theories. The dashed line corresponds to the Euler-Bernouilli model.

10.2.1 Thin-walled theories

When analyzing the wave propagation in structural parts featuring generic thin-walled cross-sections, such as C-, T- or L-section stiffeners, local beam models are not convenient. Theories like TE lose accuracy when non-compact sections are studied. In this case, HLE model allow the user to discretize the thin-walled cross-section with hierarchical expansion domains, which are able to capture very short waves traveling over the flanges of the beam and throughout the structure, as illustrated in Fig. 10.4.

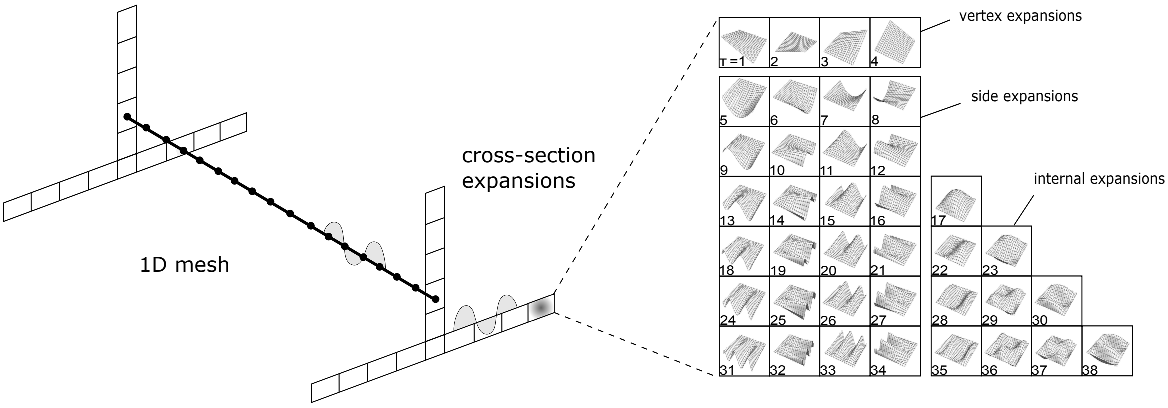

Fig. 10.4 HLE modeling of beams

10.3 1D elements for wave propagation

For the purposes of the present research, it is sought to solve the dynamic problem in the time domain. The FEM is selected to solve the 1D problem due to its versatility for the modeling of generic geometries and defects. Future works may be dedicated to the investigation of analytical solutions for the wave problem, such as close-form Navier solutions [79], radial basis functions [176] or dynamic stiffness method [143]. Using the FEM for dynamic problems, the generalized displacements, $\boldsymbol{u}_\tau$, become a function of the longitudinal direction, y, and the time, t. Interpolating we obtain:

$$\boldsymbol{u}_\tau(y,t) = N_i(y)\,\boldsymbol{u}_{\tau i}(t), \qquad i = 1,...,n, \;\; n = p_b + 1, \tag{10.7}$$

where $\boldsymbol{u}_{\tau i}$ are the unknowns of the dynamic problem and p_b is the polynomial order of the beam element. In order to efficiently solve the problem, higher-order Lagrange shape functions are implemented to interpolate the unknowns along the beam axis. The one-dimensional polynomial basis is defined in the interval [-1,1] as:

$$N_i(\varsigma) = \prod_{i=1, i\neq j}^{p_b} \frac{\varsigma - \varsigma_i}{\varsigma_j - \varsigma_i}, \qquad j = 1,...,n, \tag{10.8}$$

with the roots ς_i being equidistant. Other methods such as SEM make use of a Gauss-Lobatto-Legendre grid which enables it to easily diagonalize the mass matrix [106]. In that manner, very efficient explicit solvers can be derived for the time domain problem. However, in the present implementation the focus is on the comparison between different higher-order structural theories, which not always allow for this kind of discretization over the transverse domain. The implicit time scheme used in this formulation is described at the end of the section.

10.3.1 Governing equations

The equation of the wave propagation problem can be written as

$$\int_V \delta \boldsymbol{u}^T \rho\, \ddot{\boldsymbol{u}}\, dV + \int_V \delta \boldsymbol{\varepsilon}^T \boldsymbol{\sigma}\, dV = \int_S \delta \boldsymbol{u}^T P_S\, dS. \tag{10.9}$$

The first term corresponds to the virtual inertial work, δL_{ine}, the second is the virtual elastic energy, δL_{int}, and the last refers to the virtual external work, δL_{ext}, assuming that only surface loads are applied. Now, introducing Eqs. (10.6), (10.7), (3.29), (3.31) into (10.9), and given the virtual displacements $\delta \boldsymbol{u} = F_s N_j \delta \boldsymbol{u}_{sj}$, the governing equations are written as:

$$\delta \boldsymbol{u}_{sj}^T \mathbf{M}^{ij\tau s} \ddot{\boldsymbol{u}}_{\tau i} + \delta \boldsymbol{u}_{sj}^T \mathbf{K}^{ij\tau s} \boldsymbol{u}_{\tau i} = \delta \boldsymbol{u}_{sj}^T \mathbf{P}^{sj}, \tag{10.10}$$

where $\mathbf{K}^{ij\tau s}$ and $\mathbf{M}^{ij\tau s}$ are the 3×3 fundamental nucleus of the stiffness and mass matrices, respectively, and $\mathbf{P}^{i\tau}$ is the 3×1 force vector. They are defined as:

$$\mathbf{M}^{ij\tau s} = \int_l \int_\Omega F_s N_j\, \rho\, \boldsymbol{I}_3\, F_\tau N_i\, dl\, d\Omega, \tag{10.11}$$

$$\mathbf{K}^{ij\tau s} = \int_l \int_\Omega (\mathbf{D} F_s N_j)^T\, \mathbf{C} \mathbf{D} F_\tau N_i\, dl\, d\Omega, \tag{10.12}$$

$$\mathbf{P}^{sj} = \int_S F_s N_j P_S\, dS. \tag{10.13}$$

As in the previous chapters, the Gaussian quadrature is employed to compute the integrals. Finally, via assembly of the fundamental nucleus, the equations of motion of the system are defined as:

$$\mathbf{M}\ddot{\mathbf{U}} + \mathbf{K}\mathbf{U} = \mathbf{P}, \tag{10.14}$$

where $\mathbf{M}$, $\mathbf{K}$ and $\mathbf{P}$ are the global arrays of the dynamic problem and $\mathbf{U}$ and $\ddot{\mathbf{U}}$ are the displacement and acceleration vectors, respectively.

10.3.2 Time integration scheme

In time-domain analyses the equation of motion, Eq. 10.14, has to be discretized in time as well. Due to the high frequencies that are typically involved in GUW, the time steps must be quite small. Depending on the element size and the material properties, the Courant-Friedrich-Levy condition [52] states that

$$\Delta t \leq \frac{l_e}{c_g}, \tag{10.15}$$

where Δt is the time increment and l_e is the size of the finite element. Values of the order of 10^{-8} s and smaller might be needed for typical aluminum plates [68]. There are two types of integration schemes:

- explicit methods, in which the equilibrium state at a certain step depends only from the solutions of the previous steps. The most well-known method is probably the central difference method.
- implicit methods, in which the equilibrium state is evaluated taking into account the previous and current steps. An example of this class of time integration is the Newmark method.

In GUW and SHM applications, explicit time schemes are often preferred due to the existence of lumping techniques [56] which allow it to obtain diagonal mass matrices. Therefore, the inversion of the dynamic stiffness matrix becomes trivial. This is indeed the major advantage of the SEM, which avoids solving the system of equations and only involves matrix multiplications to advance in time. However, explicit schemes are conditionally stable and there is an upper bound for the size ot the time step, above which the solution may diverge.

In this research, the goal is to compare and assess different structural theories, therefore it is not always possible to diagonalize the mass matrix. Subsequently, the advantages of the explicit time schemes are lost. For this reason, an implicit Newmark method [138] is chosen for all models tested. Accordingly, the displacement and velocities at a certain time $t+\Delta t$ are defined as:

$$\begin{aligned} \dot{\mathbf{U}}_{t+\Delta t} &= \dot{\mathbf{U}}_t + [(1-\gamma)\ddot{\mathbf{U}}_t + \gamma\ddot{\mathbf{U}}_{t+\Delta t}], \\ \mathbf{U}_{t+\Delta t} &= \mathbf{U}_t + \dot{\mathbf{U}}_t\Delta t + [(1/2-\beta)\ddot{\mathbf{U}}_t + \beta\ddot{\mathbf{U}}_{t+\Delta t}]\Delta t^2, \end{aligned} \tag{10.16}$$

where γ and β are parameters that control the integration stability and accuracy. An unconditionally stable scheme is obtained for $\gamma = 1/2$ and $\beta = 1/4$. Generally speaking, the temporal refinement in GUW problems could make the use of implicit solvers too expensive, although the computational cost can be massively reduced when only linear effects are accounted. In linear regimes, the matrices of problem do not change in time, and, therefore, the triangularization of the dynamic stiffness matrix can be performed only once at the initial steps of the analysis [13], as follows:

1. Assembly of the mass matrix **M** and stiffness **K** (the damping is neglected)
2. Assign the time step Δt and compute the dynamic stiffness matrix

$$\bar{\mathbf{K}} = \mathbf{K} + \frac{1}{\Delta t^2 \beta}\mathbf{M} \tag{10.17}$$

3. Initialize $\mathbf{U}_0$, $\dot{\mathbf{U}}_0$ and $\ddot{\mathbf{U}}_0$ for $t = t_0$.
4. Factorize the dynamic stiffness matrix $\bar{\mathbf{K}} = \mathbf{L}\,\mathbf{D}\,\mathbf{L}^T$
5. Start the loop on the time steps
6. Compute the dynamic force vector at $t + \Delta t$:

$$\bar{\mathbf{P}}_{t+\Delta t} = \mathbf{P}_{t+\Delta t} + \mathbf{M}\,(\frac{1}{\Delta t^2 \beta}\mathbf{U}_t + \frac{1}{\Delta t \beta}\dot{\mathbf{U}}_t + \Big(1 - \frac{1}{2\beta}\Big)\ddot{\mathbf{U}}_t) \tag{10.18}$$

7. Solve at current time step $\mathbf{U}_{t+\Delta t} = \bar{\mathbf{K}}^{-1}\,\bar{\mathbf{P}}_{t+\Delta t}$
8. Compute $\dot{\mathbf{U}}$ and $\ddot{\mathbf{U}}$ at current step:

$$\dot{\mathbf{U}}_{t+\Delta t} = \frac{\gamma}{\Delta t \beta}(\mathbf{U}_{t+\Delta t} - \mathbf{U}_t) + \Big(1 - \frac{\gamma}{\beta}\Big)\dot{\mathbf{U}}_t + \Big(1 - \frac{\gamma}{2\beta}\Big)\Delta t\,\ddot{\mathbf{U}}_t \tag{10.19}$$

$$\ddot{\mathbf{U}}_{t+\Delta t} = \frac{1}{\Delta t^2 \beta}(\mathbf{U}_{t+\Delta t} - \mathbf{U}_t) - \frac{1}{\Delta t \beta}\dot{\mathbf{U}}_t + \Big(\frac{1}{2\beta} - 1\Big)\ddot{\mathbf{U}}_t \tag{10.20}$$

Applied to the Newmark time scheme, we obtain a solver which is unconditionally stable and that only involves one factorization followed by matrix multiplications at each iteration, resulting in massive savings in terms of computational time.

10.4 Examples

This section includes the assessment of the formulation for time domain analyses of Lamb waves. First, a benchmark test is performed to show the convergence properties of the higher-order structural theories here proposed. Subsequently, a C-section beam is modeled to show the 3D capabilities of the model in generic structures.

10.4.1 Benchmark problem

The method to evaluate the accuracy of the proposed approach is based on the benchmark problem proposed by Wilberg et al. [212]. The GUW problem is shown in Fig. 10.5. It consists of an aluminum strip of thickness, d, equal to 2 mm and length, L, equal to 500 mm. Plane strain assumptions are applied. The excitation is a wave packet of central frequency $f = 477.5$ kHz and $n = 32$ cycles is generated by two parallel forces located at $y = 0$ and $z = \pm d/2$ with magnitude $F_{1,2} = F_0 sin(\omega t) sin(\frac{\omega t}{2n})$. If the forces have the same direction, the antisymmetric mode A_0 is excited; otherwise, the symmetric mode S_0 is excited. Symmetric conditions are applied at $y = 0$. The material data can be found in Table 10.1.

Table 10.1 Material properties of the Aluminum strip.

Young's modulus, E	70×10^9 Pa
Poisson ratio, ν	0.33
Density, ρ	2700 kg/m^3
Longitudinal speed, c_1	6197 m/s
Transversal speed, c_2	3121 m/s

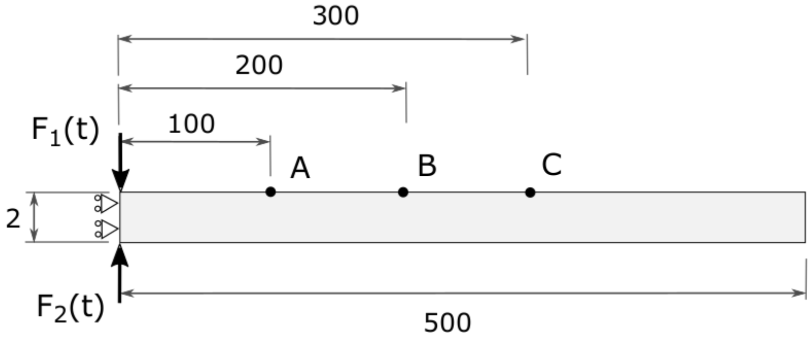

Fig. 10.5 Geometrical features of the metallic strip used in the numerical assessment. Distances in mm.

The proposed example is interesting in that an analytical solution is available, see for instance Graff [82] or Giurgiutiu [80]. In order to get it, one has to solve the Rayleigh-Lamb equations, Eq. (10.1), which provide the relation between the wave number, k, and the angular frequency, ω. Then, the time-dependent displacement fields and the dispersion curves of the phase and group velocity are obtained straightforwardly. For the current problem, the following values are obtained:

$$c_{p_{S0}} \simeq 5316\, m/s, \qquad c_{p_{A0}} \simeq 2298\, m/s, \tag{10.21}$$

$$c_{g_{S0}} \simeq 5130\, m/s, \qquad c_{g_{A0}} \simeq 3126\, m/s. \tag{10.22}$$

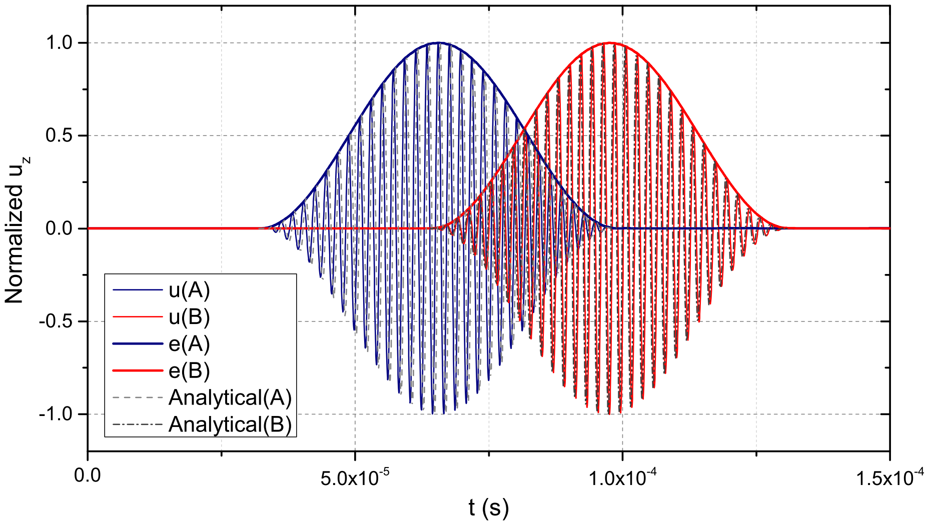

Fig. 10.6 Time signal of the normalized vertical displacement of the anti-symmetric Lamb wave at points A and B.

Figure 10.6 shows the vertical displacements (u(A) and u(B)) and the envelopes (e(A) and e(B)) of the anti-symmetric wave at points A and B obtained from a fine model of fourth-order HLE beam elements and the analytical equations. The quality of the numerical model is quantified by evaluating the time-of-flight (TOF) of the wave packet from one station to the other. For this purpose, the following procedure is performed. First, the Hilbert transform is applied to the time signal. At point A:

$$H_A(u(t)) = \frac{1}{\pi} \int_{-\infty}^{\infty} u_A(\tau) \frac{1}{t-\tau}\, d\tau. \tag{10.23}$$

Then, the envelope of the time signal can be computed as:

$$e_A(t) = \sqrt{H_A^2 + u_a^2}. \tag{10.24}$$

Subsequently, the centroid of the envelop corresponds to:

$$t_A = \frac{\int_0^{t_{max}} e_A(t)\, t\, dt}{\int_0^{t_{max}} e_A(t)\, dt}. \tag{10.25}$$

Finally, the TOF is computed as $t_B - t_A$. The error is computed comparing to the analytical solution.

Quality of the longitudinal mesh

In order to assess the convergence rates of the longitudinal mesh, a fine HLE model of fourth polynomial order is used for the transverse expansion as it assures a minimum contribution to the total error. Figure 10.7 includes the convergence rates of the A_0 and S_0 modes for different polynomial orders. Linear 2-node (B2) to sixth-order 7-node (B7) elements are considered in the study. The abscissa of the plots, χ, is the parameter of the discretization, defined as:

$$\chi = \frac{n\lambda}{L}, \tag{10.26}$$

where n is the total number nodes and $\lambda = c_p/f$. This parameter is proportional to the number of degrees of freedom per wavelength, therefore it gives an idea of the mesh density. Note that, since λ is proportional to the phase speed, see Eq. (10.22), χ is different for the S_0 and A_0 modes. From the convergence results, one can observe that for equal mesh densities, the convergence of higher-order elements is clearly increased. In fact, linear and quadratic elements are not recommended as highly refined meshes are needed to get convergent solutions.

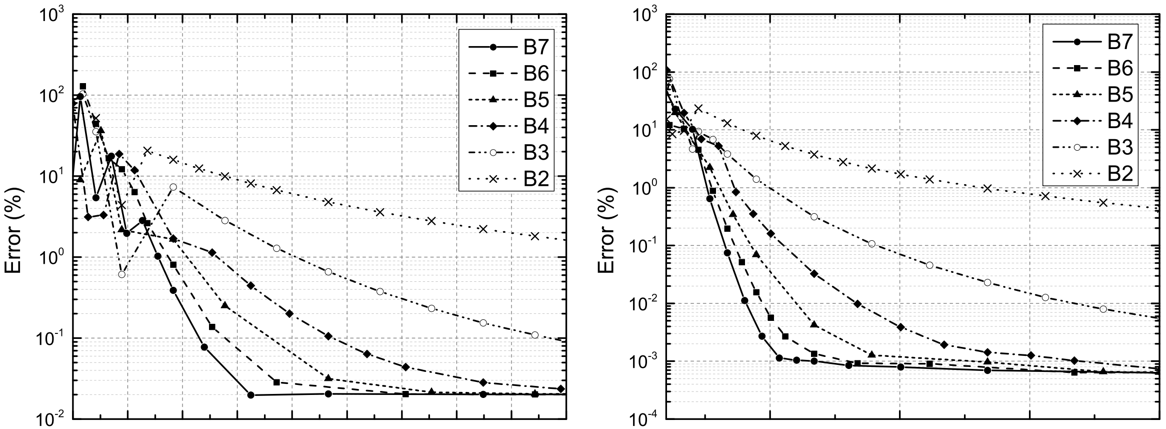

(a) A_0 mode (b) S_0 mode

Fig. 10.7 Convergence analyses for the A_0 and S_0 waves propagating along the aluminum strip.

The effects of shear locking in lower-order elements are studied as well. The results obtained from elements with full integration of first, second and third order (B2, B3 and B4, respectively) are compared to those of locking-free beam elements (MITC2, MITC3 and MITC4), introduced in Chapter 4. Figure 10.8 shows that the effect of locking is minimum in GUW problems due to the fact that a high number of elements is inherently necessary to capture the short wavelengths, therefore the shear energy terms of the stiffness matrix are always well approximated.

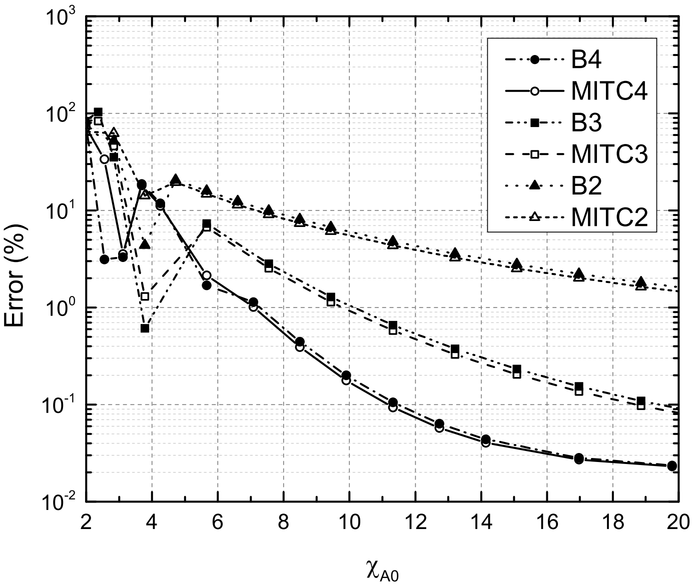

Fig. 10.8 Comparison between full integrated elements and MITC elements (A_0).

Evaluation of structural theories

In this section, the assessment and performance of different classical to higher-order structural theories for the simulation of Lamb waves is addressed. According to the convergence analysis of the 1D discretization, 200 B7 elements ($\chi_{A0} = 11.56$, $\chi_{S0} = 26.74$) are employed along the y-axis, ensuring a negligible numerical error. The same procedure to evaluate the quality of the model is carried out on the following theories:

- Classical theories: Euler-Bernoulli (E-B) and Timoshenko (T).
- TE: from first (TE1) to seventh order (TE7).
- HLE: from first (HL1) to seventh order (HL7).

The results are included in Fig. 10.9. The left-hand plot shows the error of the classical and TE models for increasing orders, whereas the right-hand plot shows the HLE solutions. Both A_0 (white squares) and S_0 (black dots) modes are analyzed. Similar rates are obtained

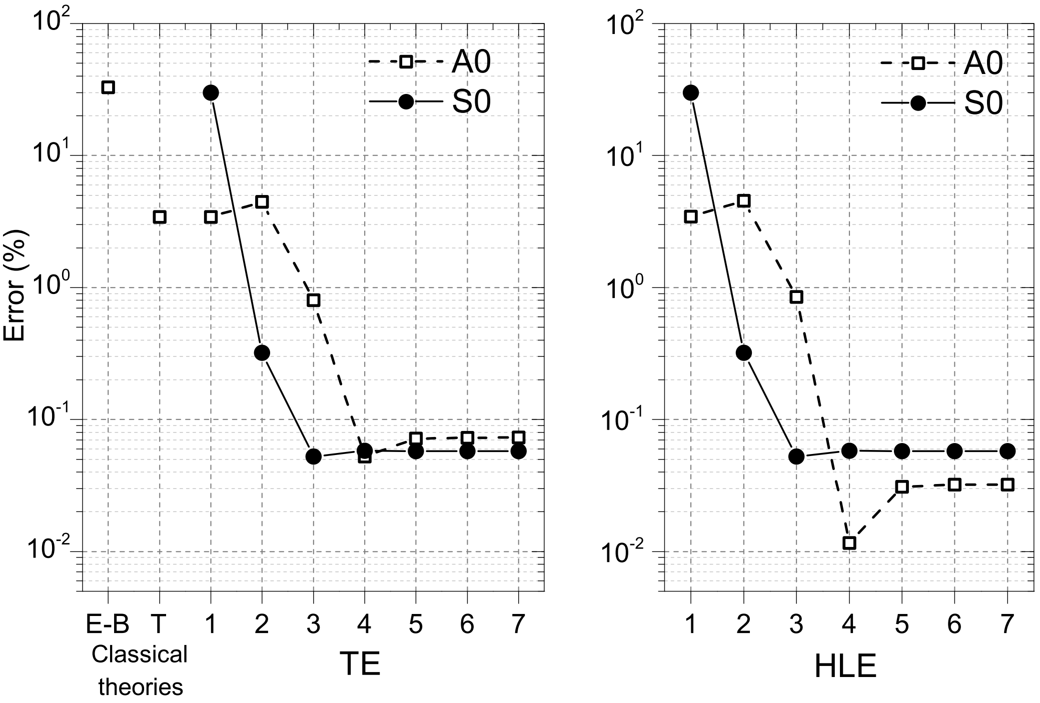

Fig. 10.9 Convergence of the p-order on the transverse direction for A_0 and S_0 modes.

from TE and HLE models, showing that the computation of the A_0 wave is always more critical: to achieve 1 % of error, a quadratic model is enough for the S_0 wave, although a third-order expansion is needed for the A_0 mode.

In SHM systems, both modes are simultaneously excited by the piezoelectric transducers. A second example is now considered to study how accurate can be each structural theory in this case. The same problem of Fig. 10.5 is considered again, but in this case with the force only applied at the top face. A Hanning window of $f = 200$ kHz and $n = 10$ cycles is generated and the time signal is evaluated at midspan of the metallic strip, at $y = 0.25$ m. The most relevant results of this study are shown in Fig. 10.10. The following remarks can be made:

- Only models that include kinematic terms in the thickness direction can capture the S_0 waves. Classical models such as Timoshenko and Mindlin do not foreseen this mode for the given load application.
- Models that include a linear variation in the transverse direction (TE1 and HL1) are able to capture the appearance of the S_0 mode and show equivalent results for the A_0 mode. However, the error in the resultant group velocity of the S_0 mode is still high. Indeed, it is possible to observe how the reflected wave (S0r) is almost unnoticed during the time of the analysis.

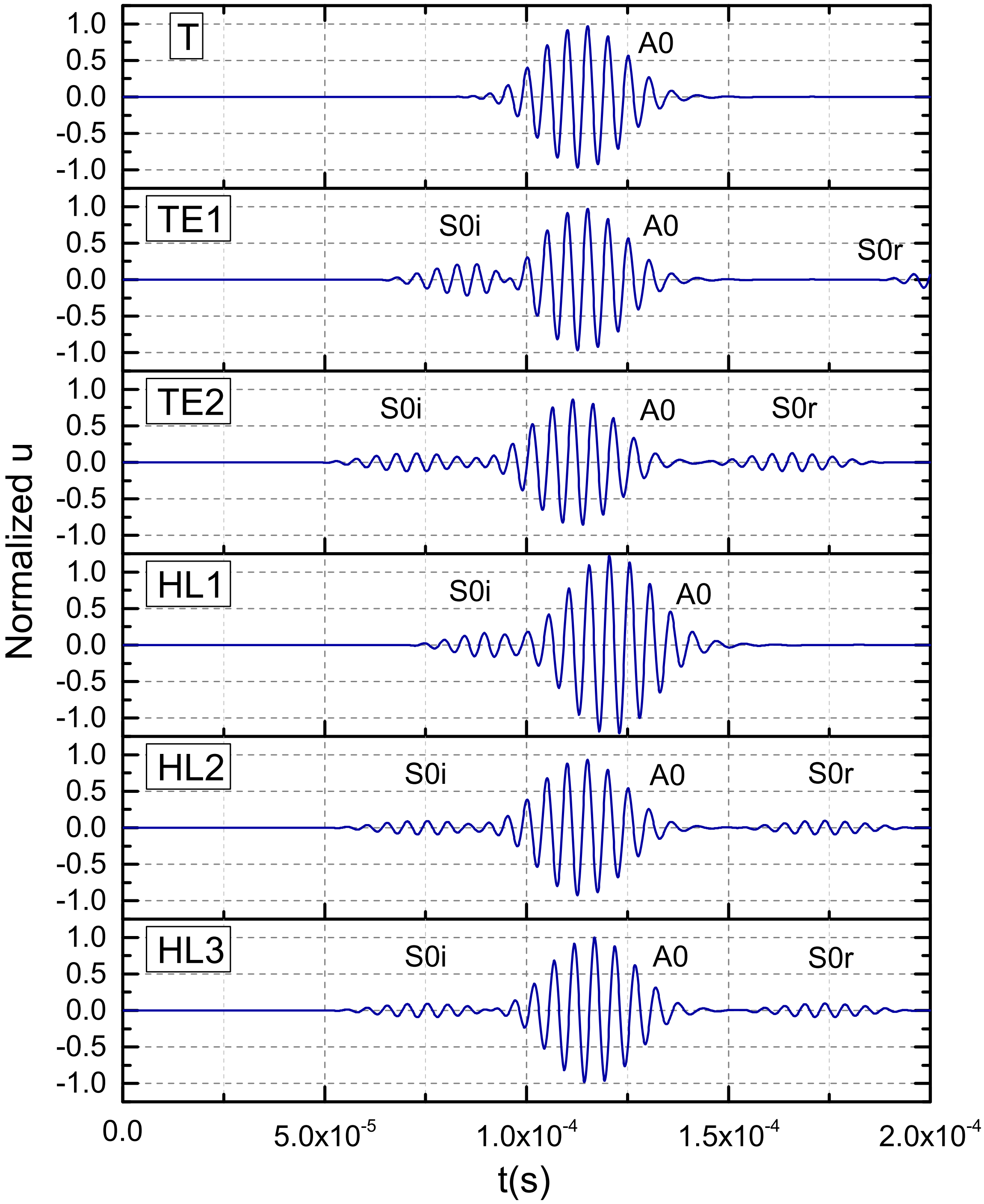

Fig. 10.10 A_0 and S_0 modes in a metallic strip for a single force excitation of 200 kHz.

- Second-order kinematics (TE2 and HL2) clearly improve the accuracy of the model. As shown in Fig. 10.9, the error in the S_0 mode rapidly decreases. Both the incident (S0i) and reflected (S0r) symmetric waves are captured at the evaluated point.

Higher-order modes

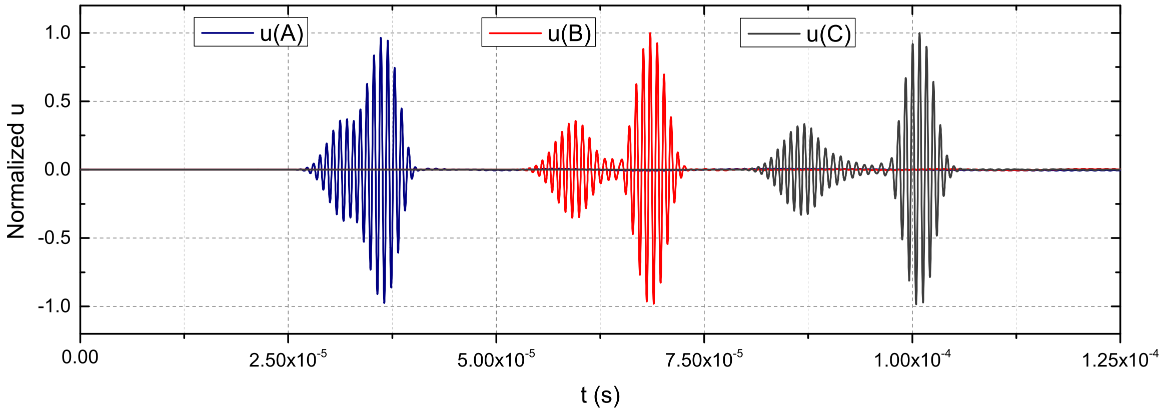

Fig. 10.11 A_0 and A_1 waves at three different stations ($y_A = 100$ mm in blue, $y_B = 200$ mm in red and $y_C = 300$ mm in grey) for a signal burst of 1.2 MHz.

When the excited frequency is greater than the cut-off value, a higher-order mode (A_1, S_1, ...) must be considered. This modes exhibit even more complex displacement fields, which are difficult to capture using standard FEM discretizations. An interesting application of the proposed models is to be able to accurately represent this modes without the need of altering the longitudinal mesh. To show this capability, an anti-symmetric packet of $f = 1.2$ MHz and $n = 5$ is generated at $y = 0$, leading to the appearance of A_0 and A_1 waves. The model employs 200 B7 and a fifth-order expansion HL5. The time step is set as 2×10^{-8} s. Figure 10.11 shows the detected displacements at three different points along the aluminum strip, whose locations are: $y_A = 100$ mm (blue signal), $y_B = 200$ mm (red signal) and $y_C = 300$ mm (grey signal). The A_1 mode is clearly visible and it is almost entirely decoupled from the A_0 mode already at point B. An snapshot of the propagating waves at $t = 6 \times 10^{-5}$ s is included in Fig. 10.12, where one can observe the differences between the displacement fields of each mode.

10.4.2 Lamb waves in thin-walled beams

When it comes to simulate the wave propagation in thin-walled structures, such as stiffeners or box beams, HLE theories represent an efficient alternative to solid and plate formulations. Plate elements are typically used for this kind of analysis, although as it is demonstrated in

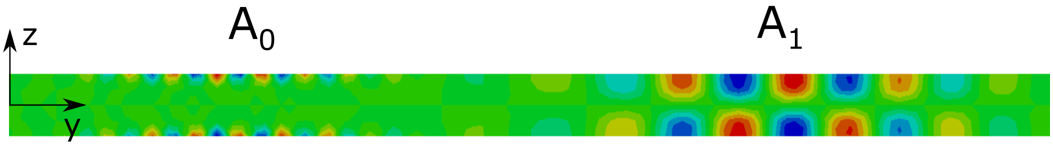

Fig. 10.12 A_0 and A_1 modes at $t = 6 \times 10^{-5}$ for a signal burst of 1.2 MHz.

the previous section, they lack in capturing all the physics of the problem. Solid models are able to represent correctly the corners of the structure, although the aspect ratio constraints make their use prohibitively expensive in real applications. Using HLE beams, the user can model the cross-section with 2D hierarchical domains and the longitudinal axis via a 1D mesh of higher-order elements. This methodology simplifies greatly the modeling phase and allows to control the accuracy/cost trough the order of the theory.

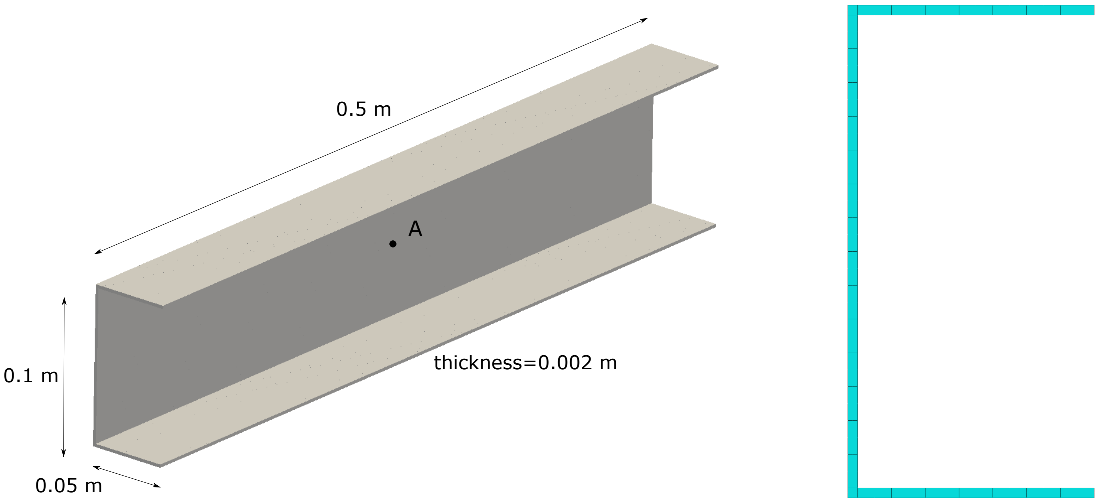

(a) Geometry

(b) Section

Fig. 10.13 Geometry and cross-section mesh of the C-section beam.

To illustrate this capability, a C-section beam made of aluminum is modeled and the propagation of the Lamb waves over the time is computed. The geometrical features of the structure are shown in Fig. 10.13 (a), whereas the discretization of HLE over the C-section is included in (b). A second order expansion is used for the section domains and 50 B5 elements are placed along the beam axis, being the total number of DOFs equal to 92,259. A single excitation of 100 Hz and 5 cycles is applied at the center of the web. An screenshot of the propagating waves is shown in Fig. 10.14. It is possible to observe that the wavefront over the web is clearly affected by the reflections at the top and bottom flanges. Also, the model is able to capture the propagation over the flanges and the reflections at the free-edges.

Figure 10.15 shows a cut plot of the structure at the same time, where one can observe the complex mechanisms which arise at the corners of the section.

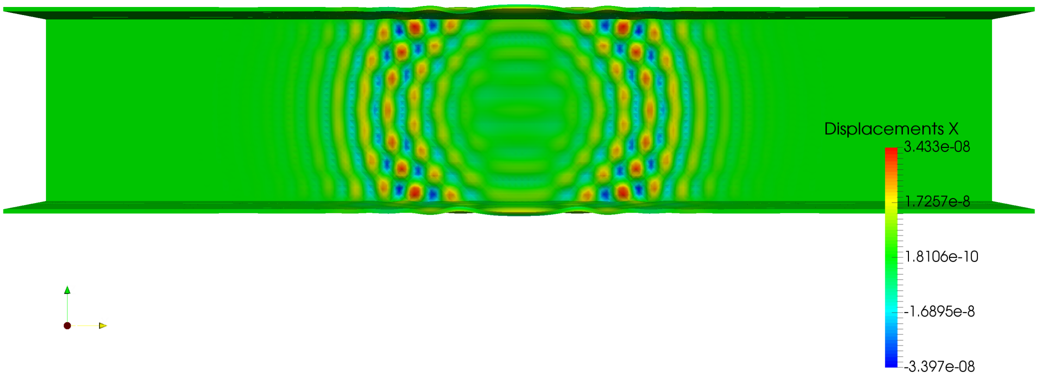
Displacements X
3.433e-08
1.7257e-8
1.8106e-10
-1.6895e-8
-3.397e-08

Fig. 10.14 Screeshoot of the propagating waves at 5.6 $\times 10^{-}5$ s.

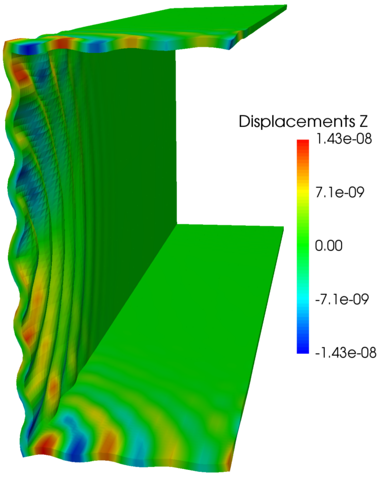
Displacements Z
1.43e-08
7.1e-09
0.00
-7.1e-09
-1.43e-08

Fig. 10.15 Cut of the C-beam.

Chapter 11

Structural theories for Lamb wave simulation in laminated structures

This chapter demonstrates the potential of multilayered theories for the simulation of guided ultrasonic waves in composite laminates. Differently from the previous developments of the thesis, plate models are employed here due to their geometrical advantages for the modeling of laminated structures. The numerical challenge represented by the Lamb wave simulation in thin-walled structures is even more difficult when dealing with composite materials. The anisotropy of the material and the heterogeneity across the stack of plies lead to the appearance of more complex wave modes and scatterings. For this reason, the simulation of damage detection systems must account for high-fidelity kinematics which can capture the 3D motion of Lamb waves. Plate models based on the first-order shear deformation theory (FSDT) are common choice among researchers to analyze efficiently the propagation of Lamb waves in large parts. However, the poor kinematic assumptions of these models neglect some physical effects of the wave propagation, such as the symmetric modes and the related mode conversions. On the other hand, 3D elements can be used to model the stack of plies ensuring a layer wise resolution, although the computational size of the numerical problem rises extremely quickly as the number of layers increases or the domain of interest becomes larger. As a middle ground between the latter two approaches, different types of structural theories for plate elements are tested and presented here as a tool to provide high-fidelity time-domain solutions for laminated structures with acceptable numerical expenses.

11.1 Lamb waves in composites

The introduction of composite materials in lightweight aeronautic structures has come together with new challenges to ensure their safe service at all times. Although these advanced structures have been investigated for many decades, their application in primary load bearing components is considerably recent and the experience in the damage mechanisms of these structures at a long time scale is still reduced. Moreover, typically used composite laminates show different classes of defects in comparison to their traditionally metallic counterparts, such as delaminations or intralaminar cracks, which sometimes can be difficult to detect in regular inspections. Under these circumstances, it is clear that on-line SHM systems should be seen not only as a mean to optimize the inspection campaigns and reduce the maintenance costs, but also as a support for the safe deployment of these new structures in the market.

Although the term Lamb wave was given originally to guided waves propagating in isotropic plates with free boundaries [110], it is common to generalize its use to ultrasonic elastic waves in thin-walled media, including composite laminates. Unlike in metallic plates, due to the directionality of the mechanical properties in anisotropic media the wave front is not circular anymore and the phase and group speeds must be calculated as a function of the azimuth angle. In addition, shear horizontal modes usually coexist with the symmetric and anti-symmetric modes. An illustration of the fundamental modes which may appear in anisotropic plates under a generic excitation is shown in Figure 11.1.

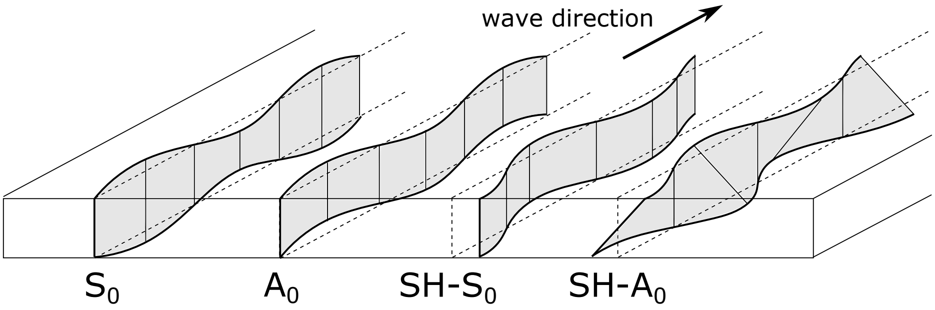

Fig. 11.1 Illustration of the fundamental modes of Lamb waves in an anisotropic plate, including out-of-plane symmetric (S_0), out-of-plane antisymmetric (A_0), shear horizontal symmetric (SH-S_0) and shear horizontal antisymmetric (SH-A_0).

In composite laminates, the heterogeneities of the carbon fiber reinforced polymers (CFRP) and the change of mechanical properties between the different plies have substantial effects on the resulting wave modes. First, the chosen stacking sequence determines the predominant propagation directions of each of the fundamental modes, which may result in complex shapes of the wavefront. Also, continuous mode conversions [111] of the long-wavelength symmetric mode (S_0) into the shorter and slower antisymmetric mode (A_0) are observed in experimental tests. These conversions, which also appear under the presence of geometrical discontinuities such as reinforcements or defects, make it more complicated for SHM systems to elaborate useful information out of the detected signals.

11.1.1 Numerical considerations

Numerical simulations are used to support the experimental measurements and to provide a better understanding of the scattering of the signals detected by the piezoelectric sensors under the presence of defects. In this topic, one the most reliable and adopted approaches to capture the complex Lamb modes is the use of 3D FEM models. Both *h*-methods (standard FEM [103]) and *p*-methods (SEM [68], p-FEM [212], IGA [211]) can be used to discretize the stack of plies with a mesh of solid elements which are able to provide a good approximation of the displacement fields over the thickness of the plate. However, in this kind of layer wise approaches, the number of elements increases dramatically with the number of layers [136]. For this reason, these models are not feasible to study typical thin-walled composite structures used for aerospace applications and are only employed to perform local analysis [140].

A second widely adopted approach is the use of dimensionally reduced models based on Mindlin kinematics, usually known as FSDT plates. This approach exploits the geometry of thin-walled structures to reduce drastically the computational costs by accounting only for the displacements and the out-of-plane rotations of the particles located in the mid-plane. In this manner, the size of the numerical problems becomes independent of the number of layers, thus larger domains and generic laminates can be studied [107, 178]. The issue of FSDT plates here is that the Mindlin kinematics cannot capture the 3D phenomena involved in Lamb wave propagation, which results in that some physics cannot be properly captured. First, all the out-of-plane symmetric modes are neglected due to the omission of stretching effects, limiting these solutions to approximated in-plane modes.

Also, the dispersive nature of Lamb waves imply that the modes change depending on the excited frequency. Schulte et al. [179] showed through the computation of the dispersion curves that, although FSDT-based models can provide a good accuracy for the low frequency range, the computed phase and group speed steadily differ from those of the 3D elasticity as the frequency increases. In addition, the representation of complex geometries such as reinforcements or joints, is usually done through numerical artifacts which reduce the fidelity of the model, among these rigid elements and offsets.

To overcome some of the aforementioned issues of FSDT elements, this chapter proposes the use of refined multi-layered theories for plates. The basic idea is that by enriching the

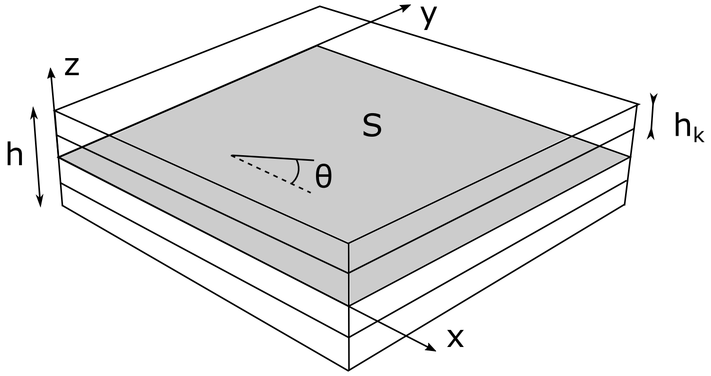

Fig. 11.2 Coordinate reference systems for plate elements.

kinematic field of the plate element, more physical effects can be included in the model, and therefore the complex shapes of the Lamb modes in the thickness direction can be systematically approximated. The user can then optimize the resolution according to the desired accuracy, making it possible to perform very efficient simulations. Both ESL and LW approaches are adopted in the present development. The main advantage of ESL plates is that the kinematic assumptions are independent of the number of layers, thus the size of the computational problem remains fairly low. On the other hand, LW models make independent assumptions for each layer, therefore the number of degrees of freedom is proportional to the number of layers. In addition, an interesting modeling technique based on HLE is introduced for the study of joints, reinforcements or delaminations using a mixed ESL-LW approach.

11.2 Higher-order plate elements for wave propagation

Consider the reference system illustrated in Fig. 11.2 for composite plates. The x and y coordinates define the plane of propagation of the waves, and the z coordinate is parallel to the stacking direction. In the small displacement range, the geometrical relations of the plate element are written as:

$$\begin{Bmatrix} \varepsilon_{xx} \\ \varepsilon_{yy} \\ \varepsilon_{zz} \\ \varepsilon_{xz} \\ \varepsilon_{yz} \\ \varepsilon_{xy} \end{Bmatrix} = \begin{bmatrix} \frac{\partial}{\partial x} & 0 & 0 \\ 0 & \frac{\partial}{\partial y} & 0 \\ 0 & 0 & \frac{\partial}{\partial z} \\ \frac{\partial}{\partial z} & 0 & \frac{\partial}{\partial x} \\ 0 & \frac{\partial}{\partial z} & \frac{\partial}{\partial y} \\ \frac{\partial}{\partial y} & \frac{\partial}{\partial x} & 0 \end{bmatrix} \begin{Bmatrix} u_x \\ u_y \\ u_z \end{Bmatrix} \tag{11.1}$$

Considering an orthotropic layer, the the Hooke's law provides the stress-strain relations as:

$$\begin{Bmatrix} \sigma_{xx} \\ \sigma_{yy} \\ \sigma_{zz} \\ \sigma_{xz} \\ \sigma_{yz} \\ \sigma_{xy} \end{Bmatrix} = \begin{bmatrix} \tilde{C}_{11} & \tilde{C}_{12} & \tilde{C}_{13} & 0 & 0 & \tilde{C}_{16} \\ \tilde{C}_{12} & \tilde{C}_{22} & \tilde{C}_{23} & 0 & 0 & \tilde{C}_{26} \\ \tilde{C}_{13} & \tilde{C}_{23} & \tilde{C}_{33} & 0 & 0 & \tilde{C}_{36} \\ 0 & 0 & 0 & \tilde{C}_{44} & \tilde{C}_{45} & 0 \\ 0 & 0 & 0 & \tilde{C}_{45} & \tilde{C}_{55} & 0 \\ \tilde{C}_{16} & \tilde{C}_{26} & \tilde{C}_{36} & 0 & 0 & \tilde{C}_{66} \end{bmatrix} \begin{Bmatrix} \varepsilon_{xx} \\ \varepsilon_{yy} \\ \varepsilon_{zz} \\ \varepsilon_{xz} \\ \varepsilon_{yz} \\ \varepsilon_{xy} \end{Bmatrix} \tag{11.2}$$

where the stiffness matrix of the material, $\tilde{C}$, is written here in the global reference system shown in Fig. 11.2. Therefore, its components, $\tilde{C}_{\alpha\beta}$, depend on the mechanical properties of the ply and the orientation angle θ, see Chapter 3.

11.2.1 Thickness expansions

Among all the models based on the ESL approach, the FSDT is probably the most adopted in the literature and can be found in the majority of the commercial FEM codes. The FSDT displacements are based on Mindlin's kinematics:

$$u_x(x,y,z,t) = u_{x_0}(x,y,t) + z\,\phi_y(x,y,t), \tag{11.3}$$

$$u_y(x,y,z,t) = u_{y_0}(x,y,t) - z\,\phi_x(x,y,t), \tag{11.4}$$

$$u_z(x,y,z,t) = u_{z_0}(x,y,t). \tag{11.5}$$

Note that the FSDT unknowns are 5 in total accounting for 3 displacements and 2 out-of-plane rotations. According to the CUF, the kinematics of the plate model can be extended systematically to account for all possible deformations of the plate section. In a compact form, the displacement field of a CUF plate can be written as:

$$\boldsymbol{u}(x,y,z,t) = F_\tau(z)\,\boldsymbol{u}_\tau(x,y,t) \qquad \tau = 1,\dots,M, \tag{11.6}$$

where F_τ are arbitrary 1D functions of the thickness coordinate, z, $\boldsymbol{u}_\tau$ are the expansion unknowns, which vary over the xy-plane, and τ is the index of the expansion terms. The choice and definition of the F_τ functions depends on the desired multi-layered approach, i.e ESL or LW. Two polynomial expansions are used in this work: TE and HLE.

TE

Higher-order ESL models can be generated by adopting a thickness expansion of the type $F_\tau = z^p$, p being the polynomial order. In such a manner, a third-order TE model is defined by the following kinematics:

$$\begin{aligned} u_x(x,y,z,t) &= u_{x_0}(x,y,t) + z\,u_{x_1}(x,y,t) + z^2\,u_{x_2}(x,y,t) + z^3\,u_{x_3}(x,y,t), && (11.7)\\ u_y(x,y,z,t) &= u_{y_0}(x,y,t) + z\,u_{y_1}(x,y,t) + z^2\,u_{y_2}(x,y,t) + z^3\,u_{y_3}(x,y,t), && (11.8)\\ u_z(x,y,z,t) &= u_{z_0}(x,y,t) + z\,u_{z_1}(x,y,t) + z^2\,u_{z_2}(x,y,t) + z^3\,u_{z_3}(x,y,t), && (11.9) \end{aligned}$$

which account for a total of 12 DOF, including displacements, rotations and higher-order warpings.

HLE

A convenient method to derive LW models is to generate non-local hierarchical expansions with nodal unknowns at the extremes. This kind of functions can be obtained from 1D Legendre polynomials:

$$\begin{aligned} L_0 &= 1, && (11.10)\\ L_1 &= s, && (11.11)\\ L_p &= \frac{2p-1}{p} s L_{p-1}(s) - \frac{p-1}{p} L_{p-2}(s), \quad p = 2,3,4,... && (11.12) \end{aligned}$$

Subsequently, a set of thickness expansions can be defined as:

$$\begin{aligned} F_1(r) &= \frac{1}{2}(1-r), && (11.13)\\ F_2(r) &= \frac{1}{2}(1+r), && (11.14)\\ F_p(r) &= \sqrt{\frac{2p-1}{p}} \int_{-1}^{r} L_{p-1}(r)\,dr, \quad p = 2,3,4,... && (11.15) \end{aligned}$$

Note that these functions are defined in the natural domain [-1, 1], thus a Jacobian transformation is employed to map them into the thickness of each ply. The first two equations are equal to 1 at bottom and top of the layer thickness, respectively. The higher-order expansions are equal to zero at the limits of the domain and are introduced hierarchically into the set as the polynomial order increases. When used to create LW modes, a mesh of these HLE 1D domains is used in the thickness direction to represent the stack of plies and the C^0

condition for the displacement solutions is imposed by assembling the nodal unknowns at the interfaces.

11.2.2 Finite element matrices

2D FEM models are created by splitting the domain over the *xy*-plane into plate elements. Accordingly, the expansion unknowns, $\boldsymbol{u}_\tau$, are interpolated over the 2D space via shape functions, as follows:

$$\boldsymbol{u}_\tau(x,y,t) = N_i(x,y)\,\boldsymbol{u}_{\tau i}(t), \qquad i = 1,...,N, \tag{11.16}$$

where $\boldsymbol{u}_{\tau i}$ are the generalized unknowns of the dynamic problem, and i is the nodal index. Due to their higher convergence rates in wave propagation analyses (see 10.4.1), higher-order Lagrangian polynomials are chosen as interpolating functions. The 1D Lagrangian polynomials can be defined in the natural space as:

$$\phi_m(\xi) = \prod_{m=1,m\neq n}^{p_{FE}} \frac{\xi - \xi_m}{\xi_n - \xi_m}, \qquad m,n = 1,...,p_{FE}+1. \tag{11.17}$$

If equidistant nodes are placed over the element space, the following rule applies:

$$\xi_m = -1 + 2(m-1)/p_{FE}, \tag{11.18}$$

with p_{FE} being the order of the plate element. The 2D polynomial basis can be then obtain as

$$N_i(\xi,\eta) = \phi_m(\xi)\,\phi_n(\eta), \qquad \xi,\eta \in [-1,1]. \tag{11.19}$$

Similarly to the previous chapter, using the thickness expansions and the plate interpolations, Eq. (11.6) and (11.16), respectively, the geometrical (Eq. (11.1)) and constitutive relations (Eq. (11.2)), the fundamental nuclei of the equation of motion, Eq. (10.10), are now written as:

$$\mathbf{M}^{ij\tau s} = \int_h \int_S F_s N_j \rho \boldsymbol{I}_3 F_\tau N_i \, dS\, dz, \tag{11.20}$$

$$\mathbf{K}^{ij\tau s} = \int_h \int_S (\mathbf{D} F_s N_j)^T \tilde{\mathbf{C}} \mathbf{D} F_\tau N_i \, dS\, dz, \tag{11.21}$$

$$\mathbf{P}^{sj} = \int_S F_s N_j P_S \, dS, \tag{11.22}$$

where $dS = dx \times dy$ and $\boldsymbol{I}_3$ is the 3 × 3 identity matrix. These integrals are decoupled into thickness and in-plane domains. Therefore, considering an orthotropic layer, the explicit form of the fundamental nuclei can be written as:

- Mass matrix (non-zero terms):

$$\begin{aligned}
M_{xx}^{ij\tau s} &= \rho\, I_{ij}\, E_{\tau s} \\
M_{yy}^{ij\tau s} &= \rho\, I_{ij}\, E_{\tau s} \\
M_{zz}^{ij\tau s} &= \rho\, I_{ij}\, E_{\tau s}
\end{aligned} \tag{11.23}$$

- Stiffness matrix:

$$\begin{aligned}
K_{xx}^{ij\tau s} = &\ \tilde{C}_{44}\, I_{ij}\, E_{\tau_{,z} s_{,z}} + \tilde{C}_{11}\, I_{i_{,x} j_{,x}}\, E_{\tau s} + \tilde{C}_{16}\, I_{i_{,y} j_{,x}}\, E_{\tau s} + \tilde{C}_{16}\, I_{i_{,x} j_{,y}}\, E_{\tau s} + \\
&\ \tilde{C}_{66}\, I_{i_{,y} j_{,y}}\, E_{\tau s} \\
K_{xy}^{ij\tau s} = &\ \tilde{C}_{45}\, I_{ij}\, E_{\tau_{,z} s_{,z}} + \tilde{C}_{16}\, I_{i_{,x} j_{,x}}\, E_{\tau s} + \tilde{C}_{12}\, I_{i_{,y} j_{,x}}\, E_{\tau s} + \tilde{C}_{66}\, I_{i_{,x} j_{,y}}\, E_{\tau s} + \\
&\ \tilde{C}_{26}\, I_{i_{,y} j_{,y}}\, E_{\tau s} \\
K_{xz}^{ij\tau s} = &\ \tilde{C}_{44}\, I_{i_{,x} j}\, E_{\tau s_{,z}} + \tilde{C}_{45}\, I_{i_{,y} j}\, E_{\tau s_{,z}} + \tilde{C}_{16}\, I_{i j_{,x}}\, E_{\tau_{,z} s} + \tilde{C}_{36}\, I_{i j_{,y}}\, E_{\tau_{,z} s} \\
K_{yx}^{ij\tau s} = &\ \tilde{C}_{45}\, I_{ij}\, E_{\tau_{,z} s_{,z}} + \tilde{C}_{16}\, I_{i_{,x} j_{,x}}\, E_{\tau s} + \tilde{C}_{66}\, I_{i_{,y} j_{,x}}\, E_{\tau s} + \tilde{C}_{12}\, I_{i_{,x} j_{,y}}\, E_{\tau s} + \\
&\ \tilde{C}_{26}\, I_{i_{,y} j_{,y}}\, E_{\tau s} \\
K_{yy}^{ij\tau s} = &\ \tilde{C}_{55}\, I_{ij}\, E_{\tau_{,z} s_{,z}} + \tilde{C}_{66}\, I_{i_{,x} j_{,x}}\, E_{\tau s} + \tilde{C}_{26}\, I_{i_{,y} j_{,x}}\, E_{\tau s} + \tilde{C}_{26}\, I_{i_{,x} j_{,y}}\, E_{\tau s} + \\
&\ \tilde{C}_{22}\, I_{i_{,y} j_{,y}}\, E_{\tau s} \\
K_{yz}^{ij\tau s} = &\ \tilde{C}_{45}\, I_{i_{,x} j}\, E_{\tau s_{,z}} + \tilde{C}_{55}\, I_{i_{,y} j}\, E_{\tau s_{,z}} + \tilde{C}_{36}\, I_{i j_{,x}}\, E_{\tau_{,z} s} + \tilde{C}_{23}\, I_{i j_{,y}}\, E_{\tau_{,z} s} \\
K_{zx}^{ij\tau s} = &\ \tilde{C}_{13}\, I_{i_{,x} j}\, E_{\tau s_{,z}} + \tilde{C}_{36}\, I_{i_{,y} j}\, E_{\tau s_{,z}} + \tilde{C}_{44}\, I_{i j_{,x}}\, E_{\tau_{,z} s} + \tilde{C}_{45}\, I_{i j_{,y}}\, E_{\tau_{,z} s} \\
K_{zy}^{ij\tau s} = &\ \tilde{C}_{36}\, I_{i_{,x} j}\, E_{\tau s_{,z}} + \tilde{C}_{23}\, I_{i_{,y} j}\, E_{\tau s_{,z}} + \tilde{C}_{45}\, I_{i j_{,x}}\, E_{\tau_{,z} s} + \tilde{C}_{55}\, I_{i j_{,y}}\, E_{\tau_{,z} s} \\
K_{zz}^{ij\tau s} = &\ \tilde{C}_{33}\, I_{ij}\, E_{\tau_{,z} s_{,z}} + \tilde{C}_{44}\, I_{i_{,x} j_{,x}}\, E_{\tau s} + \tilde{C}_{45}\, I_{i_{,y} j_{,x}}\, E_{\tau s} + \tilde{C}_{45}\, I_{i_{,x} j_{,y}}\, E_{\tau s} + \\
&\ \tilde{C}_{55}\, I_{i_{,y} j_{,y}}\, E_{\tau s}
\end{aligned} \tag{11.24}$$

- Loading vector:

$$\begin{aligned}
P_x^{i\tau} &= P_S\, F_\tau\, I_i \\
P_y^{i\tau} &= P_S\, F_\tau\, I_i \\
P_z^{i\tau} &= P_S\, F_\tau\, I_i
\end{aligned} \tag{11.25}$$

The terms $I_{i_{(,x)(,y)} j_{(,x)(,y)}}$ and $E_{\tau_{(,z)} s_{(,z)}}$, are the FE and thickness integrals, respectively. The FE integrals are defined as:

$$I_{i_{(,x)(,y)} j_{(,x)(,y)}} = \int_S N_{i_{(,\xi)(,\eta)}} N_{j_{(,\xi)(,\eta)}} |\boldsymbol{J}_S|\, d\xi\, d\eta \tag{11.26}$$

$$I_i = \int_S N_i\, |\boldsymbol{J}_S|\, d\xi\, d\eta \tag{11.27}$$

where $\boldsymbol{J}_S$ is the Jacobian matrix of the finite element. The computation of the integrals is performed numerically via Gaussian quadrature. Since higher-order polynomials are used as shape functions, the locking effects are minimum and full integration is adopted in all cases.

Subsequently, the integral terms of the thickness coordinate are

$$E_{\tau_{(,z)} s_{(,z)}} = \int_h F_{\tau_{(,z)}} F_{s_{(,z)}} dz. \tag{11.28}$$

When laminated structures are considered, the computation of these terms depends on the selected multi-layered theory, as shown in the following.

ESL

TE kinematics are used in this work to generate higher-order ESL models. In this case, the integration in the thickness direction is performed as

$$E_{\tau_{(,z)} s_{(,z)}} = \sum_{k=1}^{n_l} \tilde{C}^k_{\alpha\beta} \int_{z_b^k}^{z_t^k} F_{\tau_{(,z)}} F_{s_{(,z)}} \, dz \tag{11.29}$$

where z_b^k and z_t^k are the bottom and top coordinates, respectively, of layer k and n_l is the total number of layers. Note that the material coefficients, $\tilde{C}^k_{\alpha\beta}$, are now included inside the $E_{\tau_{(,z)} s_{(,z)}}$ terms. If the laminate is made of different materials, the same procedure applies for the densities in the fundamental nuclei of the mass matrix (Eq. (11.23).

LW

On the other hand, LW modes make use of independent expansions for each layer, thus the thickness integrals are computed for each layer, readily:

$$E^k_{\tau_{(,z)} s_{(,z)}} = \tilde{C}^k_{\alpha\beta} \int_{h_k} F_{\tau_{(,z)}} F_{s_{(,z)}} \, dz = \tilde{C}^k_{\alpha\beta} \int_{-1}^{+1} F_{\tau_{(,r)}} F_{s_{(,r)}} \, |\boldsymbol{J}_z| \, dr. \tag{11.30}$$

where $\boldsymbol{J}_z$ is the Jacobian of the transformation between r and z.

Mixed LW-ESL

Thanks to the characteristics of HLE, a different class of ESL model can be implemented by representing the stacking of plies in the natural domain, $r \in [-1, 1]$, using a LW Jacobian transformation. Then, the Legendre functions are integrated via Gaussian quadrature, as follows:

$$E^{q}_{\tau_{(,z)}s_{(,z)}} = \sum_{k=1}^{n_l^q} \tilde{C}^{k}_{\alpha\beta} \int_{z_b^k}^{z_t^k} F_{\tau_{(,z)}} F_{s_{(,z)}} \, dz = \sum_{k=1}^{n_l^q} \tilde{C}^{k}_{\alpha\beta} \int_{r_b^k}^{r_t^k} F_{\tau_{(,r)}} F_{s_{(,r)}} \, |\boldsymbol{J}_r^k| dr \tag{11.31}$$

The main advantage of this approach is that it allows to group a set of plies, n_l^q, into mathematical layers, represented by q. Each of these mathematical layers are described with an ESL approach, while LW kinematics are defined over the thickness of the whole laminate. For the sake of clarity, the different multi-layered approaches are illustrated in Fig. 11.3. Note that $|\boldsymbol{J}_r^k|$ makes it possible to perform the Gaussian quadrature in the interval $[r_b^k, r_t^k]$. This modeling technique can be used to generate optimal models for the wave propagation in lap joints and multicomponent structures, or to study efficiently the scattering of the Lamb waves in delaminated areas.

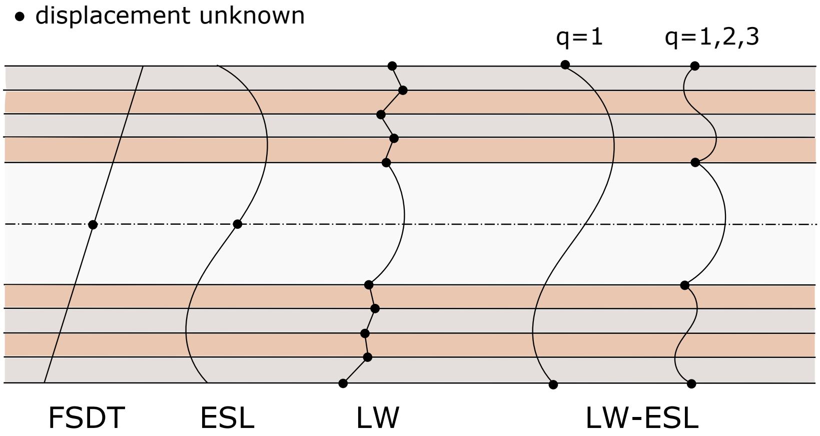

Fig. 11.3 Illustration of the different multi-layered approaches implemented in the present chapter. The curved lines represent possible displacement solutions over the thickness and the dots show the location of the pure displacement unknowns. For the sake of clarity, the stretching effects are not included.

11.3 Examples

Two numerical cases are included in this section. The first shows the assessment of the proposed approach through the computation of the time of flight in different laminates. The second demonstrates the potential of the method to capture the scattering of the waves in complex structures.

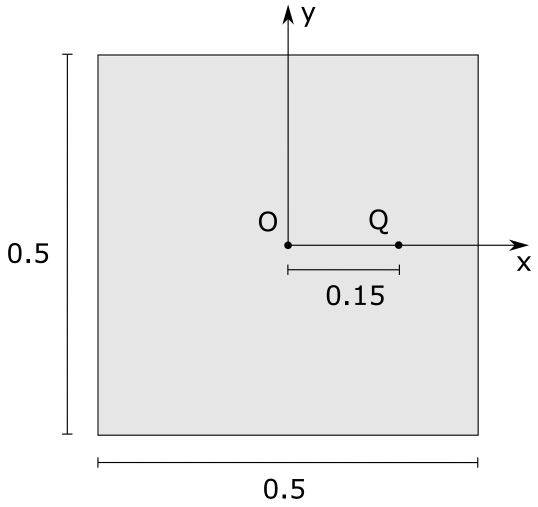

Fig. 11.4 Top view of the composite plate studied. Units in m.

11.3.1 Laminates

The first numerical example shows the assessment of the proposed plate elements for the Lamb wave analysis of composite laminates. The ply properties are those of a T300/F593 CFRP: $E_1 = 128.1$ GPa, $E_2 = E_3 = 8.2$ GPa, $G_{12} = G_{13} = 4.7$ GPa, $G_{23} = 3.44$ GPa, $\nu_{12} = \nu_{13} = 0.27$ GPa, $\nu_{23} = 0.2$ and $\rho = 1570$ kg/m^3. The ply thickness is equal to 215 μm. The in-plane dimensions of the composite plate are 0.5 × 0.5 m, and in all cases a stack of 8 layers is considered, resulting in an overall thickness of 1.72 mm. The fundamental Lamb modes are excited in the model by means of two point forces placed at top and bottom of the plate in its center, in correspondence to point O of Fig. 11.4. A wave packet of central frequency equal to 100 kHz and 5 cycles is simulated. The antisymmetric mode A_0 is excited when the two forces are applied in-phase, whereas the symmetric modes S_0 and SH_0 appear when the forces have opposite directions. A convergent mesh of 80 × 80 cubic elements is employed to discretize the plate.

The accuracy of the higher-order models here proposed is measured via the computation of the time of flight of the propagating waves along the x direction between points O and Q (see Fig. 11.4). Following the method exposed in [212], the time of flight is calculated from the maximum value of the signal envelope, $e_Q(t)$, computed at point Q from the Hilbert transform of the displacement values, $H_Q(u)$, as follows:

$$H_Q(u(t)) = \frac{1}{\pi} \int_{-\infty}^{\infty} u_Q(\tau) \frac{1}{t-\tau} \, d\tau, \tag{11.32}$$

$$e_Q(t) = \sqrt{H_Q^2 + u_Q^2}. \tag{11.33}$$

Then, the corresponding group speed of the fundamental Lamb waves in that direction can be directly obtained as the ratio between the distance OQ and the time of flight of the signal peak.

Figures 11.5 and 11.6 show screenshots of the waves propagating over the unidirectional laminate, i.e. all 8 layers oriented towards x. These plots, obtained with a third-order HLE model (HL3), are in good agreement with those of the same numerical case from Li *et al.* [118]. It can be observed that the wavefronts of both A_0 and the S_0 modes exhibit an elliptical shape, with the longer axis aligned with the fiber direction. Also, the shear horizontal mode, SH_0, can be seen from the contour plots of the in-plane displacements in the y direction, see Fig. 11.6 (b).

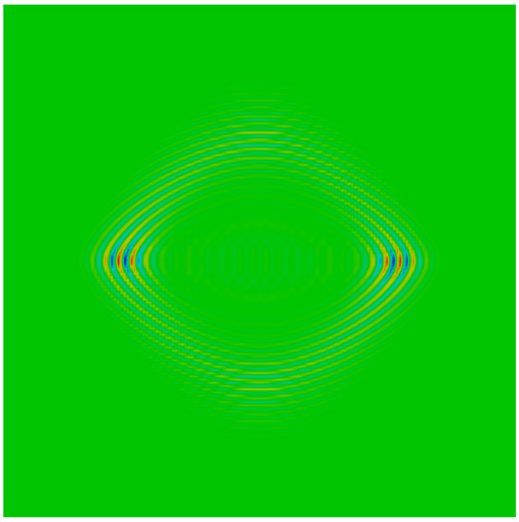

Fig. 11.5 Contour plot of the vertical displacements (u_z) at $t = 7.5 \times 10^{-5}$ s showing the A_0 mode over the unidirectional composite plate.

Table 11.1 shows the computed group velocities in x of the antisymmetric, c_{gA0_x}, and symmetric, c_{gS0_x}, modes for the unidirectional composite plate. FSDT and HLE solutions are included. The error is calculated by comparing these solutions to those of the SAFE method, which have been obtained from the code GUIGUW [20]. From these results it can be stated that, as expected, the error in the calculation of the A_0 mode is greater than that of the S_0 mode, which has a longer wavelength. Also, for the current transverse excitation, the FSDT cannot capture the symmetric mode S_0. For the antisymmetric mode, the improvement of the resolution is not noticeable until the third-order expansion (HL3). It is worth noting that the equal values of the group velocities in Table 11.1 reflect the fact that the differences in the computed time of flight are smaller than the time step chosen for the Newmark solver, that in this case is $\Delta t = 2 \times 10^{-7}$. Indeed, no visible improvement can be seen for higher-order expansions in the computation of the symmetric mode.

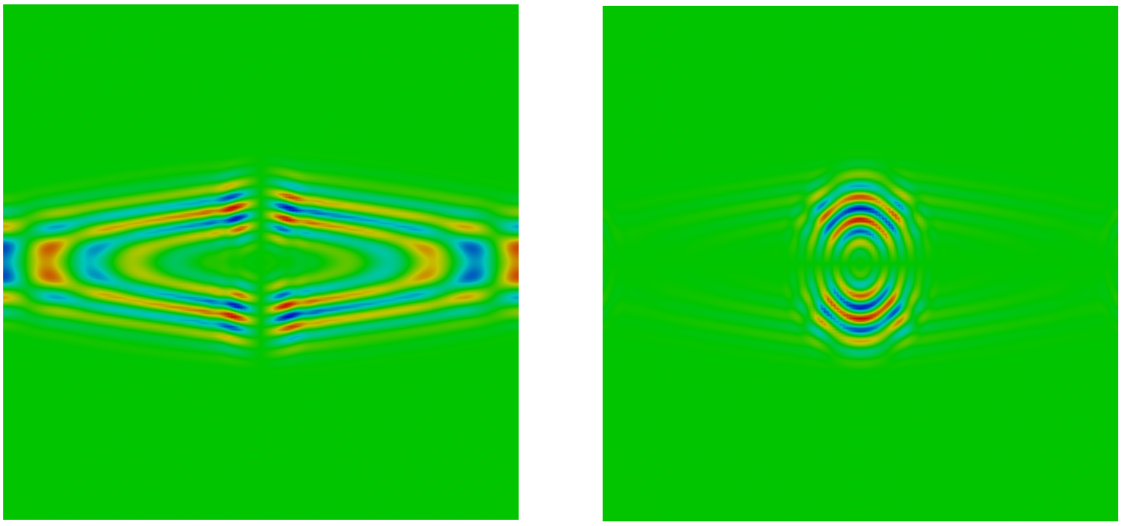
(a) u_x (b) u_y

Fig. 11.6 Contour plots of the in-plane displacements along x (a) and along y (b) at $t = 5 \times 10^{-5}$ s showing the S_0 mode and the SH_0 mode, respectively.

Table 11.1 Computed group velocities of the fundamental Lamb waves propagating in the unidirectional laminate.

Model	c_{gA0_x} [m/s]	Error [%]	c_{gS0_x} [m/s]	Error [%]
SAFE[20]	1730	-	9052	-
FSDT	1884	8.90	-	-
HL1	1884	8.90	9036	0.18
HL2	1884	8.90	9036	0.18
HL3	1773	2.49	9036	0.18

Subsequently, similar analyses are performed on two multi-layered plates with the following stacking sequences: $[0°_2/90°_2]_S$ and $[45°/\text{-}45°/0°/90°]_S$. The challenge here is to prove if the proposed ESL approaches are able to provide similar levels of accuracy as LW models for the wave propagation in composites. It is reasonable to assume that LW models are able to provide 3D accuracy [155], although the computational costs may be also extremely high when dealing with typical laminates used in aerospace structures. Table 11.2 includes the group speeds of the A_0 mode along x for the two composite laminates considered and their correspondent error with respect to the SAFE solutions. The following remarks can be made:

1. The numerical error of all models is less in the $[45°/\text{-}45°/0°/90°]_S$, showing that for quasi-isotropic laminates the kinematic assumptions can be relaxed.
2. FSDT plate elements overestimate the values of the velocities in both laminates.
3. LW solutions are in good agreement with the SAFE references.
4. ESL models based on TE and HLE kinematics provide very similar accuracy. This result proves the validity of the ESL approach based on HLE kinematics as compared to more standard TE theories.
5. The differences between higher-order ESL and LW models for the dynamic problem are acceptable in both cases.

Table 11.2 Computed group velocities of the A_0-wave propagating in the unidirectional laminate.

Model	$[0/90]_S$ c_{gA0_x}	Error [%]	$[0/90/45/\text{-}45]_S$ c_{gA0_x}	Error [%]
SAFE[20]	1591	-	1631	-
FSDT	1781	11.97	1769	8.45
ESL-TE3	1641	3.15	1607	1.48
ESL-HL3	1641	3.15	1606	1.53
LW-HL2	1559	1.99	1599	1.95

Figures 11.7 and 11.8 show screenshots of the propagating waves at different instants in the two composite laminates for the FSDT, ESL-TE and LW plate models here proposed. All the wavefronts exhibit very similar shapes, although in the FSDT case a larger surface has been swept by the waves in comparison to the other models at the same time. Also, in Fig. 11.8 it is possible to notice some differences in the amplitude of the vertical displacements, u_z, between the LW and ESL, although the time signals are in good agreement.

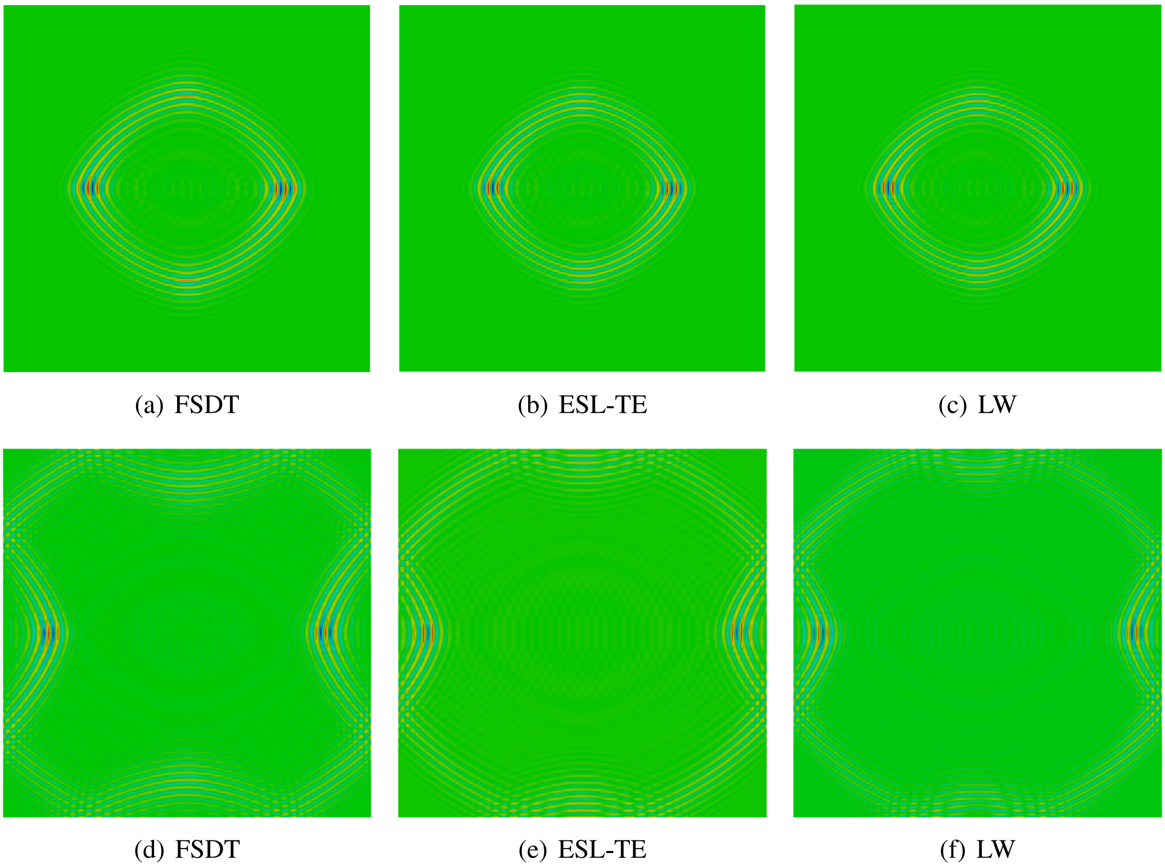
(a) FSDT (b) ESL-TE (c) LW

(d) FSDT (e) ESL-TE (f) LW

Fig. 11.7 Plots of the vertical displacements, u_z, at $t = 7.5 \times 10^{-5}$ s (a-c) and $t = 1.5 \times 10^{-4}$ s (d-f) showing the A_0 waves over the $[0°_2/90°_2]_S$ laminate.

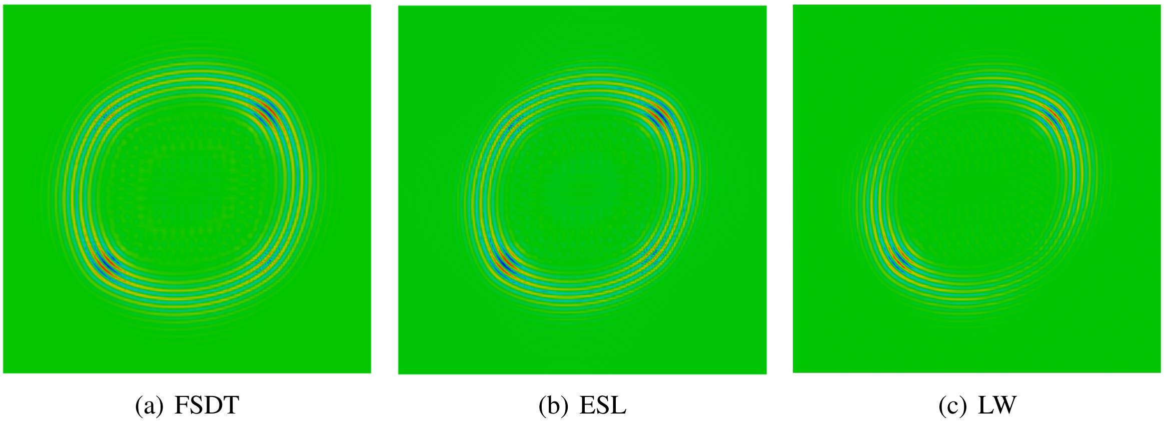
(a) FSDT (b) ESL (c) LW

Fig. 11.8 Plots of the vertical displacements, u_z, at $t = 1.125 \times 10^{-4}$ s showing the A_0 waves over the $[45°/\text{-}45°/0°/90°]_S$ laminate.

11.3.2 Single-lap debond

The previous example demonstrates the suitability of HLE-based ESL models for the computation of the propagating speeds of the Lamb waves in generic composite laminates. The intention now is to show the capabilities of the mixed ESL-LW approach to model complex geometries and analyze efficiently the scattering of the waves under the presence of defects. With this purpose in mind, a composite single-lap joint (SLJ) is considered consisting of two different laminates of T300/F593 material, the same as the previous examples, attached with an EA9313 epoxy adhesive. The adhesive is isotropic with the following mechanical properties: $E = 2.274$ GPa, $\nu = 0.36$ and $\rho = 1100$ kg/m^3. The stacking sequences of the two laminates are:

- laminate 1: 8 layers $[90°/0°]_{2S}$, overall thickness $h_1 = 1.72$ mm.
- laminate 2: 10 layers $[90°/(45°/\text{-}45°)_2]_S$, overall thickness $h_2 = 2.15$ mm.

The thickness of the adhesive layer is equal to 0.2 mm. The overall dimensions of the SLJ are 0.3 m × 0.3 m, with the bonding area placed in the center along x. Figure 11.9 shows the features of the numerical case. The whole plate is discretized with 40 × 40 cubic plate elements and symmetry conditions are applied over the side lying on the x-axis. Three zones can be differentiate in the model on the basis of the definition of the multi-layered expansion. In zones 1 and 3, the HLE-based ESL approach is adopted, whereas in the joined area the mixed ESL-LW is adopted by grouping the plies into ESL expansions within a global LW model, as shown in Fig. 11.9. Second-order polynomials (HL2) are employed in all cases. A wave packet of 2 cycles and central frequency of 100 kHz is excited in point P by means of a local pressure applied in the top surface of 2 plate elements. Due to the characteristics of HLE, displacement unknowns are placed at top and bottom of the plates, thus 3D-like loads can be imposed. Accounting for the symmetry, the model simulates a squared piezoelectric transducer of 15 mm × 15 mm. The maximum number of DOF is equal to 176,600 and a total of 2000 time steps where used to discretize a total analysis time of 3×10^{-4} s.

In addition, a small area of detachment is included, see the red section in Fig. 11.9. The modeling of the debond area in the current framework is done simply by removing the thickness domains representing the adhesive layer. In this manner, an empty space is created in the adhesive layer where the continuity of the displacement solutions along the thickness is interrupted. Figures 11.10 and 11.11 include some instants of the different modes propagating over the pristine (left-hand side) and damaged (right-hand side) structures. The plots show the total displacement values. Due to the smaller amplitude of the symmetric modes, these waves can only be observed in the contour plots by appropriately reducing the

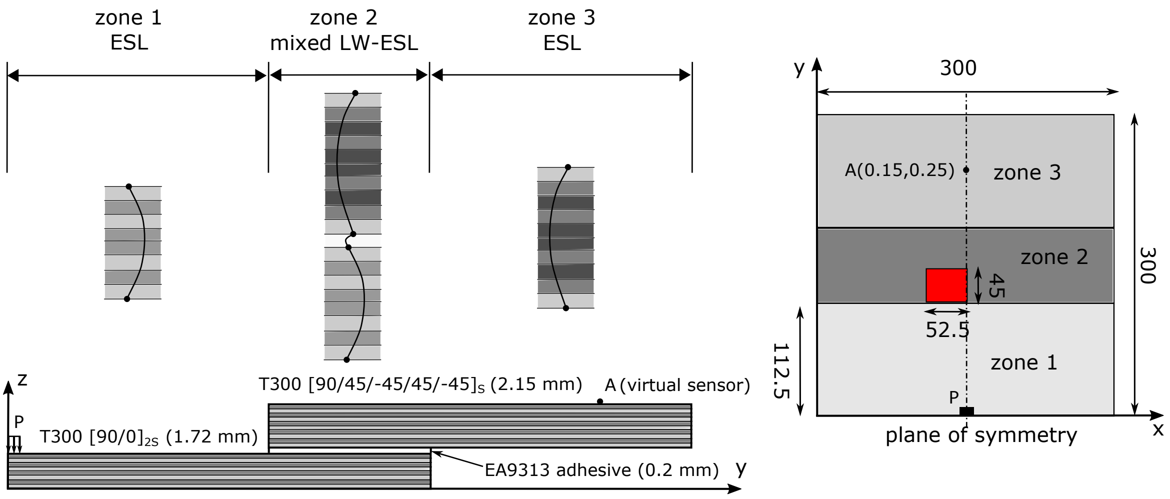
zone 1
ESL
zone 2
mixed LW-ESL
zone 3
ESL
z
P
T300 [90/0]2S (1.72 mm)
T300 [90/45/-45/45/-45]S (2.15 mm)
A (virtual sensor)
EA9313 adhesive (0.2 mm)
y
y
300
A(0.15,0.25)
zone 3
zone 2
300
45
52.5
zone 1
112.5
P
plane of symmetry
x

Fig. 11.9 Characteristics and model kinematics of the composite single-lap joint. Units in mm.

scale of the displacement magnitude. This is why the A_0 waves appear as strong red in Fig. 11.10. It is possible to observe how the principal propagation directions of the waves change from zone 1 (0° and 90°) to zone 3 (45° and -45°). The scattering of the Lamb waves in the debond is evident for both fundamental modes. It is worth noting that the model is capable of capturing the mode conversion of the long S_0 waves into shorter A_0 waves when they encounter the sudden change in the thickness at the joint area. Finally, Fig. 11.12 shows the scattering in the time signals recovered at point A for both the pristine and damaged structure. This kind of solutions are of special interest for the SHM for the further understanding of the propagation of Lamb waves in reinforced composite structures and for the optimization of the sensor placement in these systems.

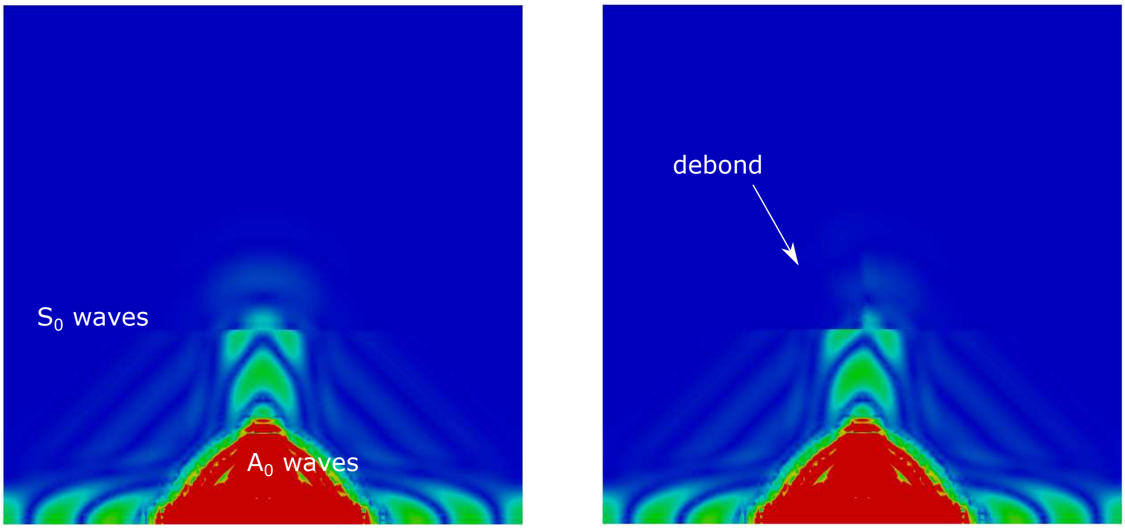

(a) Pristine, $t = 3 \times 10^{-5}$s (b) Damaged, $t = 3 \times 10^{-5}$s

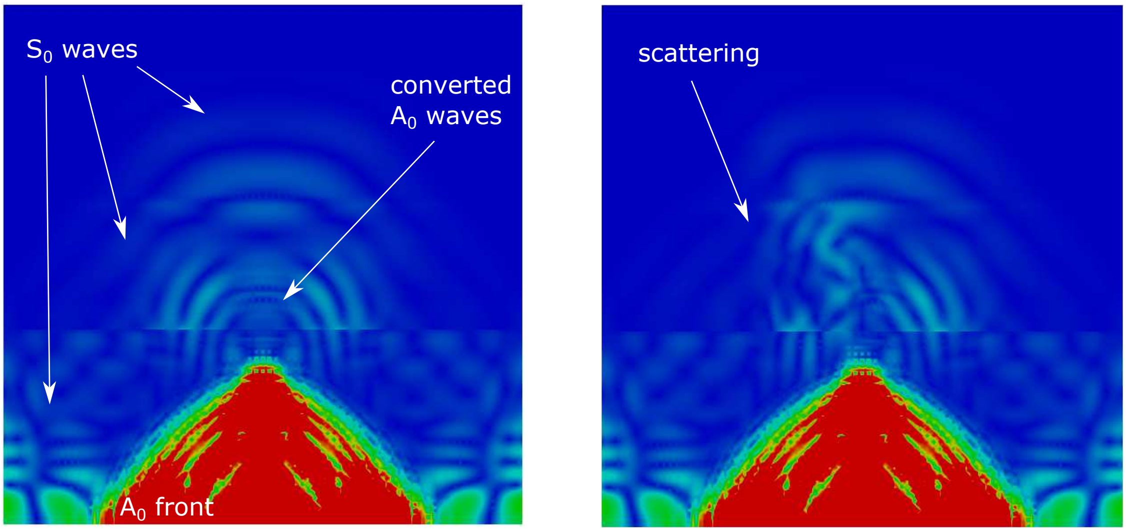

(c) Pristine, $t = 4.5 \times 10^{-5}$s (d) Damaged, $t = 4.5 \times 10^{-5}$s

Fig. 11.10 Scaled plots showing the S_0 waves propagating over the pristine, (a) and (c), and the damaged, (b) and (d), lap joints.

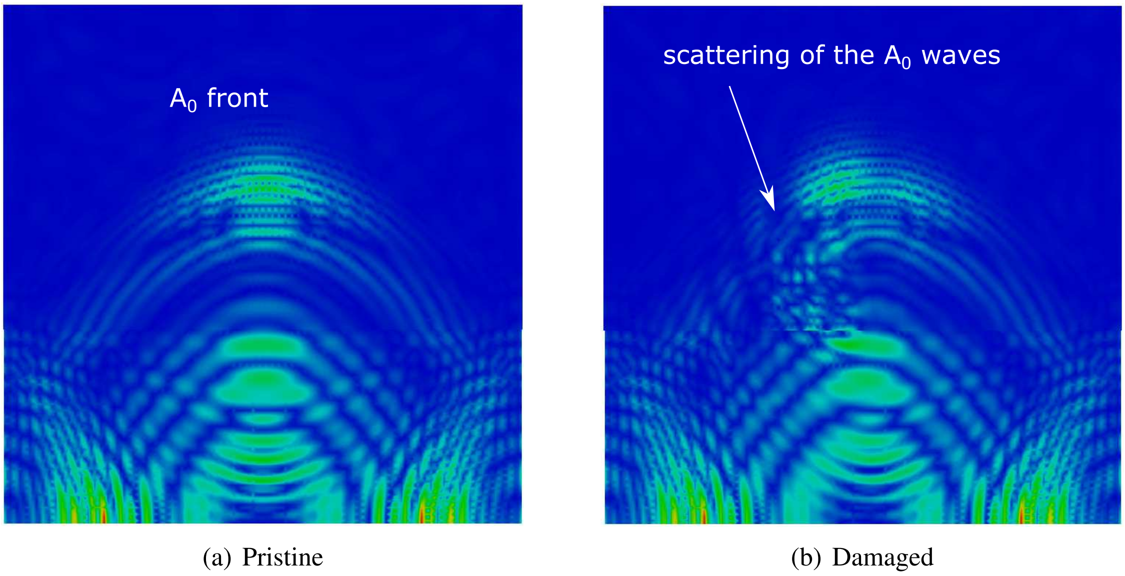

(a) Pristine (b) Damaged

Fig. 11.11 Contour plot showing the A_0 waves over the lap joint at $t = 1.2 \times 10^{-4}$ s.

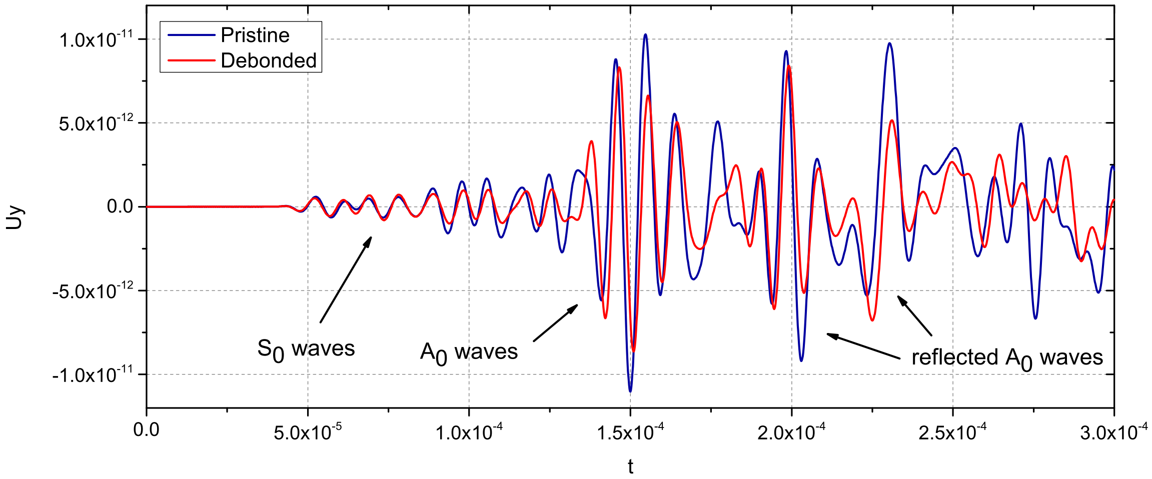

Fig. 11.12 In-plane displacements,u_y, over time obtained at point A.

Conclusions

The present thesis proposes the use of hierarchical structural theories for the mechanical analysis of composite structures at different scales. Exploiting the properties of the Carrera unified formulation (CUF) as a generator of refined beam models, a non-local structural theory was devised using Legendre polynomials of higher-order. The model, denoted to as hierarchical Legendre expansion (HLE), exhibits certain interesting characteristics for the mechanical analysis of composite structures. It enforces the adoption of a component wise (CW) approach for the simulation of composite structures, by which the constituents of the material, e.g. ply, fiber or matrix, are modeled as kinematically independent of each other. It decouples the numerical discretization in the different spatial dimensions thus overcoming the aspect ratio constraints of standard finite elements. It also allows it to link the resolution of the analysis to the polynomial order of the structural theory, which is increased easily via a user input parameter.

During the course of this research, several features have been added to the aforementioned modeling framework. A non-isoparametric mapping based on the blending function method (BFM) was implemented to compute the exact volume in curved structural bodies. The shear and membrane locking of the beam elements were mitigated by means of the mixed interpolation of tensorial components (MITC) method, which provides a better approximation of the transverse shear and membrane deformations. The Reissner's mixed variational theorem (RMVT) was adopted to derive mixed beam elements which fulfill the interlaminar equilibrium conditions in composite laminates a priori. The model was also applied in a micromechanics framework using the mechanics of structure genome (MSG) theory, the focus being on accurate computation of the effective properties and local fields of periodically heterogeneous composites. Finally, several refined approaches based on the HLE were investigated for the analysis of the propagation of Lamb waves for structural health monitoring (SHM) applications.

Probably the most powerful characteristic of the present formulation is that all the aforementioned developments can be coded by means of the same logic statements, that is expanding the building block of the model, called the fundamental nucleus, over the transverse terms and nodal indexes to build the element stiffness matrix. Eventual modifications of the variational statement, geometrical relations, constituent equations and/or kinematic assumptions are only reflected in the mathematical expressions of the fundamental nucleus. This capability made it possible to generate and test a variety of composite and metallic models for different problems using always the same modeling framework.

Main results

The main results obtained during the course of the doctoral research are summarized in the following.

- Exploiting the CW approach, the local solution fields over the heterogeneous material were computed showing high levels of accuracy and without compromising the computational cost of the analysis. 3D stress solutions were obtained at all the scales, overcoming the limitations of standard finite elements for composites.
- The CW approach based on HLE was proven to be suitable for the modeling of microstructures. The homogenized properties and local solutions obtained are comparable to those of the best micromechanics tools available.
- Mixed stress-displacement beam elements were successfully introduced as a tool to compute the correct interlaminar stresses in composite laminates. Otherwise, displacement-based models were only able to approximate the equilibrium conditions axiomatically via refinement of the kinematic assumptions.
- The computation of the transverse stresses at the free edges of generic laminated structures was investigated. The results were in very good agreement with the analytical references and reduced the cost of the numerical simulation by orders of magnitude for generic geometries and loadings.
- In the topic of structural health monitoring (SHM), HLE models demonstrated excellent convergence properties in Lamb wave simulations. The time-domain FEM analyses were optimized by decoupling the numerical discretizations in the waveguide and transverse directions.
- The adoption of different multilayered approaches in Lamb wave simulations showed many advantages with respect to classical plate elements. By virtue of the 3D kinematics, HLE-based plate elements were able to capture all the wave modes propagating

over the plane. It was also proven that the model can simulate the scattering of Lamb waves in composite laminates under discontinuities or defects very efficiently.

Future work

The modeling framework proposed in this thesis shall be considered as an starting point for subsequent extensions and applications. Firstly, it is expected to include geometrical and physical non-linearities in further developments. In particular, by adding these capabilities into the formulation, complex composite problems such as the prediction of fiber kinking or the micromechanics analysis of textiles could be studied with remarkable efficiency. Another line of research is focused in the implementation of the proposed modeling tools for laminated structures in a global-local framework, which can be used to recover the 3D stress fields on particular zones of interest. Finally, in the topic of SHM, a multi-dimensional approach will be considered in which refined beam, plate and solid elements will be assembled via superposition of the displacement unknowns located in the geometrical boundaries of the represented domains.

References

[1] (2014). *DIGIMAT user's manual (Release 5.1.2)*. e-Xstream MSC Software Company.

[2] (2017). *ASTM D3039/D3039M-17 Standard Test Method for Tensile Properties of Polymer Matrix Composite Materials*. ASTM International, West Conshohocken, PA.

[3] Aboudi, J. (1982). A continuum theory for fiber-reinforced elastic-viscoplastic composites. *International Journal of Engineering Science*, 20(5):605 – 621.

[4] Aboudi, J., Arnold, S., and Bednarcyk, B., editors (2013). *Micromechanics of Composite Materials*. Butterworth-Heinemann, Oxford.

[5] Aboudi, J., Pindera, M., and Arnold, S. (2001). Linear thermoelastic higher-order theory for periodic multiphase materials. *Journal of Applied Mechanics*, 68(5):697 – 707.

[6] Arya, H., Shimpi, R., and Naik, N. (2002). A zigzag model for laminated composite beams. *Composite Structures*, 56(1):21 – 24.

[7] Ashwell, D. and Gallagher, R. H. (1976). *Finite element for thin shells and curved members*. Willey, London.

[8] Atluri, S. N., Iura, M., and Vasudevan, S. (2001). A consistent theory of finite stretches and finite rotations, in space-curved beams of arbitrary cross-section. *Computational Mechanics*, 27(4):271–281.

[9] Babu, C. R. and Prathap, G. (1986). A linear thick curved beam element. *International Journal for Numerical Methods in Engineering*, 23(7):1313–1328.

[10] Banan, M., Karami, G., and Farshad, M. (1989). Finite element analysis of curved beams on elastic foundations. *Computers & Structures*, 32(1):45 – 53.

[11] Barlow, J. (1976). Optimal stress locations in finite element models. *International Journal for Numerical Methods in Engineering*, 10(2):243–251.

[12] Bartoli, I., Marzani, A., di Scalea, F. L., and Viola, E. (2006). Modeling wave propagation in damped waveguides of arbitrary cross-section. *Journal of Sound and Vibration*, 295(3):685 – 707.

[13] Bathe, K. J. (1996). *Finite element procedure*. Prentice hall.

[14] Bathe, K.-J. and Dvorkin, E. N. (1986). A formulation of general shell elements—the use of mixed interpolation of tensorial components. *International Journal for Numerical Methods in Engineering*, 22(3):697–722.

[15] Becker, W. (1993). Closed-form solution for the free-edge effect in cross-ply laminates. *Composite Structures*, 26(1):39 – 45.

[16] Bednarcyk, B. and Arnold, S. (2002). Mac/gmc 4.0 user's manual,volume 2: keywords manual, tm 2002-212077. *Journal of Constructional Steel Research*, 2.

[17] Belytschko, T., Stolarski, H., Liu, W., Carpenter, N., and J.S.-J., O. (1985). Stress projection for membrane and shear locking in shell finite elements. *Comput. Methods Appl. Mech. Engrg*, 51:221–258.

[18] Bensoussan, A., Lions, J., and Papanicolaou, G. (1978). *Asymptotic Analysis for Periodic Structures*. North-Holland.

[19] Berdichevskii, V. (1977). On averaging of periodic systems. *Journal of Applied Mathematics and Mechanics*, 41(6):1010 – 1023.

[20] Bocchini, P., Marzani, A., and Viola, E. (2011). Graphical user interface for guided acoustic waves. *Journal of Computing in Civil Engineering*, 25(3):202–210.

[21] Brewer, J. and Lagace, P. (1988). Quadratic stress criterion for initiation of delamination. *Journal of composite materials*, 22(12):1141–1155.

[22] Bucalem, M. and Bathe, K.-J. (1993). Higher-order MITC general shell elements. *International Journal for Numerical Methods in Engineering*, 36(21):3729–3754.

[23] Carrera, E. (1996). C0 Reissner-Mindlin multilayered plate elements including zig-zag and interlaminar stress continuity. *International Journal for Numerical Methods in Engineering*, 39(11):1797–1820.

[24] Carrera, E. (1997). C0z requirements - models for the two dimensional analysis of multilayered structures. *Composite Structures*, 37(3):373 – 383.

[25] Carrera, E. (1998). Evaluation of layerwise mixed theories for laminated plates analysis. *AIAA Journal*, 36(5):830–839.

[26] Carrera, E. (2001). Developments, ideas, and evaluations based upon reissner's mixed variational theorem in the modeling of multilayered plates and shells. *Applied Mechanics Reviews*, 54:301 – 329.

[27] Carrera, E. (2003a). Historical review of zig-zag theories for multilayered plates and shells. *Applied Mechanics Reviews*, 56(3):287–308.

[28] Carrera, E. (2003b). Theories and finite elements for multilayered plates and shells: a unified compact formulation with numerical assessment and benchmarking. *Archives of Computational Methods in Engineering*, 10(3):216–296.

[29] Carrera, E., Cinefra, M., Zappino, E., and Petrolo, M. (2014). *Finite Element Analysis of Structures Through Unified Formulation*. John Wiley and Sons, Ltd.

[30] Carrera, E., de Miguel, A. G., and Pagani, A. (2017a). Extension of MITC to higher-order beam models and shear locking analysis for compact, thin-walled, and composite structures. *International Journal for Numerical Methods in Engineering*, 112(13):1889–1908.

[31] Carrera, E., de Miguel, A. G., and Pagani, A. (2017b). Hierarchical one-dimensional finite elements based on Legendre polynomial expansions. *International Journal of Mechanical Sciences*, 120:286 – 900.

[32] Carrera, E. and Demasi, L. (2002). Classical and advanced multilayered plate elements based upon PVD and RMVT. part 1: Derivation of finite element matrices. *International Journal for Numerical Methods in Engineering*, 55(2):191–231.

[33] Carrera, E. and Filippi, M. (2014). Variable kinematic one-dimensional finite elements for the analysis of rotors made of composite materials. *Journal of Engineering for Gas Turbines and Power*, 136(9):art. n. 092501.

[34] Carrera, E. and Giunta, G. (2010). Refined beam theories based on Carrera's unified formulation. *International Journal of Applied Mechanics*, 2(1):117–143.

[35] Carrera, E., Maiarù, M., and Petrolo, M. (2012). Component-wise analysis of laminated anisotropic composites. *International Journal of Solids and Structures*, 49:1839–1851.

[36] Carrera, E. and Pagani, A. (2014a). Free vibration analysis of civil engineering structures by component-wise models. *Journal of Sound and Vibration*, 333(19):4597–4620.

[37] Carrera, E. and Pagani, A. (2014b). Multi-line enhanced beam model for the analysis of laminated composite structures. *Composites: Part B*, 57:112–119.

[38] Carrera, E. and Pagani, A. (2015). Evaluation of the accuracy of classical beam FE models via locking-free hierarchically refined elements. *International Journal of Mechanical Sciences*, 100:169–179.

[39] Carrera, E., Pagani, A., and Petrolo, M. (2013a). Component-wise method applied to vibration of wing structures. *Journal of Applied Mechanics*, 80(4):art. no. 041012 1–15.

[40] Carrera, E., Pagani, A., and Petrolo, M. (2013b). Use of Lagrange multipliers to combine 1D variable kinematic finite elements. *Computers & Structures*, 129:194–206.

[41] Carrera, E. and Petrolo, M. (2012a). Refined beam elements with only displacement variables and plate/shell capabilities. *Meccanica*, 47(3):537–556.

[42] Carrera, E. and Petrolo, M. (2012b). Refined one-dimensional formulations for laminated structure analysis. *AIAA Journal*, 50(1):176–189.

[43] Cavalcante, M. A., Pindera, M.-J., and Khatam, H. (2012). Finite-volume micromechanics of periodic materials: Past, present and future. *Composites Part B: Engineering*, 43(6):2521 – 2543.

[44] Cavalcante, M. A., Pindera, M.-J., and Khatam, H. (2013). Generalized FVDAM theory for periodic materials undergoing finite deformations—part I: Framework. *Journal of Applied Mechanics*, 81(2):021005.

[45] Chinosi, C., Della Croce, L., and Scapolla, T. (1998). Hierarchic finite elements for thin Naghdi shell model. *International Journal of Solids and Structures*, 35(16):1863 – 1880.

[46] Cho, M. and Kim, H. S. (2000). Iterative free-edge stress analysis of composite laminates under extension, bending, twisting and thermal loadings. *International Journal of Solids and Structures*, 37(3):435 – 459.

[47] Cho, M. and Parmerter, R. (1993). Efficient higher order composite plate theory for general lamination configurations. *AIAA Journal*, 31(7):11299 – 1306.

[48] Cho, M. and Yoon, J. Y. (1999). Free-edge interlaminar stress analysis of composite laminates by extended kantorovich method. *AIAA Journal*, 37(5):656–660.

[49] Christensen, R. and Lo, K. (1979). Solutions for effective shear properties in three phase sphere and cylinder models. *Journal of the Mechanics and Physics of Solids*, 27(4):315 – 330.

[50] Cinefra, M., Chinosi, C., and Della Croce, L. (2013). MITC9 shell elements based on refined theories for the analysis of isotropic cylindrical structures. *Mechanics of Advanced Materials and Structures*, 20(2):91–100.

[51] Corporation, M. (2010). MD Nastran 2010 Quick Reference Guide.

[52] Courant, R., Friedrichs, K., and Lewy, H. (1928). Über die partiellen Differenzengleichungen der mathematischen Physik. *Mathematische Annalen*, 100:32–74.

[53] Crisfield, M. (1984). A quadratic Mindlin element using shear constraints. *Computers & Structures*, 18(5):833 – 852.

[54] Crossman, F. W. and Wang, A. (1982). The dependence of transverse cracking and delamination on ply thickness in graphite/epoxy laminates. *Damage in Composite Materials: Basic Mechanisms, Accumulation, Tolerance, and Characterization*, pages 118 – 139.

[55] Datta, S. K., Shah, A. H., Bratton, R. L., and Chakraborty, T. (1988). Wave propagation in laminated composite plates. *The Journal of the Acoustical Society of America*, 83(6):2020–2026.

[56] Dauksher, W. and Emery, A. (1997). Accuracy in modeling the acoustic wave equation with Chebyshev spectral finite elements. *Finite Elements in Analysis and Design*, 26(2):115 – 128.

[57] Dawe, D. (1974). Numerical studies using circular arch finite elements. *Computers & Structures*, 4(4):729 – 740.

[58] de Miguel, A., Carrera, E., and Pagani, A. (2018a). Accurate evaluation of interlaminar stresses in composite laminates via mixed one-dimensional formulation. *AIAA Journal*, 56:4582 – 4594.

[59] de Miguel, A., Pagani, A., and Carrera, E. (2018b). Efficient finite element analysis of lamb waves and damage detection. Submitted.

[60] de Miguel, A., Pagani, A., Yu, W., and Carrera, E. (2017). Micromechanics of periodically heterogeneous materials using higher-order beam theories and the mechanics of structure genome. *Composite Structures*, 180:484 – 496.

[61] de Miguel, A., Pietro, G. D., Carrera, E., Giunta, G., and Pagani, A. (2018c). Locking-free curved elements with refined kinematics for the analysis of composite structures. *Computer Methods in Applied Mechanics and Engineering*, 337:481 – 500.

[62] De Pietro, G., de Miguel, A., Carrera, E., Giunta, G., Belouettar, S., and Pagani, A. (2017). Strong and weak form solutions of curved beams via carrera's unified formulation. Submitted.

[63] Dedè, L., Jäggli, C., and Quarteroni, A. (2015). Isogeometric numerical dispersion analysis for two-dimensional elastic wave propagation. *Computer Methods in Applied Mechanics and Engineering*, 284:320 – 348. Isogeometric Analysis Special Issue.

[64] Delsanto, P., Whitcombe, T., Chaskelis, H., and Mignogna, R. (1992). Connection machine simulation of ultrasonic wave propagation in materials. I: the one-dimensional case. *Wave Motion*, 16(1):65 – 80.

[65] Dhanesh, N., Kapuria, S., and Achary, G. G. S. (2017). Accurate prediction of three-dimensional free edge stress field in composite laminates using mixed-field multiterm extended kantorovich method. *Acta Mechanica*, 228(8):2895–2919.

[66] Doherty, W. and Wilson, E.L. Taylor, R. (1969). Stress analysis of axisymmetric solids utilizing higher order quadrilateral finite elements. *Structural Engineering Laboratory, University of California, Berkeley, CA*.

[67] D'Ottavio, M., Vidal, P., Valot, E., and Polit, O. (2013). Assessment of plate theories for free-edge effects. *Composites Part B: Engineering*, 48:111 – 121.

[68] Duczek, S., Joulaian, M., Düster, A., and Gabbert, U. (2014). Numerical analysis of lamb waves using the finite and spectral cell methods. *International Journal for Numerical Methods in Engineering*, 99(1):26–53.

[69] Dvorkin, E. and Bathe, K. (1984). A continuum mechanics based four-node shell element for general non-linear analysis. *Engineering Computations*, 1(1):77–88.

[70] E. Carrera, M. Filippi, E. Z. (2013). Laminated beam analysis by polynomial, trigonometric, exponential and zig-zag theories. *European Journal of Mechanics A/Solids*. Published.

[71] E. Carrera, G. Giunta, M. P. (2011). *Beam structures: classical and advanced theories*. John Wiley and Sons.

[72] Ericksen, J. and Truesdell, C. (1957). Exact theory of stress and strain in rods and shells. *Archive for Rational Mechanics and Analysis*, 1(1):295 – 323.

[73] Euler, L. (1744). *De curvis elasticis*. Lausanne and Geneva: Bousquet.

[74] Falzon, B. and Tan, W. (2017). *Virtual Testing of Composite Structures: Progress and Challenges in Predicting Damage, Residual Strength and Crashworthiness*. Springer, Cham.

[75] Ferreira, A., Roque, C., and Jorge, R. (2005). Analysis of composite plates by trigonometric shear deformation theory and multiquadrics. *Computers & Structures*, 83(27):2225 – 2237.

[76] Fish, J. and Yu, Q. (2002). Computational mechanics of fatigue and life predictions for composite materials and structures. *Computer Methods in Applied Mechanics and Engineering*, 191(43):4827 – 4849.

[77] Flanagan, G. (1994). An efficient stress function approximation for the free-edge stresses in laminates. *International Journal of Solids and Structures*, 31(7):941 – 952.

[78] Fried, I. (1973). Shape functions and the accuracy of arch finite elements. *AIAA Journal*, 11(3):287 – 291.

[79] Giunta, G., Biscani, F., Belouettar, S., and Carrera, E. (2011). Analysis of thin-walled beams via a one-dimensional unified formulation through a Navier-type solution. *International Journal of Applied Mechanics*, 03(03):407–434.

[80] Giurgiutiu, V. (2014). *Structural Health Monitoring with Piezoelectric Wafer Active Sensors (Second Edition)*. Academic Press, Oxford, second edition edition.

[81] Gordon, W. and Hall, C. (1973). Transfinite element methods: Blending-function interpolation over arbitrary curved element domains. *Numerische Mathematik*, 21(2):109–129.

[82] Graff, K. F. (1975). *Wave Motion in Elastic Solids*. Dover Publications, Inc, USA.

[83] Groh, R. and Weaver, P. (2015). On displacement-based and mixed-variational equivalent single layer theories for modelling highly heterogeneous laminated beams. *International Journal of Solids and Structures*, 59(Supplement C):147 – 170.

[84] Group, E. (2013). *Virtual Performance Solution. Solver Notes Manual.*

[85] Ham, S. and Bathe, K.-J. (2012). A finite element method enriched for wave propagation problems. *Computers & Structures*, 94-95:1 – 12.

[86] Hashin, Z. (1980). Failure criteria for unidirectional fiber composites. *Journal of applied mechanics*, 47(2):329–334.

[87] Hashin, Z. and Shtrikman, S. (1962). A variational approach to the theory of the elastic behaviour of polycrystals. *Journal of the Mechanics and Physics of Solids*, 10(4):343 – 352.

[88] Hassani, B. and Hinton, E. (1998). A review of homogenization and topology optimization i—homogenization theory for media with periodic structure. *Computers & Structures*, 69(6):707 – 717.

[89] Hayashi, T. (1967). Analytical study of interlaminar shear stresses in a laminated composite plate. *Transaction of Japan Society for Aeronautical Engineering and Space Science*, 66:43–48.

[90] Hill, R. (1952). The elastic behaviour of a crystalline aggregate. *Proceedings of the Physical Society. Section A*, 65(5):349.

[91] Hinton, M., Kaddour, A., and Soden, P. (2000). *Failure Criteria in Fibre-Reinforced-Polymer Composites. The World-Wide Failure Exercise*. Oxford: Elsevier.

[92] Hu, N., Liu, Y., Li, Y., Peng, X., and Yan, B. (2010). Optimal excitation frequency of Lamb waves for delamination detection in cfrp laminates. *Journal of Composite Materials*, 44(13):1643 – 1663.

[93] Huang, H. C. and Hinton, E. (1986). A new nine node degenerated shell element with enhanced membrane and shear interpolation. *International Journal for Numerical Methods in Engineering*, 22(1):73–92.

[94] Hughes, T. and Cohen, M. (1978). The 'heterosis' finite element for plate bending. *Computers & Structures*, 9(5):445 – 450.

[95] Hughes, T., Cohen, M., and Haroun, M. (1978). Reduced and selective integration techniques in the Finite Element Analysis of plates. *Nuclear Engineering and Design*, 46(1):203 – 222.

[96] Jang, J. and Pinsky, P. M. (1987). An assumed covariant strain based 9-node shell element. *International Journal for Numerical Methods in Engineering*, 24(12):2389–2411.

[97] Jones, R. M. (1998). *Mechanics of composite materials*. Taylor and Francis Ltd., London, UK, 2^{nd} edition.

[98] Kaddour, A. and Hinton, M. (2012). Input data for test cases used in benchmarking triaxial failure theories of composites. *Journal of Composite Materials*, 46(19-20):2295–2312.

[99] Kant, T., Owen, D., and Zienkiewicz, O. (1982). A refined higher-order C° plate bending element. *Computers & Structures*, 15(2):177 – 183.

[100] Kapania, R. and Raciti, S. (1989a). Recent advances in analysis of laminated beams and plates, part I: Shear effects and buckling. *AIAA Journal*, 27(7):923–935.

[101] Kapania, R. and Raciti, S. (1989b). Recent advances in analysis of laminated beams and plates, part II: Vibrations and wave propagation. *AIAA Journal*, 27(7):935–946.

[102] Kassapoglou, C. and Lagace, P. A. (1987). Closed form solutions for the interlaminar stress field in angle-ply and cross-ply laminates. *Journal of Composite Materials*, 21(4):292–308.

[103] Ke, W., Castaings, M., and Bacon, C. (2009). 3D finite element simulations of an air-coupled ultrasonic NDT system. *NDT & E International*, 42(6):524 – 533.

[104] Kim, J. G. and Kim, Y. Y. (1998). A new higher-order hybrid-mixed curved beam element. *International Journal for Numerical Methods in Engineering*, 43(5):925–940.

[105] Komatitsch, D. and Tromp, J. (2002a). Spectral-element simulations of global seismic wave propagation — I. validation. *Geophysical Journal International*, 149(2):390–412.

[106] Komatitsch, D. and Tromp, J. (2002b). Spectral-element simulations of global seismic wave propagation—i. validation. *Geophysical Journal International*, 149(2):390–412.

[107] Kudela, P., Ż., A., Krawczuk, M., and Ostachowicz, W. (2007a). Modelling of wave propagation in composite plates using the time domain spectral element method. *Journal of Sound and Vibration*, 302(4):728 – 745.

[108] Kudela, P., Krawczuk, M., and Ostachowicz, W. (2007b). Wave propagation modelling in 1D structures using spectral finite elements. *Journal of Sound and Vibration*, 300(1):88 – 100.

[109] Lamb, H. (1889). On the deformation of an elastic shell. *Proceedings of the London Mathematical Society*, s1-21(1):119–146.

[110] Lamb, H. (1917). On waves in an elastic plate,. *Roy. Soc. Lond. Proc. Ser. A*, 93:114 – 128.

[111] Lammering, R., Gabbert, U., Sinapius, M., Schuster, T., and Wierach, P., editors (2018). *Lamb-Wave Based Structural Health Monitoring in Polymer Composites*. Springer, Cham, Switzerland.

[112] Lee, B. C. and Staszewski, W. J. (2003). Modelling of Lamb waves for damage detection in metallic structures: Part I. Wave propagation. *Smart Materials and Structures*, 12(5):804.

[113] Lee, P.-S., Noh, H.-C., and Choi, C.-K. (2008). Geometry-dependent MITC method for a 2-node iso-beam element. *Structural Engineering and Mechanics*, 29(2):2203–221.

[114] Lekhniskii, S. (1968). *Anisotropic plates*. Gordon & Breach, New York. translated from 2nd russian Edition by S.W. Tsai and T. Cheron.

[115] Lekhnitskii, S. (0000). Strength calculation of composite beams. *Vestnik inzhen i tekhnikov*. No 9.

[116] Lessard, L. B., Schmidt, A. S., and Shokrieh, M. M. (1996). Three-dimensional stress analysis of free-edge effects in a simple composite cross-ply laminate. *International Journal of Solids and Structures*, 33(15):2243 – 2259.

[117] Li, D., Liu, Y., and Zhang, X. (2015). An extended layerwise method for composite laminated beams with multiple delaminations and matrix cracks. *International Journal for Numerical Methods in Engineering*, 101(6):407–434.

[118] Li, F., Peng, H., X., S., Wang, J., and Meng, G. (2012). Wave propagation analysis in composite laminates containing a delamination using a three-dimensional spectral element method. *Mathematical Problems in Engineering*, 659849.

[119] LLorca, J., González, C., Molina-Aldareguía, J. M., Segurado, J., Seltzer, R., Sket, F., Rodríguez, M., Sádaba, S., Muñoz, R., and Canal, L. P. (2011). Multiscale modeling of composite materials: a roadmap towards virtual testing. *Advanced Materials*, 23(44):5130–5147.

[120] Lo, K., Christensen, R., and Wu, E. (1977). A high-order theory of plate deformation. Part 2: laminated plates. *Journal of Applied Mechanics*, 44:669.

[121] Love, A. E. H. (1888). The small free vibrations and deformation of a thin elastic shell. *Philosophical Transactions of the Royal Society of London. A*, 179:491–546.

[122] Lowe, M. J. S. (1995). Matrix techniques for modeling ultrasonic waves in multilayered media. *IEEE Transactions on Ultrasonics, Ferroelectrics, and Frequency Control*, 42(4):525–542.

[123] MacNeal, R. (1982). Derivation of element stiffness matrices by assumed strain distributions. *Nuclear Engineering and Design*, 70(1):3 – 12.

[124] Macneal, R. and Harder, R. (1985). A proposed standard set of problems to test finite element accuracy. *Finite Elements in Analysis and Design*, 1(1):3 – 20.

[125] Maiarù, M., Petrolo, M., and Carrera, E. (2017). Evaluation of energy and failure parameters in composite structures via a component-wise approach. *Composites Part B*, 108:53–64.

[126] Malkus, D. and Hughes, T. (1978). Mixed finite element methods — reduced and selective integration techniques: A unification of concepts. *Computer Methods in Applied Mechanics and Engineering*, 15(1):63 – 81.

[127] Martin, E., Leguillon, D., and Carrère, N. (2010). A twofold strength and toughness criterion for the onset of free-edge shear delamination in angle-ply laminates. *International Journal of Solids and Structures*, 47(9):1297 – 1305.

[128] Matsunaga, H. (2002). Interlaminar stress analysis of laminated composite beams according to global higher-order deformation theories. *Composite Strucutures*, 55:105–114.

[129] Mittelstedt, C. and Becker, W. (2004). Interlaminar stress concentrations in layered structures: Part i - a selective literature survey on the free-edge effect since 1967. *Journal of Composite Materials*, 38(12):1037–1062.

[130] Mori, T. and Tanaka, K. (1973). Average stress in matrix and average elastic energy of materials with misfitting inclusions. *Acta Metallurgica*, 21(5):571 – 574.

[131] Moser, F., Jacobs, L. J., and Qu, J. (1999). Modeling elastic wave propagation in waveguides with the finite element method. *NDT & E International*, 32(4):225 – 234.

[132] Murakami, H. (1986). Laminated composite plate theory with improved in-plane responses. *Journal of Applied Mechanics*, 53(3):661 – 666.

[133] Murakami, H., Reissner, E., and Yamakawa, J. (1996). Anisotropic beam theories with shear deformation. *Journal of Applied Mechanics*, 63(3):660 – 668.

[134] Murakami, H. and Toledano, A. (1990). A High-Order Mixture Homogenization of Bi-laminated Composites. *Journal of Applied Mechanics*, 57:388.

[135] Murakami, H. and Yamakawa, J. (1997). Dynamic response of plane anisotropic beams with shear deformation. *Journal of Engineering Mechanics*, 123(12):1268–1275.

[136] Murat, B. I. S., Khalili, P., and Fromme, P. (2016). Scattering of guided waves at delaminations in composite plates. *The Journal of the Acoustical Society of America*, 139(6):3044–3052.

[137] Nemat-Nasser, S. and Hori, M. M. (1993). *Micromechanics : overall properties of heterogeneous materials*. Amsterdam New York North-Holland.

[138] Newmark, N. (1959). A method of computation for structural dynamics. *Journal of the Engineering Mechanics Division*, 85(3):67 – 94.

[139] Ng, C.-T. and Veidt, M. (2011a). Scattering of the fundamental anti-symmetric Lamb wave at delaminations in composite laminates. *The Journal of the Acoustical Society of America*, 129(3):1288–1296.

[140] Ng, C.-T. and Veidt, M. (2011b). Scattering of the fundamental anti-symmetric lamb wave at delaminations in composite laminates. *The Journal of the Acoustical Society of America*, 129(3):1288–1296.

[141] Noor, A. K. and Peters, J. M. (1981). Mixed models and reduced/selective integration displacement models for nonlinear analysis of curved beams. *International Journal for Numerical Methods in Engineering*, 17(4):615–631.

[142] Obenchain, M. B. and Cesnik, C. E. S. (2013). Producing accurate wave propagation time histories using the global matrix method. *Smart Materials and Structures*, 22(125024).

[143] Pagani, A., Boscolo, M., Banerjee, J., and Carrera, E. (2013). Exact dynamic stiffness elements based on one-dimensional higher-order theories for free vibration analysis of solid and thin-walled structures. *Journal of Sound and Vibration*, 332(23):6104 – 6127.

[144] Pagani, A., de Miguel, A., and Carrera, E. (2017a). Component-wise analysis of laminated structures by hierarchical refined models with mapping features and enhanced accuracy at layer to fiber-matrix scales. *Mechanics of Advanced Materials and Structures*. In Press.

[145] Pagani, A., de Miguel, A., and Carrera, E. (2017b). Cross-sectional mapping for refined beam elements with applications to shell-like structures. *Computational Mechanics*, 59:1031–1048.

[146] Pagano, N. (1969a). Exact solutions for composite laminates in cylindrical bending. *Journal of Composite Materials*, 3(3):398–411.

[147] Pagano, N. (1969b). Exact solutions for composite laminates in cylindrical bending. *Journal of Composite Materials*, 3(3):398–411.

[148] Pagano, N. (1970). Influence of shear coupling in cylindrical bending of anisotropic laminates. *Journal of Composite Materials*, 4(3):330–343.

[149] Pagano, N. (1974). On the calculation of interlaminar normal stress in composite laminate. *Journal of Composite Materials*, 8:65–81.

[150] Paley, M. and Aboudi, J. (1992). Micromechanical analysis of composites by the generalized cells model. *Mechanics of Materials*, 14(2):127 – 139.

[151] Pandya, B. and Kant, T. (1988). Higher-order shear deformable theories for flexure of sandwich plates. Finite element evaluations. *International Journal of Solids and Structures*, 24(12):1267 – 1286.

[152] Park, K. and Flaggs, D. (1985). A symbolic fourier synthesis of a one-point integrated quadrilateral plate element. *Computer Methods in Applied Mechanics and Engineering*, 48(2):203 – 236.

[153] Park, K. and Stanley, G. (1986). A curved C^0 shell element based on assumed natural-coordinate strains. *Journal of Applied Mechanics*, 53(2):278–290.

[154] Peng, B., Goodsell, J., Pipes, R., and Yu, W. (2016). Generalized free-edge stress analysis using mechanics of structure genome. *Journal of Applied Mechanics*, 83(10):101013–7.

[155] Petrolo, M., Kaleel, I., Pietro, G. D., and Carrera, E. (2018). Wave propagation in compact, thin-walled, layered, and heterogeneous structures using variable kinematics finite elements. *International Journal for Computational Methods in Engineering Science and Mechanics*, 19(3):207–220.

[156] Pian, T. (1964). Derivation of element stiffness matrices by assumed stress distributions. *AIAA Journal*, 2(7):1333–1336.

[157] Pipes, R. and Pagano, N. (1970). Interlaminar stresses in composite laminates under uniform axial extension. *Journal of Composite Materials*, 4(4):538–548.

[158] Pipes, R. and Pagano, N. (1974). Interlaminar stresses in composite laminates - an approximate elasticity solution. *Journal of Applied Mechanics*, 41(3):668–672.

[159] Pipes, R. B. (1971). Moiré analysis of the interlaminar shear edge effect in laminated composites. *Journal of Composite Materials*, 5(2):255–259.

[160] Prathap, G. and Bhashyam, G. R. (1982). Reduced integration and the shear-flexible beam element. *International Journal for Numerical Methods in Engineering*, 18(2):195–210.

[161] Puppo, A. and Evensen, H. (1970). Interlaminar shear in laminated composites under generalized plane stress. *Journal of Composite Materials*, 4(2):204–220.

[162] Raju, I. and Crews, J. H. (1981). Interlaminar stress singularities at a straight free edge in composite laminates. *Computers and Structures*, 14(1):21 – 28.

[163] Rao, M., Desai, Y., and Chistnis, M. (2001). Free vibrations of laminated beams using mixed theory. *Composite Structures*, 52:149–160.

[164] Reddy, J. N. (1980). A penalty plate-bending element for the analysis of laminated anisotropic composite plates. *International Journal for Numerical Methods in Engineering*, 15(8):1187–1206.

[165] Reddy, J. N. (1984). A simple higher-order theory for laminated composite plates. *Journal of Applied Mechanics*, 51(4):745 – 752.

[166] Reddy, J. N. (1986). A simple higher-order theory for laminated composites. *Journal of Applied Mechanics*, 51:745–752.

[167] Reddy, J. N. (1987). A generalization of two-dimensional theories of laminated composite plates. *Communications in Applied Numerical Methods*, 3(3):173–180.

[168] Reddy, J. N. (1989). On refined computational models of composite laminates. *International Journal for Numerical Methods in Engineering*, 27(2):361–382.

[169] Reddy, J. N. (1997). On locking-free shear deformable beam finite elements. *Computer Methods in Applied Mechanics and Engineering*, 149:113–132.

[170] Reddy, J. N. (2004). *Mechanics of laminated composite plates and shells. Theory and Analysis*. CRC Press, 2^{nd} edition.

[171] Reissner, E. (1944). On the theory of bending of elastic plates. *Journal of Mathematics and Physics*, 23(1-4):184–191.

[172] Reissner, E. (1973). On one-dimensional large-displacement finite-strain beam theory. *Studies in Applied Mathematics*, 52(2):87–95.

[173] Reissner, E. (1984). On a certain mixed variational theorem and a proposed application. *International Journal for Numerical Methods in Engineering*, 20(7):1366–1368.

[174] Reissner, E. (1986). On a mixed variational theorem and on shear deformable plate theory. *International Journal for Numerical Methods in Engineering*, 23(2):193–198.

[175] Robbins, D. H. and Reddy, J. N. (1993). Modelling of thick composites using a layerwise laminate theory. *International Journal for Numerical Methods in Engineering*, 36(4):655–677.

[176] Rodrigues, J., Roque, C., Ferreira, A., Carrera, E., and Cinefra, M. (2011). Radial basis functions–finite differences collocation and a unified formulation for bending, vibration and buckling analysis of laminated plates, according to Murakami's zig-zag theory. *Composite Structures*, 93(7):1613 – 1620.

[177] Saeedi, N., Sab, K., and Caron, J.-F. (2012). Delaminated multilayered plates under uniaxial extension. part i: Analytical analysis using a layerwise stress approach. *International Journal of Solids and Structures*, 49(26):3711 – 3726.

[178] Schulte, R. T. and Fritzen, C.-P. (2011). Simulation of wave propagation in damped composite structures with piezoelectric coupling. *Journal of Theoretical and Applied Mechanics*, 49(3).

[179] Schulte, R. T., Fritzen, C.-P., and Moll, J. (2010). Spectral element modelling of wave propagation in isotropic and anisotropic shell-structures including different types of damage. *IOP Conference Series: Materials Science and Engineering*, 10(1):012065.

[180] Scordelis, A. and Lo, K. (1964). Computer analysis of cylindrical shells. *J. Am. Concrete Inst.*, 61:561–593.

[181] Sertse, H. M., Goodsell, J., Ritchey, A. J., Pipes, R. B., and Yu, W. (2017). Challenge problems for the benchmarking of micromechanics analysis: Level I initial results. *Journal of Composite Materials*, 0(0):1–20.

[182] Shimpi, R. P. and Ghugal, Y. M. (2001). A new layerwise trigonometric shear deformation theory for two-layered cross-ply beams. *Composites Science and Technology*, 61(9):1271 – 1283.

[183] Smith, M. (2009). *ABAQUS/Standard User's Manual, Version 6.9*. Simulia.

[184] Spilker, R. and Munir, N. (1980). The hybrid-stress model for thin plates. *International Journal for Numerical Methods in Engineering*, 15(8):1239–1260.

[185] Stolarski, H. and Belytschko, T. (1982). Membrane locking and reduced integration for curved elements. *Journal of Applied Mechanics*, 49(1):172 – 176.

[186] Sun, C. and Vaidya, R. (1996). Prediction of composite properties from a representative volume element. *Composites Science and Technology*, 56(2):171 – 179.

[187] Surana, K. and Nguyen, S. (1990). Two-dimensional curved beam element with higher-order hierarchical transverse approximation for laminated composites. *Computers & Structures*, 36(3):499–511.

[188] Surana, K., N. S. (1990). Two-dimensional curved beam element with higherorder hierarchical transverse approximation for laminated composites. *Computers and Structures*, 36:499–511.

[189] Szabó, B. and Babuška, I. (1991). *Finite Element Analysis*. John Wiley and Sons, Ltd.

[190] Tahani, M. (2007). Analysis of laminated composite beams using layerwise displacement theories. *Composite Structures*, 79(4):535 – 547.

[191] Tahani, M. and Nosier, A. (2003). Edge effects of uniformly loaded cross-ply composite laminates. *Materials and Design*, 24(8):647 – 658.

[192] Tessler, A. (2015). Refined zigzag theory for homogeneous, laminated composite, and sandwich beams derived from reissner's mixed variational principle. *Meccanica*, 50(10):2621–2648.

[193] Tessler, A., Di Sciuva, M., and Gherlone, M. (2007). Refinement of timoshenko beam theory for composite and sandwich beams using zigzag kinematics. Technical Report 215086, National Aeronautics and Space Administration.

[194] Tessler, A. and Dong, S. (1981). On a hierarchy of conforming Timoshenko beam elements. *Computers & Structures*, 14(3):335 – 344.

[195] Tessler, A. and Spiridigliozzi, L. (1986). Curved beam elements with penalty relaxation. *International Journal for Numerical Methods in Engineering*, 23(12):2245–2262.

[196] Timoshenko, S. P. (1922). On the transverse vibrations of bars of uniform cross section. *Philosophical Magazine*, 43:125–131.

[197] Touratier, M. (1991). An efficient standard plate theory. *International Journal of Engineering Science*, 29(8):901 – 916.

[198] Tufekci, E. and Arpaci, A. (2006). Analytical solutions of in-plane static problems for non-uniform curved beams including axial and shear deformations. *Structural Engineering & Mechanics*, 22(2):131 – 150.

[199] Turner, M., Clough, R., Martin, H., and Topp, L. (1956). Stiffness and deflexion analysis of complex structures. *Journal of the Aeronautical Sciences*, 23(9):805–823.

[200] Varadan, T. and Bhaskar, K. (1991). Bending of laminated orthotropic cylindrical shells—an elasticity approach. *Composite Structures*, 17(2):141 – 156.

[201] Vidal, P., Gallimard, L., and Polit, O. (2015). Assessment of variable separation for finite element modeling of free edge effect for composite plates. *Composite Structures*, 123:19 – 29.

[202] Vidal, P., P. O. (2011). A sine finite element using a zig-zag function for the analysis of laminated composite beams. *Composites*, 43:1671–1682.

[203] Vlasov, V. (1961). *Thin-walled elastic beams*. Israel Program for Scientific Translations.

[204] Wang, A. and Crossman, F. W. (1977). Some new results on edge effect in symmetric composite laminates. *Journal of Composite Materials*, 11(1):92–106.

[205] Washizu, K. (1964). Some considerations on a naturally curved and twisted slender beam. *Journal of Mathematics and Physics*, 43(1-4):111–116.

[206] Washizu, K. (1968). *Variational Methods in Elasticity and Plasticity*. Pergamon, Oxford.

[207] Washizu, K. (1974). *Variational Methods in Elasticity and Plasticity*. Elsevier Science & Technology.

[208] Whitcomb, J., Raju, I., and Goree, J. (1982). Reliability of the finite element method for calculating free edge stresses in composite laminates. *Computers and Structures*, 15(1):23 – 37.

[209] Whitney, J. and Sun, C. (1973). A higher order theory for extensional motion of laminated composites. *Journal of Sound and Vibration*, 30(1):85 – 97.

[210] Whitney, J. M. (1972). Stress analysis of thick laminated composite and sandwich plates. *Journal of Composite Materials*, 6(3):426–440.

[211] Willberg, C. (2013). *Development of a new isogeometric finite element and its application for Lamb wave based structural health monitoring*. PhD thesis, Institute for Mechanics, Otto-von-Guericke-University of Magdeburg.

[212] Willberg, C., Duczek, S., Perez, J. V., Schmicker, D., and Gabbert, U. (2012). Comparison of different higher order finite element schemes for the simulation of Lamb waves. *Computer Methods in Applied Mechanics and Engineering*, 241-244:246 – 261.

[213] Williams, T. O. (2005a). A three-dimensional, higher-order, elasticity-based micromechanics model. *International Journal of Solids and Structures*, 42(3–4):971 – 1007.

[214] Williams, T. O. (2005b). A two-dimensional, higher-order, elasticity-based micromechanics model. *International Journal of Solids and Structures*, 42(3–4):1009 – 1038.

[215] Yim, H. and Choi, Y. (2000). Simulation of ultrasonic waves in various types of elastic media using the mass spring lattice model. *Materials Evaluation*, 58(7):889 – 896.

[216] Yin, W. (1994). Free-edge effects in anisotropic laminates under extension, bending, and twisting, part ii: Eigenfunction analysis and the results for symmetric laminates. *Journal of Applied Mechanics*, 61(2):416–421.

[217] Yu, W. (2016). A unified theory for constitutive modeling of composites. *Journal of Mechanics of Materials and Structures*, 11(4):379–411.

[218] Yu, W. and Hodges, D. (2004). An asymptotic approach for thermoelastic analysis of laminated composite plates. *Journal of Engineering Mechanics*, 130(5):531–540.

[219] Yu, W., Hodges, D., and Ho, J. (2012). Variational asymptotic beam sectional analysis - an updated version. *International Journal of Engineering Science*, 59:40 – 64. Special Issue in honor of Victor L. Berdichevsky.

[220] Yu, W. and Liu, X. (2017). Swiftcomp. https://cdmhub.org/resources/scstandard.

[221] Yu, W. and Tang, T. (2007). Variational asymptotic method for unit cell homogenization of periodically heterogeneous materials. *International Journal of Solids and Structures*, 44(11):3738 – 3755.

[222] Yuan, K.-Y., Huang, Y.-S., and Pian, T. H. H. (1993). New strategy for assumed stresses for 4-node hybrid stress membrane element. *International Journal for Numerical Methods in Engineering*, 36(10):1747–1763.

[223] Zienkiewicz, O. and Hinton, E. (1976). Reduced integration, function smoothing and non-conformity in finite element analysis (with special reference to thick plates). *Journal of the Franklin Institute*, 302(5):443 – 461.

[224] Zienkiewicz, O. and Taylor, R. (1977a). *The finite element method*, volume 3. McGraw-hill London.

[225] Zienkiewicz, O. and Taylor, R. (1977b). *The finite element method*, volume 3. McGraw-hill London.

[226] Zienkiewicz, O. C., Taylor, R. L., and Too, J. M. (1971). Reduced integration technique in general analysis of plates and shells. *International Journal for Numerical Methods in Engineering*, 3(2):275–290.

[227] Zlámal, M. (1978). Superconvergence and reduced integration in the finite element method. *Mathematics of Computation*, 32(143):663–685.

Appendix A

2D Legendre polynomials

This section shows all the expansion functions of HLE models from the first to the eighth polynomial order. Note that the set of functions of a HLp model includes all the polynomials from 1st to p^{th} order.

1st order

$$\begin{aligned}F_1 =&\frac{1}{4}(1-r)(1-s)\\ F_2 =&\frac{1}{4}(1+r)(1-s)\\ F_3 =&\frac{1}{4}(1+r)(1+s)\\ F_4 =&\frac{1}{4}(1-r)(1+s)\end{aligned}$$

2nd order

$$\begin{aligned}F_5 =&\frac{1}{2}(1-s)\sqrt{6}(r^2-1)/4\\ F_6 =&\frac{1}{2}(1+r)\sqrt{6}(s^2-1)/4\\ F_7 =&\frac{1}{2}(1+s)\sqrt{6}(r^2-1)/4\\ F_8 =&\frac{1}{2}(1-r)\sqrt{6}(s^2-1)/4\end{aligned}$$

3^{rd} order

$$
\begin{aligned}
F_9 &= \frac{1}{2}(1-s)\sqrt{10}r(r^2-1)/4 \\
F_{10} &= \frac{1}{2}(1+r)\sqrt{10}s(s^2-1)/4 \\
F_{11} &= \frac{1}{2}(1+s)\sqrt{10}r(r^2-1)/4 \\
F_{12} &= \frac{1}{2}(1-r)\sqrt{10}s(s^2-1)/4
\end{aligned}
$$

4^{th} order

$$
\begin{aligned}
F_{13} &= \frac{1}{2}(1-s)\sqrt{14}(5r^2-1)(r-1)(r+1)/16 \\
F_{14} &= \frac{1}{2}(1+r)\sqrt{14}(5s^2-1)(s-1)(s+1)/16 \\
F_{15} &= \frac{1}{2}(1+s)\sqrt{14}(5r^2-1)(r-1)(r+1)/16 \\
F_{16} &= \frac{1}{2}(1-r)\sqrt{14}(5s^2-1)(s-1)(s+1)/16 \\
F_{17} &= \frac{1}{16}\sqrt{6}(r^2-1)\sqrt{6}(s^2-1)
\end{aligned}
$$

5^{th} order

$$
\begin{aligned}
F_{18} &= \frac{1}{2}(1-s)3\sqrt{2}r(7r^2-3)(r-1)(r+1)/16 \\
F_{19} &= \frac{1}{2}(1+r)3\sqrt{2}s(7s^2-3)(s-1)(s+1)/16 \\
F_{20} &= \frac{1}{2}(1+s)3\sqrt{2}r(7r^2-3)(r-1)(r+1)/16 \\
F_{21} &= \frac{1}{2}(1-r)3\sqrt{2}s(7s^2-3)(s-1)(s+1)/16 \\
F_{22} &= \frac{1}{16}\sqrt{10}r(r^2-1)\sqrt{6}(s^2-1) \\
F_{23} &= \frac{1}{16}\sqrt{6}(r^2-1)\sqrt{10}s(s^2-1)
\end{aligned}
$$

6^{th} order

$$F_{24} = \frac{1}{2}(1-s)\sqrt{22}(r-1)(r+1)(21r^4-14r^2+1)/32$$
$$F_{25} = \frac{1}{2}(1+r)\sqrt{22}(s-1)(s+1)(21s^4-14s^2+1)/32$$
$$F_{26} = \frac{1}{2}(1+s)\sqrt{22}(r-1)(r+1)(21r^4-14r^2+1)/32$$
$$F_{27} = \frac{1}{2}(1-r)\sqrt{22}(s-1)(s+1)(21s^4-14s^2+1)/32$$
$$F_{28} = \frac{1}{64}\sqrt{14}(5r^2-1)(r-1)(r+1)\sqrt{6}(s^2-1)$$
$$F_{29} = \frac{1}{16}\sqrt{10}r(r^2-1)\sqrt{10}s(s^2-1)$$
$$F_{30} = \frac{1}{64}\sqrt{6}(r^2-1)\sqrt{14}(5s^2-1)(s-1)(s+1)$$

7^{th} order

$$F_{31} = \frac{1}{2}(1-s)\sqrt{26}r(r-1)(r+1)(33r^4-30r^2+5)/32$$
$$F_{32} = \frac{1}{2}(1+r)\sqrt{26}s(s-1)(s+1)(33s^4-30s^2+5)/32$$
$$F_{33} = \frac{1}{2}(1+s)\sqrt{26}r(r-1)(r+1)(33r^4-30r^2+5)/32$$
$$F_{34} = \frac{1}{2}(1-r)\sqrt{26}s(s-1)(s+1)(33s^4-30s^2+5)/32$$
$$F_{35} = \frac{1}{64}3\sqrt{2}r(7r^2-3)(r-1)(r+1)\sqrt{6}(s^2-1)$$
$$F_{36} = \frac{1}{64}\sqrt{14}(5r^2-1)(r-1)(r+1)\sqrt{10}s(s^2-1)$$
$$F_{37} = \frac{1}{64}\sqrt{10}r(r^2-1)\sqrt{14}(5s^2-1)(s-1)(s+1)$$
$$F_{38} = \frac{1}{64}\sqrt{6}(r^2-1)3\sqrt{2}s(7s^2-3)(s-1)(s+1)$$

8^{th} order

$$
\begin{aligned}
F_{39} =& \frac{1}{2}(1-s)\sqrt{30}(r-1)(r+1)(429r^6-495r^4+135r^2-5)/256 \\
F_{40} =& \frac{1}{2}(1+r)\sqrt{30}(s-1)(s+1)(429s^6-495s^4+135s^2-5)/256 \\
F_{41} =& \frac{1}{2}(1+s)\sqrt{30}(r-1)(r+1)(429r^6-495r^4+135r^2-5)/256 \\
F_{42} =& \frac{1}{2}(1-r)\sqrt{30}(s-1)(s+1)(429s^6-495s^4+135s^2-5)/256 \\
F_{43} =& \frac{1}{128}\sqrt{22}(r-1)(r+1)(21r^4-14r^2+1)\sqrt{6}(s^2-1) \\
F_{44} =& \frac{1}{64}3\sqrt{2}r(7r^2-3)(r-1)(r+1)\sqrt{10}s(s^2-1) \\
F_{45} =& \frac{1}{256}\sqrt{14}(5r^2-1)(r-1)(r+1)\sqrt{14}(5s^2-1)(s-1)(s+1) \\
F_{46} =& \frac{1}{64}\sqrt{10}r(r^2-1)3\sqrt{2}s(7s^2-3)(s-1)(s+1) \\
F_{47} =& \frac{1}{128}\sqrt{6}(r^2-1)\sqrt{22}(s-1)(s+1)(21s^4-14s^2+1)
\end{aligned}
$$